Investigation of Perovskite/Spinel Oxides−Based Oxygen Electrocatalysts for Electrochemical Energy Storage and Conversion

by

Yaqian Zhang

A thesis submitted in partial fulfillment of the requirements for the degree of

Doctor of Philosophy

in

Chemical Engineering

Department of Chemical and Materials Engineering
University of Alberta

Abstract

Energy storage and conversion devices, such as fuel cells, metal-air batteries (MABs) and water electrolyzers, provide significant approaches for renewable energy storage, which address the challenge of intermittent generation from renewable energy system. However, the practical application of fuel cells and/or MABs is often hampered by the sluggish kinetics of oxygen reduction reaction (ORR) and/or oxygen evolution reaction (OER). The development of efficient, stable and low-cost oxygen electrocatalysts is critical to realize the practically viable electrochemical devices, and to advance those sustainable technologies. So far, noble-metals-based electrocatalysts, such as Pt, Ir, Ru, have been exclusively used as electrochemical catalysts in oxygen reaction and hydrogen reaction. Although the precious metal-based-electrocatalyst demonstrated remarkable catalytic activities, their high cost and limited availability have impeded their practical application.

For transition metal oxides to become more competitive oxygen reduction reaction (ORR) catalysts, substantial progress is required to advance their enhanced catalytic activity and durability. I demonstrated a novel method to fabricate high-performance perovskite electrocatalyst *via* combining nano architecture designs, internal structures engineering, and Ag nanoparticles (NPs) *in situ* exsolution. The synthesized Ag-$(PrBa)_{0.95}Mn_2O_5$ (Ag-$PBMO_5$) catalyst exhibits favorable ORR catalytic activity in terms of overpotential ($E_{onset} \sim 0.92$ V vs RHE and $E_{1/2} \sim 0.81$ V vs RHE), and outperforms the Pt/C with respect to durability. Several characterization techniques, including transmission electron microscopy (TEM), X-ray energy dispersive spectroscopy (EDX), X-ray photoelectron spectroscopy (XPS) etc., were applied alongside density functional theory calculations to understand the possible active sites and the synergistic coupling effects that

contributed to the high ORR performance. The introduction of a secondary electrocatalyst (Ag NPs) through *in situ* exsolution leads to significant ligand effect and facilitates electron transfer and ion migration within the oxygen reduction reaction.

Inspired by the optimal performance achieved on perovskite oxides with multicomponent and sufficient active centers through *in-situ* exsolution, further effort was made towards this direction in developing cobalt phosphide - $PrBa_{0.5}Sr_{0.5}Co_{1.5}Fe_{0.50}O_{5+\delta}$ (CoP-PBSCF). The CoP-PBSCF was successfully prepared *via* an *in-situ* exsolution and post phosphatization process. The integration of CoP and perovskite oxides endowed synergistically active sites, which subsequently contributed to extended functionalities and better activities. The CoP-PBSCF demonstrates a significantly enhanced trifunctional electrocatalytic activity towards ORR/OER and hydrogen evolution reaction (HER). The as-synthesized multifunctional electrocatalysts have been successfully applied for the application of both Zn-air batteries and overall water splitting.

Besides non-stoichiometric perovskite oxides, other alternative oxygen electrocatalysts could be spinel oxides. Ultrafine sub-10 nm $MnFe_2O_4$ crystals were grown on the ultrathin $NiCo_2O_4$ nanosheets, leading to a highly effective surface area and a strong cooperative effect. The distinct architecture and complex composition afford an excellent bifunctional oxygen electrocatalytic activity in alkaline condition. The practical rechargeable Zn-air battery with the resulting hybrid ($MnFe_2O_4$/$NiCo_2O_4$) electrocatalyst demonstrates a high round-trip efficiency (a low discharge-charge voltage gap of 0.81 V at a reversible current density of 10 mA cm^{-2}) and an outstanding durability, which outperforms the commercial bifunctional Pt/Ru/C electrocatalyst. This work holds the promise to open a new possibility in designing novel transition metal based bifunctional catalysts as the alternatives to the noble metals for the application in energy related devices.

Preface

This thesis is an original work by Yaqian Zhang (Y. Q. Zhang) under the supervision of Dr. Jing-Li Luo (Luo, J-L.).

Chapter 1 is the introduction that contains the background knowledge and principles of electrochemical oxygen reduction/evolution at room and elevated temperatures.

Chapter 2 covers the literature survey of oxygen electrocatalysts for electrochemical storage and conversion based on the previous studies.

Chapter 3 briefly introduces the employed methodologies and characterizations.

Chapter 4 of this thesis has been published as Y. Q. Zhang, H. B. Tao, J. Liu, Y. F. Sun, J. Chen, B. Hua, T. Thundat, J. L. Luo, A rational design for enhanced oxygen reduction: Strongly coupled silver nanoparticles and engineered perovskite nanofibers. Nano Energy 38 (2017) 392−400.

Chapter 5 of this thesis is to be submitted to Advanced Energy Materials for publication as Y. Q. Zhang, H. B. Tao, J. L. Luo, *In situ* growth of CoP nanoparticles on perovskite oxide nanofibers as an optimized trifunctional electrocatalysts in alkaline condition.

Chapter 6 of this thesis has been published as Y. Q. Zhang, M. Li, B. Hua, Y. Wang, Y. F. Sun, J. L. Luo, A strongly cooperative spinel nanohybrid as an efficient bifunctional oxygen electrocatalyst for oxygen reduction reaction and oxygen evolution reaction. Appl. Catal., B. 236 (2018) 413−419.

Chapter 7 of the thesis includes the summary and future prospects.

Appendix I of this thesis has been published as Y. Q. Zhang, J. H. Li, Y. F. Sun, B. Hua, J. L. Luo, Highly active and redox-stable Ce-doped LaSrCrFeO-based cathode catalyst for CO_2 SOECs. ACS Appl. Mater. Interfaces. 8 (2016) 6457−6463.

Appendix II of this thesis has been published as B. Hua, Y.Q. Zhang, N. Yan, M. Li, Y.F. Sun, J. Chen, J. Li, J. L. Luo, The excellence of both worlds: developing effective double perovskite oxide catalyst of oxygen reduction reaction for room and elevated temperature applications. Adv Funct. Mater. 26 (2016) 4106.

Chapter 4, 5, 6 and Appendix I are my original work. I was responsible for designing and conducting all the experiments, data collection, data analysis, as well as writing the manuscripts.

Appendix II summarizes the research work conducted in collaboration with Dr. B. Hua in our group. Dr. B. Hua performed the material selections and all the electrochemical test and analysis at elevated temperature. I was responsible for material synthesis and all the electrochemical tests at room temperature.

For the above work, H. B. Tao worked on the DFT simulation part. Dr. J. Liu and Dr. T. Thundat provided valuable instruction and discussion on electrospinning fabrication. Y. Wang was the summer student, who involved in part of material synthesis work. Dr. J. Chen assisted with the TEM characterization and interpretations. Dr. M. Li, Dr. B. Hua and Dr. Y. F. Sun assisted with part of characterization work. Dr. J. H. Li helped with CO_2-TPD and O_2-TPD tests. Dr. J. L. Luo was the supervisory author and was involved in concept formation. Dr. B. Hua, and Dr. J. L Luo provided valuable discussions, comments, suggestions and feedbacks for manuscript writing and revision.

Acknowledgements

First of all, I would like to express my sincerely gratitude to my supervisor, Dr. Jing-Li Luo, for her continuous support, guidance, and great inspiration. The constant critical feedback, and encouragement I received from her helps me in every steps through this journey. She inspired me to always stay motivated, to think critically, to grow as a researcher, and to further pursue my career in research.

My deep appreciation goes to my supervisor committing members, Dr. Anastasia Elias and Dr. Hongbo Zeng for their thoughtful suggestions and assistance during my research progress. I offer my sincere appreciation to Dr. Thomas Thundat. I thank him for his valuable instructions in materials science, and his deep discussions with me in my research project.

I would like to thank all my colleagues, Dr. Yifei Sun, Mr. Hongbiao Tao, Dr. Bin Hua, Dr. Jun Liu, Dr. Subiao Liu, Dr. Meng Li, Dr. Jianhui Li, Dr. Ming Xiong, Dr. Elaheh Davari, Mr. Zhou Chen, Mr. Tengfei Li, Mr. Kaiyang Li, and Dr. Jing Shen for their great help and collaboration during my research in the lab. I would also like to thank our undergraduate students in Dean's Research Program, Mr. Milan Djumic, Miss. Eunbit Cho, and Mr. Daniel Sabac.

I want to acknowledge Dr. Jian Chen from Nanotechnology Research Centre, National Research Council Canada. Thank you for helping conduct the TEM measurements and analysis, for encouraging me to get interested in crystallography and electron microscopy, and for being a great mentor to me.

For technique support and assistant, I would also like to thank Dr. Shihong Xu, Dr. Anqiang He, Dr. Nancy Zhang, Mr. Peng Li and Mrs. Diane Caird for their assistance/suggestions in materials characterizations.

I would like to acknowledge the funding agencies: Natural Sciences and Engineering Research Council of Canada (NSERC), Albert Innovate-Technology Future (AITF) Graduate Scholarship, Chevron Graduate Scholarship, and Captain Thomas Farrell Greenhalgh Memorial Graduate Scholarship.

My special thanks go to my family. Thanks for always being there for me, for raising me with unconditional love, and for encouraging me in the academic path I chose.

Table of Contents

List of Tables

List of Figures

List of Symbols

ΔG	Gibbs free energy
V_M”	Metal vacancies
$V_O^{\bullet\bullet}$	Oxygen vacancies
$M_i^{\bullet\bullet}$	Metal interstitial
O_i”	Oxygen interstitial
e_g	σ*-anti-bonding electron
$E_{1/2}$	Half-wave potential
E_{10}	Potential at mA 10 cm^{-2}
R	Resistances
S	Cross-section area
L	Length
j_L	Measured limited current density
ω	Electrode rotating rate
C_{dl}	Double layer capacitace
R_s	Electrolyte resistance
R_f	Electrode film resistance
R_{ct}	Charge transfer resistance
R_Ω	Ohmic resistances
Eq.	Equation

List of Abbreviations

MABs	Metal-air batteries
ZABs	Zinc-air batteries
ORR	Oxygen reduction reaction
OER	Oxygen evolution reaction
RHE	Reversible hydrogen electrode
SHE	Standard hydrogen potential
PEM	Proton-exchange membrane
HER	Hydrogen evolution reaction
HOR	Hydrogen oxidation reaction
PEMFC	Proton-exchange membrane fuel cells
SOFCs	Solid oxide fuel cells
SOECs	Solid oxide electrolysis cells
DFT	Density functional theory
LSV	Linear sweep voltammetry
CV	Cyclic voltammetry
NPs	Nanoparticles
CNTs	Carbon nanotubes
VA-NCNTs	Vertically aligned carbon nanotubes
NPMC	Nitrogen and phosphorus co-doped mesoporous carbon foams
I-V	Current density-voltage
I-P	Current density-power density
BSCF	$Ba_{0.5}Sr_{0.5}Co_{0.8}Fe_{0.2}O_{3-\delta}$

CB	Carbon black
AB	Acetylene black
rGO	Reduced-Graphene oxide
BSCFO	$Ba_{0.5}Sr_{0.5}Co_{0.8}Fe_{0.2}O_{3-\delta}$
LSCO	$La_{0.8}Sr_{0.2}CoO_{3-\delta}$
NBSCO	$NdBa_{0.25}Sr_{0.75}Co_2O_{5+\delta}$
3DOM-LFO	3D macroporous $LaFeO_3$
NP-LFO	$LaFeO_3$ nanoparticles
LSCO	$La_{0.5}Sr_{0.5}CoO_{2.91}$
Fe_3O_4/ N-GAs	Fe_3O_4/ N-doped graphene aerogels
Co_3O_4 NW	Co_3O_4 nanowires
GDL	Gas diffusion layer
RDE	Rotation disk electrode
K-L	Koutecky-Levich equation
EIS	Electrochemical Impedance Spectroscopy
J-V	Current-voltage
XRD	X-ray Diffraction
FESEM	Field Emission Scanning Electron Microscopy
EDX	Energy dispersive X-ray spectroscopy
TEM	Transmission electron microscopy
ETEM	Environmental transmission electron microscope
STEM	Scanning transmission electron microscopy
TGA	Thermogravimetry analysis

XPS	X-ray photoelectron spectroscopy
BET	Brunauer–Emmett–Teller
O_2-TPD	O_2 Temperature programmed desorption
CO_2-TPD	CO_2 Temperature programmed desorption
TEC	Thermal expansion coefficient
NPs	Nanoparticles
$PBMO_5$	$(PrBa)_{0.95}Mn_2O_{5+\delta}$
TG-DTA	Thermogravimetric and differential thermal analysis
HRTEM	High resolution electron transmission electron microscopy
HAADF	High angle annular dark field
FFT	Fast Fourier transformation
BE	Binding energy
E_{onset}	Onset potential
$E_{1/2}$	Half wave potential
E_{10}	Potential at 10 mA cm^{-2}
DMF	N-dimethylformamide
PVP	Poly(vinylpyrrolidone)
$PBAMO_3$	$(Pr_{0.5}Ba_{0.5})_{0.95}Ag_{0.05}MnO_{3-\delta}$
Ag + $PBMO_5$	Ag + $Pr_{0.95}Ba_{0.95}Mn_2O_{5-\delta}$
VASP	Vienna Ab initio Simulation Package
PAW	Projector-augmented plane-wave
GGA	Generalized gradient approximation
PW91	Perdew and Wang (PW91)

CoP-PBSCF	CoP – $PrBa_{0.5}Sr_{0.5}Co_{1.5}Fe_{0.5}O_{5+\delta}$
A-PBSCF	$(PrBa_{0.5}Sr_{0.5})_{0.95}(Co_{1.5}Fe_{0.5})_{0.95}Co_{0.05}O_{5+\delta}$
STEM-BF	Scanning transmission electron microscopy Bright-field
NSs	Nanosheets
PABA	p-aminobenzoic acid
ICP-AES	Inductively coupled plasma-atomic emission spectroscopy
CPE	Constant phase elements
GC	Glassy carbon
LSCrF	$La_{0.7}Sr_{0.3}Cr_{0.5}Fe_{0.5}O_{3-\delta}$
TPB	Triple-phase boundaries
LSCM	$La_{0.75}Sr_{0.25}Cr_{0.5}Mn_{0.5}O_{3-\delta}$
LSCrF	$La_{0.7}Sr_{0.3}Cr_{0.5}Fe_{0.5}O_{3-\delta}$
Ce-LSCrF	$La_{0.65}Sr_{0.3}Ce_{0.05}Cr_{0.5}Fe_{0.5}O_{3-\delta}$
PEMFCs	Proton exchange membrane fuel cells
OCV	Open-circuit voltage
PPD	Peak power density

Chapter 1. Introduction

In the Fifth Assessment Report from the Intergovernmental Panel on Climate Change, significant increase of total greenhouse gas (GHG) emission has been stated from the year of 1970 to 2010.[1] The increased GHG emission is mainly resulted from the unprecedented growth of energy demand and industrial processes. The accompanying issues on climate change have sparked great interests in searching for renewable energy.[1b]

Energy conversion and storage devices, which can address the challenge of daily and seasonal intermittent generation of renewable energy, provide promising approaches for the utilization of renewable energy. In particular, electrochemical conversion and storage devices, such as regenerative fuel cells and batteries, are among the key technologies in the game-changing movement of green transportations and portable electronics. In batteries and fuel cells, electricity is generated by converting chemical energy into electrical energy *via* redox reactions. The redox reactions, including oxidation and reduction half reactions, take place at the anode and cathode, respectively, while a potential difference is built up between the opposite electrodes. On the contrary, the energy is stored by transforming the electrical energy into the form of chemical energy through a reversed reaction. The difference between reversible fuel cells and batteries, has to do with where the energy is stored.

Fuel cells are open systems where chemical energy is delivered from the outside of the cells, in the form of hydrogen and hydrocarbon while for conventional batteries, energy storage and conversion generally occur in the same component inside the system.[1b] As a promising post lithium-ion technology, metal-air batteries (MABs) combine the characteristics adopted from both

conventional batteries (a pure metal as the anode/negative electrode) and fuel cells (oxygen from air as the reactant). [1a, 2]

Figure 1.1 shows the comparison of energy and power densities of various devices. As compared to the secondary batteries such as lithium ion batteries, lead–acid batteries and nickel–cadmium batteries, MABs show a significantly higher energy density, approaching to that of fuel cells.[3] Moreover, among MABs, zinc-air batteries (ZABs) possess the highest commericial available energy density, but with lower manufacturing cost, which makes them the promising energy devices of next generation.[1a] However, the efficiency of both fuel cells and MABs is still being limited by the sluggish kinetics of the oxygen reduction reaction (ORR) and/or oxygen evolution reaction (OER) in the air electrode.

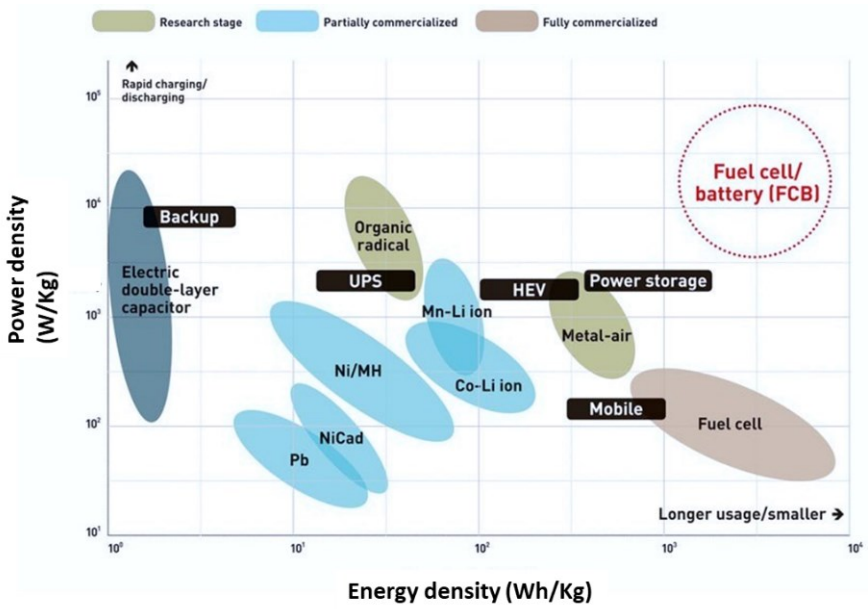

Figure 1.1 Ragone plot comparing the performance of various batteries (energy density vs. output density). [3]

1.1 Basic introduction of the electrochemical oxygen electrocatalysis

The ORR is a key electrochemical reaction in fuel cells and MABs, which involves multistep electron transfer and complicated intermediate species. Typically, there are two different proposed ORR reaction mechanisms known as the direct four-electron reaction and a two-plus-two electron transfer mechanism. The electrochemistry taking place at the air electrode varies with the employed electrolytes (aqueous, nonaqueous and solid-state). These electrochemical reactions are listed as follows[4]:

For ORR occurring in aqueous alkaline solution,

Direct four-electron reaction:

$$O_2 + 2H_2O + 4e^- \rightarrow 4OH^- \quad \text{(Eq. 1.1)}$$

Two-plus-two electron transfer reaction:

$$O_2 + H_2O + 2e^- \rightarrow OH^- + HO_2^- \quad \text{(Eq.1.2)}$$

$$HO_2^- + H_2O + 2e^- \rightarrow 3OH^- \quad \text{(Eq. 1.3)}$$

For ORR occurring in aqueous acid solution,

Direct four-electron reaction:

$$O_2 + 4H^+ + 4e^- \rightarrow 2H_2O \quad \text{(Eq. 1.4)}$$

Two-plus-two electron transfer reaction:

$$O_2 + 2H^+ + 2e^- \rightarrow H_2O_2 \quad \text{(Eq. 1.5)}$$

$$H_2O_2 + 2H^+ + 2e^- \rightarrow 2H_2O \quad \text{(Eq. 1.6)}$$

For ORR occurring in an aprotic electrolyte,

$$O_2 + 4e^- \rightarrow 2O^{2-} \quad \text{(Eq. 1.7)}$$

The standard potential for the half-cell ORR reaction is 1.23 V vs. reversible hydrogen electrode (RHE) at room temperature. When the RHE potential is used as a reference, the thermodynamic free energy (ΔG) becomes pH independent, and the measured potential (vs. RHE) does not change with the pH.[5] When we correlate pH-dependent standard hydrogen potential (SHE) and the PH-independent RHE, the following equation is used:

$$E(RHE) = E(SHE) + \frac{RT}{nF}\ln\frac{p(H2)^{1/2}}{a_{H+}} = E(SHE) + 0.0591 \times pH \quad \text{(Eq. 1.8)}$$

The OER is a reverse process of the ORR. Oxygen is generated at the triple phase boundary of the electrode when a certain potential is applied to the system. The OER is of prime importance for the application of MABs and electrolysis. Similarly, when OER happens in MABs, proton-exchange membrane (PEM) electrolysis and solid oxide electrolysis cells, the OER also varies with different electrolytes.

For OER occurring in alkaline solution:

$$4OH^- \rightarrow O_2 + 2H_2O + 4e^- \quad \text{(Eq. 1.9)}$$

For OER occurring in aqueous acid solution:

$$2H_2O \rightarrow O_2 + 4H^+ + 4e^- \quad \text{(Eq. 1.10)}$$

For OER occurring in an aprotic electrolyte:

$$2O^{2-} \rightarrow O_2 + 4e^- \quad \text{(Eq. 1.11)}$$

Figure 1.2a illustrates the hydrogen and oxygen cycle for energy storage and conversion. In a similar manner, rather than using H_2 for energy storage, a metal electrode, such as Zn, Al, and Li, could be used as anode/negative electrode in MABs.[6] Figure 1.2b shows that a large overpotential is often associated with the oxygen electrocatalysis in fuel cell and water splitting.[6] The sluggish oxygen kinetics inevitably impede the efficiency and capacity of these devices in reversible fuel cells or MABs, thus limiting the application of the fuel cells and MABs.[7] Advancing the electrochemical storage devices by increasing their energy efficiency, reliability, life-time and safety is of paramount importance for the sustainable future. Therefore, extensive studies have been devoted to developing efficient oxygen electrocatalysts with high activity, low cost and high durability for ORR and/or OER process.

To date, the state-of-the-art oxygen electrocatalysts for the ORR are Pt/C and Pt-alloy/C, while the bifunctional oxygen electrocatalysts are Pt/Ru and Pt/Ir based electrocatalysts. However, the high cost and low availability of Pt and Pt-based electrocatalysts hinder their applications in fuel cells and MABs.[8] Unlike the acidic environment of proton-exchange membrane fuel cells (PEMFC), the employment of alkaline solution in MABs enables the utilization of a wide range of non-precious metal-oxide electrocatalysts.[9] This study focuses on developing highly active non-stoichiometric electrocatalysts towards ORR and/or OER in alkaline solution. In general, these electrocatalysts can also be utilized as an electrode material in solid oxide fuel cells since there is

a remarkable overlap. In the Appendix II, we show that some double perovskite oxides with ordered structure and sufficient oxygen vacancies, could be employed as oxygen electrocatalysts at room and elevated temperatures, and these electrocatalysts demonstrated excellent performances in both worlds.

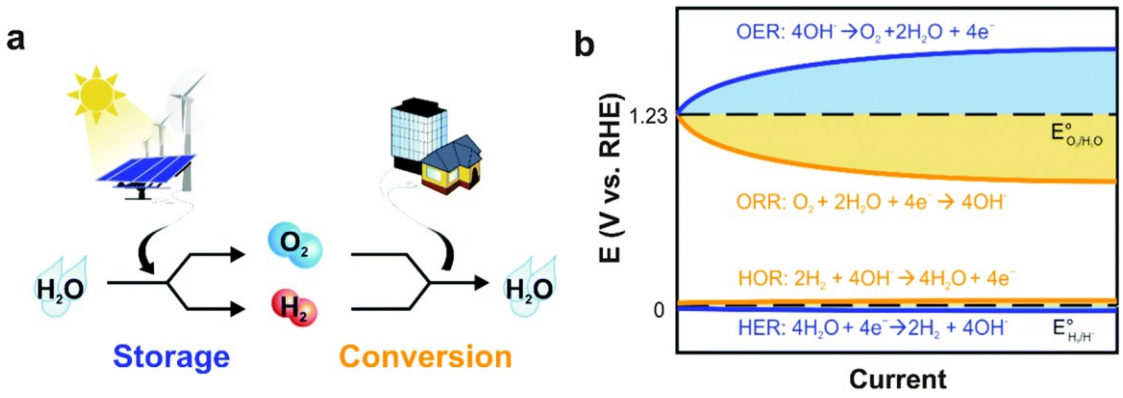

Figure 1.2 (a) Energy storage and conversion through H_2 and O_2. (b) Schematic illustration of the overpotential associated with OER, ORR, hydrogen evolution reaction (HER) and hydrogen oxidation reaction (HOR).[6] Reprinted with permission from Ref 6 Copyright (2015) Royal Society of Chemistry.

1.2 Content of the thesis

There are 7 chapters in this thesis. Chapter 1 begins with an introduction, then lists the contents of thesis. Chapter 2 is a literature review of oxygen electrocatalysts at room and elevated temperatures based on the previous studies. Chapter 3 introduces the employed methodologies and characterizations. Chapter 4 presents and discusses the design of strongly coupled silver nanoparticles and engineered perovskite nanofibers as the electrocatalysts for ORR. Chapter 5 describes and discusses the development of *in situ* growth of CoP nanoparticles on perovskite

oxide nanofibers as the optimized trifunctional electrocatalysts (ORR, OER, HER) in alkaline condition. Chapter 6 presents the synthesis of strongly cooperative spinel nanohybrids and demonstrates its application as an efficient bifunctional oxygen electrocatalyst for ORR and OER. Finally, the main conclusions as the achievements of this dissertation as well as the future prospects are presented in Chapter 7.

Besides the as-mentioned application in electrochemical devices at room temperature, the non-stoichiometric perovskite oxides have also been explored as efficient electrocatalysis in CO_2 reduction at elevated temperature in solid oxide electrolysis cells (SOECs). This part has been summarized in Appendix I. The Appendix II presents the development effective double perovskite oxide catalyst and demonstrates its excellent ORR electrocatalytic activity for room and elevated temperature applications.

1.3 References

1. (a) Edenhofer, O.; Pichs-Madruga, R.; Sokona, Y.; Seyboth, K.; Matschoss, P.; Kadner, S.; Zwickel, T.; Eickemeier, P.; Hansen, G.; Schlömer, S., IPCC special report on renewable energy sources and climate change mitigation. *Prepared By Working Group III of the Intergovernmental Panel on Climate Change, Cambridge University Press, Cambridge, UK* **2011**; (b) Stocker, T. F.; Qin, D.; Plattner, G.; Tignor, M.; Allen, S.; Boschung, J.; Nauels, A.; Xia, Y.; Bex, V.; Midgley, P., Contribution of working group I to the fifth assessment report of the intergovernmental panel on climate change. *Climate change 2013: the physical science basis* **2013**.

2. Choi, N. S.; Chen, Z.; Freunberger, S. A.; Ji, X.; Sun, Y. K.; Amine, K.; Yushin, G.; Nazar, L. F.; Cho, J.; Bruce, P. G., Challenges facing lithium batteries and electrical double-layer capacitors. *Angewandte Chemie International Edition* **2012,** *51* (40), 9994-10024.

3. Tsutsumi., A., Fuel cell/battery system Researchers' keyword commentaries. **2013**.

4. Zhao, Q.; Yan, Z.; Chen, C.; Chen, J., Spinels: controlled preparation, oxygen reduction/evolution reaction application, and beyond. *Chemical reviews* **2017,** *117* (15), 10121-10211.

5. Sawyer, D. T.; Roberts, J. L., *Experimental electrochemistry for chemists*. Wiley: 1974.

6. Hong, W. T.; Risch, M.; Stoerzinger, K. A.; Grimaud, A.; Suntivich, J.; Shao-Horn, Y., Toward the rational design of non-precious transition metal oxides for oxygen electrocatalysis. *Energy & Environmental Science* **2015,** *8* (5), 1404-1427.

7. Wang, Z.-L.; Xu, D.; Xu, J.-J.; Zhang, X.-B., Oxygen electrocatalysts in metal–air batteries: from aqueous to nonaqueous electrolytes. *Chemical Society Reviews* **2014,** *43* (22), 7746-7786.

8. (a) Liang, Y.; Li, Y.; Wang, H.; Zhou, J.; Wang, J.; Regier, T.; Dai, H., Co 3 O 4 nanocrystals on graphene as a synergistic catalyst for oxygen reduction reaction. *Nature materials*

2011, *10* (10), 780; (b) Holewinski, A.; Idrobo, J.-C.; Linic, S., High-performance Ag–Co alloy catalysts for electrochemical oxygen reduction. *Nature chemistry* **2014,** *6* (9), 828.

9. Goswami, C.; Hazarika, K. K.; Bharali, P., Transition metal oxide nanocatalysts for oxygen reduction reaction. *Materials Science for Energy Technologies* **2018**.

Chapter 2. Literature Review

2.1 Metal- and bimetal- based oxygen electrocatalysts

Among all the ORR and OER electrocatalysts, noble metals, such as Pt, Ir and Ru, have drawn the most attention. Owing to their high intrinsic electrocatalytic activity and stability in both acid and alkaline solutions, these electrocatalysts have also been chosen as benchmark electrocatalysts for ORR/OER in many studies. The noble metal-based electrocatalysts are always coupled with high-surface-area support, such as carbon black, graphene and carbon nanotubes, to form the composite catalysts. Among them, platinum carbon is one of the most commonly used metallic electrocatalyst in ORR, and it demonstrated superior catalytic activity in comparison with other noble metals and non-precious metal catalysts.

By using the density functional theory (DFT) calculations, J. K. Nørskov revealed that on various metallic electrocatalysts, the overpotential associated with ORR was strongly correlated to the adsorption energies of the surface intermediates.[1] The model proposed by Nørskov predicted a volcano-shaped relationship between the ORR catalytic activity and the oxygen adsorption energy, which well explained the reasons credited for the best performance of Pt as a metallic catalyst (Figure 2.1a). Since then, the progress made in this respect has served as a descriptor in design and synthesis of electrocatalysts with enhanced activity and stability.

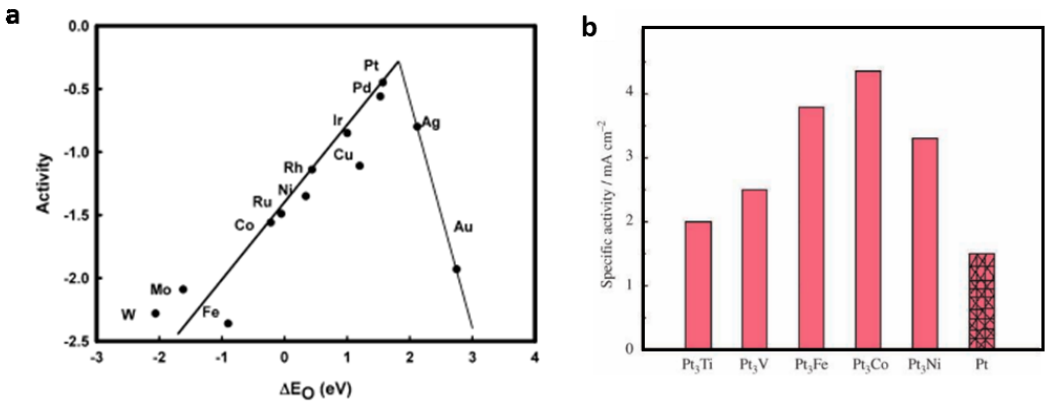

Figure 2.1 (a) The relationship between the oxygen reduction activity and the oxygen binding energy.[1] (b) Specific ORR activity of Pt and Pt_3M polycrystalline at 0.9 V vs. RHE in 0.1 M HClO4.[2] Reprinted with permission from Ref 1. Copyright (2004) American Chemical Society. Reprinted with permission from Ref 2. Copyright (2006) Wiley-VCH.

Nevertheless, the high cost and scarcity of Pt catalyst inevitably impede its practical applications in fuel cells and MABs. Introducing a transition metal to platinum to form Pt-M alloy, or ternary alloy is an effective way to reduce the required Pt loading. Yet it is of equal importance to ensure that the reduced Pt loading would not lead to a sacrificed catalytic activity or stability. At this juncture, DFT calculation successfully works as a descriptor to predict the catalytic activity and to screen different Pt-M alloy catalysts. The volcano shape in Figure 2.1a has also suggested that there is still room for improvement, theoretically, and the catalytic activity of Pt can be further enhanced by lowering the oxygen adsorption energy on Pt surface.[1]

Stamenkovic *et al.* studied a series of Pt_3M polycrystalline thin film compound (M: Ni, Co, Fe, Ti, V) for the ORR. The experimental results, together with DFT calculations, revealed that the electronic structure of the 3d transition metal had a decisive role in determining the electrocatalytic activity of Pt_3M alloy (Figure 2.1b).[2] Generally, an electrocatalyst having a high d-band energy

like Pt strongly binds O_2, which tends to impede the dissociation of surface oxide intermediates. Formation of the Pt alloy by incorporating a certain transition metal element into Pt provides a chance to lower the d-band energy of Pt, thus enhancing the ORR activity. As it is shown in Figure 2.1b, the Pt_3Ni, Pt_3Co, Pt_3Fe, Pt_3Ti and Pt_3V alloys demonstrate superior specific activity compared to the Pt electrocatalyst, among which the Pt_3Co stands out as having the highest catalytic activity.[3]

Apart from the Pt rich Pt_3M based catalysts, progresses have also been made on PtM (M: Fe, Co, Ni, Cu, Zn) based catalysts.[5] For example, Chung *et al* reported an intermetallic ordered face-centered tetragonal PtFe nanoparticles (NPs) coated with a N-doped carbon shell.[6] The PtFe/C catalysts demonstrate a remarkably high ORR activity, with specific activity being 10.5 times higher than the commercial Pt/C. Moreover, core/shell structured electrocatalysts with tunable core size and shell thickness have also been developed. As shown in Figure 2.2, Pd/FePt NPs with a Pd core (5 nm) and a FePt shell (shell thickness of 1 nm) exhibited a significantly enhanced ORR activity in comparison with the Pt/C and Pd/FePt with larger shell thickness.

Bifunctional electrocatalysts, such as Ir@Pt core-shell nanodendrites[7], $Pt_{4.5}Ru_4Ir_{0.5}$ternary catalyst[8], RuO_2–IrO_2/Pt[9] *etc.* have been developed for the application of regenerative fuel cells and MAB. However, the passivation of Pt at positive potentials pertinent to OER results in a poor stability in the cyclic process, which hinders practical application of Pt based bifunctional electrocatalysts.[10] Substantial effort and progress are required to develop alternative bifunctional electrocatalysts with enhanced catalytic activity and durability.

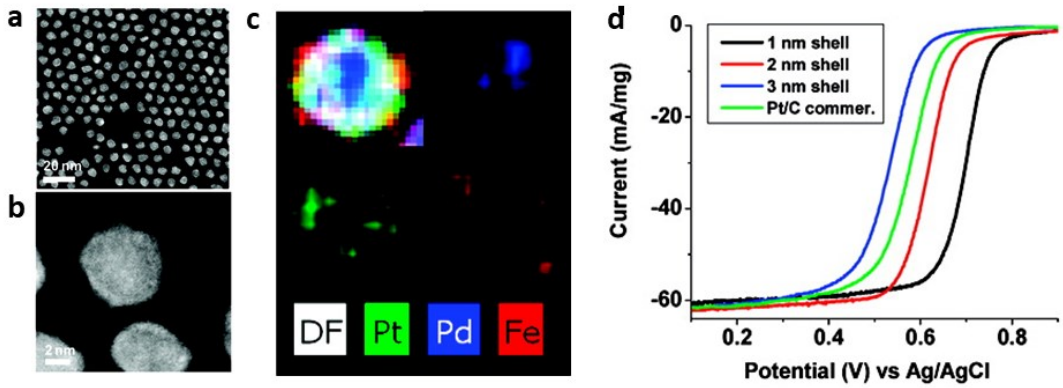

Figure 2.2 (a) and (b) HAADF-STEM at low and high-magnification; (c) elemental mapping images of the Pd/FePt NPs, (d) ORR linear sweep voltammetry (LSV) curves of the commercial Pt/C catalyst and the Pd/FePt NPs with different shell thickness.[4] Reprinted with permission from Ref 4. Copyright (2010) American Chemical Society.

2.2 Carbon based electrocatalysts

In recent years, different dimensional nanostructured carbonaceous materials with large surface areas, high electrical conductivities, substantial reactive sites and excellent mechanical stabilities have been proposed as a non-metal electrocatalyst/matrix for oxygen electrocatalyst in fuel cells and MABs. Fig. 2.3a shows some examples of different nanostructured carbon materials, such as buckminsterfullerene, carbon nanotubes (CNTS), graphene, 3D pillared CNT-graphene architecture. These carbonaceous materials vary from limited dimensions so that they are defined as 0 D, 1 D, 2 D and 3 D nanostructured carbon materials respectively. While intensive research efforts have been made in developing carbon electrocatalyst in the last decade, most studies focused on CNTs and graphene.

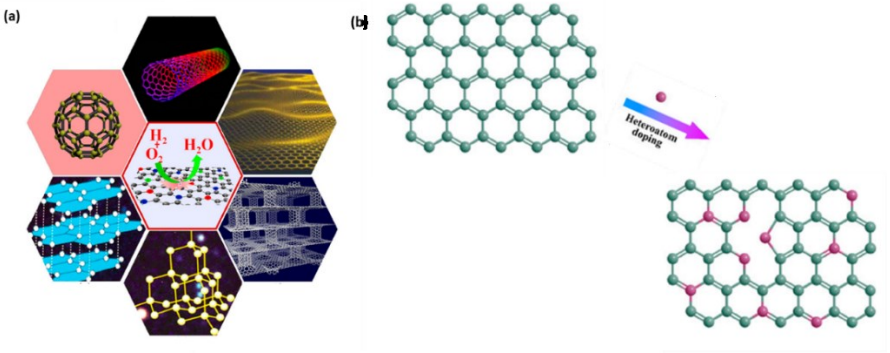

Figure 2.3 Schematic illustration of different dimensional nanostructured carbonaceous materials including graphite, diamond, C60, carbon nanotubes, graphene, and 3D graphene-CNT hybrid. (b) Schematic figure of doping graphitic carbon with heteroatoms.[11-12] Reprinted with permission from Ref 11. Copyright (2015) American Chemical Society. Reprinted with permission from Ref 12. Copyright (2012) American Chemical Society.

Researches carried out in carbon nanomaterials have shown that the introduction of heteroatoms into the graphic structure could effectively tailor the electronic properties, and simultaneously tune the electrocatalytic activities towards various reactions (Figure 2.3b). Non metal elements, such as B, N, P, S, F, have been successfully doped into the graphic lattice, and applied as efficient electrocatalysts towards ORR and OER, among which nitrogen doped carbon nanomaterials have been laboriously investigated.[11] Following the endeavor to synthesize N doped CNT, researchers found that nitrogen dopant in carbon nanotube electrocatalysts can efficiently boost the active sites for ORR. Due to the higher electronegativity of N, carbon atom neighboring to a nitrogen atom generally possesses a more positive charge density. The nitrogen-induced charge distribution was found to affect the O_2 adsorption on the surface of electrocatalysts, facilitating the side-on adsorption over the end-on adsorption mode, thus lowering the required activation overpotential.

The group of Dai reported that the nitrogen-doped vertically aligned carbon nanotubes (VA-NCNTs) demonstrated a remarkable electrocatalytic activity, with a superior stability for ORR. In 0.1 M KOH, the VA-NCNTs demonstrated an onset potential of –0.08 V (vs. Ag/AgCl) and a limited current density of 4.1 mA cm^{-2} at –0.22 V, outperformed the commercial Pt/C electrocatalysts.

Apart from the nitrogen doping, heteroatoms such as S, P, B and F doped graphene have also demonstrated enhanced ORR activities in comparison with the pristine graphene. Some recent efforts have also led to co-doping N doped graphene with a second heteroatom. For example, Qu *et al* reported the synthesis of graphene foams co-doped with nitrogen and boron [13]. The B, N co-doped graphene electrode showed a remarkable ORR activity, with an onset potential of −0.16 V (vs. SCE) for the ORR in 0.1 M KOH and exceeded the pristine graphene (−0.39 V) and single atom (B or N) doped graphene (−0.19 for N-graphene foam and −0.28 V for B-graphene foam). Most recently, a 3D nitrogen and phosphorus co-doped mesoporous carbon foam (NPMC-1000) has been developed by Dai group, and it has been successfully applied as an electrocatalyst in ZABs. [14] The NPMC-1000 catalyst showed a peak power density of 55mW cm^{-2}, approaching to that of the Pt/C catalysts in the primary zinc air batteries (Figure 2.4a). Although the N, P co-doping strategy has been proved to successfully facilitate the bifunctionality of the carbon catalysts, the OER catalytic activity is still inferior to the transition metal oxides based catalysts. An irreversibility property was found in the charging and discharging cyclic test in the rechargeable ZABs, this was likely due to the insufficient catalytic activity towards OER on NPMC-1000 electrode (Figure 2.4c). Strategies like using an optimized tri-electrode configuration in ZABs by separating the ORR and OER electrode have been suggested (Figure 2.4d).[14] Decoupling the ORR and OER electrode allows researchers to fine tune the properties of each electrode independently.

This could be a possible solution to solve the irreversibility problem in the ORR and OER process, albeit with the increased battery volume and complicated manufacturing processes.[15]

Developing robust bifunctional electrode with high electrocatalytic activity towards ORR and OER, and good stability under both reducing and oxidizing conditions is of vital importance. Synergistically coupling highly conductive carbonaceous materials with a secondary phase (e.g., transition metal oxide) is a promising approach towards this goal. This will be discussed in details in Chapter 2.3.

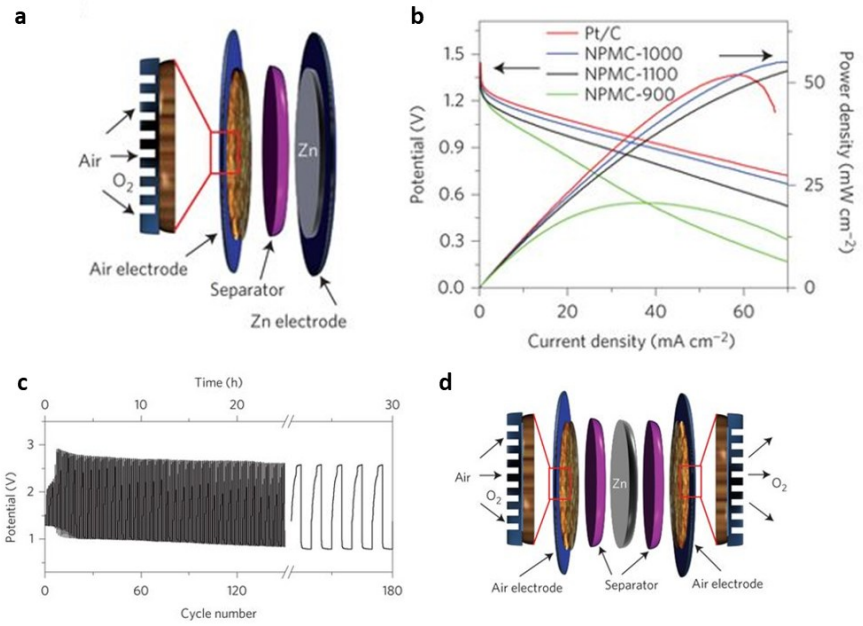

Figure 2.4 (a) Graphic of a primary Zn–air battery with Zn as a metal electrode and electrocatalysts coated GDL as an air electrode; (b) Discharging curves showing the current density-voltage (I-V) and current density-power density (I-P) of primary Zn–air batterie using Pt/C, NPMC-900, NPMC-1000, NPMC-1100 as air electrode. (c) Cyclic test (charging-discharging) based on NPMC-1000 electrocatalyst in rechargeable Zn–air batteries (current density of 2 mA cm^{-2}). (d) Graphic of the Zn–air battery with a three-electrode configuration (integrating the Zn electrode with two different

air electrodes to separate ORR and OER).[14] Reprinted with permission from Ref 14. Copyright (2015) Nature Publishing Group.

2.3 Non-stoichiometric metal oxide as oxygen electrocatalysts

The phenomenon of nonstoichiometry is found in many metal oxide systems, especially in transition metal, rare earth, lanthanide, and actinide oxides, where cations exist in various valence states. The nonstoichiometry within a metal oxide originates in several forms, such as vacancies (metal vacancies V_M" or oxygen vacancies $V_O^{\bullet\bullet}$), interstitial (metal interstitial $M_i^{\bullet\bullet}$ or oxygen interstitial O_i"), vacancies-interstitial pair (Frenkel pair), or non-intrinsic defects caused by cation partial substitution.[16] The defect-induced nonstoichiometry in metal oxides plays an important role in the catalytic system.[17] A fundamental study on oxygen electrocatalysis conducted by Otagawa in 1984 showed that the oxygen electrocatalytic activity of the transition metal strongly correlated to the ability of the loss of lattice oxygen and the ability of the forming oxygen vacancy, since it dictates how oxygenated species binding to the lattice.[18] Moreover, the defects within the nonstoichiometric oxides could significantly affect the electrical conductivities of the oxides, especially the ionic conductivities[19], while an enhanced kinetics of the oxygen electrocatalysis is often associated with an increased oxygen mobility within the metal oxide.[20] Additionally, study conducted by Stevenson revealed that anion charges, such as O^{2-}, could be reversibly stored and released within a nonstoichiometric oxide, owing to the existence of oxygen vacancies.[21] The anion charge storage originated from the oxygen-vacancy-mediated redox opens new possibilities for electrochemical energy storages devices, such as rechargeable batteries and supercapacitors. In this review section, discussion will be focused on perovskite and spinel oxides, with their significant application in fuel cells and MABs as electrocatalysts.

2.3.1 Perovskite oxide

Perovskite oxide, with the formula of ABO_3, is a class of compounds with a unique crystal structure (Figure 2.5a). In perovskite oxide crystal, the larger cation A is 12-fold coordination and the smaller cation B is 6-fold coordination with oxygen anions. Complex perovskite oxide can have different cations being partially substituted at A or B sites. A special partial substituted perovskite oxide is known as double perovskite oxide. The double perovskite oxide having the same coordinates as the single perovskite oxides possesses a general formula of $A_2BB'O_6$, $AA'B_2O_6$ or $AA'BB'O_6$. In an ordered double perovskite, the unit cell is twice of the simple perovskite, while the A, A′ or B, B′ cations are ordered on the A site or B site. Figure 2.5b shows the crystal architecture of a B site ordered double perovskite (Sr_2FeMoO_6), where the Fe cation and Mo cation were arranged repeatedly along c direction.

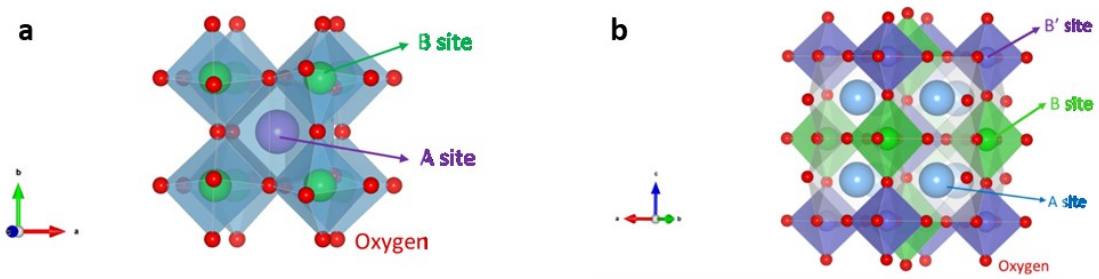

Figure 2.5 (a) Crystal structures of the simple perovskite ABO3 (Structure image generated through Vesta based on CaTiO3 structure, CIF data ID: sd_1713345) (b) Crystal structures of the simple perovskite A2BB'O6 (Structure image generated through Vesta based on Sr_2FeMoO_6 structure, CIF data ID: mp-19127)

The Goldschmidt's tolerance factor, which reveals stability and distortion of the crystal structure, can be used as a guideline for the cation substitution in perovskite oxides:

$$t = \frac{r_A + r_O}{\sqrt{2}(r_B + r_O)} \quad \text{(Eq. 2.1)}$$

In this equation, r_A, r_B and r_O are the ionic radii of *A* and *B* site elements and oxygen ion, respectively. The perovskite oxide maintains its ideal cubic structure when the tolerance factor is equal to 1, and preserves the stability of the structure when $0.89 \leq t \leq 1.06$. The deformantion of structure results in the possibility of ordered and disordered variants, leading to many interesting and intriguing properties, e.g., electrical conductivity and catalyst properties.

With the great structure and chemical flexibilities, perovskite oxides have become a new class of good candidates for the oxygen electrocatalysis.[22] Catalytic active cations can be successfully accommodated within the perovskite structure through cation substitution. The transition metal cations with multiple valence states serve as catalytic center during the ORR and/or OER process. The nonstoichiometric structure, such as oxygen vacancies or excess, helps to facilitate the oxygen anion mobility, and to tailor the electronic structure of B-site cations due to the charge compensation.

2.3.1.1 Electronic structure & intrinsic catalytic activity

Extensive research conducted by Shao-horn Yang group demonstrated that the intrinsic electrochemical catalytic activity for ORR and OER was mainly determined by the B site cation in perovskite oxide.[23] Through a systematic investigation relating electronic properties to electrocatalytic performance on more than 10 perovskite oxides, a volcano trend was found between the OER activity and electron filling in antibonding (e_g) orbitals of B sites. As shown in Figure 2.6b, the OER proceeds *via* 4 electron transfer process on perovskite oxide surface, while the O-O bond formation (step 2) and deprotonation of oxyhydroxide (step 3) were found to be the rate

determined steps (RDS) within the processes. For a perovskite oxide with a low e_g occupancy, the B site cations tend to strongly bind the intermediate oxygenate species, thus hindering the deprotonation of the oxyhydroxide group.[24] For a perovskite oxide with a high e_g occupancy, the B site cations tend to weakly bind the O^{2-} , which impedes the O-O bond formation in the OER process. Transition metals with the σ*-anti-bonding (e_g) orbital occupancy close to unity have shown excellent intrinsic reactivity in OER. The proposed descriptor serves as a design principle for the catalytic active OER electrocatalysts, and successfully direct the synthesis efforts in developing highly active OER catalysts. The $Ba_{0.5}Sr_{0.5}Co_{0.8}Fe_{0.2}O_{3-\delta}$ (BSCF), with an electron configuration of $t_{2g}^5e_g^{1.2}$, demonstrated a high intrinsic activity in OER test, which is consistent with the results predicted by the proposed descriptor. [23a]

Later, Yang and co-workers proved that the design principle and volcano trend also applied to the ORR [23b]. Within the studied lanthanide perovskites, $LaMnO_3$ with an e_g filling close to unity demonstrated the highest ORR activity (Figure 2.6c). Moreover, it has been suggested that a stronger B-O covalency can also contribute to a higher ORR activity. The ORR proceeding on perovskite transition-metal oxide catalysts is a reverse process of OER, while the OH^- regeneration (Step 1) and O_2^{2-}/OH^- displacement (Step 4) and were found to be the RDS for the ORR.[23b] Appropriate e_g occupancy (eg = ~1) and a strong B-O covalence in perovskite oxides were found to effectively facilitate the surface hydroxide displacement and hydroxide regeneration in the ORR. The descriptor proposed by Yang serves as an important design principle for the development of advanced perovskite oxides with high catalytic activity.

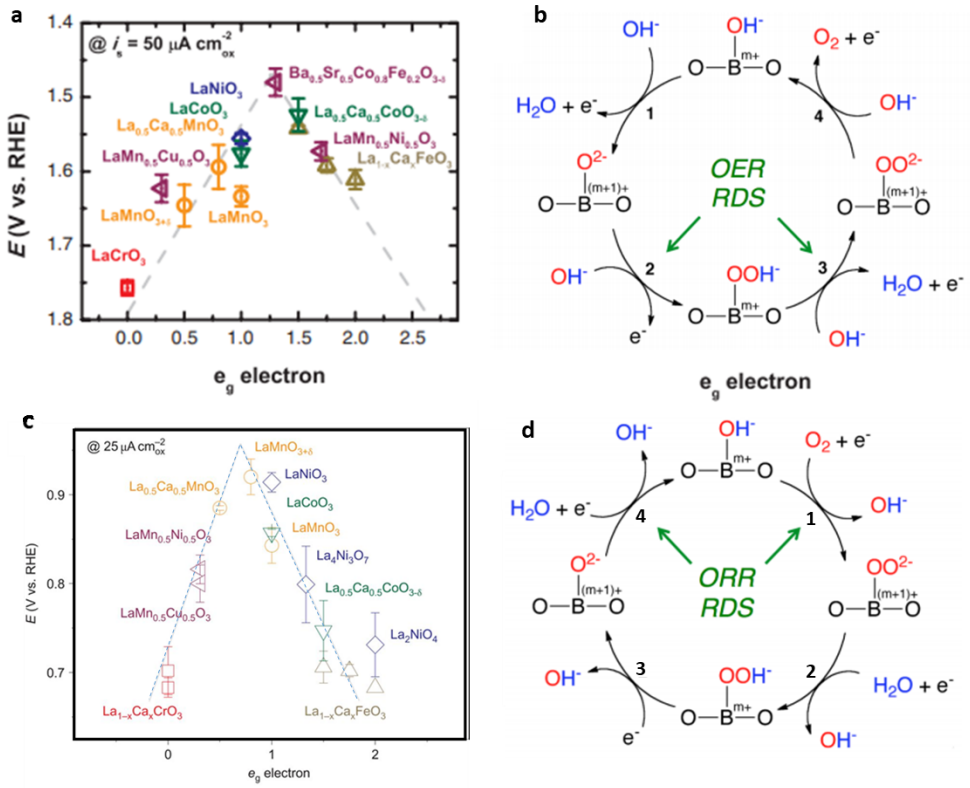

Figure 2.6 (a) The trend of the OER catalytic activity related to the eg orbital filling of the B site cation. (b) Proposed OER mechanism on perovskite oxide catalysts. [23a] (c) The relation between the ORR catalytic activity, and the e_g orbital filling of the B site cation. (d) Proposed ORR mechanism on perovskite oxide electrocatalysts. [23b] Reprinted with permission from Ref 23a. Copyright (2011) American Association for the Advancement of Science. Reprinted with permission from Ref 23b. Copyright (2011) Nature Publishing Group.

The double perovskite oxides have been widely studied as the electrode materials in SOFCs due to their intrinsic catalytic activity[25], among which, the partial substituted perovskite $LnBaM_2O_{5+\delta}$ (M = Co, Mn, Fe etc.) has drawn particular interests.[25d, 26] Due to the difference in ionic radius and polarizability, oxygen vacancy sites existing in the $LnBaM_2O_{5+\delta}$ tend to localize in layers of the rare-earth ions, as shown in Figure 2.7.[27] The ordered oxygen vacancies within the perovskite

oxides lead to a high oxygen diffusion activity and a fast oxygen exchange kinetics. A recent research on double perovskite oxide family $LnBaCo_2O_{5+\delta}$ (Ln=Pr, Sm, Gd and Ho) in alkaline environment revealed that the intrinsic OER catalytic activity of the $LnBaCo_2O_{5+\delta}$ was strongly correlated to the oxygen p band center relative to the Fermi level. It was found that the ionic radius of lanthanide greatly affected the valence state of cobalt cation, and the B-O hybridization extent. From their experimental data and computed results, conclusion can be drawn that with the ionic radius increasing from Ho to Pr, the computed oxygen p band upshifted towards the Fermi level of the B site cation. A closer O p band center to Fermi level will accompany with an enhanced oxygen exchange kinetics and an increased OER activities. The descriptor holds the promise to direct further development of efficient oxygen electrocatalysts towards regenerative fuel cells and MABs.

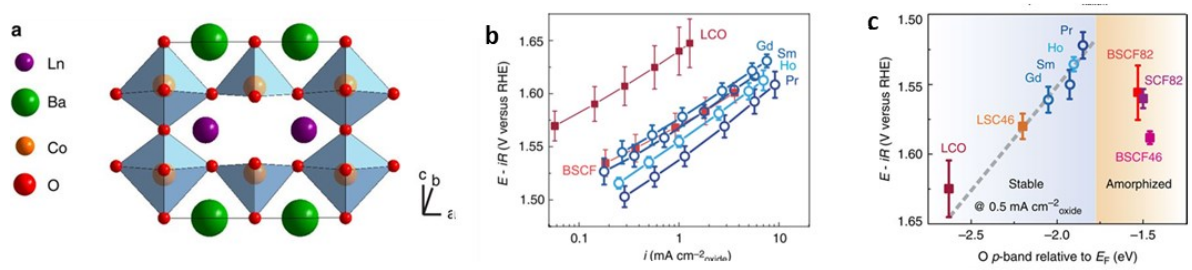

Figure 2.7 (a) Graphic of double perovskite $LnBaCo_2O_{5+\delta}$ with different coordination symmetries, (b) Intrinsic OER activities on $LnBaCo_2O_{5+\delta}$ (Ln=Pr, Sm, Gd and Ho). (c) Illustration of OER activity of $LnBaCo_2O_{5+\delta}$ (Ln=Pr, Sm, Gd and Ho) associated with the O *p*-band centre relative to E_F. [27b] Reprinted with permission from Ref 27b. Copyright (2013) Nature Publishing Group.

2.3.1.2 Extrinsic strategies for enhanced catalytic activities

As stated above, the intrinsic catalytic activity of perovskite oxides is governed by its electronic

structures, while there are still many other important factors that affecting the activity of the perovskite oxides based electrocatalyst. For example, the electrical conductivity, morphology, phase structure, crystallographic orientations *etc.* Tremendous research has been done in these areas to study the extrinsic catalytic activity of perovskite electrocatalysts. Herein, focus will be laid on the aspect of electrical conductivity and morphology, and discussion will be focused on how extrinsic strategies work in terms of enhancing the oxygen electrocatalytic activities.

2.3.1.3 Electrochemical conductivity of the perovskite oxide composite

Generally, the electrical conductivities of perovskite oxides are low at room temperature. When the perovskite oxides are evaluated as an oxygen electrocatalysts without carbon supports, an insufficient ORR activity was found, and a two-plus-two electron transfer mechanism was observed within the ORR [28]. The poor electronic conductivity and low specific surface area of perovskite oxides inevitably impede the charge transfer within the reaction due to its limited triple phase boundary sites.

Incorporating a second phase of carbonaceous material into the perovskite oxides to form perovskite/carbon composite is an effective way to boost the oxygen electrocatalytic activity, and to maximize the transition metal oxide utilization, albeit the possible carbon corrosion occurs under high polarization potential in OER process. Conductive carbon materials such as carbon black (CB) [22, 29], acetylene black (AB) [30], carbon nanotubes [31], and graphene materials [32] have been investigated as supporting matrix in perovskite oxide/carbon composites. The addition of carbon material leads to an enhanced charge transfer in the electrochemical catalytic process, accompanied by a significantly improved kinetics.

Some recent studies have shown that the addition of carbonaceous material into perovskite electrocatalysts brings the benefits beyond enhanced conductivities.[17, 28, 32a] As mentioned in the Chapter 2.2, graphene, CNT and even carbon black materials demonstrate enhanced oxygen electrocatalytic activity to a certain extent. Some researchers reported that, when forming a composite with perovskite, a synergistic catalytic effect was found between the carbon material and the perovskite oxides.[28, 31a] Moreover, it has been suggested that the incorporation of carbon material and the creation of perovskite-carbon interface would result in a band alignment and charge transfer.[32a] One of our recent studies demonstrated that, a Schottky barrier of 0.63 eV was formed between the junctions of reduced-GO (rGO) nanosheets and $La_{0.5}(Ba_{0.4}Sr_{0.4}Ca_{0.2})Co_{0.8}Fe_{0.2}O_{3-\delta}$.[32a] Introducing rGO could significantly affect the electron transport and simultaneously accelerate the reaction kinetics during the oxygen electrocatalysis.

The addition of carbonaceous components solved the problem of insufficient conductivity within the perovskite by providing an external electron pathway, while the intrinsic electronic conductivity of the perovskite was suggested to be another crucial factor for the ORR. Song investigated the relationship between the intrinsic electrical conductivities and the ORR catalytic pathway on a series of perovskite oxides [33]. Figure 2.8a shows the difference of electrical conductivity on $Ba_{0.5}Sr_{0.5}Co_{0.8}Fe_{0.2}O_{3-\delta}$ (BSCFO), $La_{0.8}Sr_{0.2}CoO_{3-\delta}$ (LSCO) and $NdBa_{0.25}Sr_{0.75}Co_2O_{5+\delta}$ (NBSCO) at various temperatures. The intrinsic electronic conductivity of the perovskite was found to be responsible for the electron transfer pathway (direct 4 electron or 2-plus-2 electron pathway) within the reaction. Generally, a direct four electron transfer pathway was favored on the surface of a conductive perovskite, while a two–step reaction with two-plus-two electron transfer mechanism was detected on less conductive perovskite. Figure 2.8b shows the reaction mechanism proposed for the high conductive/less conductive perovskite oxides. The

contact interfaces of carbon and perovskite acted as the fully polarized sites towards ORR in both NBSCO and LSCO, thus facilitating the $4e^-$ pathway.[33] For perovskite oxides with insufficient conductivity, the high ohmic resistance of the bulk perovskite lead to the formation of less polarized sites on the surface of the perovskites that far away from the contact interface. Thus, a two-step reaction is favored over the direct $4e^-$ transfer pathway.

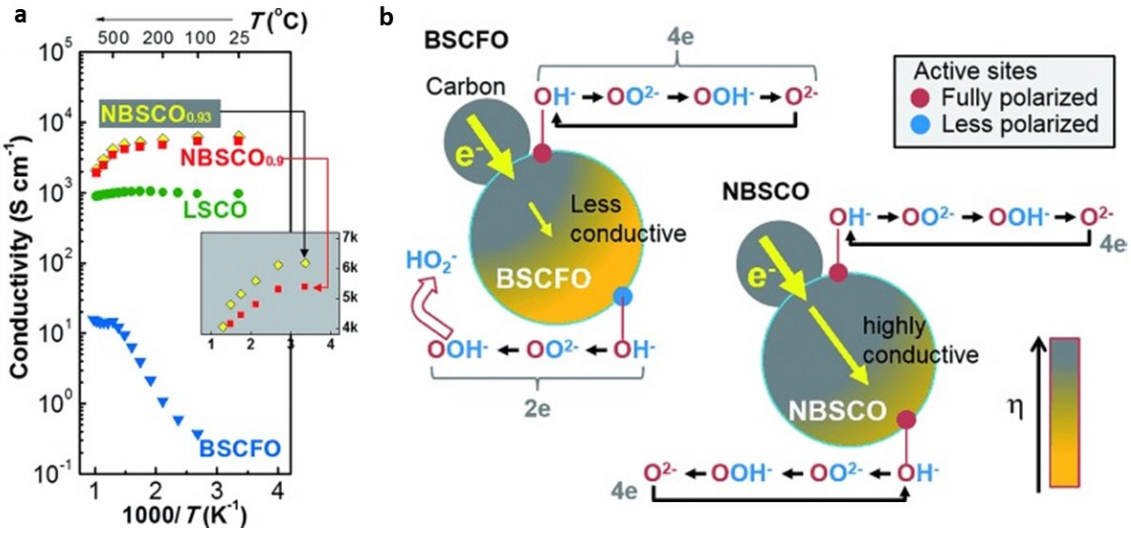

Figure 2.8 (a) Comparison of electrical conductivity of $Ba_{0.5}Sr_{0.5}Co_{0.8}Fe_{0.2}O_{3-\delta}$ (BSCFO), $La_{0.8}Sr_{0.2}CoO_{3-\delta}$ (LSCO) and $NdBa_{0.25}Sr_{0.75}Co_2O_{5+\delta}$ (NBSCO) at various temperature. (b) Reaction mechanism proposed on highly conductive perovskite (eg. NBSCO) and less conductive perovskite (e.g. BSCFO). [33] Reprinted with permission from Ref 33. Copyright (2015) Wiley-VCH.

In brief, the electrical conductivities of perovskite oxide composites have a crucial impact on their electrocatalytic activity. Enhancing the electronic conductivities, either by providing an external electron pathway or by increasing the intrinsic conductivities of the perovskite oxides, leads to an

optimized electrochemical performance and a higher energy efficiency in fuel cells and battery systems.

2.3.1.4 Morphology of perovskite oxides

Conventionally, ceramic materials like perovskite oxides are synthesized through a solid-state method, where a high sintering temperature is required to allow the solid-solid diffusion [31b]. The high sintering temperature and slow diffusion kinetics generally result in an extremely low specific surface area and low homogeneity with the impurity phase formation. Wet chemistry method, such as sol-gel, combustion and Pechini method have been developed as the alternative methods for the synthesis of perovskite oxides.[34] However, the crystallization temperature is still too high (usually above 800 °C), leading to an insufficient surface area (less than 10 $m^2 g^{-1}$) and inadequate porosity [17]. The low specific surface area and porosity act as barriers that hinders the mass transport kinetics of reactants and products towards the active sites, which results in an unsatisfactory mass specific activity [22]. Therefore, engineering surface features (i.e. morphology, particle size and pore structure) of the perovskite oxides are of great importance for optimizing the oxygen electrocatalytic activities.

It was reported that the perovskite oxide with an ordered 3D microporous structure, was successfully synthesized through a polystyrene spheres template method.[35] The polystyrene colloidal crystals were initially immersed in the metal nitrates precursor of $LaFeO_3$. The ordered 3D macroporous $LaFeO_3$ (3DOM-LFO) was obtained followed by a two-step calcination process (Figures 2.9 a, and b), while the polystyrene colloidal crystals template was removed in the heat treatment. As shown in Figure 2.9d, the 3DOM-LFO demonstrated a high specific surface area of 29.3 $m^2 g^{-1}$, while the $LaFeO_3$ nanoparticles (NP-LFO) prepared without polystyrene colloidal

crystals template showed a low surface area of 1.4 $m^2 g^{-1}$. When being applied as an electrocatalyst in Li-O_2 battery, the ordered macroporous structure of 3DOM-LFO contributed to a uniform gas/electrolyte distribution. As shown in Figures 2.9e and f, the Li–O_2 batteries with a 3DOM-LFO electrode exhibited a superior cyclic stability in comparison with the NP-LFO, owing to the efficient mass transfer in charging-discharging process during the cyclic tests. Since Li_2O_2 is gradually generated as a discharging product, macrospores structure provided sufficient void space for the Li_2O_2 growth and effectively prevented the blockage of surface active sites.

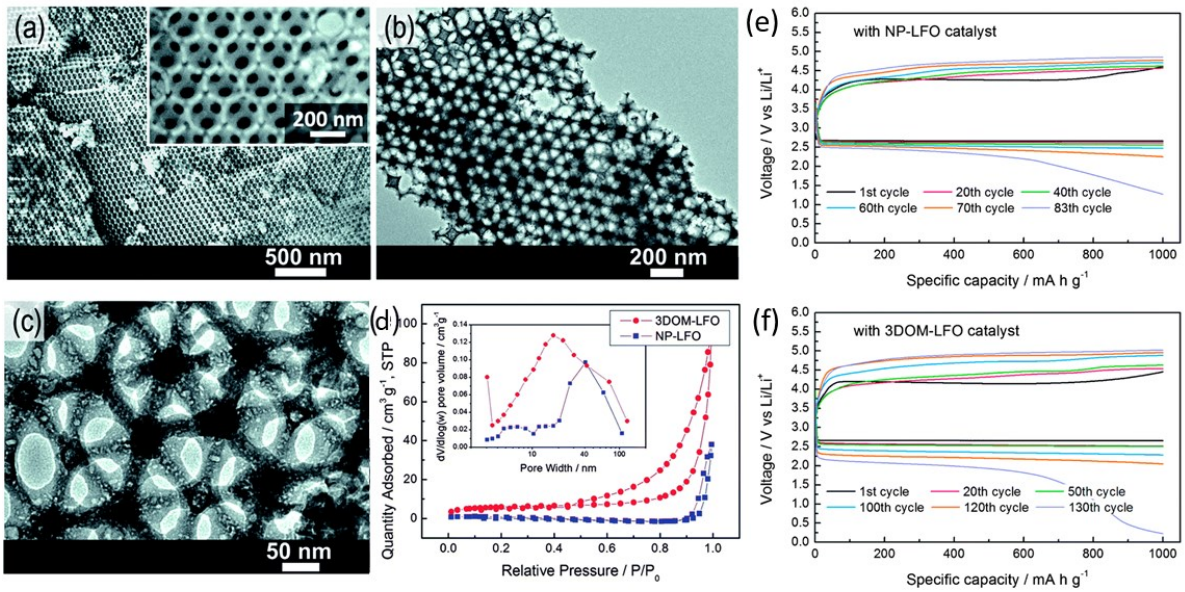

Figure 2.9 (a) FESEM image and (b) TEM image of 3D ordered macroporous $LaFeO_3$ (3DOM-LFO). (c) FESEM image of LFO nanoparticles (NP-LFO). (d) Nitrogen adsorption and desorption isotherms and pore size distribution (inset) curves of 3DOM-LFO and NP-LFO. Cyclic stability of (e) NP-LFO and (f) 3DOM-LFO in the Li-O_2 batteries.[35] Reprinted with permission from Ref 35. Copyright (2015) Royal Society of Chemistry.

Zhao *et al* reported the synthesis of the hierarchical mesoporous $La_{0.5}Sr_{0.5}CoO_{2.91}$ (LSCO) perovskite through a multistep microemulsion process and a post heat treatment (600 °C for 3 h) with a slow heating rate.[35] The resulting LSCO perovskite possessed a high specific surface area of 96.78 m^2 g^{-1} with an average pore size of 10.17 nm. The TEM and HRTEM revealed that the LSCO nanowires were self-assembled into the hierarchical structure in the emulsion process. The hierarchical mesoporous LSCO nanowires/AC afforded a significantly enhanced activity in comparison to the AC and LSCO/AC composite, showing a half-wave potential ($E_{1/2}$) of 0.72 V vs. RHE in the ORR and a potential of 1.81V at a current density of 10 mA cm^{-2} (E_{10}) in the OER. The improved performance in mesoporous LSCO nanowires/AC was attributed to the high specific surface area and distinct mesoporous structure.

Elaborate efforts have been devoted to the design and synthesis approaches, and the micro/nano perovskite oxides with various morphologies have been developed. Remarkably enhanced electrocatalytic activities have been achieved on nanostructured perovskite oxides, which can be credited to the distinct architecture, high specific surface area and rich exposed surface active sites. It is worthy to note that the electronic confinement effects within nanostructured materials will lead to a change in electronic structure compared to the bulk perovskite.[36] A further investigation is required in order to deepen our understanding of the driving mechanism on nanostructured perovskite oxides.

2.3.3 Spinel oxide based electrocatalysts

Spinels are generally formulated with AB_2X_4, where A and B are tetrahedrally and octahedrally coordinated metal cations, and X refers to chalcogen anions.[37] Typically, in a spinel compound, the A- and B-site cations can be accommodated within the structure in the form of $A^{2+}B_2^{3+}O_4$ and

$A^{4+}B_2^{2+}O_4$ [37a]. Many of spinel oxides possess interesting electronic structure, which enables their wide application in catalysis and electrochemical conversion system [38]. The Co-based spinel oxides (e.g. Co_3O_4, $MnCo_2O_4$, $NiCo_2O_4$)[39], Mn-based spinel oxides (e.g. $CoMn_2O_4$, Mn_3O_4)[40] and Fe-based spinel oxides (e.g. Fe_3O_4 and $CoFe_2O_4$)[41] have drawn particular interests in fuel cell and MABs systems. As compared to the perovskite oxides, spinel oxides generally have a low crystallization temperature. The easier synthesis of spinel oxides enables the employment of a broad synthesis method.[38] Tremendous research conducted in nanostructure design, synthesis approaches and defects engineering afford to a wide range of application of spinel oxides in fuel cells, batteries and water splitting system.

Although spinel oxides possess a high intrinsic electrocatalytic activity, the poor electronic conductivities inevitably hinder their application in electrochemical system.[38] Hybrid spinel eletrocatalysts with conductive carbon supports have been extensively studied. Recently, Klaus Müllen group reported the Fe_3O_4 nanoparticles/nitrogen-doped graphene aerogels ((Fe_3O_4/N-GAs) as an efficient electrocatalysts towards ORR (Figure 2.10). The Fe_3O_4/N-GAs electrocatalyst was initially synthesized from Fe and polypyrrole integrated graphene hybrid hydrogel, followed by a lyophilization and calcination treatment. The 3D graphene network greatly facilitated the electron transfer within the ORR process. The high specific surface area, macroporous structure, and strong coupling effect between Fe_3O_4 and N-GAs contributed to an excellent ORR activity. As shown in Figure 2.10d, an onset potential of -0.19 V vs. Ag/AgCl and an $E_{1/2}$ around -0.4 V vs. Ag/AgCl were achieved on Fe_3O_4/ N-GAs.

$Mn_XCo_{2-x}O_4$ is known as another highly active spinel oxide towards ORR. Jaephil Cho *et al* prepared a nitrogen-doped carbon-supported porous spinel oxides through a thermal

decomposition of $Mn_3(Co(CN)_6)_2{\cdot}nH_2O$/gelatin-coated Ketjenblack carbon. The porous $Mn_{1.8}Co_{1.2}O_4$/N-Ketjenblack demonstrated a high ORR activity, with the $E_{1/2}$ being only 80 mV lower than that of the commercial Pt/C in 0.1 M KOH solution. Moreover, the $Mn_{1.8}Co_{1.2}O_4$/N-Ketjenblack electrocatalyst showed a high electrocatalytic performance in the primary zinc-air battery conducted in 6 M KOH, which even outperforms the Pt/C at a high discharging current region.[42]

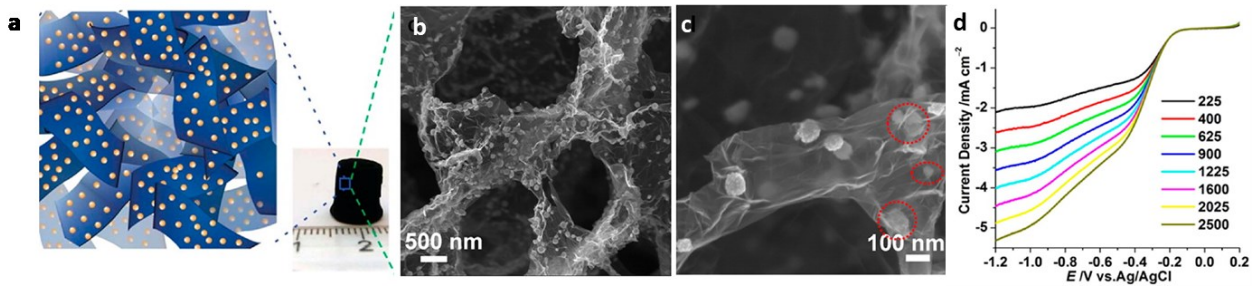

Figure 2.10 (a) Fe_3O_4/ N-doped graphene aerogels (Fe_3O_4/ N-GAs) obtained after lyophilization and calcination at 600 °C under N_2. (b) and (c) SEM images of Fe_3O_4/ N-GAs. (d) ORR polarization curves of Fe_3O_4/ N-GAs in 0.1 M KOH at various rotation speed. [41a] Reprinted with permission from Ref 41a. Copyright (2012) American Chemical Society.

Recently, Zhongwei Chen *et al* reported a binder free 3D architecture air electrode, with bifunctional Co_3O_4 nanowires directly grown on a stainless steel mesh current collector (Co_3O_4 NW grown on SS) [43]. The *in situ* growth of Co_3O_4 NW on stainless steel substrate leads to a strong coupling effect and a fast charge transfer during the electrocatalysis process. Figure 2.11a shows the SEM images of the Co_3O_4 NW on the SS mesh, the Co_3O_4 NW demonstrated an average diameter of 300 nm with an average length of 15 μm. The as-synthesized electrocatalyst (Co_3O_4 NW grown on SS) illustrated a remarkable bifunctional activity and an excellent stability in the rechargeable Zn-air battery test (Figure 2.11d and e).

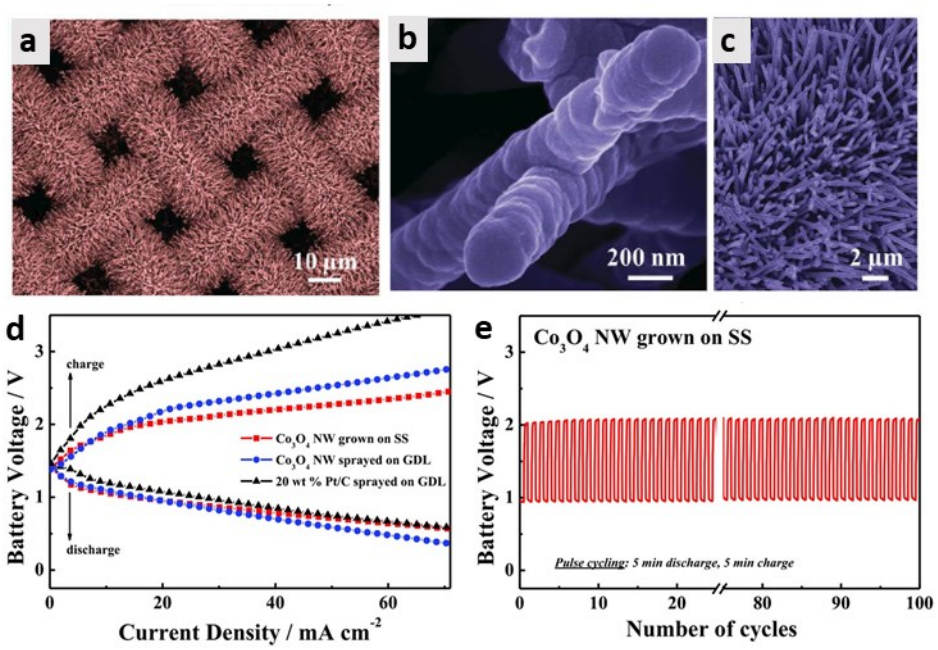

Figure 2.11 (a), (b) and (c) SEM images of the Co_3O_4 nanowires grown on stainless steel (Co_3O_4 NW grown on SS). (d) LSV of charging-discharging curves of Co_3O_4 NW grown on SS in comparison with Co_3O_4 NW sprayed on gas diffusion layer (GDL), and 20 wt% Pt/C. (e) Cyclic charging-discharging test at a fixed current of 50 mA. [43] Reprinted with permission from Ref 43. Copyright (2014) John Wiley & Sons.

2.4 Progress and thesis proposal

In the past decades, tremendous research efforts have been devoted to optimizing the ORR/OER electrocatalytic activities for fuel cells and MABs. The development of oxygen electrocatalysts for fuel cells and MABs has undergone from conventional noble metals (Pt, Pt/Ir, Pt/Ru) to carbonaceous materials and various non-stoichiometric transition metal oxides. Fundamental research, such as systematic investigations relating intrinsic material properties to oxygen

electrocatalytic performance, has also been conducted. It is found that the electronic state of transition metal cation directly determines the catalytic performances and functionality of the materials.[23] Strategies including stoichiometry engineering, cation partial substitution, architecture design as well as hybrid formation with carbon materials have been proved as the effective methods for the design of advanced electrocatalysts.[17, 29c, 31, 35] Nevertheless, the electrocatalytic activities of transition metal oxides are still inferior to the state-of-art noble metal-based catalysts. For perovskite oxides or spinel oxides to become more competitive oxygen electrocatalysts, substantial progress is required to enhance their catalytic activity and durability.

For practical applications of MABs and fuel cells, it is crucial to have a rational design of electrocatalysts that possess a high electrocatalytic activity, high conductivity and good stability with low cost. Planting precious metal nanoparticles (NPs) on the perovskites matrix to form metal/perovskite hybrids through conventional method (physical mixing or infiltration) or *in situ* exsolution has been demonstrated as an effective approach to improving the catalytic activities in solid oxide fuel cells.[44] However, metallic/perovskite hybrid has been rarely studied in aklaine fuel cell or MABs for room temperature application.[45] In addition, due to the the low specific surface area and low porosity of perovskites, it is more chanlleging to obtain a high/uniform dispersion of NPs on perovskite oxide supports than on carbon support.[46]

To fill this gap, an *in situ* exsolution method has been proposed to partially extract A-site or B site cation to the material surface, while particular attention has been paid to the enhanced oxygen electrocatalytic activity in alkaline media. By combing the strategies of *in situ* exsolution and phase transformation, a significantly enhanced ORR activity has been achieved with extremely low mass loading of Ag. Besides the *in situ* exsolution, the post functionalization of the exsolved

nanoparticles has been investigated to extend the functionality of the perovskite oxides. The incorporation of *in situ* exsolution and post-phosphatization may open up new possibilities for perovskites to be utilized as multifunctional electrocatalysts for overall water splitting/rechargeable fuel cell. Moreover, the cooperative hybrid catalytic system has also been proposed to enhance the bifunctionality of the spinel oxides. Efficient utilization of the catalyst surface and strong chemical coupling effects of the spinel hybrid afford the enhanced bifunctional catalytic activity and durability. The ultimate goal of this thesis is to develop a highly active electrocatalyst with strong durability, using the highly abundant resources.

The proposed research in this thesis is significant. The investigation of perovskite/spinel oxides based electrocatalysts provide a better understanding of the synergistic chemical coupling effects of metal/oxide system, which holds potential to further advance perovskite/spinel oxides-based oxygen electrocatalysts as the alternatives to the noble metals. Moreover, the proposed design and synthesis strategies could be extended to various heterogeneous catalysis, which is beneficial to the catalysis community in general.

2.5 References

1. Nørskov, J. K.; Rossmeisl, J.; Logadottir, A.; Lindqvist, L.; Kitchin, J. R.; Bligaard, T.; Jonsson, H., Origin of the overpotential for oxygen reduction at a fuel-cell cathode. *The Journal of Physical Chemistry B* **2004,** *108* (46), 17886-17892.

2. Stamenkovic, V.; Mun, B. S.; Mayrhofer, K. J.; Ross, P. N.; Markovic, N. M.; Rossmeisl, J.; Greeley, J.; Nørskov, J. K., Changing the activity of electrocatalysts for oxygen reduction by tuning the surface electronic structure. *Angewandte Chemie* **2006,** *118* (18), 2963-2967.

3. Greeley, J.; Stephens, I.; Bondarenko, A.; Johansson, T. P.; Hansen, H. A.; Jaramillo, T.; Rossmeisl, J.; Chorkendorff, I.; Nørskov, J. K., Alloys of platinum and early transition metals as oxygen reduction electrocatalysts. *Nature chemistry* **2009,** *1* (7), 552.

4. Mazumder, V.; Chi, M.; More, K. L.; Sun, S., Core/shell Pd/FePt nanoparticles as an active and durable catalyst for the oxygen reduction reaction. *Journal of the American Chemical Society* **2010,** *132* (23), 7848-7849.

5. Yu, Y.; Yang, W.; Sun, X.; Zhu, W.; Li, X.-Z.; Sellmyer, D. J.; Sun, S., Monodisperse MPt (M= Fe, Co, Ni, Cu, Zn) nanoparticles prepared from a facile oleylamine reduction of metal salts. *Nano letters* **2014,** *14* (5), 2778-2782.

6. Chung, D. Y.; Jun, S. W.; Yoon, G.; Kwon, S. G.; Shin, D. Y.; Seo, P.; Yoo, J. M.; Shin, H.; Chung, Y.-H.; Kim, H., Highly durable and active PtFe nanocatalyst for electrochemical oxygen reduction reaction. *Journal of the American Chemical Society* **2015,** *137* (49), 15478-15485.

7. Zhang, G.; Shao, Z.-G.; Lu, W.; Li, G.; Liu, F.; Yi, B., One-pot synthesis of Ir@ Pt nanodendrites as highly active bifunctional electrocatalysts for oxygen reduction and oxygen evolution in acidic medium. *Electrochemistry Communications* **2012,** *22*, 145-148.

8. Chen, G.; Delafuente, D. A.; Sarangapani, S.; Mallouk, T. E., Combinatorial discovery of bifunctional oxygen reduction—water oxidation electrocatalysts for regenerative fuel cells. *Catalysis Today* **2001,** *67* (4), 341-355.

9. Zhang, Y.; Wang, C.; Wan, N.; Mao, Z., Deposited RuO2–IrO2/Pt electrocatalyst for the regenerative fuel cell. *International Journal of Hydrogen Energy* **2007,** *32* (3), 400-404.

10. Jung, K.-N.; Jung, J.-H.; Im, W. B.; Yoon, S.; Shin, K.-H.; Lee, J.-W., Doped lanthanum nickelates with a layered perovskite structure as bifunctional cathode catalysts for rechargeable metal–air batteries. *ACS applied materials & interfaces* **2013,** *5* (20), 9902-9907.

11. Dai, L.; Xue, Y.; Qu, L.; Choi, H.-J.; Baek, J.-B., Metal-free catalysts for oxygen reduction reaction. *Chemical reviews* **2015,** *115* (11), 4823-4892.

12. Dai, L., Functionalization of graphene for efficient energy conversion and storage. *Accounts of chemical research* **2012,** *46* (1), 31-42.

13. Xue, Y.; Yu, D.; Dai, L.; Wang, R.; Li, D.; Roy, A.; Lu, F.; Chen, H.; Liu, Y.; Qu, J., Three-dimensional B, N-doped graphene foam as a metal-free catalyst for oxygen reduction reaction. *Physical Chemistry Chemical Physics* **2013,** *15* (29), 12220-12226.

14. Zhang, J.; Zhao, Z.; Xia, Z.; Dai, L., A metal-free bifunctional electrocatalyst for oxygen reduction and oxygen evolution reactions. *Nature nanotechnology* **2015,** *10* (5), 444.

15. (a) Li, Y.; Gong, M.; Liang, Y.; Feng, J.; Kim, J.-E.; Wang, H.; Hong, G.; Zhang, B.; Dai, H., Advanced zinc-air batteries based on high-performance hybrid electrocatalysts. *Nature communications* **2013,** *4*, 1805; (b) Toussaint, G.; Stevens, P.; Akrour, L.; Rouget, R.; Fourgeot, F., Development of a rechargeable zinc-air battery. *ECS Transactions* **2010,** *28* (32), 25-34.

16. Sørensen, O. T., *Nonstoichiometric oxides*. Elsevier: 2012.

17. Chen, D.; Chen, C.; Baiyee, Z. M.; Shao, Z.; Ciucci, F., Nonstoichiometric oxides as low-cost and highly-efficient oxygen reduction/evolution catalysts for low-temperature electrochemical devices. *Chemical reviews* **2015,** *115* (18), 9869-9921.

18. Bockris, J. O. M.; Otagawa, T., The electrocatalysis of oxygen evolution on perovskites. *Journal of the Electrochemical Society* **1984,** *131* (2), 290-302.

19. Kofstad, P., Defects and transport properties of metal oxides. *Oxidation of metals* **1995,** *44* (1-2), 3-27.

20. Du, Z.; Yang, P.; Wang, L.; Lu, Y.; Goodenough, J.; Zhang, J.; Zhang, D., Electrocatalytic performances of LaNi1−xMgxO3 perovskite oxides as bi-functional catalysts for lithium air batteries. *Journal of Power Sources* **2014,** *265*, 91-96.

21. Mefford, J. T.; Hardin, W. G.; Dai, S.; Johnston, K. P.; Stevenson, K. J., Anion charge storage through oxygen intercalation in LaMnO 3 perovskite pseudocapacitor electrodes. *Nature materials* **2014,** *13* (7), 726.

22. Zhang, Y.-Q.; Tao, H.-B.; Liu, J.; Sun, Y.-F.; Chen, J.; Hua, B.; Thundat, T.; Luo, J.-L., A rational design for enhanced oxygen reduction: Strongly coupled silver nanoparticles and engineered perovskite nanofibers. *Nano energy* **2017,** *38*, 392-400.

23. (a) Suntivich, J.; May, K. J.; Gasteiger, H. A.; Goodenough, J. B.; Shao-Horn, Y., A perovskite oxide optimized for oxygen evolution catalysis from molecular orbital principles. *Science* **2011,** *334* (6061), 1383-1385; (b) Suntivich, J.; Gasteiger, H. A.; Yabuuchi, N.; Nakanishi, H.; Goodenough, J. B.; Shao-Horn, Y., Design principles for oxygen-reduction activity on perovskite oxide catalysts for fuel cells and metal–air batteries. *Nature chemistry* **2011,** *3* (7), 546.

24. Rossmeisl, J.; Qu, Z.-W.; Zhu, H.; Kroes, G.-J.; Nørskov, J. K., Electrolysis of water on oxide surfaces. *Journal of Electroanalytical Chemistry* **2007,** *607* (1-2), 83-89.

25. (a) Sengodan, S.; Choi, S.; Jun, A.; Shin, T. H.; Ju, Y.-W.; Jeong, H. Y.; Shin, J.; Irvine, J. T.; Kim, G., Layered oxygen-deficient double perovskite as an efficient and stable anode for direct hydrocarbon solid oxide fuel cells. *Nature materials* **2015,** *14* (2), 205; (b) Huang, Y.-H.; Dass, R. I.; Xing, Z.-L.; Goodenough, J. B., Double perovskites as anode materials for solid-oxide fuel cells. *Science* **2006,** *312* (5771), 254-257; (c) Zhou, Q.; He, T.; Ji, Y., SmBaCo2O5+ x double-perovskite structure cathode material for intermediate-temperature solid-oxide fuel cells. *Journal of Power Sources* **2008,** *185* (2), 754-758; (d) Yoo, S.; Jun, A.; Ju, Y. W.; Odkhuu, D.; Hyodo, J.; Jeong, H. Y.; Park, N.; Shin, J.; Ishihara, T.; Kim, G., Development of double-perovskite compounds as cathode materials for low-temperature solid oxide fuel cells. *Angewandte Chemie* **2014,** *126* (48), 13280-13283; (e) Kim, S.; Jun, A.; Kwon, O.; Kim, J.; Yoo, S.; Jeong, H. Y.; Shin, J.; Kim, G., Nanostructured double perovskite cathode with low sintering temperature for intermediate temperature solid oxide fuel cells. *ChemSusChem* **2015,** *8* (18), 3153-3158.

26. Kim, G.; Wang, S.; Jacobson, A.; Reimus, L.; Brodersen, P.; Mims, C., Rapid oxygen ion diffusion and surface exchange kinetics in PrBaCo 2 O 5+ x with a perovskite related structure and ordered A cations. *Journal of Materials Chemistry* **2007,** *17* (24), 2500-2505.

27. (a) Frontera, C.; Garcia-Munoz, J.; Llobet, A.; Aranda, M. A. G., Selective spin-state switch and metal-insulator transition in GdBaCo 2 O 5.5. *Physical Review B* **2002,** *65* (18), 180405; (b) Grimaud, A.; May, K. J.; Carlton, C. E.; Lee, Y.-L.; Risch, M.; Hong, W. T.; Zhou, J.; Shao-Horn, Y., Double perovskites as a family of highly active catalysts for oxygen evolution in alkaline solution. *Nature communications* **2013,** *4*, 2439.

28. Fabbri, E.; Mohamed, R.; Levecque, P.; Conrad, O.; Kötz, R.; Schmidt, T. J., Ba0. 5Sr0. 5Co0. 8Fe0. 2O3-δ Perovskite Activity towards the Oxygen Reduction Reaction in Alkaline Media. *ChemElectroChem* **2014,** *1* (2), 338-342.

29. (a) Davari, E.; Ivey, D. G., Synthesis and electrochemical performance of manganese nitride as an oxygen reduction and oxygen evolution catalyst for zinc–air secondary batteries. *Journal of Applied Electrochemistry* **2017,** *47* (7), 815-827; (b) Davari, E.; Johnson, A. D.; Mittal, A.; Xiong, M.; Ivey, D. G., Manganese-cobalt mixed oxide film as a bifunctional catalyst for rechargeable zinc-air batteries. *Electrochimica Acta* **2016,** *211*, 735-743; (c) Hua, B.; Li, M.; Sun, Y.-F.; Zhang, Y.-Q.; Yan, N.; Chen, J.; Thundat, T.; Li, J.; Luo, J.-L., A coupling for success: Controlled growth of Co/CoOx nanoshoots on perovskite mesoporous nanofibres as high-performance trifunctional electrocatalysts in alkaline condition. *Nano Energy* **2017,** *32*, 247-254.

30. (a) Wu, Z.; Sun, L.-P.; Xia, T.; Huo, L.-H.; Zhao, H.; Rougier, A.; Grenier, J.-C., Effect of Sr doping on the electrochemical properties of bi-functional oxygen electrode PrBa1− xSrxCo2O5+ δ. *Journal of Power Sources* **2016,** *334*, 86-93; (b) Lu, F.; Sui, J.; Su, J.; Jin, C.; Shen, M.; Yang, R., Hollow spherical La0. 8Sr0. 2MnO3 perovskite oxide with enhanced catalytic activities for the oxygen reduction reaction. *Journal of Power Sources* **2014,** *271*, 55-59.

31. (a) Lee, D. U.; Park, H. W.; Park, M. G.; Ismayilov, V.; Chen, Z., Synergistic bifunctional catalyst design based on perovskite oxide nanoparticles and intertwined carbon nanotubes for rechargeable zinc–air battery applications. *ACS applied materials & interfaces* **2014,** *7* (1), 902-910; (b) Lee, D. U.; Park, M. G.; Park, H. W.; Seo, M. H.; Ismayilov, V.; Ahmed, R.; Chen, Z., Highly active Co-doped LaMnO3 perovskite oxide and N-doped carbon nanotube hybrid bi-functional catalyst for rechargeable zinc–air batteries. *Electrochemistry Communications* **2015,** *60*, 38-41.

32. (a) Hua, B.; Li, M.; Zhang, Y. Q.; Sun, Y. F.; Luo, J. L., All-In-One Perovskite Catalyst: Smart Controls of Architecture and Composition toward Enhanced Oxygen/Hydrogen Evolution Reactions. *Advanced Energy Materials* **2017,** *7* (20), 1700666; (b) Park, H. W.; Lee, D. U.; Zamani,

P.; Seo, M. H.; Nazar, L. F.; Chen, Z., Electrospun porous nanorod perovskite oxide/nitrogen-doped graphene composite as a bi-functional catalyst for metal air batteries. *Nano Energy* **2014,** *10*, 192-200; (c) Molina-García, M. A.; Rees, N. V., Dual-doped graphene/perovskite bifunctional catalysts and the oxygen reduction reaction. *Electrochemistry Communications* **2017,** *84*, 65-70.

33. Lee, D. G.; Gwon, O.; Park, H. S.; Kim, S. H.; Yang, J.; Kwak, S. K.; Kim, G.; Song, H. K., Conductivity-Dependent Completion of Oxygen Reduction on Oxide Catalysts. *Angewandte Chemie* **2015,** *127* (52), 15956-15959.

34. Wu, H.; Zhu, X., Perovskite Oxide Nanocrystals—Synthesis, Characterization, Functionalization, and Novel Applications. In *Perovskite Materials-Synthesis, Characterisation, Properties, and Applications*, InTech: 2016.

35. Xu, J.-J.; Wang, Z.-L.; Xu, D.; Meng, F.-Z.; Zhang, X.-B., 3D ordered macroporous LaFeO 3 as efficient electrocatalyst for Li–O 2 batteries with enhanced rate capability and cyclic performance. *Energy & environmental science* **2014,** *7* (7), 2213-2219.

36. Yang, F.; Deng, D.; Pan, X.; Fu, Q.; Bao, X., Understanding nano effects in catalysis. *National Science Review* **2015,** *2* (2), 183-201.

37. (a) Wei, S.-H., Electronic Structure and Stability of Spinel Oxides. *Japanese Journal of Applied Physics* **2000,** *39* (S1), 251; (b) Elaheh, D., Bifunctional Electrocatalysts For Rechargeable Zinc-air Batteries. **2017**.

38. Zhao, Q.; Yan, Z.; Chen, C.; Chen, J., Spinels: controlled preparation, oxygen reduction/evolution reaction application, and beyond. *Chemical reviews* **2017,** *117* (15), 10121-10211.

39. (a) Ryu, W.-H.; Yoon, T.-H.; Song, S. H.; Jeon, S.; Park, Y.-J.; Kim, I.-D., Bifunctional composite catalysts using Co3O4 nanofibers immobilized on nonoxidized graphene nanoflakes for

high-capacity and long-cycle Li–O2 batteries. *Nano letters* **2013,** *13* (9), 4190-4197; (b) Hamdani, M.; Singh, R.; Chartier, P., Co3O4 and Co-based spinel oxides bifunctional oxygen electrodes. *Int. J. Electrochem. Sci* **2010,** *5* (4), 556-577; (c) Zhang, L.; Zhang, S.; Zhang, K.; Xu, G.; He, X.; Dong, S.; Liu, Z.; Huang, C.; Gu, L.; Cui, G., Mesoporous NiCo 2 O 4 nanoflakes as electrocatalysts for rechargeable Li–O 2 batteries. *Chemical communications* **2013,** *49* (34), 3540-3542; (d) Ge, X.; Liu, Y.; Goh, F. T.; Hor, T. A.; Zong, Y.; Xiao, P.; Zhang, Z.; Lim, S. H.; Li, B.; Wang, X., Dual-phase spinel MnCo2O4 and spinel MnCo2O4/nanocarbon hybrids for electrocatalytic oxygen reduction and evolution. *ACS applied materials & interfaces* **2014,** *6* (15), 12684-12691; (e) Wei, C.; Feng, Z.; Scherer, G. G.; Barber, J.; Shao-Horn, Y.; Xu, Z. J., Cations in Octahedral Sites: A Descriptor for Oxygen Electrocatalysis on Transition-Metal Spinels. *Advanced Materials* **2017,** *29* (23), 1606800.

40. (a) Dai, L.; Liu, M.; Song, Y.; Liu, J.; Wang, F., Mn3O4-decorated Co3O4 nanoparticles supported on graphene oxide: Dual electrocatalyst system for oxygen reduction reaction in alkaline medium. *Nano Energy* **2016,** *27*, 185-195; (b) Feng, J.; Liang, Y.; Wang, H.; Li, Y.; Zhang, B.; Zhou, J.; Wang, J.; Regier, T.; Dai, H., Engineering manganese oxide/nanocarbon hybrid materials for oxygen reduction electrocatalysis. *nano research* **2012,** *5* (10), 718-725; (c) Liu, Y.; Li, J.; Li, W.; Li, Y.; Chen, Q.; Zhan, F., Nitrogen-doped graphene aerogel-supported spinel CoMn2O4 nanoparticles as an efficient catalyst for oxygen reduction reaction. *Journal of Power Sources* **2015,** *299*, 492-500.

41. (a) Wu, Z.-S.; Yang, S.; Sun, Y.; Parvez, K.; Feng, X.; Müllen, K., 3D nitrogen-doped graphene aerogel-supported Fe3O4 nanoparticles as efficient electrocatalysts for the oxygen reduction reaction. *Journal of the American Chemical Society* **2012,** *134* (22), 9082-9085; (b) Indra, A.; Menezes, P. W.; Sahraie, N. R.; Bergmann, A.; Das, C.; Tallarida, M.; Schmeißer, D.; Strasser,

P.; Driess, M., Unification of catalytic water oxidation and oxygen reduction reactions: amorphous beat crystalline cobalt iron oxides. *Journal of the American chemical society* **2014,** *136* (50), 17530-17536.

42. Lee, J. S.; Nam, G.; Sun, J.; Higashi, S.; Lee, H. W.; Lee, S.; Chen, W.; Cui, Y.; Cho, J., Composites of a Prussian Blue Analogue and Gelatin-Derived Nitrogen-Doped Carbon-Supported Porous Spinel Oxides as Electrocatalysts for a Zn–Air Battery. *Advanced Energy Materials* **2016,** *6* (22), 1601052.

43. Lee, D. U.; Choi, J. Y.; Feng, K.; Park, H. W.; Chen, Z., Advanced Extremely Durable 3D Bifunctional Air Electrodes for Rechargeable Zinc-Air Batteries. *Advanced Energy Materials* **2014,** *4* (6), 1301389.

44. B. Hua; M. Li; Y. F. Sun; J. H. Li; J. L. Luo. Enhancing perovskite electrocatalysis of solid oxide cells through controlled exsolution of nanoparticles. *ChemSusChem* **2017,** *10* (17), 3333-3341.

45. Y. Gao; J. Wang; Y.-Q. Lyu; K. Lam; F. Ciucci. In situ growth of Pt 3 Ni nanoparticles on an A-site deficient perovskite with enhanced activity for the oxygen reduction reaction. *Journal of Materials Chemistry A* **2017,** *5* (14), 6399-6404.

46. S.-A. Park; E.-K. Lee; H. Song; Y.-T. Kim. Bifunctional enhancement of oxygen reduction reaction activity on Ag catalysts due to water activation on LaMnO3 supports in alkaline media. *Scientific reports* **2015,** *5*, 13552.

Chapter 3. Methodologies and Characterizations

3.1 Electrochemical analysis

3.1.1 Electrochemical test using rotation disk electrode (RDE) at room temperature

The RDE is a type of hydrodynamic analysis in electrochemical system. It is a widely used technique to rapidly screen the oxygen electrocatalyst, and to investigate the electron transfer mechanism in the ORR process. In the hydrodynamic analysis, the rate of mass transfer is significantly faster than the static state. The high rotation speed helps to eliminate the mass transfer effect of O_2 reactant in the ORR or product in the OER test, so that the measured current density is mainly governed/limited by the electron transfer kinetics.[1] The RDE technique enables the evaluation of reaction kinetics of the ORR and OER.

As shown in Figure 3.1, the catalyst-coated glassy carbon RDE was used as the working electrode for ORR or OER tests, while a thick Pt wire and Ag/AgCl (sat. KCl) were used as the counter electrode and reference electrode, respectively.

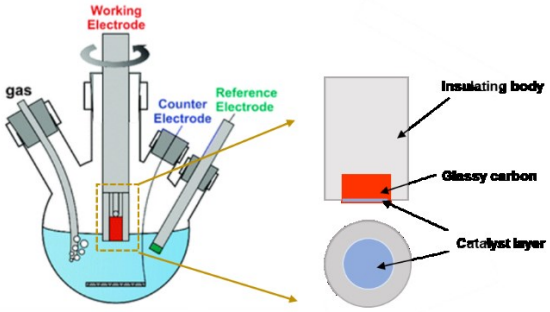

Figure 3.1 Schematic figure of rotation disk electrode test in three-electrode system. [2] Reprinted with permission from Ref 6 Copyright (2015) Royal Society of Chemistry.

All the electrochemical tests were conducted using an impedance/gain-phase analyzer (Solartron 1255) and an electrochemical interface (Solartron 1287). Prior to starting the tests, pure oxygen (99.9%) was purged into the electrolyte for 30 min to obtain oxygen saturated solution. Linear sweep voltammetry (LSV) were conducted in a voltage scan range of 0.1 V to -0.8 V (vs. Ag/AgCl, sat. KCl) with rotating speeds of 400, 900, 1600 and 2500 rpm for the ORR test, and in a voltage scan range of 0.1 V to 1.0 V (vs. Ag/AgCl, sat. KCl) at a rotation speed of 1600 rpm for the OER test. While for HER measurements, the LSVs were measured from -0.8 to -1.6 V vs. Ag/AgCl at a scan rate of 20 mV s^{-1} in Ar-saturated KOH solution. A consistent uncompensated resistance of ~45 Ω and ~5 Ω were measured in 0.1 and 1.0 M KOH respectively through high frequency impedance and were correspondingly corrected in the polarization curves ($E = E_{measured} - iR$). All the potentials were converted to the values relative to RHE, with $E_{RHE} = E + 0.197 + 0.0591\ PH$. The Koutecky-Levich (K-L) equation (Eq. 3.1, Eq. 3.2 and Eq. 3.3) were applied to determine the electron transfer numbers in the ORR,

$$\frac{1}{J} = \frac{1}{J_k} + \frac{1}{J_l} \quad \text{(Eq. 3.1)}$$

$$J_k = \mathrm{nFAkC_{O_2}} \quad \text{(Eq. 3.2)}$$

$$J_l = 0.62\mathrm{nFC_{O_2}D_{O_2}^{2/3}}\upsilon^{-1/6}\omega^{1/2} = \mathrm{B}\omega^{1/2} \quad \text{(Eq. 3.3)}$$

where J, J_k and J_l are the measured current density, kinetic current density, and film diffusion limiting current density (mA cm^{-2}), respectively. A is the area of the glassy carbon electrode (0.196 cm^{-2}), F is the Faraday constant (96500 C mol^{-1}), C_{O_2} is the bulk oxygen concentration in 0.1 M KOH (1.2 $\times 10^{-6}$ mol cm^{-3}), D_{O_2} is the oxygen diffusion coefficient in 0.1 M KOH (1.9×10^{-5} cm^2 s^{-1}), v is the kinematic viscosity of the 0.1 M KOH solution (0.01 cm^2 s^{-1}), ω is the electrode

rotation rate (rad s^{-1}), k is the electron transfer rate constant for the ORR. Increased current densities were observed with enhanced rotation rates due to the narrowed diffusion layers. Figure 3.2 shows the typical linear sweep voltammetry curves of ORR/OER. The onset potentials are determined from intersection of tangents between the baseline and the signal current. The half-wave potential ($E_{1/2}$) is corresponding to the potential where the current density is equal to half of the limited current density. The E_{10} refers to the potential, at which point a current density of 10 mA cm^{-2} is delivered. The Electrochemical Impedance Spectroscopy (EIS) measurements were conducted from 10^5 Hz to 0.1 Hz with a 10 mV amplitude.

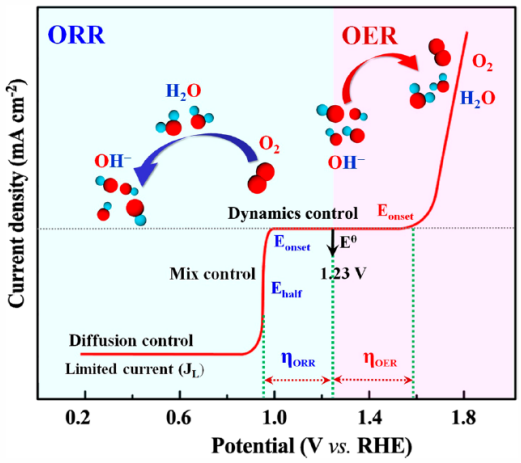

Figure 3.2. Typical linear sweep voltammetry curves of ORR/OER. [3] Reprinted with permission from Ref 3 Copyright (2017) American Chemical Society.

3.1.2 Rechargeable zinc-air battery assembly and tests

A homemade rechargeable zinc-air battery was constructed, with a zinc plate anode and an electrocatalyst coated GDL cathode. The cell was filled with 6 M KOH and 0.2 M zinc acetate to

ensure reversible Zn electrochemical reaction. The catalyst inks for the rechargeable zinc air battery (2 mg mL^{-1}) were prepared by sonicating 10 mg electrocatalysts, 3 mL isopropyl alcohol, 1 mL deionized water and 1 mL of 5wt. % Nafion (Aldrich). The cathode was prepared by drop casting the catalyst inks onto the center area of GDL (7/16" in diameter), followed by drying under ambient condition until a mass loading of 0.5 mg cm^{-2} was achieved. The battery tests were conducted by sweeping LSVs at 10 mV s^{-1} with Solartron 1287. The galvanostatic discharge-charge cycling was measured at a current density of 10mA cm^{-2}, and each cycle was set to be 10 min charge and 10 min discharge.

3.1.3 Electrochemical analysis in SOFCs and SOECs at elevated temperatures

In the SOFC test, Au paste was painted on both electrodes and then baked in air at 750 °C for 2 h. Then, Pt mesh was applied on the paste as the current collector that was connected with Pt wires. The open-circuit electrochemical impedance spectroscopy (EIS) measurement of the symmetrical cells was carried out at temperatures ranging from 500 to 700 °C in air. The anode support cell (anode side) was sealed to an alumina tube using the Ceramabond glass sealant (Aremco Product, Inc.) and reduced *in-situ* in H_2 at 650 °C for 2 h prior to the electrochemical measurements. The open-circuit EIS, the current-voltage (J-V) and power density curves of the full cell were obtained at temperatures ranging from 550 to 650 °C in H_2. The flow rates of H_2 and air were 40 ml min^{-1} and 150 ml min^{-1}, respectively.

In the SOEC test, Au paste (Heraeus C5729) was painted on both sides of the cell as the electrode current collectors. The silver wire with the diameter of 0.5 mm was connected to the current collectors using silver paste plus (SPI Supplies). The fabricated cell was sealed on a coaxial two-tube set up with Ceramabond 503 and tested at 850 °C on Thermolyne tubular furnace. The AC

impedance measurements of the cells were conducted in the atmosphere of CO_2/CO at the open circuit voltage and various applied voltages (0, 0.5, 0.7, 1.0, 1.2 V vs OCV) from 10^5 to 0.1 Hz with a 10 mV amplitude using Solartron 1255B frequency response analyzer and Solartron 1287 instrument. The inlet gases were controlled at a flow rate of 50 mL min^{-1} using mass flow meters. The outlet gases from the cathode side were evaluated by online gas chromatograph.

3.2 Materials Characterizations

X-ray Diffraction (XRD): The phase formation was analyzed by X-ray diffraction (XRD) using a Rigaka D/max-2500 X-ray diffractometer with a Cu Kα radiation generated at 40 kV and 44 mA with a scan rate of 2° min^{-1}. The XRD data was analyzed through Jade Software.

Field Emission Scanning Electron Microscopy (FESEM): The micromorphology of the materials was imaged using a Zeiss Sigma 300 VP FESEM equipped with secondary and backscattered electron detectors, an in-lens electron detector, and a Bruker energy dispersive X-ray spectroscopy (EDX) system.

Transmission electron microscopy (TEM): The TEM characterization was performed using the H-9500 environmental transmission electron microscope (ETEM) with an accelerating voltage of 300 kV, and probe corrected JEOL JEM-ARM200CF electron microscope with cold field emission gun at 200 kV. Scanning transmission electron microscopy (STEM) with energy-dispersive X-ray spectroscopy (EDX) was carried out on the JEOL JEM-ARM200CF, and JOEL 2200 FS with Schottky field emission gun at 200kV.

Thermogravimetry analysis (TGA): The oxygen nonstoichiometry was analyzed by thermogravimetry analysis (TGA) on SDT Q600 (TA instrument) at a heating rate of 10 ºC min^{-1}

under 5% H_2/N_2.

X-ray photoelectron spectroscopy (XPS): The XPS analysis was performed using Kratos Analytical AXIS 165 with monochromatic Al Kα source ($h\nu$ = 1486.6 eV). The spectra were referenced to C 1s bonding energy (284.6 eV) and fitted with Gaussian-Lorenz function and Shirley-type background subtraction method.

N_2 adsorption/desorption: The Brunauer–Emmett–Teller (BET) specific surface areas and pore size distribution were measured by the N_2 adsorption/desorption method, and it was analyzed with a Quantachrome Autosorb IQ.

O_2 Temperature programmed desorption (O_2-TPD): The test was carried out using a home-built temperature programmed apparatus. The sample was firstly treated in Ar at 500 °C for 1h to remove all the adsorbed species before cooling down to room temperature. Then it was exposed to O_2 for 2h. After purging the analysis chamber with Ar for 1 h at room temperature, the system was heated up to 900 °C in the stream of Ar. The released O_2 was monitored and recorded continuously as a function of the temperature by the QIC-20 detector (Atmospheric Gas Analysis System).

CO_2 Temperature programmed desorption (CO_2-TPD): The CO_2-TPD was recorded with a Micromeritics AutoChem II 2920 instrument. The CO_2-TPD was conducted from 100 ºC to 900 ºC at 10 ºC min^{-1} with He flow of 30 ml min^{-1}. The released CO_2 was monitored and recorded continuously as a function of the temperature by the QIC-20 detector (Atmospheric Gas Analysis System).

Zeta potential: The surface charge was measured by zeta potential analyzer (Zetasizer Nano,

Malvern).

Thermal expansion coefficient (TEC): The TEC of perovskite oxide was measured using a dilatometer (Linseis, L75 Platinum series). The heating rate was 5 °C min^{-1}.

Determination of nonstoichiometric oxygen: The initial oxygen content of perovskite at room temperature was determined using iodometric titration method. 20 mg of perovskite powder was placed in an Erlenmeyer flask followed by adding a small amount of 2M KI solution. Then, 3.5 M HCl was added to completely dissolve the powders. During this process, a stream of N_2 flow was used to blanket the solution. The clear solution was titrated with a 0.01 M $Na_2S_2O_3$ solution using starch as the indicator.

Electrical conductivity test: The electrical conductivities of perovskite samples were evaluated using a four-probe DC arrangement in a temperature range from 25 °C to 750 °C. Gold paste and wires were applied to both sides of the sintered perovskite oxides bars. The sample was heated up to 750 °C for 2 h in air. The electrical conductivity σ (S cm^{-1}) of the bar sample were determined using the following equations:

$$\sigma = \frac{1}{R} \times \frac{L}{S} \quad \text{(Eq. 3.4)}$$

where S is the cross-section area (cm^{-2}), *R* is the resistance (Ω), and L is the length of the bar (cm).

3.3 References

1. Bard, A. J.; Faulkner, L. R.; Leddy, J.; Zoski, C. G., *Electrochemical methods: fundamentals and applications*. wiley New York: 1980; Vol. 2.

2. Hong, W. T.; Risch, M.; Stoerzinger, K. A.; Grimaud, A.; Suntivich, J.; Shao-Horn, Y., Toward the rational design of non-precious transition metal oxides for oxygen electrocatalysis. *Energy & Environmental Science* **2015,** *8* (5), 1404-1427.

3. Zhao, Q.; Yan, Z.; Chen, C.; Chen, J., Spinels: controlled preparation, oxygen reduction/evolution reaction application, and beyond. *Chemical reviews* **2017,** *117* (15), 10121-10211.

Chapter 4. A Rational Design for Enhanced Oxygen Reduction: Strongly Coupled Silver Nanoparticles and Engineered Perovskite Nanofibers

4.1 Abstract

For perovskites to become more competitive ORR catalysts, substantial progress is required to advance their enhanced catalytic activity and durability. Herein, a novel method is described to achieve high-performance perovskite ORR catalyst *via* combining nano architecture designs, internal structures engineering, and Ag nanoparticles (NPs) *in situ* exsolution. The as-synthesized Ag-$(PrBa)_{0.95}Mn_2O_{5+\delta}$ catalyst exhibits favorable ORR activity with durability superior to the state-of-the-art Pt/C in alkaline solution. Several characterization techniques were applied alongside density functional theory calculations to understand the possible active sites and the synergistic coupling effects that contributed to the high ORR performance. The strong interfacial anchoring of Ag NPs on the ordered oxygen deficient perovskites leads to significant ligand effect and facilitates electron transfer and ion migration within the oxygen reduction reaction. The systematic engineering of perovskites described here represents a brand-new approach to developing highly active and stable catalyst for energy conversion and storage.

4.2. Introduction

The discovery of highly active and cost-effective catalysts for energy conversion and storage is a key step in dealing with greenhouse gas emissions and the energy crisis. The ORR is an essential but sluggish process for many electrochemistry device, such as fuel cells and metal–air batteries.[1] Large amounts of precious-metal electrocatalysts, e.g., Pt and its alloys, are commonly required to achieve satisfactory ORR performance. Nevertheless, the high cost, low availability, poor stability and susceptibility to fuels (e.g., Methanol) of Pt all inevitably impede the industrial scale applications of Pt-based electrocatalysts. [1a, 2] There have been considerable efforts devoted to developing Pt-free alternative eletrocatalysts in the alkaline media, including carbonaceous materials[3], transition metal oxide[4], transition metal chalcogenides[5], and iron-coordinated complex[6]. Perovskite oxides, as one of such alternatives, have drawn particular interest due to their promising electrochemical performance and excellent stability in alkaline environment.

Perovskite oxides, ABO_3, possess great structural and chemical flexibilities, enabling them to be easily tailored to meet the requirement for efficient ORR, and bringing them under the spotlight as a new class of strong candidates for ORR catalysis.[4a] Generally, any perovskite oxides containing transition metals in the B-site with an σ*-antibonding (e_g) orbital occupancy close to unity have shown excellent intrinsic reactivity in ORR.[7] This offers an important direction to tailor the intrinsic reactivity of perovskite oxides towards ORR. Over the past decade, substantial progress has been achieved in understanding and upgrading the intrinsic ORR reactivity of perovskite oxides, albeit much work still remains for advancing perovskite catalysts to be a feasible substitute for the state-of-the-art Pt/C. Among the main factors for establishing the catalytic

systems with high ORR performance are the intrinsic activity, defect chemistry, high surface area, well-designed structure and adequate conductivity.

So far, extensive investigations have focused on these issues and various strategies have been proposed to address them. It has been shown that the generation of oxygen vacancies within the perovskite oxide can be an effective way to boost catalytic performance because the complex defects may govern the oxygen exchange kinetics and ionic diffusion rates, thus favorably contributing to the ORR process.[8] The degree of vacancy formation is closely related to the B-O covalence in the perovskite, which is defined as the relative positions of the Fermi level compared with the O p-band center in the crystal.[8c] Planting precious metal nanoparticles (NPs) on the perovskites matrix to form metal/perovskite hybrids has also been demonstrated as an effective approach to significantly improving their activities.[9] For example, Ag was found to have a synergistic effect when coupled with $LaMnO_3$, which was attributed to the interactive effect of water activation on oxyphilic Mn sites and oxygen activation on Ag sites.[9b] In fact, Ag shows great promise as an alternative because of its superior ORR activity, cost-effectiveness and excellent durability.[2] Additionally, the low surface area and inadequate porosity of perovskite oxides act as barriers to hamper the mass transport kinetics of reactants and products towards the active sites. Thus, the optimization of the ORR activity of perovskite catalysts calls for a rational design in light of their macroscopic features (i.e. morphology, particle size and pore structure).[10]

Inspired by the above approaches, this study proposes to combine the following three strategies to advance perovskite for ORR: 1) construct a mesoporous fibrous architecture, 2) tune the internal crystal structure to form A-site deficient layered perovskite with large amounts of ordered oxygen vacancies, and 3) ensure strong intercalation of Ag NPs in the perovskite via *in situ* exsolution.

The electrochemical performance, morphology, crystal structure, and electronic configuration of the novel catalyst, demonstrate its superiority towards ORR. Thus, the significance of the present work is in three-fold: 1) it presents a well-designed nanocomposite that shows high reactivity, cost-effectiveness, tunability and robustness in ORR, 2) it demonstrates the synergistic chemical coupling effects of metal/oxide nanohybrids, and 3) it exemplifies the systematic engineering of perovskite into promising catalysts for various applications.

4.3. Results and discussions

We first present the design concept and fabrication protocol of the catalyst. As shown in Figure 4.1, a simple synthesis strategy was used to obtain the $(PrBa)_{0.95}Mn_2O_{5+\delta}$ ($PBMO_5$) layered perovskites nanofiber catalyst decorated with Ag NPs (denoted as Ag-$PBMO_5$). The precursor was initially electrospun into the nanowires, followed by a two-step heat treatment process. The first heating step, at 800 °C in air for 2 h, was carried out to thermally decompose the organics and nitrates to form the single composition $Pr_{0.475}Ba_{0.475}Ag_{0.05}MnO_{3-\delta}$ ($PBAMO_3$) perovskite. Thereby, the mesoporous fibrous structure was constructed and the catalytically active Ag was successfully incorporated at the atomic-level. The second heating step, at 550 °C in 5% H_2/N_2 for 2 h, was conducted to trigger the tiny Ag NPs from the host lattice and tune the internal structure of the perovskite. The exsolved Ag NPs were firmly anchored on the surface of the perovskite, while the crystal reconstruction led to the formation of A-site deficient layered structure with a large amount of ordered oxygen vacancies in $PBMO_5$. Such a strong interfacial interaction of Ag NPs with the oxygen-deficient layered perovskites was predicted to exhibit high activity and durability for ORR electrocatalysis. Several characterization techniques were applied to monitor the evolution of the catalyst in terms of its chemical composition, microstructure and crystal texture.

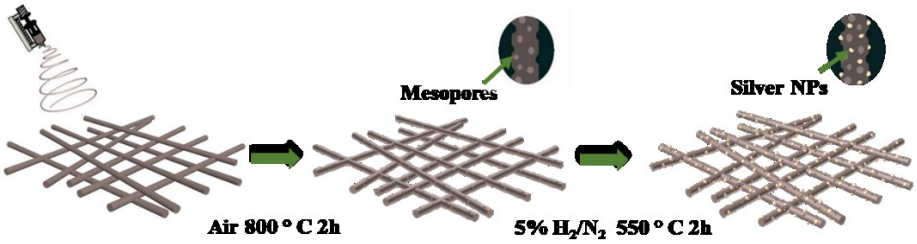

Figure 4.1 (a) Schematic illustration of the systematic engineering of perovskite into highly efficient ORR catalyst.

The X-ray diffraction (XRD) pattern of $PBAMO_3$ was indexed using $Pr_{0.5}Ba_{0.5}MnO_{3-\delta}$ with the Pm-3m space group, as shown in Figure 4.2, along with the Rietveld refinement results (Table 4.1). The obtained cell parameters were in good agreement with those of $Pr_{0.5}Ba_{0.5}MnO_{3-\delta}$, which indicates the successful formation of pristine perovskite (cubic/minor hexagonal).[11] Scanning transmission electron microscope-energy dispersive X-ray spectroscopy (STEM-EDX) elemental mappings of $PBAMO_3$, shown in Figure 4.3, confirm that Ag atoms were distributed throughout the bulk perovskite. As expected, during the second heating step, Ag atoms precipitated from the lattice while the perovskite underwent a phase change to step down from 'O_3' to 'O_5'. These results were supported by the XRD survey (Figure 4.2).

Table 4.1 The refined lattice parameters of the as-prepared samples.

Sample name	Space group	a (Å)	b (Å)	c (Å)	α (°)	β (°)	γ (°)
$PBAMO_3$	$Pm\bar{3}m$ (221)	3.89(7)	3.89(7)	3.89(7)	90	90	90
Ag-$PBMO_5$	P4/mmm (123)	3.89(4)	3.89(4)	7.79(9)	90	90	90

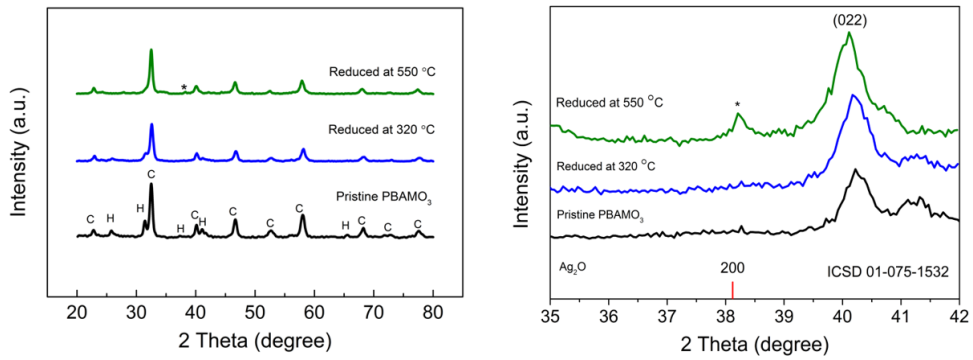

Figure 4.2 XRD patterns of pristine $PBAMO_3$, $PBAMO_3$ reduced at 320 and 550 °C.

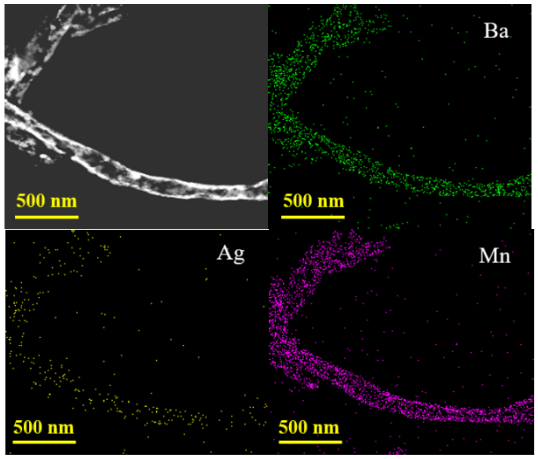

Figure 4.3 HAADF image and the corresponding element mapping of pristine porous $PBAMO_3$ nanofibers.

The direct evidence for Ag exsolution and phase change was also *in operando* monitored by thermogravimetric and differential thermal analysis (TG-DTA), for which two exothermic peaks at 300 °C and 350 °C were observed (Figure 4.4a). TG-DTA results for Ag-free $(Pr_{0.5}Ba_{0.5})_{0.95}MnO_{3-\delta}$, verified that the exothermic process at 350 °C is associated with the phase change from 'O_3' to 'O_5' (Figure 4.4b).[12] This implies that Ag atoms were first triggered out and then the unit cell was doubled along the c-direction, with Mn cations sandwiched between the PrO_x

and BaO layers (Figure 4.4a). The morphology of Ag-$PBMO_5$ (Figure 4.4c) demonstrates the entanglement of fine interconnected fibers, indicating that the fabrication method presented here can effectively engrave the catalyst to expose more pores and surface areas. Similar fibrous morphology was also found on the pristine $PBAMO_3$ as well as the $(Pr_{0.5}Ba_{0.5})_{0.95}MnO_{3-\delta}$ catalyst (Figure 4.4d and e). The quantitative evidence of the above observation was provided by the Brunauer–Emmett–Teller (BET) analysis. The engineered perovskite had an average pore size of 2.8 nm and a BET specific surface area of 37.4 $m^2\ g^{-1}$ (Figure 4.4f), substantially higher than those of the perovskites synthesized through the conventional methods.[12-13] Multiple mesopores function as the immediate reservoirs for products/reagents, which enables the fast transfer of products/reagents to and from the mesopores.[10a]

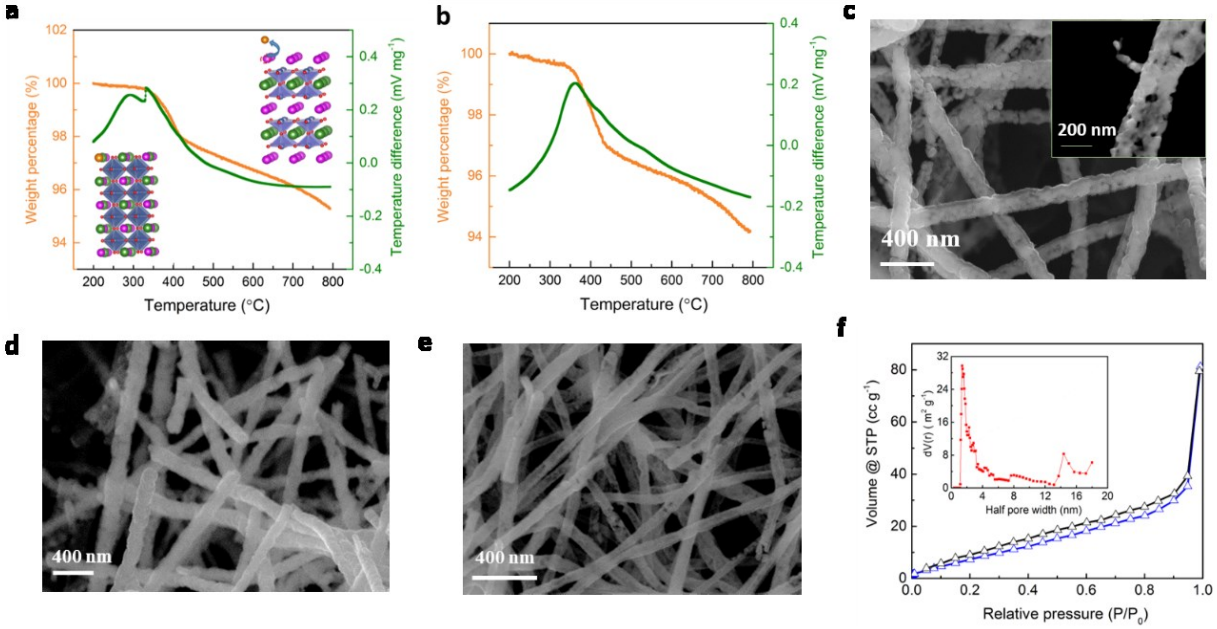

Figure 4.4 (a) TG-DTA curve of $PBAMO_3$ in 5% H_2/N_2; (b) TG-DTA curve of $(Pr_{0.5}Ba_{0.5})_{0.95}MnO_{3-\delta}$ in 5% H_2/N_2; FESEM images of (c) Ag-$PBMO_5$, (d) $(Pr_{0.5}Ba_{0.5})_{0.95}MnO_{3-\delta}$ and (e) $PBAMO_3$ nanofibers; (f) N_2 adsorption and desorption isotherm curves with BJH pore size distribution (inset).

STEM-EDX and atom-scale high resolution TEM (HRTEM) allowed for detailed information about the chemical and structural evolutions being investigated. Figure 4.5a shows the high angle annular dark field (HAADF) image of an Ag-$PBMO_5$ and its line-scanning profiles taken along the arrow marked in the image; the figure clearly reveals that Ag NPs were exsolved from the perovskite matrix. Figures 4.5b and c illustrate the HRTEM images along the [100] zone axes of $PBAMO_3$ and Ag-$PBMO_5$ grains, respectively, together with their corresponding diffractograms obtained by fast Fourier transformation (FFT). In accordance with the XRD results, the indexed diffractograms indicate that the perovskite changed from cubic ($PBAMO_3$) to tetragonal structure (Ag-$PBMO_5$). In addition to the main reflections from the cubic perovskite structure, strong superlattice reflections at ± 1/2 $[001]^*$ are shown in the diffractogram of Ag-$PBMO_5$. The enlarged HRTEM image shown as inset intuitively illustrates a doubled periodicity along the [001] direction. In Figures 4.5 d, e and f, it can be seen that NPs with diameters of 5-10 nm are socketed into the perovskite matrix. The pinned structures ensure strong interfacial interactions between the NPs and perovskite parent, thus facilitating the electron transfer between the perovskite matrix and Ag while enhancing the durability of exsolved NPs. More interestingly, the HRTEM and the corresponding diffractogram show a well-defined cubic Ag_2O NP with d-spacings of d = 2.47(8) Å and 2.73(5) Å indexed on the (200) and (11-1) planes, respectively, this implies that the exsolved Ag NPs reoxidized. Although these Ag_2O NPs would be reduced to metallic Ag upon electrochemical tests (Figure S4.1), such an incoherent result guided us to explore its intrinsic high ORR activity [9d].

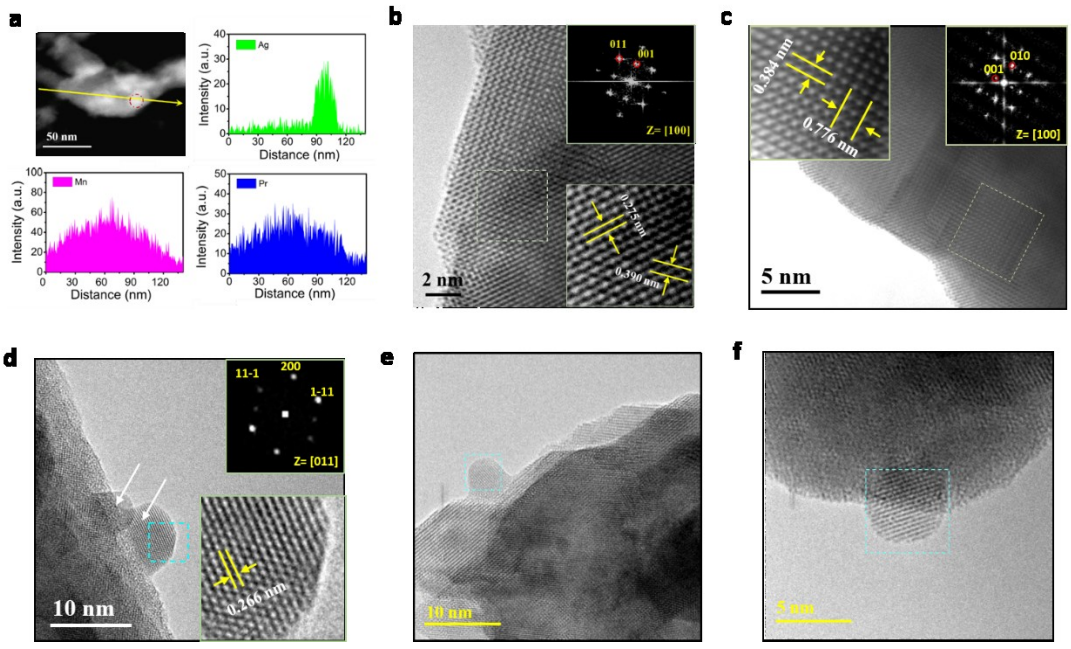

Figure 4.5 (a) HAADF image of Ag-$PBMO_5$ nanofiber with line-scan profiles; (b) HRTEM images and the corresponding simulations of pristine $PBAMO_3$ perovskite, confirming the idea cubic structure (a=b=c) prior to reduction. (c) HRTEM image of $PBAMO_5$ and corresponding diffractogram; (d), (e) and (f) HRTEM image of exsolved Ag_2O nanoparticles on $PBMO_5$ nanofiber. An enlarged image and corresponding diffractogram are shown as insets in Figure (d).

Sequentially, X-ray photoelectron spectroscopy (XPS) measurements were performed to track the oxidation states of Ag at different synthesis stages (Figure 4.6a). For the pristine $PBAMO_3$, no metallic Ag was detected since the binding energy (BE) of the Ag $3d_{5/2}$ peak at 367.7 eV corresponds to Ag_2O. After being treated in the 5% H_2/N_2 at 320 °C, the Ag 3d peak spilt into two doublets tentatively assigned to two different species, i.e., metallic Ag (368.4 eV) and Ag_2O (367.7 eV).[14] It is not surprising to find an additional increase in the ratio of Ag^+ with the elevation of the reduction temperature because the amount of adsorbed oxygen species is proportional to the reduction temperature (*vide infra*), resulting in the oxidation of nanosized Ag. For all of the

samples, the O1s spectra could be fitted into four peaks, which correspond to lattice oxygen (~529.1 eV for O^{2-}), highly oxidative oxygen species (~530.5 eV for O_2^{2-}/O^-), hydroxyl groups/adsorbed oxygen (~531.5 eV for –OH/O_2) and adsorbed molecular water (~532.9 eV for H_2O). The XPS results manifest that the fully ordered perovskite (reduced at 550 °C) catalyst has the highest concentration of highly oxidative oxygen species and hydroxyl groups or surface adsorbed oxygen (Figure 4.6b and Figure 4.6c), which suggests the presence of highly enriched surface oxygen vacancies.[15] The increased absorbed hydroxyl on the catalyst surface is related to the stronger covalency of the B-O bond, which is beneficial to the kinetic aspect of the ORR process [16]. Also, the average valence of Mn cations in the fully reduced catalyst (550 °C) was 2.9 (calculated from the XPS survey in Figure S4.2). Because of the basic high spin state of Mn in the perovskite, the Ag-$PBMO_5$ possessed an electronic configuration of $t_{2g}^3 e_g^{1.1}$ which achieved an optimized orbital filling towards ORR.[7a, 17]

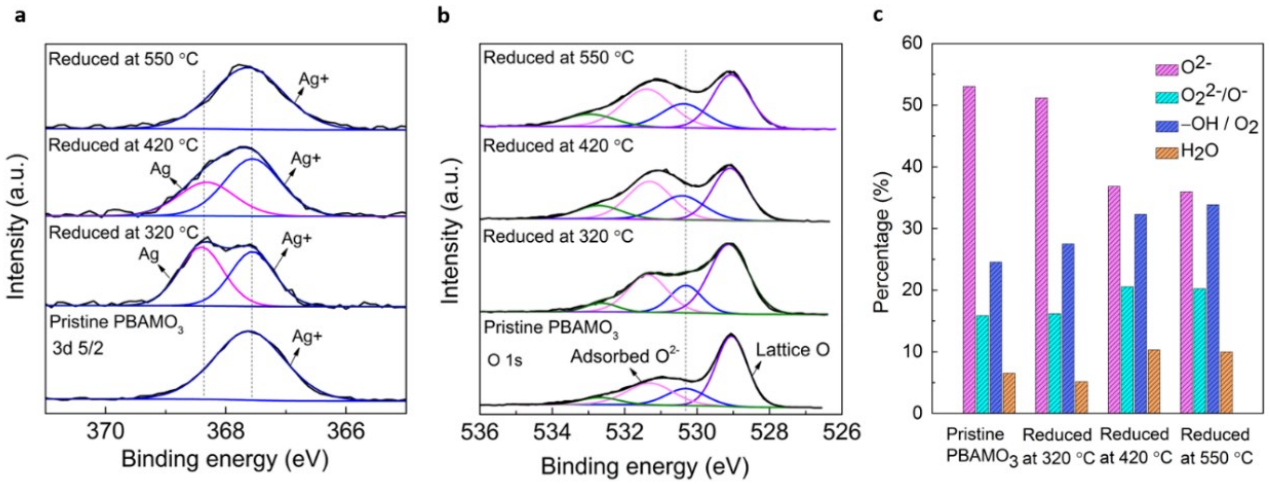

Figure 4.6 The XPS profiles of the $PBAMO_3$ samples reduced at different temperatures. (a) Ag 3d spectrum and its simulations; (b) O1s spectrum and its simulations; (c) Quantitative analysis of different oxygen species.

In general, the characterization results have predicted the excellent ORR catalytic activity of the Ag-$PBMO_5$ composite. We initially performed linear sweep voltammetry (LSV, 1600 rpm) tests on the Ag-$PBMO_5$ catalyst in O_2-saturated 0.1 M KOH solution to estimate its ORR catalytic activity (Figure 4.7a). As the benchmarks, the ORR catalytic activities of $Pr_{0.5}Ba_{0.5}MnO_{3-\delta}$, $PBMO_5$, $PBAMO_3$, the physically mixed Ag + $Pr_{0.95}Ba_{0.95}Mn_2O_{5-\delta}$ (denoted as Ag + $PBMO_5$), carbon black, the physically mixed Ag/C and the commercial Pt/C catalysts were examined (Figure 4.8), and the comparisons of their E_{onset} and $E_{1/2}$ are shown in Figure 4.7b and Table 4.1. The results revealed that the Ag-$PBMO_5$ catalyst demonstrated considerably higher catalytic activity in comparison to the $Pr_{0.5}Ba_{0.5}MnO_{3-\delta}$ and $PBMO_5$ catalysts. The ORR E_{onset} and $E_{1/2}$ of the Ag-$PBMO_5$ catalyst were 0.92 V vs RHE and 0.81 V vs RHE, respectively. This shows that the Ag-$PBMO_5$ catalyst outperformed its predecessors, i.e., $PBMO_5$ catalyst (E_{onset} 0.84 V vs RHE and $E_{1/2}$ 0.74 V vs RHE), $Pr_{0.5}Ba_{0.5}MnO_{3-\delta}$ catalyst (E_{onset} 0.82 V vs RHE and $E_{1/2}$ 0.73 V vs RHE) and Ag + $PBMO_5$ composite (E_{onset} 0.86 V vs RHE and $E_{1/2}$ 0.77 V vs RHE). The relatively more positive E_{onset} and $E_{1/2}$ of the Ag-$PBMO_5$ catalyst indicate its superior ORR catalytic activity and a better catalyst than most of the alternatives up to date.[1a, 18] Additionally, the Ag-$PBMO_5$ catalyst possessed higher limited current densities than those of the $Pr_{0.5}Ba_{0.5}MnO_{3-\delta}$, $PBMO_5$ and Ag + $PBMO_5$ catalysts, further demonstrating an enhancement of ORR catalytic activity.

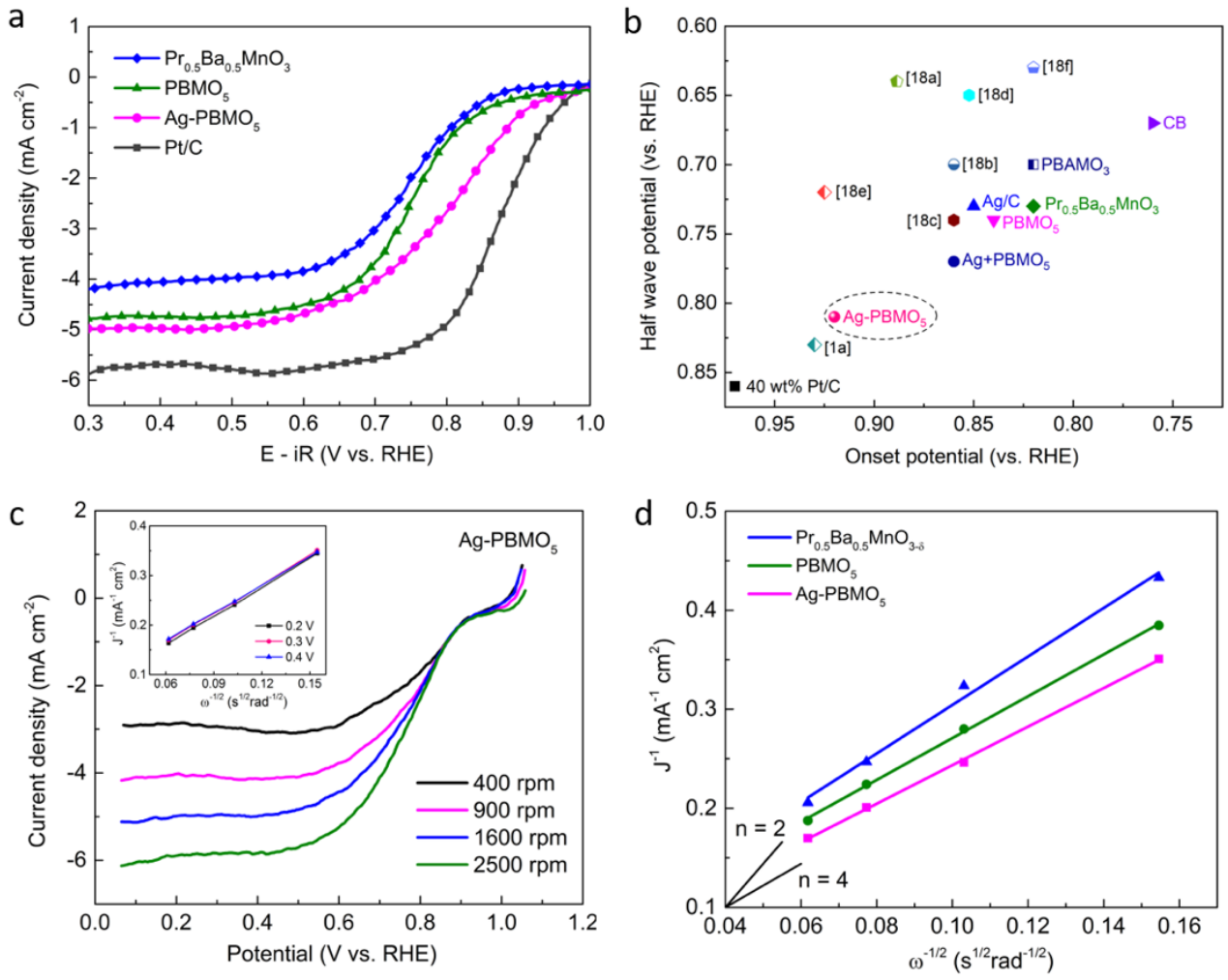

Figure 4.7 Electrochemical tests for the related catalysts. (a) ORR LSV curves at 1600 rpm for $Pr_{0.5}Ba_{0.5}MnO_{3-\delta}$, $PBMO_5$, $Ag\text{-}PBMO_5$, and 40 wt% Pt/C; (b) Summary of ORR E_{onset} and $E_{1/2}$ for $Pr_{0.5}Ba_{0.5}MnO_{3-\delta}$, $PBMO_5$, and $Ag\text{-}PBMO_5$ and some typical ORR catalysts from the reference, respectively[1a, 18]; (c) ORR LSV curves for $Ag\text{-}Pr_{0.95}Ba_{0.95}Mn_2O_{5-\delta}$ at different rotating speeds inserted with the Koutecky-Levich plots; (d) Electron transfer number of $Pr_{0.5}Ba_{0.5}MnO_{3-\delta}$, $PBMO_5$, $Ag\text{-}PBMO_5$ derived from K-L plots at 0.3 V vs RHE.

Table 4.2 A comparison of the onset potential (E_{onset}) and the half-wave reduction potentials (E1/2) for ORR electrocatalysts published recently

	Onset potential	Half wave Potential	
$Pr_{0.5}Ba_{0.5}MnO_{3-\delta}$/C	**0.82 V**	**0.73 V**	This study
$Pr_{0.475}Ba_{0.475}Ag_{0.05}MnO_{3-\delta}$	**0.82 V**	**0.70 V**	This study
$(Pr_{0.5}Ba_{0.5})Mn_2O_{5+\delta}$/C	**0.84 V**	**0.74 V**	This study
Ag+ $Pr_{0.95}Ba_{0.95}Mn_2O_{5+\delta}$/C	**0.86 V**	**0.77 V**	This study
Ag-$Pr_{0.95}Ba_{0.95}Mn_2O_{5+\delta}$/C	**0.92 V**	**0.81 V**	This study
$Pr_{0.475}Ba_{0.475}Ag_{0.05}MnO_{3-\delta}$ reduced at 320 °C	**0.85 V**	**0.73 V**	This study
$Pr_{0.475}Ba_{0.475}Ag_{0.05}MnO_{3-\delta}$ reduced at 420 °C	**0.89 V**	**0.78 V**	This study
Commercial Pt/C (40 wt%)	**0.97 V**	**0.86 V**	This study
Ag/C	**0.85 V**	**0.73 V**	This study
Carbon black	**0.76 V**	**0.67 V**	This study
$NdBa_{0.75}Ca_{0.25}Co_{1.5}Fe_{0.5}O_{5+\delta}$	**0.86 V**	**0.74 V**	Adv. Funct. Mater., 2016, 26, 4106
$LaTi_{0.65}Fe_{0.35}O_{3-\delta}$ nanoparticles decorated N-doped C nanorods	**0.92 V**	**0.72 V**	Nano Energy, 2015, 15, 92
Co_3O_4/N-rmGO	**0.93 V**	**0.83 V**	Nat. Mater., 2011, 10, 780
N, S, O-doped mesoporous carbon	**N/A**	**0.75 V**	J. Am. Chem. Soc., 2014 136, 8875
Fe−N/C	**0.92 V**	**0.81 V**	J. Am. Chem. Soc., 2014, 136, 11027
C−$MnFe_2O_4$	**N/A**	**0.81 V**	Nano Lett. 2013, 13, 2947
Ag (111)	**0.88 V**	**0.64 V**	Electrochimica Acta, 2007, 52, 2264
N-doped porous carbon	**0.86 V**	**0.70 V**	Energy Environ Sci.2014, 7, 442
Fe_3O_4–Co_3O_4 yolk–shell	**0.84 V**	**0.65 V**	J. Mater. Chem. 2012, 22, 19132
Hollow spherical $La_{0.8}Sr_{0.2}MnO_3$	**0.82 V**	**0.63 V**	J. Power Sources, 2014, 271, 55.

To understand the electron transfer pathway, LSV tests, at rotating speeds of 400 to 2500 rpm, were carried out on the Ag-$PBMO_5$ catalyst and the other related samples (Figure 4.7c and Figure 4.8). The number of transferred electrons is calculated based on the Koutecky-Levich analysis at various potentials (insets in Figure 4.7c and Figure 4.8). It is exciting to have found that the calculated electron transfer numbers are close to 4 for both $PBMO_5$ and Ag-$PBMO_5$ catalysts,

while it is 3.6 for $Pr_{0.5}Ba_{0.5}MnO_{3-\delta}$, indicating the four-electron transfer pathways in the deficient layer perovskite based catalyst (Figure 4.7d). Such reaction process suggests a high energy efficiency in theory.

In addition to the superior catalytic activity, the durability and stability of the catalysts are also crucial for their practical applications. The long term stability of the Ag-$PBMO_5$ catalyst was examined by measuring the LSV curves before and after the 10k CV cycles in O_2-saturated 0.1 M KOH solution. The corresponding ORR LSV curves of the Ag-$PBMO_5$ catalyst at a rotation speed of 1600 rpm, before and after cycling, are shown in the Figure 4.9a. It can be seen that the $E_{1/2}$ slightly shifted 23 mV in the negative direction after the stability test. In contrast, the $E_{1/2}$ of Pt/C catalyst shifted more than 42 mV after an identical testing (Figure 4.9b), indicating the superior stability of the Ag-$PBMO_5$ catalyst. Moreover, the chronoamperometric tests show that the Ag-$PBMO_5$ exhibited merely 9 % reduction in the relative current density after 50,000 s test, whereas the relative current of Pt/C continuously decreased to 72% under the same testing condition (Figure 4.9c). The stability of the Ag-$PBMO_5$ is also supported by HRTEM. The HRTEM image of Ag-$PBMO_5$ after long term catalytic test shows a clear surface and unchanged structure (Figure S4.3). To elucidate the practical applicability of Ag-$PBMO_5$, its methanol tolerance was also examined (Figure 4.9d). In the case of Pt/C, its operating current experienced an immediate drop in the presence of methanol, an indication of a pronounced poisoning effect of methanol on Pt/C catalyst. In contrast, the high-performance of Ag-$PBMO_5$ was maintained with negligible degradation under the same condition, attributable to its excellent methanol tolerance.

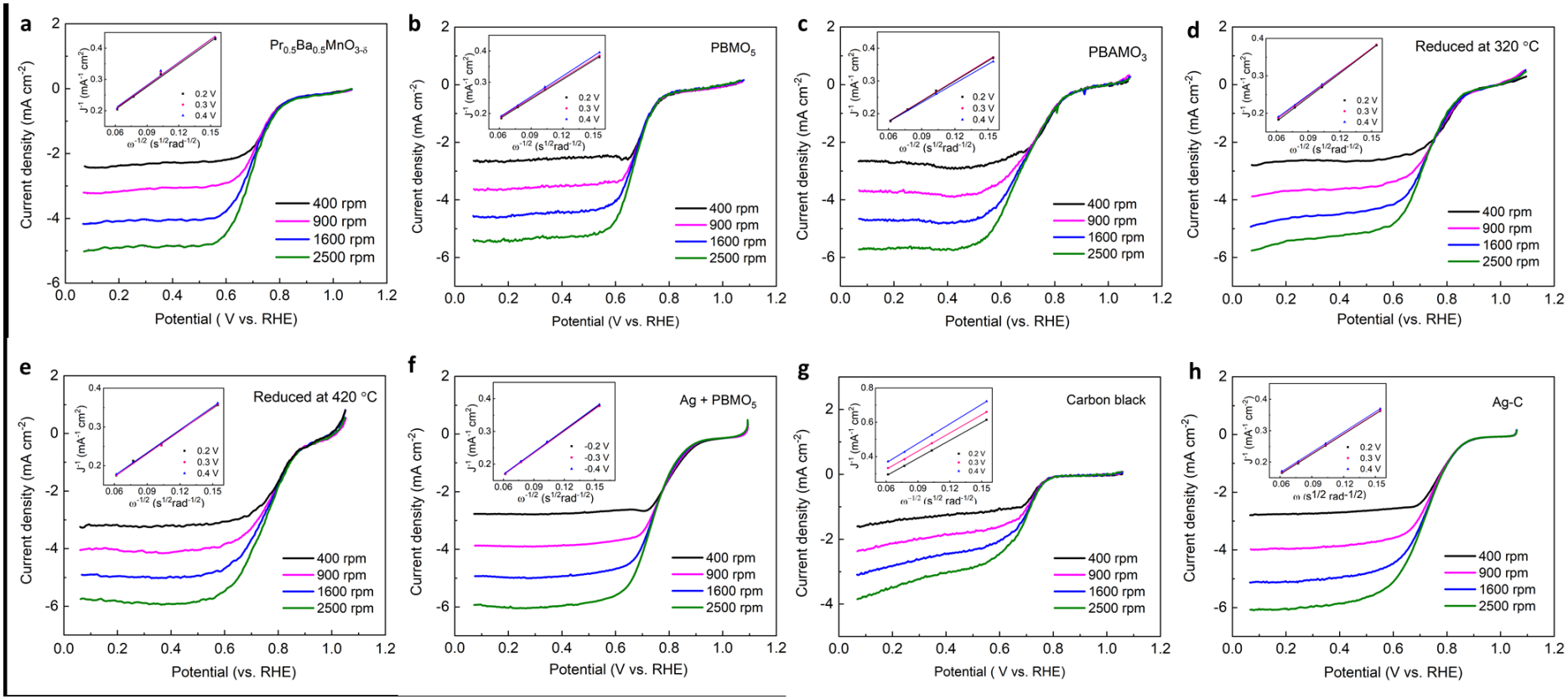

Figure 4.8 ORR LSV curves using a RDE on (a) $Pr_{0.5}Ba_{0.5}MnO_3$, (b) $PBMO_5$, (c) $PBAMO_3$, (d) $PBAMO_3$ reduced at 320 °C, (e) $PBAMO_3$ reduced at 420 °C, (f) Ag + $PBMO_5$, (g) Carbon black and (h) Ag/C at different rotating speeds inserted with the Koutecky-Levich plots.

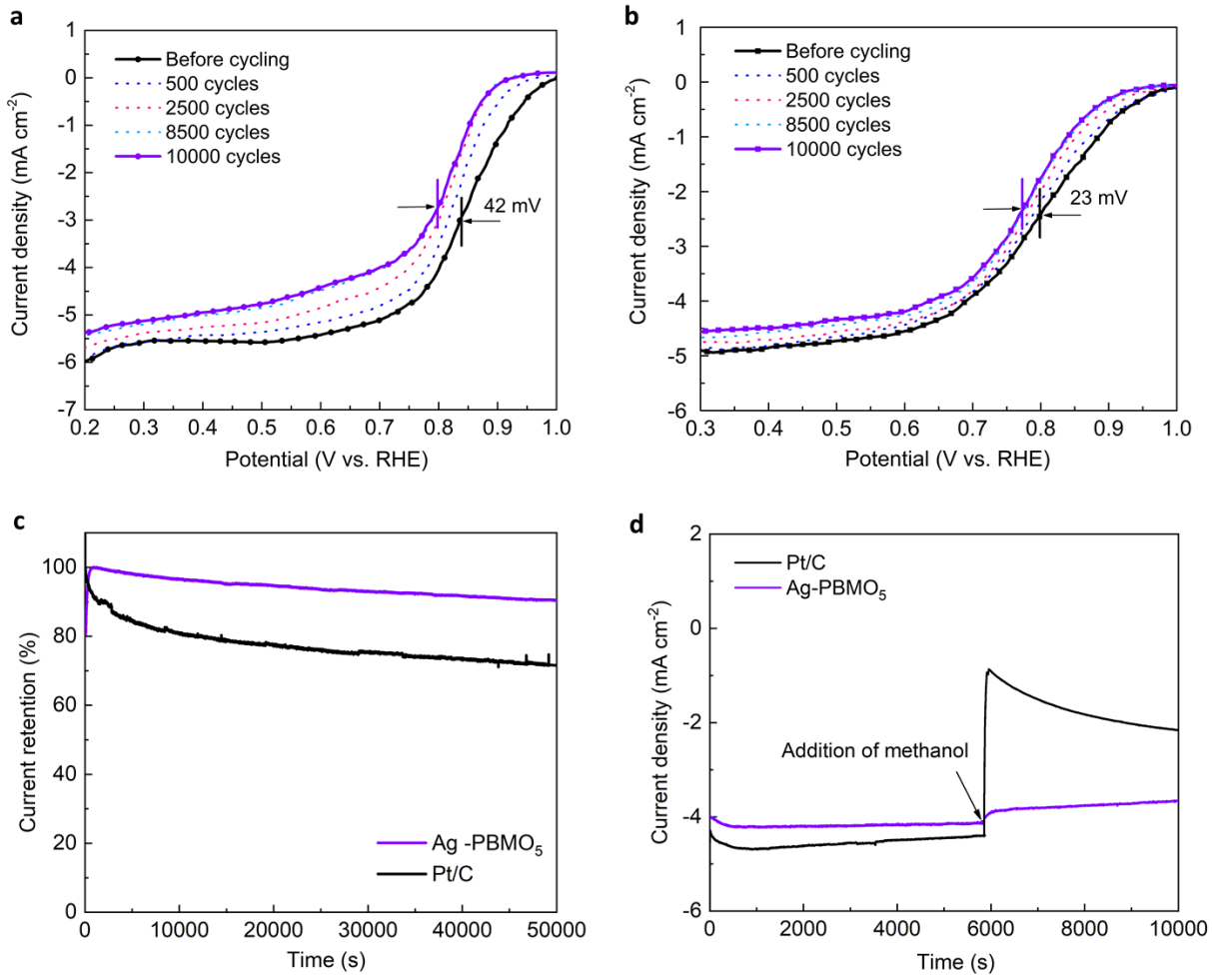

Figure 4.9 (a) ORR LSV curves for Ag-$PBMO_5$ before and after 10k CV cycles; (b) ORR LSV curves for commercial Pt/C before and after 10k CV cycles; (c) Current retention of chronoamperometric responses for Ag- $PBMO_5$ and Pt/C in O_2 saturated 0.1 M KOH at potential of 0.6 V vs. RHE (d) Durability test of Ag-$PBMO_5$ and comercial Pt/C at potential of 0.6 V vs. RHE in O_2 saturated 0.1 M KOH with and without presence of methanol (3 M).

Many factors collectively contribute to the superior catalytic activity of the Ag-$PBMO_5$ composite including crystal texture, chemical compositions, and elemental valence state (electronic configuration) among others. As for the $PBMO_5$ perovskite, two fundamental aspects account for

its excellent ORR performance. Firstly, the reconstruction of the crystal led to the formation of layered perovskites with interior ordered oxygen defects. The ordered defect structure favours charge transfers within the perovskite in the ORR process, facilitating the intrinsic catalytic activity of the perovskite. Secondly, the valence of Mn^{3+} originating from the phase engineered perovskite yields a unity e^g occupancy, which moderates the intermediate binding strength on Mn sites and contributes to the electrocatalytc activity of $PBMO_5$. The suggested catalytic mechanism of ORR on perovskite is shown in Figure 4.10a and is based on the reverse cycle proposed by Shaohorn Yang *et al*.[7a] On this basis, the Ag-$PBMO_5$ composite possesses two other distinct features that boost the ORR: A-site deficiency and socketed Ag NPs. These two features will be discussed in the following section on DFT calculations. It is important to note that the position of the oxygen p-band relative to the Fermi level is what determines the metal–oxygen hybridization, B-O bond covalency, oxygen vacancy concentration and oxygen mobility within the perovskite, all having significant impact on ORR kinetics.[7, 19] This was adopted as the descriptor for the ORR in the DFT calculations.

To evaluate the effect of A-site deficiency, both the surface and bulk O p-band centers were computed by DFT on tetragonal $PrBaMn_2O_5$ and $PBMO_5$. The DFT on A-site deficient $PBMO_5$ was calculated based on 2×2×4 supercells with a Pr vacancy and a Ba vacancy, respectively. As shown in Figure 10b and c, the surface O p-band center, relative to the Fermi level, reached to 2.27 eV (Ba vacancy) and 2.10 eV (Pr vacancy) in the A-site deficient perovskite $PBMO_5$, significantly lower than the pristine $PrBaMn_2O_5$ (2.46 eV). The results obtained from bulk O p-band are quite similar to the surface conditions (Figure 4.10c). The formation of A-site deficient perovskites likely contributed to higher oxygen exchange kinetics by lowering the energy of oxygen vacancy formation [20].

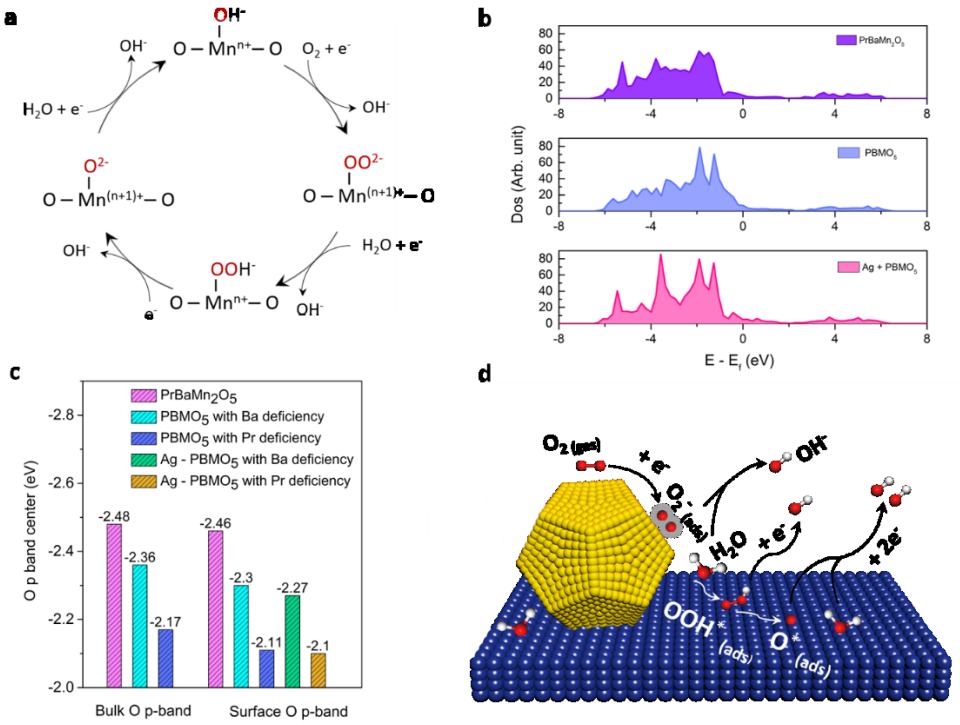

Figure 4.10 (a) Catalytic mechanism on perovskite oxide catalysts ($PBMO_5$) for ORR. (b) Surface oxygen P-DOS of $PrBaMn_2O_5$, $PBMO_5$ and Ag+$PBMO_5$ (with Pr vacancy in the supercell). (c) Summary of the computed O p-band center versus the Fermi level for the related samples; (d) Proposed ORR schematic on Ag-$PBMO_5$.

The *in-situ* exsolution generally resulted in an emergent effect of particle pinning on parent support. In consideration of the difference in work function as well as the close coupling between Ag and manganite perovskite, charge transfer is expected to occur on the interface between exsolved Ag and $PBMO_5$ surface. [21] To examine the electronic structure of the Ag-$PBMO_5$, the surface O p-band center and the electron occupancy in s, p, d orbitals on Mn sites were computed from the DFT based on 2×2×4 supercell with a Ag atom added to the surface of the (001) plane. As shown in the DFT simulated electron occupied states (Table S4.1), a significant ligand effect between $PBMO_5$ and the socketed Ag nanoparticles was found. The increase in electron occupancy in s, p,

d orbitals on Mn sites indicates the charge transfer from Ag to Mn sites within the interface, which suggests that the strong interfacial effects of Ag and $PBMO_5$ lead to the immediate electronic structure of Ag and $PBMO_5$. Previous studies on metallic electrocatalysts have revealed a fundamental relationship in electrocatalytic trends on the ORR activity and d-band center energy. [22] Particularly, the specific catalytic activity and the d-band center energy demonstrate a volcano behaviour. Electrocatalysts, having a low d-band energy, such as Ag and Au, generally exhibit low adsorption energies of reactive intermediates, resulting in an insufficient ORR activity.[22b] However, in the case of Ag-$PBMO_5$, owing to charge transfer, the d-band orbitals of the Ag atoms are not completely filled and vacancies are generated, this consequently narrows the d-orbital of Ag and up-shifts the d-band center of Ag atom [21]. The Ag atom with an up-shifted d-band center is expected to bond O_2 more strongly, and simultaneously split O-O more efficiently. Therefore, charge transfer plays a crucial role in the enhancement of the ORR activity.

In addition to the ligand effect, the strong interfacial anchoring structure also results in a significant interparticle cooperation, which enables an improved ensemble effect between Ag and $PBMO_5$. In a Ag NP pinned manganite perovskite, the oxygen deficient perovskite plays a crucial role in surface hydroxide regeneration, while the socketed Ag NPs are more efficient for the oxygen activation processes.[23] The significant increase of Ag-$PBMO_5$ electrochemical activity can be attributed to the bifunctional effect of Ag nanoparticles and deficient-ordered perovskite because of oxygen activation on noble metals as well as water activation on oxophilic transition metal sites. Similar phenomena have also been found in the Ag/MnO_x composites. [21b]

The synergistic catalytic mechanism of ORR on Ag-$PBMO_5$ is summarized in the Figure 4.10d: O_{2gas} which has been dissolved in the KOH solution is firstly adsorbed on the surface of Ag to form

O_{2ads}. Then, the adsorbed O_{2ads} on the Ag surface can gain an electron to form O_{2ads}^-. Sequentially, the adsorbed H_2O molecule on the high oxophilicity of B-site $PBMO_5$ terminal provides a proton to an adsorbed oxygen specie (O_{ads}^-) on an adjacent Ag site. In this step, O_2^- accept a proton from H_2O to form OOH^*. A hydroxide ion is generated simultaneously with protonation. Evidence has been provided that on perovskites surface, the O_{2ads}^- formation with a simultaneous charge transfer process appears to be the rate-determining step[7a]–this step occurs more efficiently on Ag atoms.[21a] In our case, the interaction between the adsorbed O_2 and the socketed Ag NPs may facilitate O_{2ads} activation and dissociation. The generated OOH* would gain another electron and dissociate into O* and OH^- in the step that follows. It is interesting to note that in some composites, such as Ag or Pt with metal oxide (Mn, Ti, W), the generated intermediate oxygen containing species tend to transfer over to the metal oxides because of the higher oxophilicity of the Mn site. [9b, 21] In the final step, the produced O* reacts with another adsorbed H_2O molecule on the perovskite terminal and forms two OH^-. Over the entire process, the close contact between Ag and $PBMO_5$ within the socketed structure facilitates electron transfer and ion migration during the oxygen reduction reaction, which is likely to provide a promoted ensemble effect between Ag and $PBMO_5$ in comparison to the Ag+$PBMO_5$ that synthesized through physical mixing.

4.4. Conclusions

In summary, a novel ORR catalyst composed of nanoscale Ag attached to the A-site deficient perovskite network was developed. The synthesized Ag-$PBMO_5$ catalyst exhibits favorable ORR catalytic activity in terms of overpotential (E_{onset} ~ 0.92 V vs RHE and $E_{1/2}$ ~ 0.81 V vs RHE), and outperforms the Pt/C with respect to durability. The statement is theoretically supported that the synergistic chemical coupling effects of Ag and perovskite lead to the significant ligand action and

interparticle cooperation. Herein, the exceptional properties of Ag-$PBMO_5$ should be attributed to the rationally designed nanoarchitectures, surface oxygen vacancies, A-site deficiency and dual phase catalyst systems. Such protocols demonstrate the systematic engineering of perovskites into promising catalysts, opening up exciting new possibilities to develop advanced catalysts not only for oxygen-based electrochemical applications but also for catalysis community in general.

4.5 Experimental section

4.5.1 Synthesis of various catalysts

$Ba(NO_3)_2$ (assay 100.0%), $AgNO_3$ (assay 100.0%), and N, N-dimethylformamide (DMF, assay ≥ 99.9%) were purchased from Fisher Scientific Cooperation. $Pr(NO_3)_3 \cdot 6H_2O$ (assay ≥ 99.9%) and $Mn(NO_3)_2 \cdot 4H_2O$ (assay ≥ 97.0%), poly(vinylpyrrolidone) (PVP, assay 12 to 12.8% nitrogen, average M.W 1,300,000) were purchased from Acros Organics. In a typical experiment, desired amounts of metal nitrate and PVP were dissolved in DMF and the solution was stirred for 12 h at ambient temperature to form the homogenous precursor required for electrospinning. The concentration of the ABO_3 perovskite was 0.15 M in the precursor solution. The PVP in the metal nitrates solution was kept at a weight ratio of 15 wt% to reach to a viscosity for achieving an appropriate polymer entanglement by the electric field. The solution was loaded into a plastic syringe (10 mL) with a stainless steel spinneret (D ¼ 0.5 mm). A 20 kV voltage was applied between a spinneret and an aluminium foil collector at a distance of 15 cm. The supply rate of the precursor in the electrospinning set-up was 0.3 mL h^{-1}. The electrospun nanofibers were collected from the aluminum foil, dried at 100 °C for 1h, and sintered at 800 °C for 2 h to form the pure phase of $(Pr_{0.5}Ba_{0.5})_{0.95}Ag_{0.05}MnO_{3-\delta}$ (denoted as $PBAMO_3$) (Figure 4.11). The $(Pr_{0.5}Ba_{0.5})_{0.95}MnO_{3-\delta}$ and A-site deficient $(Pr_{0.5}Ba_{0.5})_{0.95}MnO_{3-\delta}$ were synthesized in a similar

method. The as-synthesized $(Pr_{0.5}Ba_{0.5})_{0.95}Ag_{0.05}MnO_{3-\delta}$ and A-site deficient $(Pr_{0.5}Ba_{0.5})_{0.95}MnO_{3-\delta}$ were further treated in 5% H_2/N_2 for 2 h at 550 °C to form Ag-$Pr_{0.95}Ba_{0.95}Mn_2O_{5-\delta}$ and $Pr_{0.95}Ba_{0.95}Mn_2O_{5-\delta}$ ($PBMO_5$). Also, the treatment temperatures of 320 °C and 420 °C were used to illustrate the exsolution process of Ag and the phase change of the perovskite.

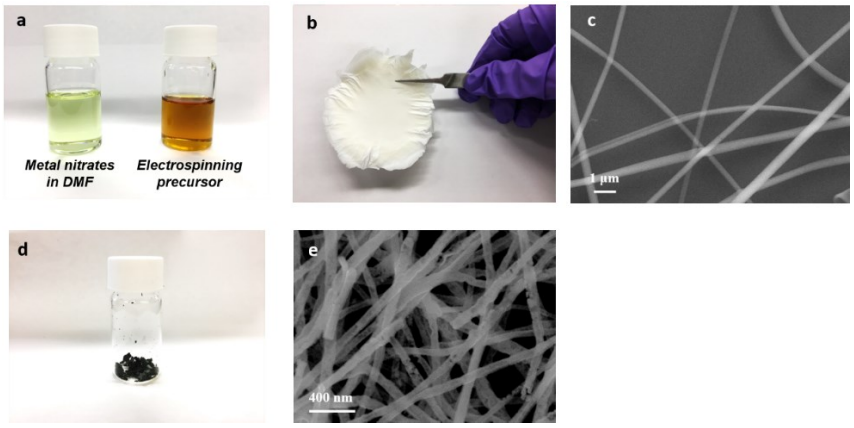

Figure 4.11 (a) images of the metal nitrate solution (0.15 M metal nitrates dissolved in DMF) and electrospinning precursor (0.15 M metal nitrates with 30 wt% of PVP); (b) images of the electrospun nanofiber before calcination (peeled from the target collector); (c) FESEM of the electrospun nanofiber before calcination; (d) Pristine $PBAMO_3$ perovskite obtained from the calcination, and (d) FESEM of the Pristine $PBAMO_3$ perovskite.

For comparison purpose, a composite catalyst Ag + $Pr_{0.95}Ba_{0.95}Mn_2O_{5-\delta}$ (denoted as Ag + $PBMO_5$) was prepared through a traditional physical mixing method. $AgNO_3$ (0.127 g) and sodium citrate dihydrate (0.570 g, 99%, Alfa Aesar) were first dissolved in 100 mL DI water. The as-synthesized $PBMO_5$ (0.16 g) was also dispersed in DI water (50 mL), and the dispersion was ultra-sonicated for 1 h. $NaBH_4$ (0.01 g) was dissolved separately in DI water (10 mL) and added dropwise to the $AgNO_3$/sodium citrate solution under vigorous stirring, a yellowish-brown Ag colloid is then formed. Subsequently, 4.424 mL Ag colloid solution was added to the $PBMO_5$ dispersion.

The benchmark catalyst Ag/C was synthesized using the same method, with 0.17 g carbon black (Cabot) dispersed in 50 mL DI water. Then, 100 mL of the Ag colloid was added to the carbon dispersion. The suspension was collected through centrifugation after settling down for 24 h, washed with DI water three times, and dried in an oven at 60 °C. The morphologies of the as-synthesized Ag/C are shown in Figue 4.12.

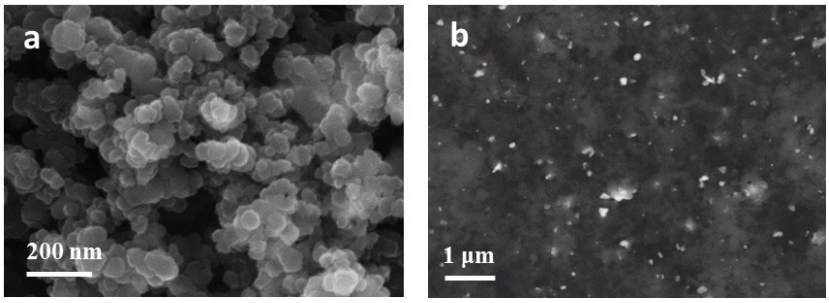

Figure 4.12 Ag/C naoparticles, FESEM images from (a) secondary electrons and (b) back-scattered electrons.

4.5.2 Preparation of electrodes

Catalyst inks were prepared by sonicating 10 mg of the as-synthesized perovskite with 10 mg of carbon black (Cabot) in a solution containing 200 µL of 5wt. % Nafion (Aldrich) and 800 µL of isopropyl alcohol (Fisher Scientific Cooperation). For comparison, catalyst ink of pure carbon black was made with the same chemical composition without the addition of perovskite. 5 µL of the catalysts ink was dispersed on a 5 mm pre-polished glassy carbon rotating disk electrode (RDE, Pine instrument) and was dried in air for 1 h before the test. The loading amount of the perovskite catalyst was 0.255 mg_{ox} cm^{-2}. The Ag/C catalyst ink was prepared from the as-prepared 32 wt% Ag/C with a loading amount of 0.167 mg_{Ag} cm^{-2}. The Pt/C catalyst ink was prepared with commercial 40 wt% Pt/C (Alfa Aesar) as described elsewhere. [24] The 40 wt.% Pt/C catalyst was

dispersed in a mixture of deionized water, isopropyl alcohol and 5wt.% Nafion (Aldrich) (v:v:v = 4:1:0.04). After being sonicated for 1 h, 15 μL of the Pt/C catalysts ink was dropped onto the glassy carbon electrode to achieve a loading amount of 10.2 μg_{Pt} cm^{-2}.

4.5.3 Electrochemical tests

Electrochemical measurements were conducted at room temperature with a three electrode system using Electrochemical Interface Solartron Analytical 1287 and Solartron 1255B frequency response analyzer. Cyclic voltammograms were conducted in Ar and O_2 saturated 0.1 M KOH solution from 0.1 V to -0.9 V (vs. Ag/AgCl, sat. KCl) at a scan rate of 20 mV s^{-1}. Cyclic voltammetry based accelerated degradation tests were conducted by cycling between -0.6 to 0.1 V vs Ag/AgCl at 150 mV s^{-1} for 10 k cycles. The EIS measurements were conducted in the 1 M KOH solution with the sample loading amount as previously mentioned for preparation of catalysts.

4.5.4 Computational

The Vienna Ab initio Simulation Package (VASP) was adopted to carry out the density functional theory (DFT) calculations with the projector-augmented plane-wave (PAW) method. The generalized gradient approximation (GGA) parameterized by Perdew and Wang (PW91) was selected to treat the exchange-correlation function. Bulk perovskites, with and without vacancy, were simulated with 2×2×4 supercell and were fully relaxed. Mn terminated surface (001) was built using asymmetric 8-layer and 10 Å vacuum layer was created based on a relaxed bulk perovskite. The bottom two layers of the surface were fixed, while the other layers were internally relaxed. All calculations were performed in the ferromagnetic state and Mn 3d electrons were treated with Hubbard U correction with U_{eff} = 4 eV. A plane-wave cutoff energy of 600 eV was

used for the expansion of Kohn-sham orbitals. Monkhorst-Pack grids of 4×4×2 and 4×4×1 k-points were used for bulk and surface, respectively. Finally, the centroid of the PDOS of O 2p band relative to the Fermi level was taken as the effective O p-band center.

4.6 References

1. (a) Liang, Y.; Li, Y.; Wang, H.; Zhou, J.; Wang, J.; Regier, T.; Dai, H., Co3O4 nanocrystals on graphene as a synergistic catalyst for oxygen reduction reaction. *Nature materials* **2011,** *10* (10), 780-786; (b) Whitesides, G. M.; Crabtree, G. W., Don't forget long-term fundamental research in energy. *science* **2007,** *315* (5813), 796-798; (c) Cao, L.; Lv, F.; Liu, Y.; Wang, W.; Huo, Y.; Fu, X.; Sun, R.; Lu, Z., A high performance O 2 selective membrane based on CAU-1-NH 2@ polydopamine and the PMMA polymer for Li–air batteries. *Chemical Communications* **2015,** *51* (21), 4364-4367.

2. Holewinski, A.; Idrobo, J.-C.; Linic, S., High-performance Ag–Co alloy catalysts for electrochemical oxygen reduction. *Nature chemistry* **2014,** *6* (9), 828.

3. (a) Sofer, Z. k.; Jankovský, O. e.; Šimek, P.; Klímová, K. i.; Macková, A.; Pumera, M., Uranium-and thorium-doped graphene for efficient oxygen and hydrogen peroxide reduction. *ACS nano* **2014,** *8* (7), 7106-7114; (b) Lai, L.; Potts, J. R.; Zhan, D.; Wang, L.; Poh, C. K.; Tang, C.; Gong, H.; Shen, Z.; Lin, J.; Ruoff, R. S., Exploration of the active center structure of nitrogen-doped graphene-based catalysts for oxygen reduction reaction. *Energy & Environmental Science* **2012,** *5* (7), 7936-7942; (c) Yang, Z.; Yao, Z.; Li, G.; Fang, G.; Nie, H.; Liu, Z.; Zhou, X.; Chen, X. a.; Huang, S., Sulfur-doped graphene as an efficient metal-free cathode catalyst for oxygen reduction. *ACS nano* **2011,** *6* (1), 205-211.

4. (a) Jung, J. I.; Jeong, H. Y.; Lee, J. S.; Kim, M. G.; Cho, J., A bifunctional perovskite catalyst for oxygen reduction and evolution. *Angewandte Chemie International Edition* **2014,** *53* (18), 4582-4586; (b) Liu, Y.; Cao, L.-J.; Cao, C.-W.; Wang, M.; Leung, K.-L.; Zeng, S.-S.; Hung, T.; Chung, C.; Lu, Z.-G., Facile synthesis of spinel CuCo 2 O 4 nanocrystals as high-performance

cathode catalysts for rechargeable Li–air batteries. *Chemical Communications* **2014,** *50* (93), 14635-14638.

5. (a) Tan, S. M.; Chua, C. K.; Sedmidubský, D.; Sofer, Z.; Pumera, M., Electrochemistry of layered GaSe and GeS: applications to ORR, OER and HER. *Physical Chemistry Chemical Physics* **2016,** *18* (3), 1699-1711; (b) Wu, G.; Cui, G.; Li, D.; Shen, P.-K.; Li, N., Carbon-supported Co1. 67Te2 nanoparticles as electrocatalysts for oxygen reduction reaction in alkaline electrolyte. *Journal of Materials Chemistry* **2009,** *19* (36), 6581-6589.

6. (a) Lin, L.; Zhu, Q.; Xu, A.-W., Noble-metal-free Fe–N/C catalyst for highly efficient oxygen reduction reaction under both alkaline and acidic conditions. *Journal of the American Chemical Society* **2014,** *136* (31), 11027-11033; (b) Jiang, W.-J.; Gu, L.; Li, L.; Zhang, Y.; Zhang, X.; Zhang, L.-J.; Wang, J.-Q.; Hu, J.-S.; Wei, Z.; Wan, L.-J., Understanding the High Activity of Fe–N–C Electrocatalysts in Oxygen Reduction: Fe/Fe3C Nanoparticles Boost the Activity of Fe–N x. *Journal of the American Chemical Society* **2016,** *138* (10), 3570-3578.

7. (a) Suntivich, J.; Gasteiger, H. A.; Yabuuchi, N.; Nakanishi, H.; Goodenough, J. B.; Shao-Horn, Y., Design principles for oxygen-reduction activity on perovskite oxide catalysts for fuel cells and metal–air batteries. *Nature chemistry* **2011,** *3* (7), 546; (b) Hong, W. T.; Risch, M.; Stoerzinger, K. A.; Grimaud, A.; Suntivich, J.; Shao-Horn, Y., Toward the rational design of non-precious transition metal oxides for oxygen electrocatalysis. *Energy & Environmental Science* **2015,** *8* (5), 1404-1427.

8. (a) Jung, J. I.; Jeong, H. Y.; Kim, M. G.; Nam, G.; Park, J.; Cho, J., Fabrication of Ba0. 5Sr0. 5Co0. 8Fe0. 2O3–δ Catalysts with Enhanced Electrochemical Performance by Removing an Inherent Heterogeneous Surface Film Layer. *Advanced Materials* **2015,** *27* (2), 266-271; (b) Xu, X.; Su, C.; Zhou, W.; Zhu, Y.; Chen, Y.; Shao, Z., Co-doping Strategy for Developing Perovskite

Oxides as Highly Efficient Electrocatalysts for Oxygen Evolution Reaction. *Advanced Science* **2016,** *3* (2); (c) Mefford, J. T.; Rong, X.; Abakumov, A. M.; Hardin, W. G.; Dai, S.; Kolpak, A. M.; Johnston, K. P.; Stevenson, K. J., Water electrolysis on La1-xSrxCoO3-[delta] perovskite electrocatalysts. *Nature communications* **2016,** *7*; (d) Chen, D.; Chen, C.; Baiyee, Z. M.; Shao, Z.; Ciucci, F., Nonstoichiometric oxides as low-cost and highly-efficient oxygen reduction/evolution catalysts for low-temperature electrochemical devices. *Chem. Rev* **2015,** *115* (18), 9869-9921; (e) Zhu, Y.; Zhou, W.; Shao, Z., Perovskite/Carbon Composites: Applications in Oxygen Electrocatalysis. *small* **2017**.

9. (a) Zhu, Y.; Zhou, W.; Chen, Y.; Yu, J.; Xu, X.; Su, C.; Tadé, M. O.; Shao, Z., Boosting oxygen reduction reaction activity of palladium by stabilizing its unusual oxidation states in perovskite. *Chemistry of Materials* **2015,** *27* (8), 3048-3054; (b) Park, S.-A.; Lee, E.-K.; Song, H.; Kim, Y.-T., Bifunctional enhancement of oxygen reduction reaction activity on Ag catalysts due to water activation on LaMnO3 supports in alkaline media. *Scientific reports* **2015,** *5*; (c) Serra, J. M.; Buchkremer, H.-P., On the nanostructuring and catalytic promotion of intermediate temperature solid oxide fuel cell (IT-SOFC) cathodes. *Journal of Power Sources* **2007,** *172* (2), 768-774; (d) Zhu, Y.; Zhou, W.; Ran, R.; Chen, Y.; Shao, Z.; Liu, M., Promotion of oxygen reduction by exsolved silver nanoparticles on a perovskite scaffold for low-temperature solid oxide fuel cells. *Nano letters* **2015,** *16* (1), 512-518.

10. (a) Zhao, Y.; Xu, L.; Mai, L.; Han, C.; An, Q.; Xu, X.; Liu, X.; Zhang, Q., Hierarchical mesoporous perovskite La0. 5Sr0. 5CoO2. 91 nanowires with ultrahigh capacity for Li-air batteries. *Proceedings of the National Academy of Sciences* **2012,** *109* (48), 19569-19574; (b) Park, H. W.; Lee, D. U.; Zamani, P.; Seo, M. H.; Nazar, L. F.; Chen, Z., Electrospun porous nanorod perovskite oxide/nitrogen-doped graphene composite as a bi-functional catalyst for metal air batteries. *Nano*

Energy **2014,** *10*, 192-200; (c) Xu, J. J.; Xu, D.; Wang, Z. L.; Wang, H. G.; Zhang, L. L.; Zhang, X. B., Synthesis of Perovskite-Based Porous La0. 75Sr0. 25MnO3 Nanotubes as a Highly Efficient Electrocatalyst for Rechargeable Lithium–Oxygen Batteries. *Angewandte Chemie International Edition* **2013,** *52* (14), 3887-3890.

11. Shin, T. H.; Myung, J.-H.; Verbraeken, M.; Kim, G.; Irvine, J. T., Oxygen deficient layered double perovskite as an active cathode for CO2 electrolysis using a solid oxide conductor. *Faraday Discuss.* **2015,** *182*, 227-239.

12. Sengodan, S.; Choi, S.; Jun, A.; Shin, T. H.; Ju, Y.-W.; Jeong, H. Y.; Shin, J.; Irvine, J. T.; Kim, G., Layered oxygen-deficient double perovskite as an efficient and stable anode for direct hydrocarbon solid oxide fuel cells. *Nature materials* **2015,** *14* (2), 205.

13. (a) De la Rosa, J. R.; Hernandez, A.; Rojas, F.; Ledezma, J. J., Sol–gel synthesis and characterization of novel La, Mn and Fe doped zirconia: Catalytic combustion activity of trichloroethylene. *Colloids and Surfaces A: Physicochemical and Engineering Aspects* **2008,** *315* (1), 147-155; (b) Hirano, T.; Purwanto, H.; Watanabe, T.; Akiyama, T., Self-propagating high-temperature synthesis of Sr-doped LaMnO 3 perovskite as oxidation catalyst. *Journal of alloys and compounds* **2007,** *441* (1), 263-266; (c) Zhou, X.; Zhao, Y.; Cao, X.; Xue, Y.; Xu, D.; Jiang, L.; Su, W., Fabrication of polycrystalline lanthanum manganite (LaMnO 3) nanofibers by electrospinning. *Materials Letters* **2008,** *62* (3), 470-472.

14. (a) Romand, M.; Roubin, M.; Deloume, J.-P., X-ray photoelectron emission studies of mixed selenides AgGaSe 2 and Ag 9 GaSe 6. *Journal of solid state chemistry* **1978,** *25* (1), 59-64; (b) Kaushik, V. K., XPS core level spectra and Auger parameters for some silver compounds. *Journal of Electron Spectroscopy and Related Phenomena* **1991,** *56* (3), 273-277.

15. Zhu, Y.; Zhou, W.; Yu, J.; Chen, Y.; Liu, M.; Shao, Z., Enhancing Electrocatalytic Activity of Perovskite Oxides by Tuning Cation Deficiency for Oxygen Reduction and Evolution Reactions. *Chemistry of Materials* **2016,** *28* (6), 1691-1697.

16. Du, Z.; Yang, P.; Wang, L.; Lu, Y.; Goodenough, J.; Zhang, J.; Zhang, D., Electrocatalytic performances of LaNi 1− x Mg x O 3 perovskite oxides as bi-functional catalysts for lithium air batteries. *Journal of Power Sources* **2014,** *265*, 91-96.

17. Stoerzinger, K. A.; Risch, M.; Suntivich, J.; Lü, W.; Zhou, J.; Biegalski, M. D.; Christen, H. M.; Venkatesan, T.; Shao-Horn, Y., Oxygen electrocatalysis on (001)-oriented manganese perovskite films: Mn valency and charge transfer at the nanoscale. *Energy & Environmental Science* **2013,** *6* (5), 1582-1588.

18. (a) Blizanac, B.; Ross, P.; Markovic, N., Oxygen electroreduction on Ag (111): the pH effect. *Electrochimica Acta* **2007,** *52* (6), 2264-2271; (b) Zhang, P.; Sun, F.; Xiang, Z.; Shen, Z.; Yun, J.; Cao, D., ZIF-derived in situ nitrogen-doped porous carbons as efficient metal-free electrocatalysts for oxygen reduction reaction. *Energy & Environmental Science* **2014,** *7* (1), 442-450; (c) Hua, B.; Zhang, Y. Q.; Yan, N.; Li, M.; Sun, Y. F.; Chen, J.; Li, J.; Luo, J. L., The excellence of both worlds: developing effective double perovskite oxide catalyst of oxygen reduction reaction for room and elevated temperature applications. *Advanced Functional Materials* **2016,** *26* (23), 4106-4112; (d) Ye, Y.; Kuai, L.; Geng, B., A template-free route to a Fe 3 O 4–Co 3 O 4 yolk–shell nanostructure as a noble-metal free electrocatalyst for ORR in alkaline media. *Journal of Materials Chemistry* **2012,** *22* (36), 19132-19138; (e) Prabu, M.; Ramakrishnan, P.; Ganesan, P.; Manthiram, A.; Shanmugam, S., LaTi 0.65 Fe 0.35 O 3− δ nanoparticle-decorated nitrogen-doped carbon nanorods as an advanced hierarchical air electrode for rechargeable metal-air batteries. *Nano Energy* **2015,** *15*, 92-103; (f) Lu, F.; Sui, J.; Su, J.; Jin, C.; Shen, M.; Yang, R.,

Hollow spherical La 0.8 Sr 0.2 MnO 3 perovskite oxide with enhanced catalytic activities for the oxygen reduction reaction. *Journal of Power Sources* **2014,** *271*, 55-59.

19. (a) Mueller, D. N.; Machala, M. L.; Bluhm, H.; Chueh, W. C., Redox activity of surface oxygen anions in oxygen-deficient perovskite oxides during electrochemical reactions. *Nature communications* **2015,** *6*; (b) Gupta, S.; Kellogg, W.; Xu, H.; Liu, X.; Cho, J.; Wu, G., Bifunctional perovskite oxide catalysts for oxygen reduction and evolution in alkaline media. *Chemistry–An Asian Journal* **2016,** *11* (1), 10-21; (c) Hibino, M.; Kimura, T.; Suga, Y.; Kudo, T.; Mizuno, N., Oxygen rocking aqueous batteries utilizing reversible topotactic oxygen insertion/extraction in iron-based perovskite oxides Ca1–xLaxFeO3− δ. *Scientific reports* **2012,** *2*, 601.

20. Lee, Y.-L.; Kleis, J.; Rossmeisl, J.; Shao-Horn, Y.; Morgan, D., Prediction of solid oxide fuel cell cathode activity with first-principles descriptors. *Energy & Environmental Science* **2011,** *4* (10), 3966-3970.

21. (a) Liu, J.; Liu, J.; Song, W.; Wang, F.; Song, Y., The role of electronic interaction in the use of Ag and Mn 3 O 4 hybrid nanocrystals covalently coupled with carbon as advanced oxygen reduction electrocatalysts. *Journal of Materials Chemistry A* **2014,** *2* (41), 17477-17488; (b) Slanac, D. A.; Lie, A.; Paulson, J. A.; Stevenson, K. J.; Johnston, K. P., Bifunctional catalysts for alkaline oxygen reduction reaction via promotion of ligand and ensemble effects at Ag/MnO x nanodomains. *The Journal of Physical Chemistry C* **2012,** *116* (20), 11032-11039.

22. (a) Lima, F.; Zhang, J.; Shao, M.; Sasaki, K.; Vukmirovic, M.; Ticianelli, E.; Adzic, R., Catalytic Activity− d-Band Center Correlation for the O2 Reduction Reaction on Platinum in Alkaline Solutions. *The Journal of Physical Chemistry C* **2007,** *111* (1), 404-410; (b) Nørskov, J. K.; Rossmeisl, J.; Logadottir, A.; Lindqvist, L.; Kitchin, J. R.; Bligaard, T.; Jonsson, H., Origin of

the overpotential for oxygen reduction at a fuel-cell cathode. *The Journal of Physical Chemistry B* **2004,** *108* (46), 17886-17892.

23. Slanac, D. A.; Hardin, W. G.; Johnston, K. P.; Stevenson, K. J., Atomic ensemble and electronic effects in Ag-rich AgPd nanoalloy catalysts for oxygen reduction in alkaline media. *Journal of the American Chemical Society* **2012,** *134* (23), 9812-9819.

24. Wei, C.; Feng, Z.; Scherer, G. G.; Barber, J.; Shao-Horn, Y.; Xu, Z. J., Cations in Octahedral Sites: A Descriptor for Oxygen Electrocatalysis on Transition-Metal Spinels. *Advanced Materials* **2017**.

4.7 Supporting Information

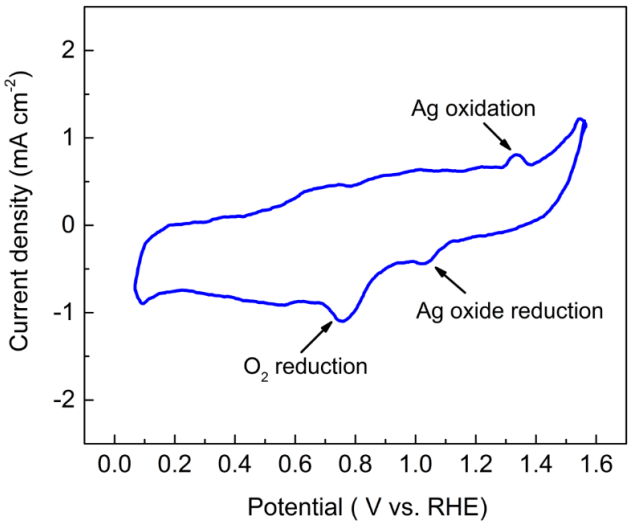

Figure S4. 1 Cyclic voltammogram curve of Ag-$PrBaMnO_5$ in 0.1 M KOH, demonstrating that the Ag_2O was reduced to Ag before the ORR process.

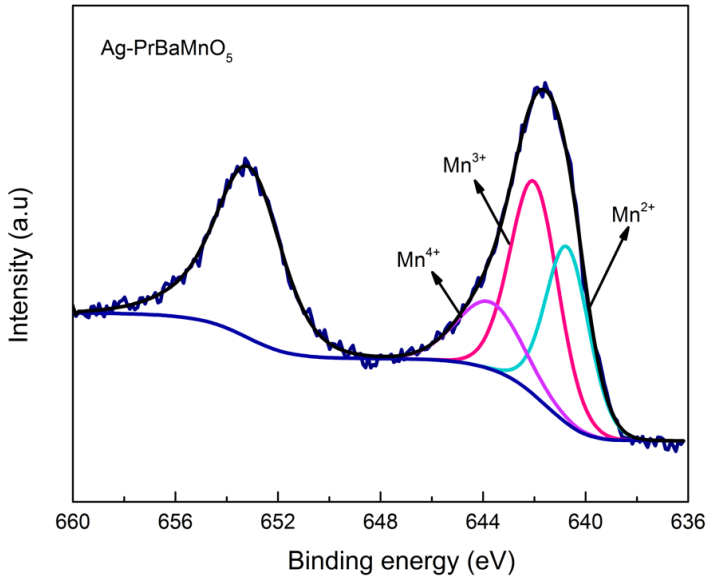

Figure S4. 2 XPS spectrum of Mn (2p) Ag-$PBMO_5$.

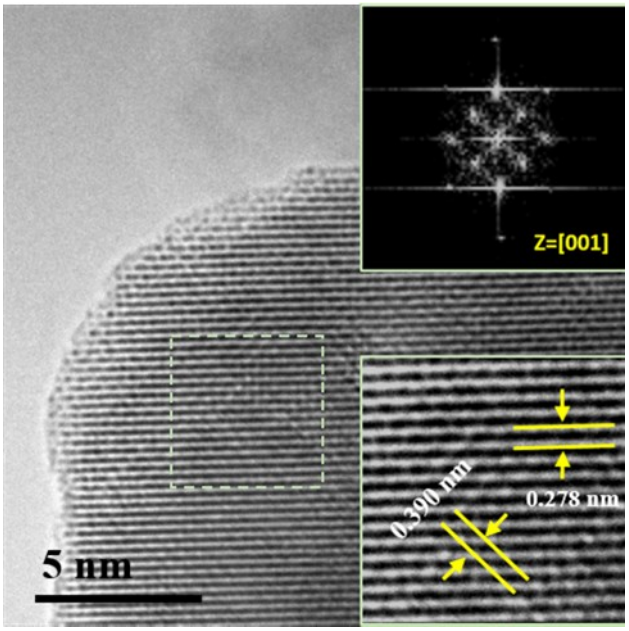

Figure S4. 3 HRTEM images of Ag-$PBMO_5$ after long term stability test, showing that both the bulk decomposition and the surface segregation were prevented.

Table S4. 1 The electron occupied states for s, p, d and the calculated charge transfer of $PBMO_5$ and Ag-$PBMO_5$.

		s	p	d	Total electron	Charge transfer
$PBMO_5$ with Ba vacancy	O	1.843	4.321	0	6.164	0.164
	Mn	0.256	6.274	4.884	11.414	1.586
Ag-$PBMO_5$ with Ba vacancy	O	1.844	4.326	0	6.170	0.170
	Mn	0.289	6.283	4.896	11.468	1.532
	Ag	0.337	0.047	9.087	9.471	1.526
$PBMO_5$ with Pr vacancy	O	1.849	4.362	0	6.211	0.211
	Mn	0.263	6.269	4.861	11.392	1.608
Ag-$PBMO_5$ with Pr vacancy	O	1.851	4.325	0	6.176	0.176
	Mn	0.294	6.279	4.867	11.440	1.56
	Ag	0.348	0.015	9.117	9.480	1.52

Chapter 5. *In situ* Growth of CoP nanoparticles on Perovskite Nanofibers as an Optimized Trifunctional Electrocatalyst in Alkaline Condition

5.1. Abstract

Developing highly active and cost–effective electrocatalyst is of prime importance for renewable energy technologies, including fuel cells, MABs and water electrolysis. Herein, a facile approach is reported to develop cobalt phosphide–$PrBa_{0.5}Sr_{0.5}Co_{1.5}Fe_{0.5}O_{5+\delta}$ (CoP-PBSCF) as a multifunctional electrocatalyst in alkaline media. We exemplify that the PBSCF can be tuned into an efficient trifunctional electrocatalyst through an intriguing "post-growth" approach. The intimate interpenetration of CoP nanoparticles (NPs) and perovskite oxides endows synergistically active sites and improved activities. The resulted electrocatalyst demonstrates excellent performances towards ORR, OER and HER with low overpotentials, as further confirmed by the practical application in Zn-air batteries and overall water splitting. A high power density of 138.0 mW cm^{-2} and a narrow charge-discharge gap of 0.840 V at 10.0 mA cm^{-2} are achieved in Zn−air batteries, while a current density of 10 mA cm^{-2} is delivered at a moderate overpotential of 440 mV in overall water splitting. The proposed protocol, thus, offers an attractive strategy in designing perovskite-based electrocatalyst with excellent performance in versatile electrochemical devices.

5.2. Introduction

The rapid growth of global energy demand, associated with the accompanying concern on climate change, has sparked an intensive interest in the exploration of renewable energy. Energy conversion and storage technologies, with an emphasis on electrochemical devices, hold great potential to secure full deployment of sustainable energy by mitigating the fluctuation of energy demand and the intermittency of renewable energy generation. Of particular interests among these advanced electrochemical technologies have been the regenerative fuel cells, and metal-air batteries. While the metal-air batteries and fuel cells are extremely attractive due to their high energy density and power density, their practical application is often hampered by the sluggish kinetics and large overpotential in ORR, OER[1, 2], and HER.[3, 4] By far, noble-metal-based catalysts have been exclusively used in fuel cells and metal-air batteries as state-of-the-art electrocatalysts, among which Pt has been explored as efficient electrocatalysts towards ORR and HER, while RuO_2 or IrO_2 have been proved to be highly active towards OER. Despite that considerable catalytic activities are achieved on precious metals, the high cost and limited availability of have inevitably impeded their large-scale application in various electrochemical devices.

Developing catalytically active and cost-effective electrocatalysts for oxygen electrocatalysis (ORR/OER) as well as HER is, thus, significantly needed.[5, 6] In the past few decades, electrocatalysts, such as carbonaceous materials, transition metal oxides (e.g., spinel and perovskite oxides), transition metal phosphides, selenides, sulfides and carbides, have been widely studied for ORR, OER and HER. Among the aforementioned noble-metal-free alternatives, perovskite oxide (ABO_3) offers competitive advantages in terms of the cost, natural reserve, intrinsic activity and stability in alkaline solution.[7, 8] The unique electronic structure and chemical defect properties enable them as an attractive alternative for the ORR/OER.[8] Extensive research

conducted on perovskite have demonstrated that the intrinsic catalytic activity for ORR and OER is strongly correlated to the electron occupancy in anti-bonding orbitals of B sites (e_g) and B−O covalency.[9, 10] Perovskite oxides, with an e_g occupancy close unity and a strong B-O covalency can give rise to a maximum intrinsic ORR and OER activities. To this end, strategies, such as partial cation substitution and oxygen-deficiency formation, have been successfully employed to tune the catalytic activity towards ORR and OER; electrocatalysts like $La_{0.3}(Ba_{0.5}Sr_{0.5})_{0.7}Co_{0.8}Fe_{0.2}O_{3-\delta}$ (LBSCF), $PrBa_{0.5}Sr_{0.5}Co_{1.5}Fe_{0.5}O_{5+\delta}$ have been developed as bifunctional electrocatalysts with enhanced activity for ORR and OER.[11, 12] Besides, the application of perovskites to catalyze HER in alkaline media has also drawn attention most recently.[13, 14, 15] Among others, the $NdBa_2Mn_2O_{5.5+\delta}$, $Ba_{0.5}Sr_{0.5}Co_{0.8}Fe_{0.2}O_{3-\delta}$ based materials have been explored as a HER electrocatalysts in alkaline media, which enables the potential application of perovskites in overall water splitting system. [14, 15] Nevertheless, their catalytic activities towards HER are still inferior to many electrocatalysts like precious metals, transition metal sulfides, phosphide etc., while substantial effort is still needed to further advance their catalytic activity for HER.

Since the oxygen catalytic reaction and hydrogen catalytic reaction occur under very different potentials, while various intermediate species (e.g. OH^-, O^{2-}, OOH^-, OH^-, H_2O, H* and H_2) are generated within these reactions, it is challenging to develop an electrocatalyst with a single component that possess favorable adsorption/desorption energies for all these species within the multipurpose electrocatalysis. [6] A rational design of electrocatalyst that features multiple active components and sufficient catalytic sites, is expected to deliver an enhanced catalytic activity in versatile electrochemical devices. Heterostructure engineering is an important approach to achieving a strong and stable interfacial contact between each component.[16, 17] Importantly, our

recent work has exemplified that the introduction of a secondary phase through *in situ* exsolution grants the possibilities to generate a strong coupled heterostructure, which consequently enables extended functionalities.[16, 18] Recent studies conducted by Shao *et al* have verified that synergistically catalytic active sites can arise from perovskite/metal nanoparticles (NPs) interface, where the perovskite oxide can facilitate the water dissociation and the *in-situ* exsolved Ni NPs play an important role in H* adsorption.[13] The *in situ* exsolution approach offers the possibility for perovskites to be utilized as multifunctional electrocatalysts for overall water splitting/rechargeable fuel cell.

Inspired by the as-mentioned approach, further investigation was made towards this direction in developing multifunctional perovskite catalysts. Herein, we demonstrate the excellence of cobalt phosphide-$PrBa_{0.5}Sr_{0.5}Co_{1.5}Fe_{0.50}O_{5+\delta}$ (CoP-PBSCF) as a trifunctional electrocatalyst towards OER/ORR and HER through an *in-situ* exsolution and phosphatization process. A strong interfacial charge transfer between CoP and perovskite was verified by X-ray photoelectron spectroscopy (XPS) and density functional theory (DFT). The intercalation of CoP into perovskite oxides brings substantial number of synergistically active sites, thus affording an enhanced catalytic activity and an extended functionality. The as-synthesized CoP-PBSCF acts as a multifunctional electrocatalyst towards catalyzing ORR, OER and HER in alkaline environment. More importantly, the excellent trifunctional electrocatalytic activities of CoP-PBSCF enable its wide application in rechargeable Zn-air batteries and water splitting systems.

5.3. Results and discussions

The preparation procedures for CoP-PBSCF were depicted in Figure 5.1. Initially, an A-site deficient perovskite oxide with controlled non-stoichiometry $(PrBa_{0.5}Sr_{0.5})_{0.95}(Co_{1.5}Fe_{0.5})_{0.95}Co_{0.05}O_{5+\delta}$ (A-PBSCF) was fabricated through electrospinning, followed by calcination at 900 °C for 2 h. On account of the versatility and size controllability of electrospinning, nanofibrous perovskite (A-PBSCF) with controllable morphology and composition was obtained at this step (Figure 5.2a, b and Fgure 5.3a). Thereafter, upon reduction, the excess Co cations in A-PBSCF were spontaneously released from the perovskite oxide lattice and emerged on the perovskite surface to form metallic Co NPs decorated perovskites Co-$PrBa_{0.5}Sr_{0.5}Co_{1.5}Fe_{0.5}O_{5+\delta}$ (denoted as H-PBSCF), as shown in Figure 5.3b. Finally, the exsolved Co NPs was transformed into CoP NPs through a phosphatization process. The combination of an *in-situ* exsolution and post phosphatization process exquisitely leads to a uniform formation of CoP on the perovskite surface.

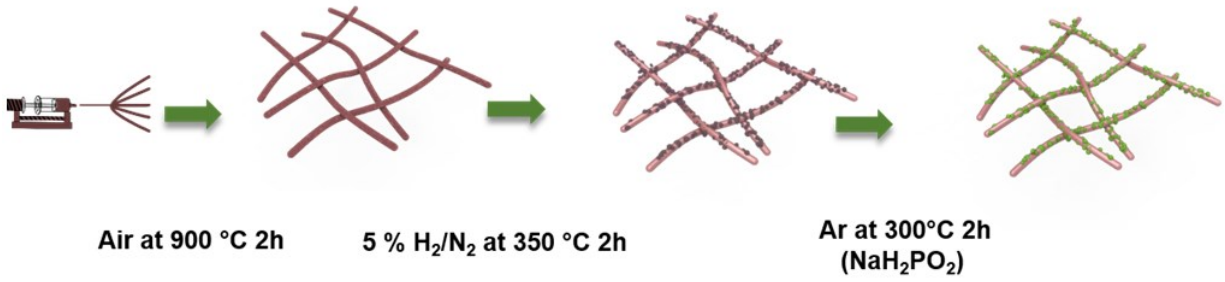

Figure 5.1 Schematic illustration of the preparation procedure for CoP-PBSCF.

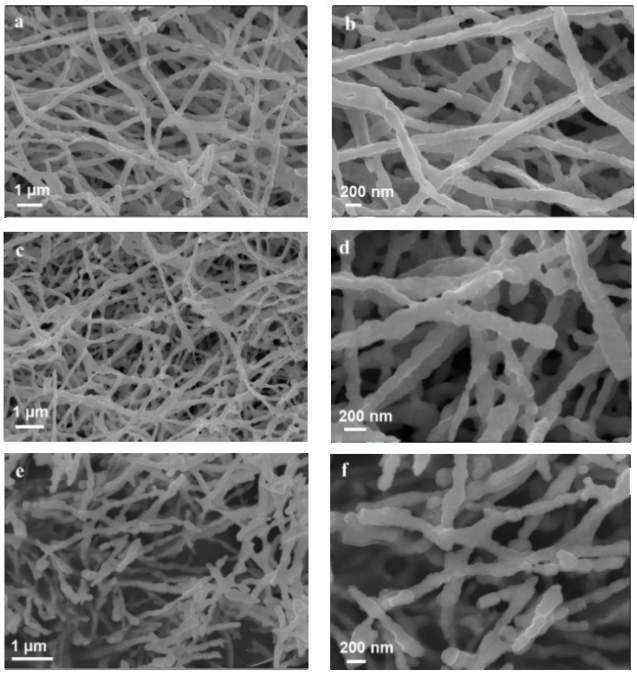

Figure 5.2 (a) and (b) Field-emission scanning electron microscopy (FESEM) image of pristine PBSCF; (c) and (d) FESEM image of H-PBSCF; (e) and (f) FESEM image of CoP- PBSCF

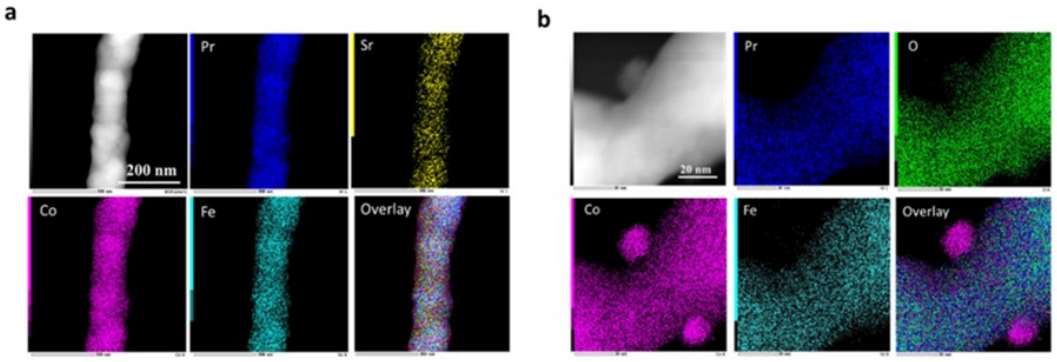

Figure 5.3 High angle annular dark field- scanning transmission electron microscopy (HAADF-STEM) image and the corresponding EDX elemental mapping profiles of (a) A-PBSCF nanofiber calcined at 900 °C and (b) H-PBSCF.

The X-ray diffraction (XRD) patterns in Figure 5.4a show the formation of single phase A-PBSCF after annealing at 900 °C, suggesting that Co cations were successfully dispersed into the

crystalline lattice without segregation. The Rietveld refinement XRD in Figure S5.1 shows a tetragonal structure of A-PBSCF with a space group of P4/mmm (a = b = 3.845 nm, c = 7.715 nm), in good agreement with the atom-scale high resolution TEM (HRTEM) results. After the post treatment of phosphatization, an emergence of additional diffraction peaks was found in the XRD pattern of CoP-PBSCF at 31.6°and 48.13°, which signified the phase formation of CoP. Moreover, no observable peaks derived from the possible destruction of perovskite or impurities such as Co and CoOx were detected in XRD pattern of the CoP-PBSCF, suggesting that the phosphatization process successfully transformed the exsolved Co NPs into ultrafine CoP NPs without deteriorating the structure of parent perovskite. Due to the Co exsolution, the A-site deficient perovskite (A-PBSCF) was reverted towards a stable stoichiometry.[19] As a result, the diffraction peaks of the perovskite experience a slight shift in CoP-PBSCF, indicative of an increased lattice parameter (Rietveld refinement: a = b = 3.891 nm, c = 7.739 nm).

The FESEM images in Figures 5.2e and f along with the scanning transmission electron microscopy bright-field (STEM-BF) image in Figure 5.4b show the morphology and structural information of the CoP-PBSCF. The CoP-PBSCF demonstrates a reticulate nanofibrous architecture with the fiber diameters ranging from 150-250 nm. A rough surface was found on CoP-PBSCF due to the post growth of CoP NPs on the perovskite surface. The HAADF image with HRTEM persuasively verifies the interpenetration of CoP nanoparticles (NPs) and perovskite oxides. The HAADF image and STEM-EDX in Figure 5.4c clearly discloses that the perovskite matrix is coupled with CoP NPs after the phosphatization process. A close observation in Figures 5.4d and e shows that the well-dispersed NPs with diameters of 5-7 nm are socketed on the perovskite surface. The crystal fringe in Figure 5.4e shows d-spacings of 2.533 and 2.470 Å, which well matches with the (200) and (11-1) planes of the CoP. Figure 5.4f illustrates the HRTEM

images along the [110] zone axes of the CoP-PBSCF together with its diffractogram patterns. The lattice fringes show d-spacings of 3.871 and 2.752 Å, which are in accordance with (002) and (-110) planes of the PBSCF. The additional reflection spot circled in the diffractogram image (Figure 5.4f) corresponds to the tetragonal superlattice along c-direction. The HRTEM along with the diffractogram suggests a double perovskite structure, where the Pr and Ba (Sr) are ordered in A site, forming a –[PrOx]–[Co(Fe)O_2]–[Ba(Sr)O]–[Co(Fe)O_2]–[PrOx]– layered structure.[20] The pristine A-PBSCF displays a similar structure with a slight volume shrink (Figure S5.2), while a uniform distribution of all the elements is detected within the perovskite fibers (Figure 5.3a).

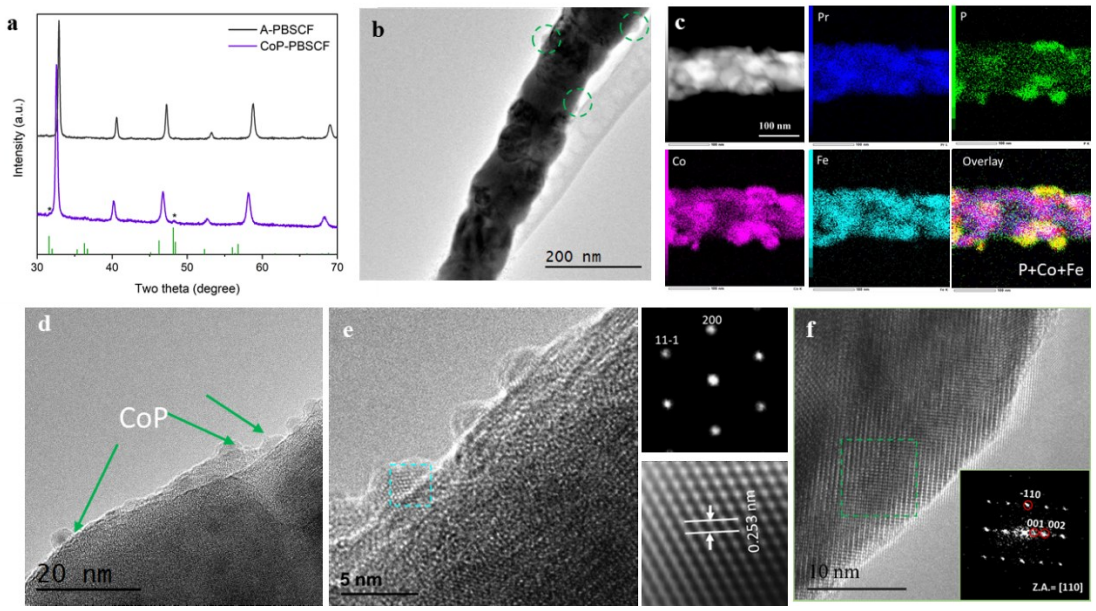

Figure 5.4 (a) XRD patterns of A-PBCCF and CoP-PBSCF, showing the CoP species are present after in-situ exsolution and phosphatization process; (b) STEM-BF images of the CoP-PBSCF; (c) HAADF-STEM image of the CoP-PBSCF and the corresponding elemental mapping; (d) HRTEM of the CoP-PBSCF; (e) HRTEM image and simulation of CoP NPs. (f) HRTEM image of the perovskite oxide in CoP-PBSCF.

The surface chemistry of the electrocatalysts was probed using the XPS. Figure 5.5a shows the XPS O1s spectra of A-PBSCF, H-PBSCF and CoP-PBSCF, where the O 1s can be deconvoluted into four different subpeaks, corresponding to the lattice oxygen (O^{2-}), highly oxidative oxygen species (O_2^{2-}/O^-), hydroxyl groups/adsorbed oxygen (-OH/O_2) and adsorbed molecular water (H_2O).[21] An increased surface adsorbed H_2O and surface adsorbed oxygen/hydroxyl was found on the surface of the H-PBSCF and CoP-PBSCF, suggesting a strong hydrophilic nature. Furthermore, the Co2p spectra in Figure 5.5b suggest the coexistence of Co^{3+}/Co^{4+} in A-PBSCF, consistent with the previous observation in $La_{0.5}(Ba_{0.4}Sr_{0.4}Ca_{0.2})_{0.5}Co_{0.8}Fe_{0.2}O_{3-\delta}$.[16] The peak located at 777.69 eV in A-PBSCF is assigned to the Ba-O interrelation, an evidence for the structural stress caused by the A-site deficiency.[22] The Ba-O interrelation peak vanished after the Co exsolution, together with the emergence of an additional weak peak at 778.16 eV (2p3/2 peak of metallic Co). This is because the perovskite was reverted towards a more stable structure, while the metallic Co was generated at the same time.[16] The CoP binding energy in CoP-PBSCF is in close proximity to the metallic Co. Due to the charge transfer between Co and P, the Co 2p 3/2 peak slightly shifted from 778.16 to 778.20 eV.[23] The Fe 2p core spectra are shown in Figure 5.5c, where a significantly increased Fe^{4+}/Fe^{3+} ratio is found on H-PBSCF and Co-PBSCF Fe 2p profile in comparison to the A-PBSCF. Provided that the high oxidation state of Fe^{4+} features an electronic configuration of t_{2g}^3 e_g^1, an optimized orbital occupancy is achieved on CoP-PBSCF.[21] In this regard, it is suggested that the strong coupling effect between the exsolved CoP NPs and the perovskite matrix can lead to a modified electronic structure within the perovskites, thereupon favoring the catalytic efficiency of the ORR/OER. In the case of P (Figure 5.5d), the P2p spectrum of CoP-PBSCF shows the binding energy of the phosphates (PO_4^{3-} or PO_3^- or P_2O_5) and phosphide.[24, 25] The presence of phosphates is presumably originated from the surface oxidation of CoP, yet some literature

suggests that the coexistence of cobalt oxide based compound would weaken the collected XPS signal of CoP.[23]

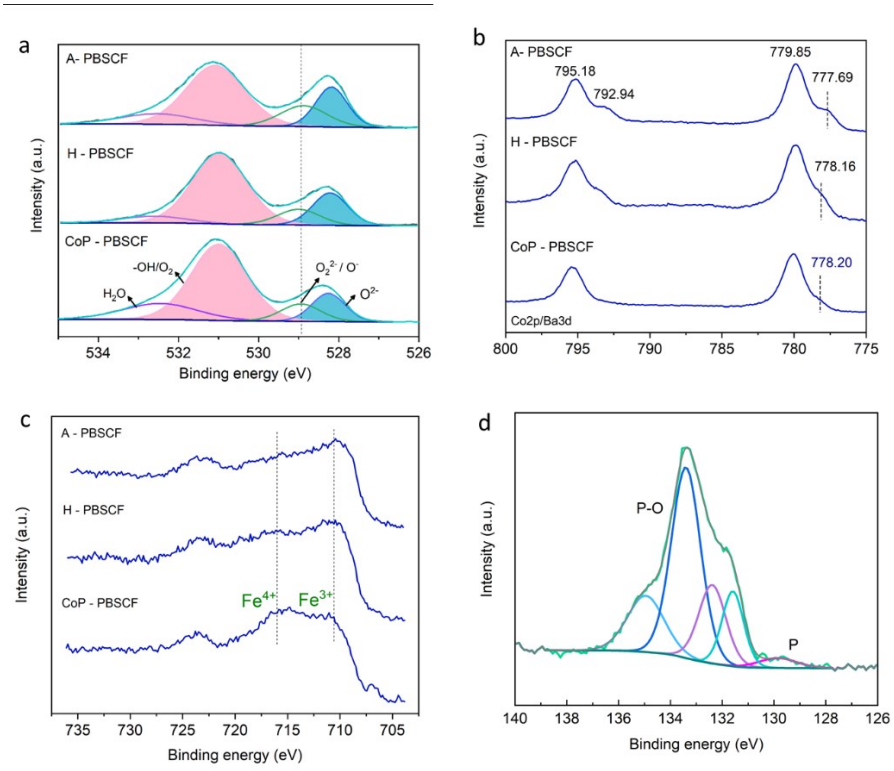

Figure 5.5 XPS spectra showing the (a) O1s spectra in A-PBSCF, H-PBSCF and CoP-PBSCF; (b) Co2p/Ba3d spectra in A-PBSCF, H-PBSCF and CoP-PBSCF; (c) Fe 2p spectra of oxygen in A-PBSCF, H-PBSCF and CoP-PBSCF.and (d) P 2p spectra in CoP-PBSCF.

The as-prepared hybrid with intimate contact between CoP and PBSCF is expected to take full advantages of its strong coupling effects and micro/mesoporous properties, thus enabling an enhanced catalytic activity and a strong durability. The electrocatalytic activities for the ORR, OER and HER were evaluated in the alkaline environment (0.1 or 1.0 M KOH) using a rotating disk electrode (RDE). Figure 5.6a shows the OER activities of CoP-PBSCF, together with pristine PBSCF, H-PBSCF, CoP and commercial IrO_2 catalyst, in 0.1 M KOH solution. The CoP-PBSCF shows a remarkably enhanced OER activity, with a small onset potential of 1.570 V (vs. RHE),

and a minimum overpotential of 378 mV at the current density of 10 mA cm^{-2} among all the studied catalysts. The OER catalytic activity of CoP-PBSCF is considerably higher in 1.0 M KOH (Figure 5.6b), coupled with overpotentials of 340 mV and 520 mV at current densities of 10 and 100 mA cm^{-2}, respectively. By contrast, significantly higher overpotentials of 640 and 600 mV at a current density of 100 mA cm^{-2} are needed for the pristine PBSCF and CoP NPs, respectively. Moreover, the CoP-PBSCF demonstrates a Tafel slope of 81.5 mV dec^{-1}, much lower than those of 108.5 and 103.6 mV dec^{-1} for pristine A-PBSCF and CoP NPs. The superior OER activity of CoP-PBSCF could be ascribed to the synergistic catalytic effect between CoP and PBSCF perovskite in a heterostructured CoP-PBSCF. It is also noteworthy that, with the partial exsolution of Co cations, the H-PBSCF demonstrates an enhanced OER activity as compared to the A-PBSCF, showing a smaller overpotential of 570 mV at a current density of 100 mA cm^{-2} and a Tafel slope of 99.0 mV dec^{-1}.

The LSV curves in Figure 5.6d confirm the ORR electrocatalytic activity of CoP-PBSCF. Apparently, the CoP-PBSCF demonstrates a more positive onset potential in comparison with A-PBSCF and CoP. Meanwhile, a half wave potential of 0.752 V was achieved over CoP-PBSCF, which is only 110 mV lower than that of Pt/C. In contrast, the A-PBSCF and CoP show half-wave potentials of 0.709 and 0.623 V, respectively. In addition, the H-PBSCF also demonstrates an enhanced ORR performance in comparison with the A-PBSCF, showing a half-wave potential of 0.733 V in 0.1 M KOH. In fact, transition metal phosphides like CoP generally possess poor ORR catalytic activities, however, these interstitial alloys could play a positive role as a conductivity modifier in hybrid catalysts owing to their superior electronic conductivity.[26 27] Thus, the incorporation of CoP into PBSCF perovskite presumably leads to an improvement in ORR activity. The enhanced electrocatalytic activity for the ORR was also confirmed by the

Tafel slopes. As shown in Figure 5.6e, the CoP–PBSCF shows a Tafel slope of 85.7 mV dec^{-1}, significantly smaller than that of A-PBSCF (122.7 mV dec^{-1}), H-PBSCF (99.8 mV dec^{-1}) and CoP (142.2 mV dec^{-1}), which indicates a faster kinetics on CoP–PBSCF. The electron transfer number of the CoP-PBSCF for the ORR was determined from the LSV curves measured at different rotation speeds (400, 900, 1600, and 2500 rpm). The Koutechy–Levich (K–L) plots inserted in Figure 5.6f demonstrate a linear relationship between $j_L^{-1}$and $\omega^{-1/2}$ (where j_L is the measured limited current density and ω is the electrode rotating rate) at various potentials. The electron transfers n was determined to be ~4.0 for the perovskite oxide based electrocatalysts, suggesting a four-electron transfer pathway over the perovskite. In contrast, the electron transfer number was measured to be ~2.0 for CoP (Figure 5.6i), indicating an inefficient electron transfer on CoP electrocatalyst.

In light of the superior electrochemical activities for both OER and ORR, the CoP-PBSCF was expected to show an excellent bifunctional electrocatalytic activity in rechargeable Zn-air batteries. We then integrated the bifunctional oxygen electrocatalysts in Zn-air batteries and evaluated their bifunctional applicability. Figure 5.7a shows the charging and discharging polarization curves of the rechargeable Zn-air batteries based on A-PBSCF, CoP-PBSCF and Pt/Ru/C air electrode. As anticipated, the Zn-air battery with CoP-PBSCF electrode demonstrates a smaller voltage gap (0.840 V at 10 mA cm^{-2} and 1.148 V at 50 mA cm^{-2}) in comparison with the A-PBSCF (0.951 V at 10 mA cm^{-2} and 1.320 V at 50 mA cm^{-2}), suggesting its excellent bifunctional activities. Notably, the rechargeable Zn-air batteries fabricated with CoP-PBSCF air electrode is competitive to the most active noble metal catalysts of Pt/Ru/C, and it even outperforms Pt/Ru/C when polarized at a relatively higher current region.

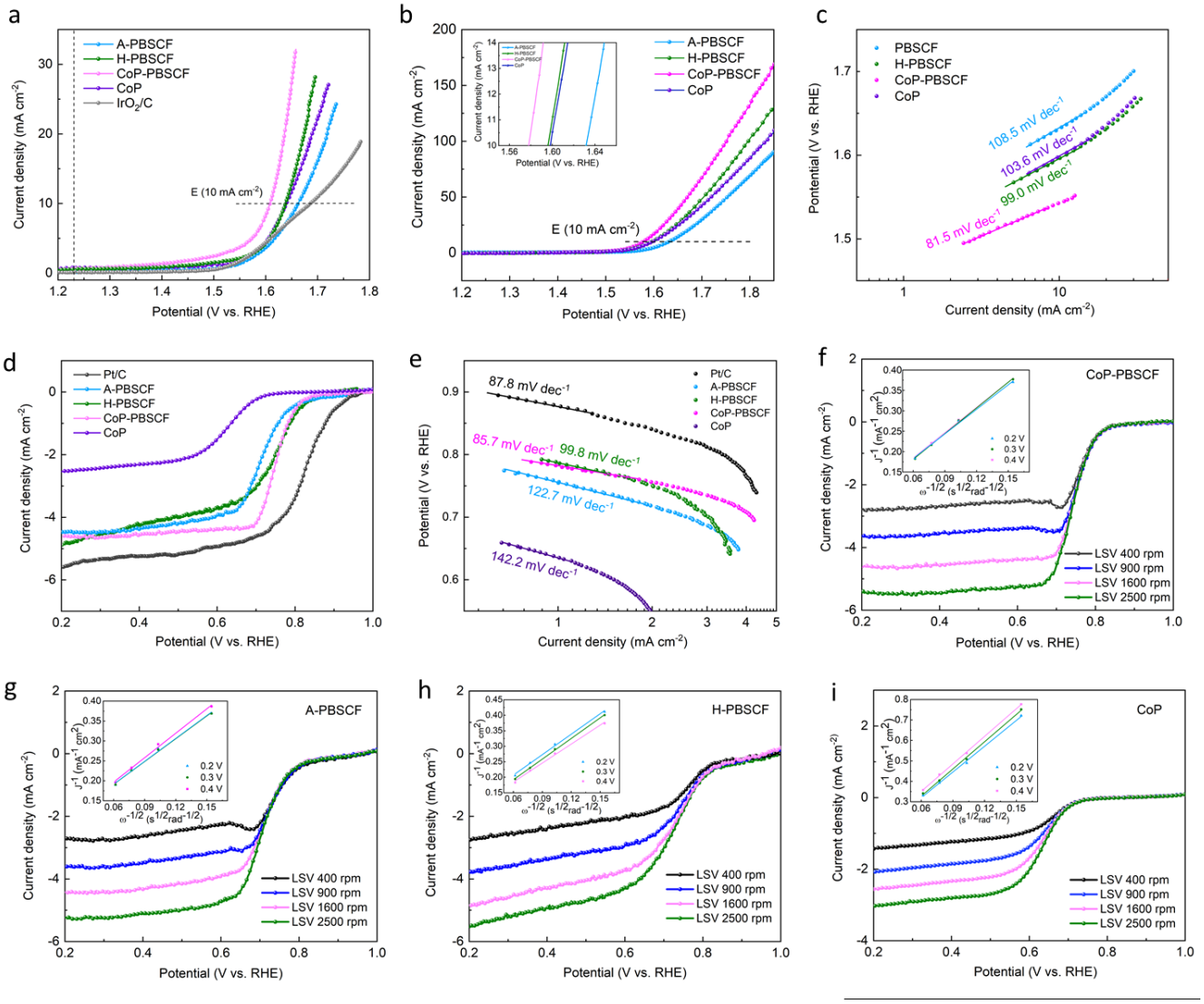

Figure 5.6 LSV curves of OER reaction on PBSCF, H-PBSCF, CoP-PBSCF, CoP and IrO_2 in (a) 0.1 M KOH and (b) 1 M KOH at 1600 rpm and (c) the corresponding Tafel curves in O_2 saturated 1 M KOH; (d) ORR LSV curves of PBSCF, H-PBSCF, CoP-PBSCF, CoP, commercial Pt/C and (e) the corresponding Tafel curves in 0.1 M KOH at 1600 rpm. (f) CoP-PBSCF, (g) A-PBSCF, (g) H-PBSCF and (i) CoP in 0.1 M KOH at different rotation speeds (400, 900, 1600, and 2500 rpm); Inset: K-L plots at various potential.

As shown in Figure 5.7b, the peak discharging power density of CoP-PBSCF reaches 138.0 mW cm^{-2}, which is comparable to the commercial Pt/Ru/C electrocatalyst (142.3 mW cm^{-2}). Moreover, the CoP-PBSCF demonstrates an exceptional rechargeability in the Zn-air batteries. As shown in Figure 5.7c, when cycled at a constant current density of 10 mA cm^{-2}, no obvious deterioration is detected on CoP-PBSCF during the operation period. The rechargeable Zn-air battery with the CoP-PBSCF retains a voltaic efficiency of 58.3 % even after 100 cyclic charging-discharging tests. The socketed structure resulted from the exsolution and phosphatization effectively prevents the loss of catalytic active NPs in the cyclic test, thus contributing to the superior electrocatalytic activity and good stability. Conversely, the battery constructed with Pt/Ru/C air electrode shows obvious degradation, with a dramatically increased overpotential after 20 h operation, which could be ascribed to the oxidative potential induced catalyst passivation and/or catalyst detachment.

Besides the optimized ORR/OER performances, the CoP-PBSCF also exhibits superior electrocatalytic activity towards HER. As shown in Figure 5.8a, the HER polarization curve of CoP-PBSCF was recorded in Ar-saturated 1.0 M KOH solution. For comparison, the HER LSV curves of A-PBSCF, H-PBSCF, CoP and commercial Pt/C were also evaluated. As anticipated, the commercial Pt/C is highly active towards HER, with an onset potential of almost 0 mV (vs. RHE) and an overpotential of 33 mV at a current density of 10 mA cm^{-2}. Note that the CoP electrocatalyst also delivers excellent activity, showing a positive onset potential of -0.196 V, and a small overpotential of -0.209 V at a current density of 10 mA cm^{-2}. Benefiting from the catalytic active site of CoP, the CoP-PBSCF displays a high activity towards HER, achieving a current density of 10 mA cm^{-2} at an overpotential of 240 mV. In contrast, a larger overpotential of 373 mV is required to reach a current density of 10 mA cm^{-2} on the A-PBSCF, which suggests an inferior catalytic activity on single component perovskite. Moreover, as demonstrated in Figure 5.8b, the

CoP-PBSCF exhibits a lower Tafel slope of 93.8 mV dec^{-1} relative to A-PBSCF (114.5 mV dec^{-1}) and H-PBSCF (97.6 mV dec^{-1}), confirming a more efficient HER on CoP-PBSCF as compared to its counterparts.

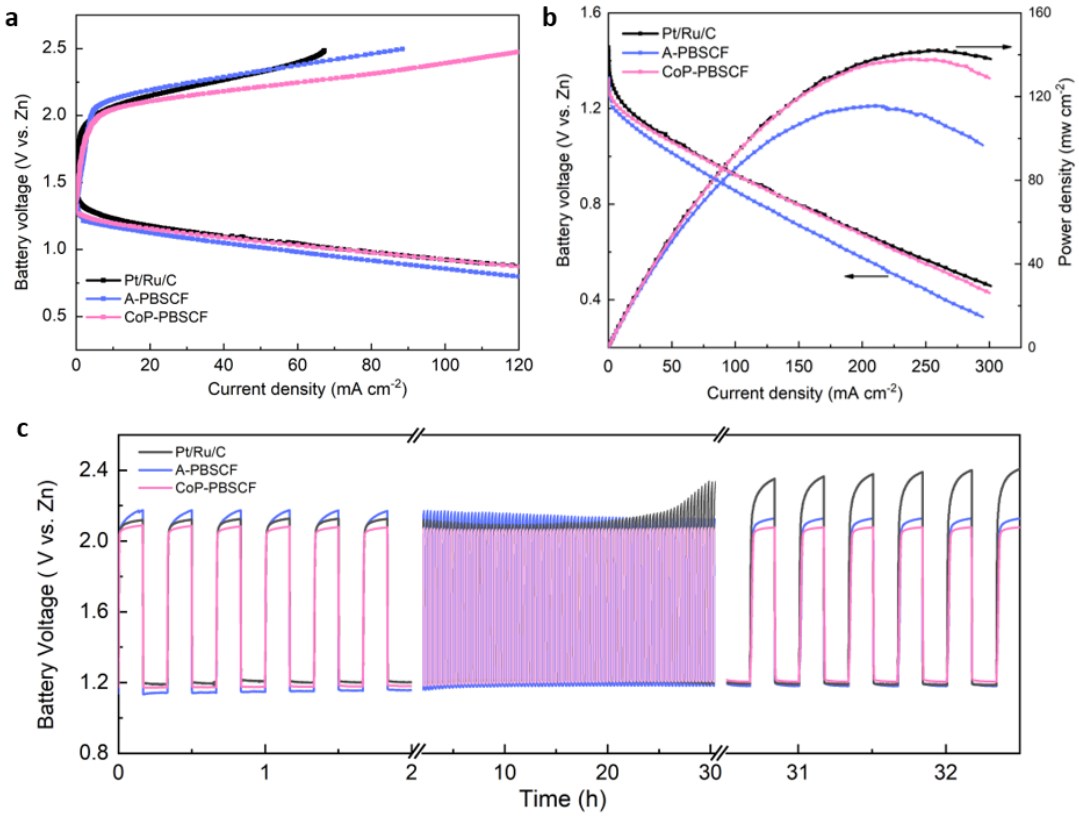

Figure 5.7 Electrochemical performance of the rechargeable Zn-air batteries using A-PBSCF, CoP-PBSCF and Pt/Ru/C air electrode. (a) Charging and discharging polarization curves of rechargeable zinc-air batteries; (b) Discharging polarization curves along with the corresponding power density. (c) Galvanostatic charge−discharge curves of A-PBSCF, CoP-PBSCF and Pt/Ru/C air electrode at a constant current density of 10 mA cm^{-2}.

The CoP-PBSCF electrocatalyst shows promising OER and HER activities in RDE tests, which suggests that the CoP-PBSCF may simultaneously serve as anode and cathode electrocatalyst in

overall water splitting system. To demonstrate its practical application, we further applied the CoP-PBSCF catalyst onto the Ni-foam substrates and evaluated the overall water splitting performance in 1.0 M KOH solution. Figure 5.8c shows the measurements of water electrolysis on a two-electrode configuration with CoP-PBSCF serving as both the anode (OER) and the cathode (HER). Expectedly, the CoP-PBSCF shows a remarkably electrochemical performance, achieving a current density of 10 mA cm^{-2} at a low overpotential of 440 mV, close to that of the Pt/C//IrO_2/C (η = 370 mV). More importantly, the CoP-PBSCF shows a strong durability in the water electrolyzer. As shown in Figure 5.8d, when polarized at a current density of 10 mA cm^{-2}, the potential remains at 1.69 V over 12 h chronopotentiometric test.

To gain further insight into the enhanced HER activity, DFT simulations were applied to calculate the hydrogen adsorption Gibbs free energy (ΔG_{H^*}), as shown in Figure 5.9a, given that the ΔG_{H^*} is often used as a descriptor for the HER. Our computational results have revealed that the H* can be favorably adsorbed on the surface of CoP, which is in a good agreement with the experimental results. The ΔG_{H^*} value on Co site of CoP is found to be -0.14 eV for Co-H* state, close to the optimal hydrogen adsorption energy. On the contrary, the pristine PBSCF possesses a ΔG_{H^*} value of 0.82 and 1.02 eV for Co-H* state and Fe-H* state on the B sites of perovskites, respectively, indicating a weak hydrogen bonding and inferior adsorption strength on perovskite surface. With regard to CoP-PBSCF, the emergence of CoP on perovskite surface leads to a strong interaction between the exsolved CoP NPs and the perovskite surface, resulting in a favorable modification in the electronic structure. The electron transfer between the exsolved CoP and perovskite yields a reduced ΔG_{H^*} value (0.76 and 0.98 eV for Co-H* state and Fe-H* state) and an enhanced H* adsorption. The modification of electronic structure contributes to an enhanced intrinsic HER activity on perovskite by facilitating the H* adsorption and accelerating the conversion of H_2.

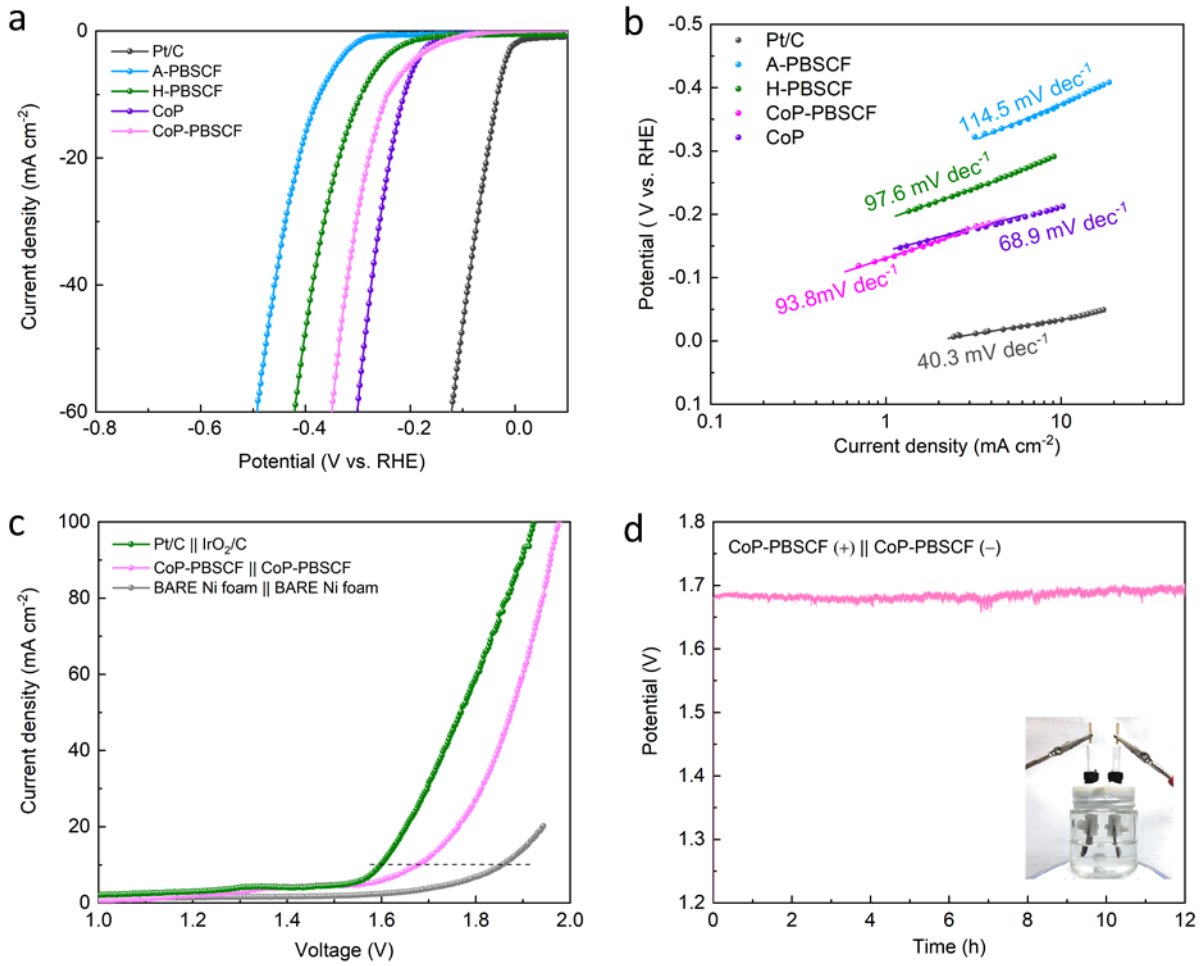

Figure 5.8 (a) HER polarization curves and (b) the corresponding Tafel curves of PBSCF, H-PBSCF, CoP-PBSCF, CoP, and commercial Pt/C in 1 M KOH; (c) Polarization curves of overall water splitting reaction on CoP-PBSCF || CoP-PBSCF, the Pt/C||IrO_2/C, and the bare Ni foam || Ni foam electrode in 1 M KOH solution (the electrocatalysts was loaded on Ni foam electrodes with a mass loading of 2 mg cm^{-2}) (d) Chronopotentiometric test of overall electrochemical water splitting on CoP-PBSCF || CoP-PBSCF at a current density of 10 mA cm^{-2}.

In addition to the enhanced intrinsic activity on perovskite surface, the strong coupling between perovskite oxides and the exsolved CoP NPs is expected to contribute to a synergistic electrocatalytic effect. It has been well documented that there are two different steps involved in

HER in the alkaline environment, including the Volmer reaction ($M + H_2O + e^- \rightarrow MH_{ads} + OH^-$), and the accompanying step of converting H_{ad} to H_2 through Heyrovský reaction or Tafel reaction.[28, 29] Previous research has verified that the transition metal oxide with its surface rich in hydroxyl group can accelerate the dissociation of H_2O in the Volmer reaction. [13, 23] Meanwhile, the OH^- generated within the Volmer reaction could be preferably adsorbed on the surface of perovskite owing to the high oxophilicity nature and strong electrostatic affinity of positively charged Co and Fe species.[23, 30] This helps to prevent the blockage of active sites on CoP. As mentioned above, owing to the desired ΔG_{H^*}, the produced H_{ad} could be efficiently converted into H_2 on CoP surface in the following step. As results, a synergy is created between PBSCF and CoP components to boost the HER activity, while the intimate contact and strong coupling of CoP and PBSCF matrix is presumably to further promote the cooperative effect. The reduced overpotential and Tafel slope of CoP-PBSCF confirm that phosphatization process effectively advances the electrocatalytic activity of HER.

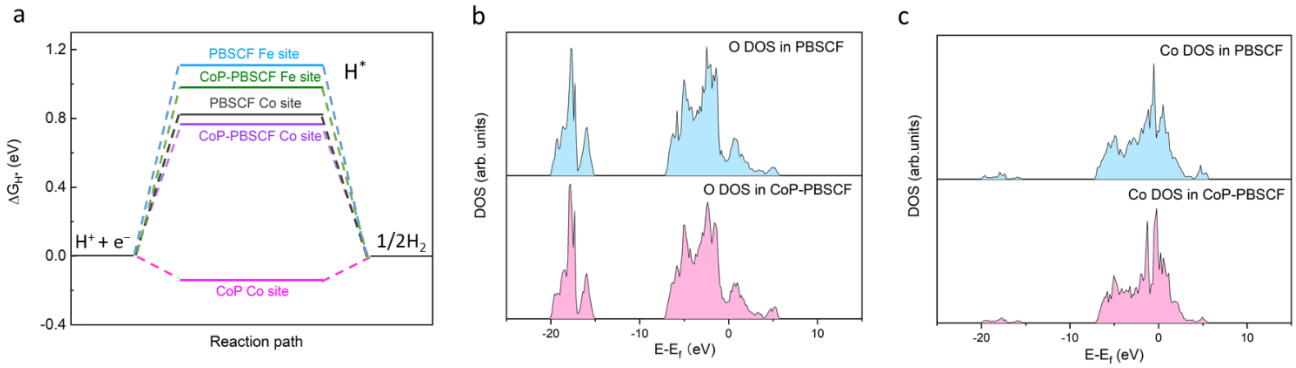

Figure 5.9 (a) HER free energy diagrams of Co-sites on CoP, and Co-sites on perovskite surface of CoP-PBSCF and PBSCF; (b) Calculated density of states of O for CoP-PBSCF and pristine PBSCF; (c) Calculated density of states of Co for CoP-PBSCF and pristine PBSCF.

Besides the enhanced HER activity, DFT calculation is also employed to investigate the origin of enhanced oxygen electrocatalytic activity. As shown in Figures 5.9 b and c, the incorporation of CoP on perovskite oxides surface results in a change in density of states within perovskite oxides. The surface O p-band center relative to the Fermi level reaches 2.70 eV in CoP-PBSCF, lower than that of pristine PBSCF (2.74 eV). The oxygen 2p character relative to Fermi level was reported to be strongly correlated to both oxygen incorporation and evolution during electrochemical reactions.[31] Moving the metal d states closer in energy to the O 2p states facilitates the metal–oxygen hybridization, B-O bond covalency and oxygen exchange kinetics, thus promoting the oxygen electrocatalysis on perovskite. [32, 33] The enhanced ORR/OER activity is likely to be attributed by the optimal electronic properties in CoP-PBSCF.

5.4. Conclusions

In summary, we have reported a facial and effective approach to developing multifunctional CoP-PBSCF electrocatalyst, whereby the ultrafine CoP NPs are socketed on perovskite oxide surface. The significantly enhanced multifunctional activity suggests that the integration of CoP contributes to synergistic catalytic sites, while the strong coupling effect and intimate contact between CoP NPs and PBSCF facilitate ion migration within the reaction. The homogeneous incorporation of semi-metallic CoP is expected to provide an optimized electron transfer path. The as-obtained electrocatalyst demonstrates superior electrocatalytic activities towards ORR/OER/HER in alkaline environment, and it has been further employed in Zn-air batteries and water splitting electrolyzer. Moreover, the proposed strategy shows the potential in designing and synthesising various nanostructured materials with extended functionalities, which broaden the application of perovskite oxide based electrocatalyst in diverse electrochemical devices.

5.5 Experimental procedure

Synthesis of A-PBSCF catalysts

$Ba(NO_3)_2$ (assay 100.0%), $Sr(NO_3)_2$ (assay ≥ 99%), $Fe(NO_3)_3 \cdot 9H_2O$ (assay ≥ 99.9%) were purchased from Fisher Scientific Cooperation. $Pr(NO_3)_3 \cdot 6H_2O$ (assay≥ 99%), $Co(NO_3)_2 \cdot 6H_2O$ (assay ≥ 99%), poly(vinylpyrrolidone) (PVP, assay 12 to 12.8% nitrogen, average M.W 1,300,000) were purchased from Acros Organics. To prepare A-PBSCF, stoichiometric amounts of metal nitrates were firstly dissolved in N, N-dimethylformamide (DMF) solvent at a total metal cations concentration of 0.60 M, followed by stirring for 12 h to form a clear solution. The as-obtained precursor was labelled as precursor A. The PVP was slowly dissolved in DMF solvent with a weight ratio of 30:100 (PVP/DMF), then labelled as precursor B. The precursor A and B were mixed at a volume ratio of 1:1 to achieve a desired viscosity. The as-obtained precursor was electrospun into fibrous materials at an applied voltage of 20 kV and a distance of 15 cm between the needle and an aluminium foil collector. The syringe pump was set at a flow rate of 0.3 mL h^{-1}. The resulting nanofibers were peeled from the collected, and then calcined at 900 °C for 2 h to form A-PBSCF.

Synthesis of H-PBSCF catalyst

The as-synthesized A site deficient PBSCF was further treated in 5% H_2/N_2 for 2 h at 350 ˚C to form Co-$PrBa_{0.5}Sr_{0.5}Co_{1.5}Fe_{0.5}O_{5+\delta}$ (H-PBSCF).

Synthesis of CoP-PBSCF catalyst

In the phosphatization process, 50 mg $NaH_2PO_2 \cdot H_2O$ (Sigma Aldrich, assay ≥ 99%) and 20 mg as-synthesized H-PBSCF were placed in two crucibles in a tube furnace on upstream and downstream side, respectively. The samples were heated up to 300 °C under Ar flow (50 ml min^{-1}) and kept at this temperature for 2 hours to yield CoP-PBSCF.

Synthesis of CoP

CoP nanoparticles were synthesized based on phosphatization of $Co(OH)_2$, according to a previous report.[32] The synthesis procedure is briefly described as below: 200 mg of $Co(NO_3)_2 \cdot 6H_2O$ and 55 mg of $C_6H_5Na_3O_7 \cdot 2H_2O$ (Sigma Aldrich, assay ⩾99.0%) were first dissolved into 100 mL of deionized water. The 1.0 M NaOH solution was added dropwise to the metal nitrate solution under vigorous stirring. The solid product $Co(OH)_2$ was precipitated from the solution after an addition of 3.5 mL NaOH solution. The solid product from at this stage was immediately centrifuged and then dried at 60 °C for 5 h under vacuum. The synthesis of CoP nanoparticles was similar to the phosphatization process described above. 50 mg $Co(OH)_2$ and 250 mg $NaH_2PO_2 \cdot H_2O$ were placed in two crucibles in a tube furnace on upstream and downstream side, respectively. The tube furnace was heated to 300 °C at a rate of 2 °C min^{-1}. The temperature was maintained at 300 °C for 2 h under Ar flow (50 mL min^{-1}) to yield the CoP nanoparticles. The CoP product was collected after being washed subsequently by water and ethanol and dried under vacuum. The FESEM image and the XRD pattern of the as-synthesized CoP is shown in Figure 5.10.

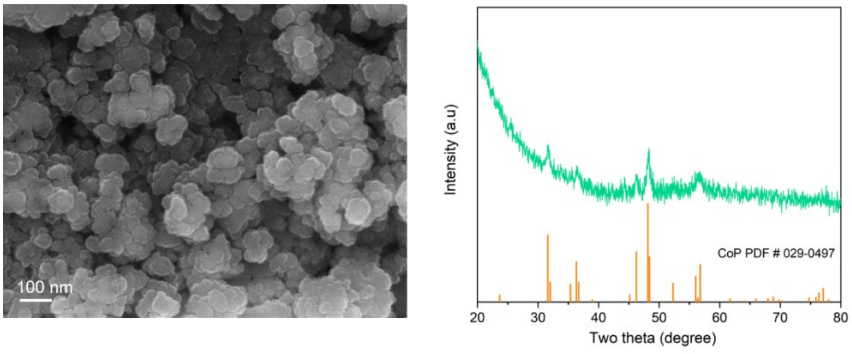

Figure 5.10 (a) FESEM image of the CoP NPs; (b) XRD pattern of the CoP NPs.

5.6 References

(1) F. Cheng; J. Chen. Metal–air batteries: from oxygen reduction electrochemistry to cathode catalysts. *Chemical Society Reviews* **2012,** *41* (6), 2172-2192.

(2) B. C. Steele; A. Heinzel. Materials for fuel-cell technologies. In *Materials For Sustainable Energy: A Collection of Peer-Reviewed Research and Review Articles from Nature Publishing Group*; World Scientific: 2011; pp 224-231.

(3) J. Wang; W. Cui; Q. Liu; Z. Xing; A. M. Asiri; X. Sun. Recent progress in cobalt - based heterogeneous catalysts for electrochemical water splitting. *Advanced materials* **2016,** *28* (2), 215-230.

(4) X. Wang; W. Li; D. Xiong; D. Y. Petrovykh; L. Liu. Bifunctional nickel phosphide nanocatalysts supported on carbon fiber paper for highly efficient and stable overall water splitting. *Advanced Functional Materials* **2016,** *26* (23), 4067-4077.

(5) C. Hu; L. Dai. Multifunctional Carbon - Based Metal - Free Electrocatalysts for Simultaneous Oxygen Reduction, Oxygen Evolution, and Hydrogen Evolution. *Advanced Materials* **2017,** *29* (9), 1604942.

(6) Y. Jia; L. Zhang; A. Du; G. Gao; J. Chen; X. Yan; C. L. Brown; X. Yao. Defect graphene as a trifunctional catalyst for electrochemical reactions. *Advanced materials* **2016,** *28* (43), 9532-9538.

(7) M. Pena; J. Fierro. Chemical structures and performance of perovskite oxides. *Chemical reviews* **2001,** *101* (7), 1981-2018.

(8) D. Chen; C. Chen; Z. M. Baiyee; Z. Shao; F. Ciucci. Nonstoichiometric oxides as low-cost and highly-efficient oxygen reduction/evolution catalysts for low-temperature electrochemical devices. *Chemical reviews* **2015,** *115* (18), 9869-9921.

(9) J. Suntivich; K. J. May; H. A. Gasteiger; J. B. Goodenough; Y. Shao-Horn. A perovskite oxide optimized for oxygen evolution catalysis from molecular orbital principles. *Science* **2011,** *334* (6061), 1383-1385.

(10) J. Suntivich; H. A. Gasteiger; N. Yabuuchi; H. Nakanishi; J. B. Goodenough; Y. Shao-Horn. Design principles for oxygen-reduction activity on perovskite oxide catalysts for fuel cells and metal–air batteries. *Nature chemistry* **2011,** *3* (7), 546.

(11) J. I. Jung; H. Y. Jeong; J. S. Lee; M. G. Kim; J. Cho. A bifunctional perovskite catalyst for oxygen reduction and evolution. *Angewandte Chemie* **2014,** *126* (18), 4670-4674.

(12) Y. Bu; O. Gwon; G. Nam; H. Jang; S. Kim; Q. Zhong; J. Cho; G. Kim. A Highly Efficient and Robust Cation Ordered Perovskite Oxide as a Bifunctional Catalyst for Rechargeable Zinc-Air Batteries. *ACS nano* **2017,** *11* (11), 11594-11601.

(13) Y. Zhu; J. Dai; W. Zhou; Y. Zhong; H. Wang; Z. Shao. Synergistically enhanced hydrogen evolution electrocatalysis by in situ exsolution of metallic nanoparticles on perovskites. *Journal of Materials Chemistry A* **2018**.

(14) X. Xu; Y. Chen; W. Zhou; Z. Zhu; C. Su; M. Liu; Z. Shao. A perovskite electrocatalyst for efficient hydrogen evolution reaction. *Advanced Materials* **2016,** *28* (30), 6442-6448.

(15) J. Wang; Y. Gao; D. Chen; J. Liu; Z. Zhang; Z. Shao; F. Ciucci. Water Splitting with an Enhanced Bifunctional Double Perovskite. *ACS catalysis* **2017,** *8* (1), 364-371.

(16) B. Hua; M. Li; Y.-F. Sun; Y.-Q. Zhang; N. Yan; J. Chen; T. Thundat; J. Li; J.-L. Luo. A coupling for success: Controlled growth of Co/CoOx nanoshoots on perovskite mesoporous nanofibres as high-performance trifunctional electrocatalysts in alkaline condition. *Nano Energy* **2017,** *32*, 247-254.

(17) B. Hua; M. Li; J.-L. Luo. A facile surface chemistry approach to bifunctional excellence for perovskite electrocatalysis. *Nano energy* **2018,** *49*, 117-125.

(18) Y.-F. Sun; Y.-L. Yang; J. Chen; M. Li; Y.-Q. Zhang; J.-H. Li; B. Hua; J.-L. Luo. Toward a rational photocatalyst design: a new formation strategy of co-catalyst/semiconductor heterostructures via in situ exsolution. *Chemical Communications* **2018,** *54* (12), 1505-1508.

(19) D. Neagu; G. Tsekouras; D. N. Miller; H. Ménard; J. T. Irvine. In situ growth of nanoparticles through control of non-stoichiometry. *Nature chemistry* **2013,** *5* (11), 916.

(20) B. Zhao; L. Zhang; D. Zhen; S. Yoo; Y. Ding; D. Chen; Y. Chen; Q. Zhang; B. Doyle; X. Xiong. A tailored double perovskite nanofiber catalyst enables ultrafast oxygen evolution. *Nature communications* **2017,** *8*, 14586.

(21) Y. Zhu; W. Zhou; J. Yu; Y. Chen; M. Liu; Z. Shao. Enhancing electrocatalytic activity of perovskite oxides by tuning cation deficiency for oxygen reduction and evolution reactions. *Chemistry of Materials* **2016,** *28* (6), 1691-1697.

(22) J. I. Jung; H. Y. Jeong; M. G. Kim; G. Nam; J. Park; J. Cho. Fabrication of Ba0. 5Sr0. 5Co0. 8Fe0. 2O3–δ Catalysts with Enhanced Electrochemical Performance by Removing an Inherent Heterogeneous Surface Film Layer. *Advanced Materials* **2015,** *27* (2), 266-271.

(23) J. Yu; Y. Zhong; X. Wu; J. Sunarso; M. Ni; W. Zhou; Z. Shao. Bifunctionality from Synergy: CoP Nanoparticles Embedded in Amorphous CoOx Nanoplates with Heterostructures for Highly Efficient Water Electrolysis. *Advanced Science* **2018**, 1800514.

(24) F. Yang; Y. Chen; G. Cheng; S. Chen; W. Luo. Ultrathin nitrogen-doped carbon coated with CoP for efficient hydrogen evolution. *ACS Catalysis* **2017,** *7* (6), 3824-3831.

(25) L. Zheng; W. Hu; X. Shu; H. Zheng; X. Fang. Ultrafine CoPx Nanoparticles Anchored on Nitrogen Doped Reduced Graphene Oxides for Superior Hydrogenation in Alkaline Media. *Advanced Materials Interfaces* **2018**, 1800515.

(26) D. Khalafallah; O. Y. Alothman; H. Fouad; K. A. Khalil. Nitrogen and carbon functionalized cobalt phosphide as efficient non-precious electrocatalysts for oxygen reduction reaction electrocatalysis in alkaline environment. *Journal of Electroanalytical Chemistry* **2018,** *809*, 96-104.

(27) Y. Liu; X. Cao; R. Kong; G. Du; A. M. Asiri; Q. Lu; X. Sun. Cobalt phosphide nanowire array as an effective electrocatalyst for non-enzymatic glucose sensing. *Journal of Materials Chemistry B* **2017,** *5* (10), 1901-1904.

(28) N. Danilovic; R. Subbaraman; D. Strmcnik; K. C. Chang; A. Paulikas; V. Stamenkovic; N. M. Markovic. Enhancing the alkaline hydrogen evolution reaction activity through the bifunctionality of Ni (OH) 2/metal catalysts. *Angewandte Chemie* **2012,** *124* (50), 12663-12666.

(29) W. Sheng; H. A. Gasteiger; Y. Shao-Horn. Hydrogen oxidation and evolution reaction kinetics on platinum: acid vs alkaline electrolytes. *Journal of The Electrochemical Society* **2010,** *157* (11), B1529-B1536.

(30) T. Devic; C. Serre. High valence 3p and transition metal based MOFs. *Chemical Society Reviews* **2014,** *43* (16), 6097-6115.

(31) D. N. Mueller; M. L. Machala; H. Bluhm; W. C. Chueh. Redox activity of surface oxygen anions in oxygen-deficient perovskite oxides during electrochemical reactions. *Nature communications* **2015,** *6*, 6097.

(32) D. N. Mueller; R. A. De Souza; J. Brendt; D. Samuelis; M. Martin. Oxidation states of the transition metal cations in the highly nonstoichiometric perovskite-type oxide Ba 0.1 Sr 0.9 Co 0.8 Fe 0.2 O 3− δ. *Journal of Materials Chemistry* **2009,** *19* (14), 1960-1963.

(33) J. Suntivich; W. T. Hong; Y.-L. Lee; J. M. Rondinelli; W. Yang; J. B. Goodenough; B. Dabrowski; J. W. Freeland; Y. Shao-Horn. Estimating hybridization of transition metal and oxygen states in perovskites from Ok-edge x-ray absorption spectroscopy. *The Journal of Physical Chemistry C* **2014,** *118* (4), 1856-1863.

(34) C.-C. Hou; S. Cao; W.-F. Fu; Y. Chen. Ultrafine CoP nanoparticles supported on carbon nanotubes as highly active electrocatalyst for both oxygen and hydrogen evolution in basic media. *ACS applied materials & interfaces* **2015,** *7* (51), 28412-28419.

5.7 Supporting information

5.7.1 Catalyst ink preparation.

To prepare the catalyst ink, 10 mg of the as-synthesized perovskite was mixed with 10 mg of carbon black (Cabot). The mixture was dispersed in a solution containing 200 µL of 5wt. % Nafion (Aldrich) and 800 µL of isopropyl alcohol (Fisher Scientific Cooperation), and then sonicated for an hour. The glassy carbon rotating disk electrode (5 mm RDE, Pine instrument) was pre-polished with 0.3 and 0.05 µm aluminum oxide suspension and rinsed with deionized water to obtain a mirror-like surface. 5 µL of the catalysts ink was dispersed on a 5 mm pre-polished glassy carbon rotating disk electrode (RDE, Pine instrument) and was dried in air for 1 h before the test. The loading amount of the perovskite catalyst was 0.255 mg_{ox} cm^{-2}.

5.7.2 Electrochemical measurements

The electrochemical tests were carried with a standard three-electrode cell, where the catalyst-coated glassy carbon RDE, the Ag/AgCl (Sat. KCl) electrode and Pt wire served as the working electrode, the reference electrode and the counter electrode, respectively. The HER and OER were conducted using both 0.1 M KOH and 1 M KOH electrolyte, while the ORR was measured using a 0.1 M KOH electrolyte. For the ORR and OER tests, the oxygen saturated 0.1 M KOH solution was prepared via purging pure oxygen (99.9%) into the electrolyte for 30 min. Linear sweep voltammetry (LSV) was conducted in a voltage scan range of 0.1 V to -0.8 V (vs. Ag/AgCl, sat. KCl) with rotating speeds of 400, 900, 1600 and 2500 rpm. For OER measurements, LSVs were measured in a voltage range of 0.1 to 1 V vs. Ag/AgCl at a scan rate of 20 mV s^{-1}. While for HER measurements, the LSVs were measured from -0.8 to -1.6 V vs. Ag/AgCl at a scan rate of 20 mV s^{-1} in Ar-saturated KOH solution.

5.7.3 DFT calculations

The first-principle calculations were carried out with the Vienna *ab initio* Simulation Package (VASP).[1–4] The electron wavefunctions were presented by the planewave basis set with an energy cutoff of 520 eV. The ionic cores and their interaction with the valence electrons were treated with the projector-augmented plane-wave (PAW) method.[5,6] The Perdew-Burke-Ernzerhof (PBE) generalized gradient approximation functional (GGA) was employed to describe the exchange–correlation interactions.[7] The spin polarization was enabled in all the calculations. The Monkhorst-Pack K-point mesh of 3×5×3 was used for the $PBSCFO_6$ unit cell.[8–10] The occupancy of the one-electron states was calculated using an electronic temperature of k_BT = 0.05 eV, while all the energies were extrapolated to T = 0 K. The structures were geometrically optimized until the force components were less than 0.06 eV/Å. The relaxed lattice constants of the $PBSCFO_6$ unit cell are a=7.664 Å, b=3.850 Å and c=7.663 Å, in good agreement with the experimental results obtained in this study, further confirming the reasonability of the above computational setups. Based on the fully relaxed unit cell, the (001) slab model was built with the vacuum thickness of 15 Å along the z axis to minimize the periodic image interactions. The slab contains seven atomic layers with Co/Fe-O as the surface termination layer. During the geometry optimization of the slab models, the bottom three atomic layers were constraint, whereas the above four layers were allowed to relax.

The effective p band center of the oxygen within the first atomic layer of the surface models was determined by taking the centroid of the projected density of states of the oxygen p states relative to the Fermi level using the commonly used formula,[10–13]

$$band\ center = \frac{\int E \cdot f(E) dE}{\int f(E) dE}$$

Where E and $f(E)$ are the electron energy and the corresponding PDOS value, respectively.

For the purpose of this study, the CoP and CoOH adsorbed surface models were subsequently built and relaxed to simulate the exsolutions of CoP on the surface of $PBSCFO_6$,[14,15] where the O p band center was calculated for the surrounding oxygen in the first layer. Moreover, to compare the catalytic activities of the three typical surfaces for hydrogen evolution reaction (HER), the Gibbs free energy diagram for HER was constructed which has been verified capable of reflecting the relative activity trend of the catalysts.[16,17] Both the Co and Fe sites on the surface were taken as the catalytic active centers for HER with the adsorption of the intermediate H at a surface coverage of 0.25.[10] The $\Delta G_{H*}$was then calculated as,[16,18]

$$\Delta G_{H*} = E_{H*} - E* - \frac{E_{H_2}}{2} + \Delta(E_{ZPE} + \int C_p dT - TS)$$

where E_{H*}, $E*$ and $E_{H_2}$are the DFT calculated electronic energies of the H adsorbed surface, the bare surface and hydrogen gas, respectively; E_{ZPE} is the zero-point vibrational energy; $\int C_p dT$ is the enthalpy correction; TS is the entropy contribution. The relevant entropy and enthalpy corrections were calculated with the suggested methods by the previous studies.[19,20]

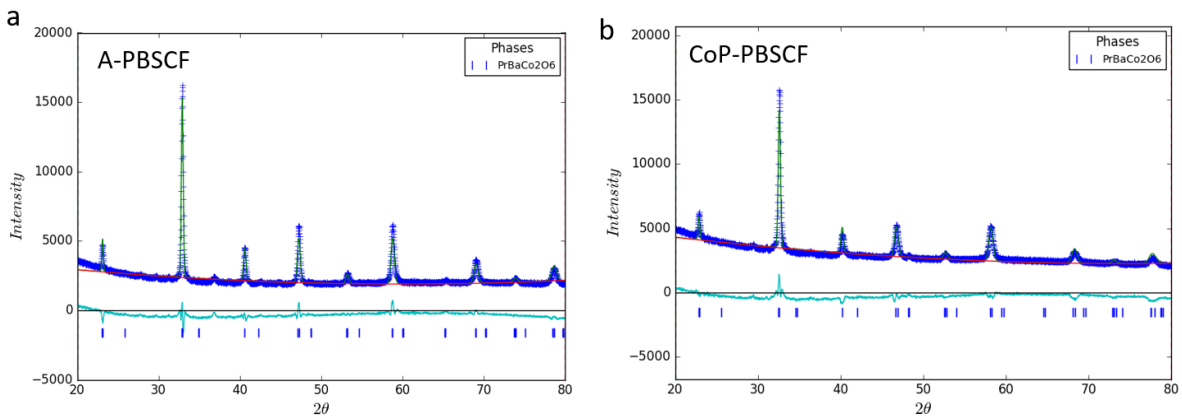

Figure S5. 1 XRD refinement data of (a) A-PBSCF and (B) CoP-PBSCF

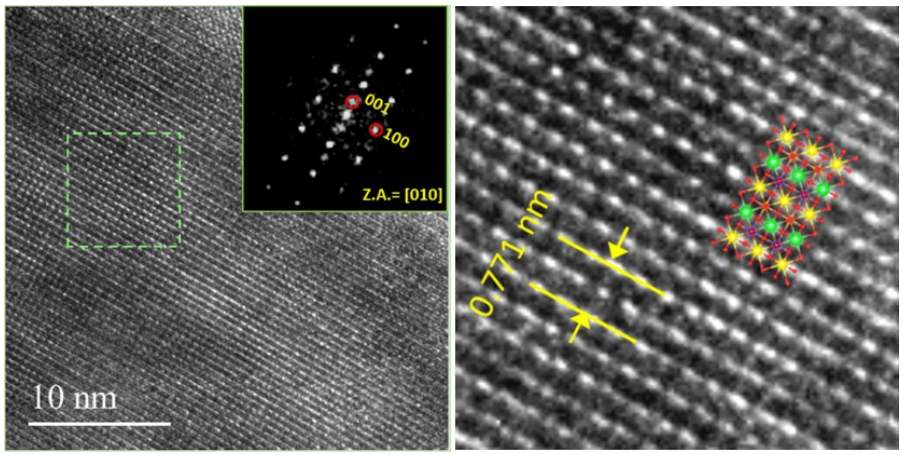

Figure S5. 2 HRTEM images of the A-PBSCF and the corresponding diffractogram.

References

1 Kresse, G.; Hafner, J. Ab Initio Molecular Dynamics for Liquid Metals. *Phys. Rev. B* **1993**, *47*, 558–561.

2 Kresse, G.; Hafner, J. Ab Initio Molecular-Dynamics Simulation of the Liquid-Metal–amorphous-Semiconductor Transition in Germanium. *Phys. Rev. B* **1994**, *49*, 14251–14269.

3 Kresse, G.; Furthmüller, J. Efficiency of Ab-Initio Total Energy Calculations for Metals and Semiconductors Using a Plane-Wave Basis Set. *Comput. Mater. Sci.* **1996**, *6*, 15–50.

4 Kresse, G.; Furthmüller, J. Efficient Iterative Schemes for Ab Initio Total-Energy Calculations Using a Plane-Wave Basis Set. *Phys. Rev. B* **1996**, *54*, 11169–11186.

5 Blöchl, P. E. Projector Augmented-Wave Method. *Phys. Rev. B* **1994**, *50*, 17953–17979.

6 Kresse, G. From Ultrasoft Pseudopotentials to the Projector Augmented-Wave Method. *Phys. Rev. B* **1999**, *59*, 1758–1775.

7 Hammer, B.; Hansen, L. B.; Nørskov, J. K. Improved Adsorption Energetics within Density-Functional Theory Using Revised Perdew-Burke-Ernzerhof Functionals. *Phys. Rev. B* **1999**, *59*, 7413–7421.

8 Monkhorst, H. J.; Pack, J. D. Special Points for Brillouin-Zone Integrations. *Phys. Rev. B* **1976**, *13*, 5188–5192.

9 Choi, S.; Yoo, S.; Kim, J.; Park, S.; Jun, A.; Sengodan, S.; Kim, J.; Shin, J.; Jeong, H. Y.; Choi, Y.; et al. Highly Efficient and Robust Cathode Materials for Low-Temperature Solid Oxide Fuel Cells: PrBa0.5Sr0.5Co2−xFe x O5+δ. *Sci. Rep.* **2013**, *3*, 2426.

10 Zhao, B.; Zhang, L.; Zhen, D.; Yoo, S.; Ding, Y.; Chen, D.; Chen, Y.; Zhang, Q.; Doyle, B.; Xiong, X.; et al. A Tailored Double Perovskite Nanofiber Catalyst Enables Ultrafast Oxygen Evolution. *Nat. Commun.* **2017**, *8*, 1–9.

11 Grimaud, A.; May, K. J.; Carlton, C. E.; Lee, Y.-L.; Risch, M.; Hong, W. T.; Zhou, J.;

Shao-Horn, Y. Double Perovskites as a Family of Highly Active Catalysts for Oxygen Evolution in Alkaline Solution. *Nat. Commun.* **2013**, *4*, 1–7.

12 Hong, W.; Stoerzinger, K. A.; Lee, Y.-L.; Giordano, L.; Grimaud, A. J. L.; Johnson, A. M.; Hwang, J.; Crumlin, E.; Yang, W.; Shao-Horn, Y. Charge-Transfer-Energy-Dependent Oxygen Evolution Reaction Mechanisms for Perovskite Oxides. *Energy Environ. Sci.* **2017**, *10*, 2190–2200.

13 Jacobs, R.; Booske, J.; Morgan, D. Understanding and Controlling the Work Function of Perovskite Oxides Using Density Functional Theory. *Adv. Funct. Mater.* **2016**, *26*, 5471–5482.

14 Gong, Q.; Wang, Y.; Hu, Q.; Zhou, J.; Feng, R.; Duchesne, P. N.; Zhang, P.; Chen, F.; Han, N.; Li, Y.; et al. Ultrasmall and Phase-Pure W2C Nanoparticles for Efficient Electrocatalytic and Photoelectrochemical Hydrogen Evolution. *Nat. Commun.* **2016**, *7*.

15 Wu, H.; Xiao, W.; Guan, C.; Liu, X.; Zang, W.; Zhang, H.; Ding, J.; Feng, Y. P.; Pennycook, S. J.; Wang, J. Hollow Mo-Doped CoP Nanoarrays for Efficient Overall Water Splitting. *Nano Energy* **2018**, *48*, 73–80.

16 Nørskov, J. K.; Rossmeisl, J.; Logadottir, A.; Lindqvist, L.; Kitchin, J. R.; Bligaard, T.; Jónsson, H. Origin of the Overpotential for Oxygen Reduction at a Fuel-Cell Cathode. *J. Phys. Chem. B* **2004**, *108*, 17886–17892.

17 Liu, S.; Tao, H.; Zeng, L.; Liu, Q.; Xu, Z.; Liu, Q.; Luo, J.-L. Shape-Dependent Electrocatalytic Reduction of CO2 to CO on Triangular Silver Nanoplates. *J. Am. Chem. Soc.* **2017**, *139*, 2160–2163.

18 Zhang, R.; Tang, C.; Kong, R.; Du, G.; Asiri, A. M.; Chen, L.; Sun, X. Al-Doped CoP Nanoarray: A Durable Water-Splitting Electrocatalyst with Superhigh Activity. *Nanoscale* **2017**, *9*, 4793–4800.

19 Cramer, C. J. *Essentials of Computational Chemistry Theories and Models*, Second Edi.;

John Willey & Sons Ltd: Chichester, 2004.

20 Rosen, J.; Hutchings, G. S.; Lu, Q.; Rivera, S.; Zhou, Y.; Vlachos, D. G.; Jiao, F. Mechanistic Insights into the Electrochemical Reduction of CO2 to CO on Nanostructured Ag Surfaces. *ACS Catal.* **2015**, *5*, 4293–4299.

Chapter 6. A Strongly Cooperative Spinel Nanohybrid as an Efficient Bifunctional Oxygen Electrocatalyst for Oxygen Reduction Reaction and Oxygen Evolution Reaction

6.1. Abstract

The development of efficient, stable and low-cost bifunctional oxygen electrocatalysts is critical to the realization of practically viable rechargeable Zn-air batteries. Herein, we report a strongly cooperative spinel nanohybrid as a promising air electrode catalyst for rechargeable Zn-air batteries. Ultrafine sub-10 nm $MnFe_2O_4$ crystals are *in situ* grown on the ultrathin $NiCo_2O_4$ nanosheets, leading to a highly effective surface area and a strong synergistic chemical coupling effect. The distinct architecture and complex composition endow an excellent bifunctional oxygen electrocatalytic activity in alkaline condition. The practical rechargeable Zn-air battery with the hybrid electrocatalyst demonstrates a high round-trip efficiency (a low discharge-charge voltage gap of 0.81 V at a reversible current density of 10 mA cm^{-2}) and an outstanding durability, which outperforms the commercial Pt/Ru/C electrocatalyst. The resulting hybrid ($MnFe_2O_4$/$NiCo_2O_4$) shows great promise as an alternative bifunctional electrocatalyst to the precious metals for the application in Zn-air batteries.

6.2. Introduction

As a promising post lithium-ion technology, rechargeable Zn–air batteries have attracted intense attention in the past decades due to their high theoretical energy and power density.[1] However, the sluggish kinetics of the ORR/OER has been the technical hurdle for the Zn-air battery application.[2] Thus, the discovery of bifunctional electrocatalysts which could efficiently drive both ORR and OER is of paramount importance. Presently, the state-of-art bifunctional electrocatalysts are noble-metal based catalysts, such as Pt/RuO_2 or Pt/IrO_2. However, the commercialization of Zn-air battery is greatly hampered by two fundamental factors associated to the Pt/RuO_2 or Pt/IrO_2: (1) the high cost, scarcity of the noble metal, and (2) the poor stability of the electrocatalysts in cyclic charging/discharging environment.[3] Therefore, it is highly desirable yet challenging to design non-noble-metal-based bifunctional electrocatalysts with efficient catalytic activity and good stability.

Mixed-valence transition metal oxides have emerged as an alternative oxygen electrocatalyst, among which a two-dimensional $NiCo_2O_4$ nanosheets (NSs) electrocatalysts with an ultrathin feature has drawn particular interest owing to its excellent intrinsic OER activity, unique architecture, rich electroactive sites, and good electronic/ionic conductivity.[4] However, an insufficient ORR activity was found on $NiCo_2O_4$ electrocatalysts, which greatly limits their application in rechargeable Zn-air batteries.[5] Therefore, considerable efforts are required to advance the bifunctionality of the $NiCo_2O_4$ NSs and to broaden their application in energy devices. Research has shown that assembling the ultrathin $NiCo_2O_4$ NSs with graphene leads to an enhanced catalytic activity derived from the synergetic chemical coupling effects between ultrathin NSs and foreign materials.[6]

Herein, we report the *in situ* growth of ultrafine $MnFe_2O_4$ nanocrystals on ultrathin $NiCo_2O_4$ NSs (denoted as $MnFe_2O_4/NiCo_2O_4$) as a highly efficient and stable bifunctional electrocatalyst. Previous studies conducted by Sun *et al* show that the monodispersed magnetite $MnFe_2O_4$ nanoparticles (NPs) supported on carbon support exhibits competitive ORR ativity to the commercial Pt/C catalysts.[7] In an endeavor to boost the bifunctionality, sub-10 nm $MnFe_2O_4$ nanocrystals have been grown on $NiCo_2O_4$ ultrathin NSs. The ultrathin NS structure of $NiCo_2O_4$ affords a high specific surface area and sufficient anchoring sites that allow subsequent integration of highly dispersed NPs. This structure enables an intimate contact between $MnFe_2O_4$ NPs and $NiCo_2O_4$ NSs, which is attributed to an efficient utilization of the catalyst surface and an extended electrochemically active surface area. The significantly enhanced bifunctional oxygen electrocatalytic activity is credited to the distinct architecture and complex composition of the $MnFe_2O_4/NiCo_2O_4$ hybrid. The $MnFe_2O_4/NiCo_2O_4$ hybrid electrocatalyst exhibits an overpotential of 0.344 V at 10 mA cm^{-2} for the OER, and a positive half-wave potential of 0.767 V (vs. reversible hydrogen electrode, RHE) for the ORR. More importantly, the rechargeable Zn-air batteries employing the $MnFe_2O_4/NiCo_2O_4$ hybrid achieve a high round-trip efficiency with a low discharge−charge voltage gap of 0.81 V at a reversible current density of 10 mA cm^{-2} as well as an excellent durability over 100 cycles.

6.3. Results and discussions

The ultrathin $NiCo_2O_4$ NSs were firstly synthesized through a p-aminobenzoic acid (PABA) intercalation method, followed by a subsequent thermal treatment.[4a, 4b] The as-synthesized $NiCo_2O_4$ NSs exhibit negative zeta potentials in neutral and alkaline media (Figure 6.1). The integration of $MnFe_2O_4$ NPs on $NiCo_2O_4$ NSs was achieved using a non-hydrolytic thermal

decomposition method with $Mn(acac)_2$ and $Fe(acac)_3$ as the sources, and oleylamine as the solvent and stabilizer.[8] Subsequently, the negatively charged $NiCo_2O_4$ NSs were introduced into the solution, which act as heterogeneous nucleation sites for the growth of $MnFe_2O_4$ NPs, owing to the charge interaction of Fe^{3+} and Mn^{2+}. In this synthesis, the loading amount of $MnFe_2O_4$ NPs was controlled by tailoring the ratio of $Fe(acac)_3$ and $Mn(acac)_2$ to the $NiCo_2O_4$. The strong anchoring of $MnFe_2O_4$ resulted from the heterogeneous nucleation led to an interfacial interaction of $MnFe_2O_4$ NPs with the ultrathin $NiCo_2O_4$ NSs, which was expected to exhibit high electrocatalytic activity and durability for oxygen electrocatalysis. For comparison, monodispersed $MnFe_2O_4$ NPs and physically mixed composite $MnFe_2O_4$+$NiCo_2O_4$ were also prepared.

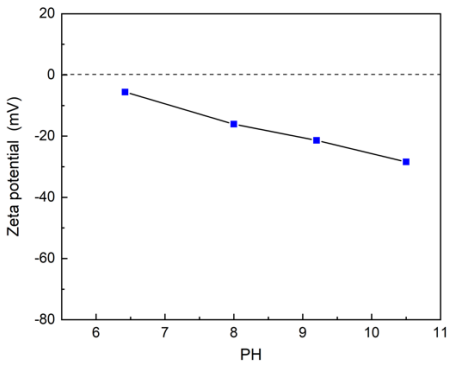

Figure 6.1 Surface charge investigation of $NiCo_2O_4$ ultrathin nanosheets with zeta potential measured at different PH.

The XRD pattern of the as-prepared electrocatalyst clearly demonstrates the formation of $MnFe_2O_4$/$NiCo_2O_4$ hybrid (Figure 6.2a), where the peak positions and relative intensities of all diffraction peaks are well matched with those of the resulting $MnFe_2O_4$ NPs, $NiCo_2O_4$ NSs and corresponding standard diffraction patterns (PDF #10-0319 and PDF #20-0781). The FESEM image of $MnFe_2O_4$/$NiCo_2O_4$ hybrid in Figure 6.2b shows the layered flower-like structure

assembled with interconnected ultrathin $NiCo_2O_4$ NSs. Figures 6.2c confirms the architecture of the $MnFe_2O_4/NiCo_2O_4$ hybrid, where the $NiCo_2O_4$ NSs are well integrated with $MnFe_2O_4$ NPs.

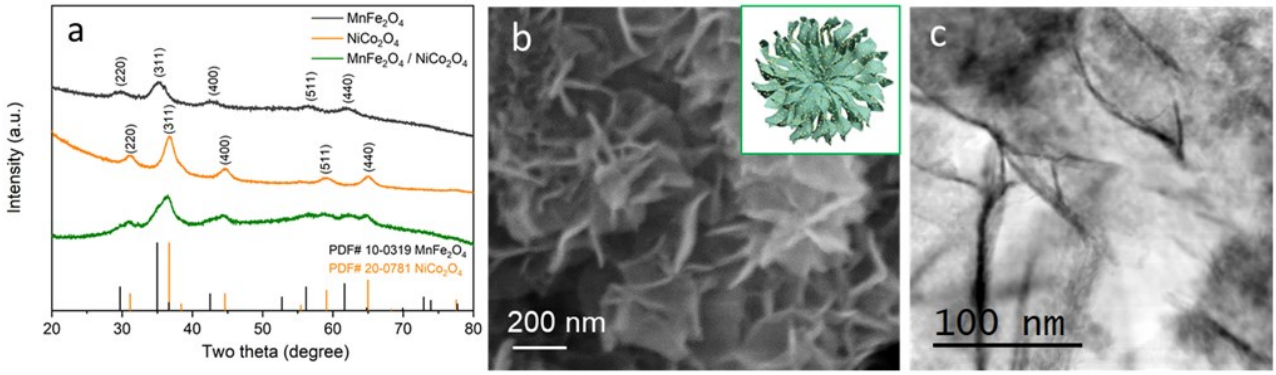

Figure 6.2 (a) XRD of $MnFe_2O_4$ NPs, $NiCo_2O_4$ NSs and $MnFe_2O_4/NiCo_2O_4$ hybrid; (b) FESEM image and (c) TEM image of $MnFe_2O_4/NiCo_2O_4$ hybrid;

From the TEM images shown in Figures 6.3a and b, the thickness of an individual $NiCo_2O_4$ NS matrix is around 6-7 nm in $MnFe_2O_4/NiCo_2O_4$ hybrid. As revealed by the Brunauer–Emmett–Teller (BET) analysis (Figure 6.3c), the $MnFe_2O_4/NiCo_2O_4$ hybrid possesses a specific surface area of 118.6 m^2 g^{-1} with substantial mesopores (similar to that of $NiCo_2O_4$ NSs, with 131.8 m^2 g^{-1}), suggesting negligible agglomeration of the hybrid after the incorporation of $MnFe_2O_4$ NPs. This undoubtedly makes the $MnFe_2O_4/NiCo_2O_4$ hybrid an excellent electrocatalyst with high surface area and abundant electroactive sites. The chemical compositions of the $MnFe_2O_4/NiCo_2O_4$ hybrid, $NiCo_2O_4$ ultrathin NS and $MnFe_2O_4$ NPs were also confirmed by energy dispersive X-ray (EDX) spectroscopy (Figures S6.1, S6.2 and S6.3) and inductively coupled plasma-atomic emission spectroscopy (ICP-AES); Based on ICP-AES result, the loading amount of $MnFe_2O_4$ NPs was estimated to be 47.2 wt.% in the $MnFe_2O_4/NiCo_2O_4$ hybrid, consistent with the set ratio. Moreover, the STEM-EDX and atom-scale high resolution TEM (HRTEM) in Figures 6.4a and b give better insights into the chemical composition and material structure. The elemental mappings of

$MnFe_2O_4/NiCo_2O_4$ hybrid (Figure 6.4a) show the homogenous distributions of Mn, Fe, Ni, Co, indicating that the ultrafine $MnFe_2O_4$ NPs are uniformly dispersed on $NiCo_2O_4$ NSs without deteriorating the structure and ultrathin feature of the $NiCo_2O_4$ NSs during the formation of $MnFe_2O_4$ NPs. As demonstrated, the exposed edges of $NiCo_2O_4$ NSs are the electroactive centers for the water oxidation reaction and could remarkably facilitate the reaction kinetics.[6b] To this end, the HRTEM was conducted; the lattice fringes with a d spacing of 2.51 Å (Figure 6.3b) on clean exposed edge of $NiCo_2O_4$ NS were observed, which correspond to the (311) plane of $NiCo_2O_4$, implying that the $NiCo_2O_4$ is preferentially exposed with {311} facets.[4c] As seen from Figure 6.4b, the diameters of the NPs coupled on the $NiCo_2O_4$ are 5-7 nm. The HRTEM of $MnFe_2O_4/NiCo_2O_4$ hybrid, along with the corresponding diffractogram, shows the d spacings of 2.94 and 4.88 Å, indexed on the (220) and (1-11) planes of $MnFe_2O_4$. This HRTEM confirms that the non-hydrolytic synthetic method offers intriguing advantages to synthesize NPs with uniform size distribution and high crystallinity.[8-9]

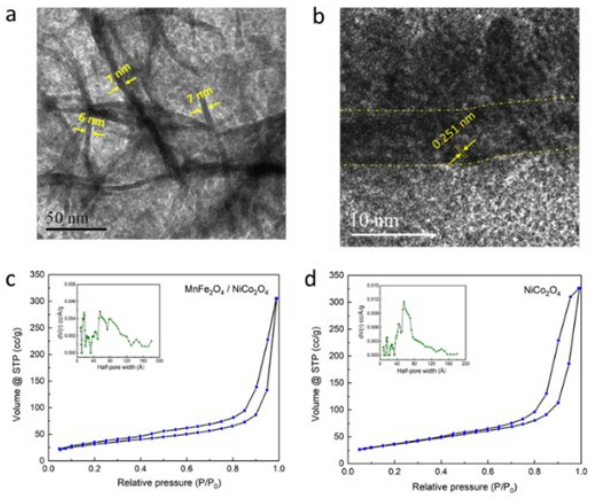

Figure 6.3 (a) TEM image and (b) HR-TEM of the vertical oriented $MnFe_2O_4$ / $NiCo_2O_4$ hybrid. N_2 adsorption and desorption isotherm curves with BJH pore size distribution (inset) of (c) $MnFe_2O_4$ / $NiCo_2O_4$ hybrid and (d) $NiCo_2O_4$.

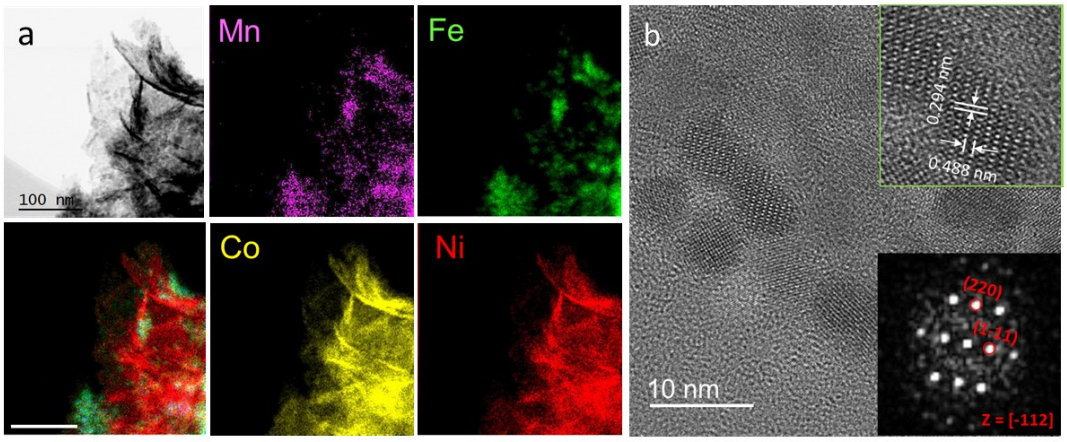

Figure 6.4 (a) Scanning transmission electron microscopy bright-field (STEM-BF) mage of $MnFe_2O_4/NiCo_2O_4$ hybrid with EDS mapping; (The scale bar is 100 nm) (b) HRTEM images of $MnFe_2O_4$ nanoparticles on $NiCo_2O_4$ NSs.

X-ray photoelectron spectroscopy (XPS) analysis was performed to study the electronic structure of Ni, Co, O in the $MnFe_2O_4/NiCo_2O_4$ hybrid and the ultrathin $NiCo_2O_4$ NSs. After loading with $MnFe_2O_4$ NPs, the Co 2p core level XPS spectra demonstrate that the electron binding energy of Co 2p experiences a decrease of ~0.4 eV. This is considered to accompany the oxidation of Co^{2+} to Co^{3+}.[10] The Co 2p core level spectra (Figure 6.5a) were deconvoluted into two spin-orbit doublets, characteristic of Co^{2+} and Co^{3+}, and one shakeup satellite (identified as "Sat."). The deconvolution results manifest that, after loading with $MnFe_2O_4$ NPs, the ratio of Co^{3+} to Co^{2+} experienced a significant increase. It has been reported that Co^{3+} center plays a decisive role in determining H_2O adsorption, and consequently enabling high ORR and OER electrocatalytic activities.[7, 11] As for the Ni 2p spectra (Figure 6.5b), two spin orbit doublets, characteristic of Ni^{2+} and Ni^{3+} species, are found in both samples. The incorporated surface Ni^{3+} species also acts as the active sites to facilitate the OER.[12]

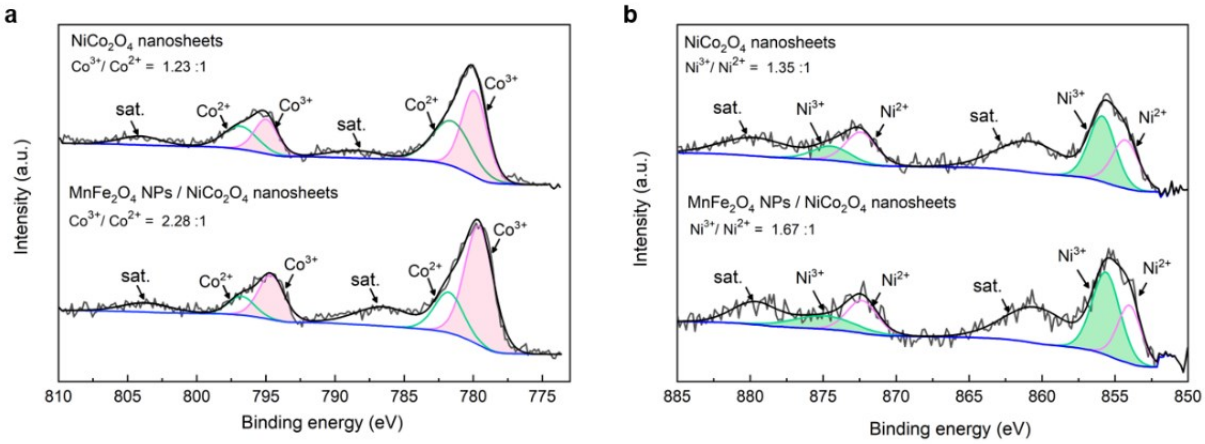

Figure 6.5 The XPS profiles of $NiCo_2O_4$ NSs and $MnFe_2O_4/NiCo_2O_4$ hybrid. (a) Co 2p spectra and its simulations; (b) Ni 2p spectra and its simulations.

Research has shown that the complex transition metal oxide generally results in complementary redox and beneficial electronic properties, and therefore is likely to show significant promise as electrocatalyst material. [13] As such, we investigated the bifunctional oxygen electrocatalytic performances of the $MnFe_2O_4/NiCo_2O_4$ hybrid for ORR and OER. The ORR electrocatalytic activities were first investigated by the cyclic coltammetry (CV) in O_2 and Ar saturated 0.1 M KOH, respectively. Using the $MnFe_2O_4/NiCo_2O_4$ hybrid, a more positive onset potential was achieved, and the peak potential shifted from 0.695 V ($NiCo_2O_4$ NSs) to 0.779 V vs. Reversible Hydrogen Electrode (RHE) (Figure 6.6).

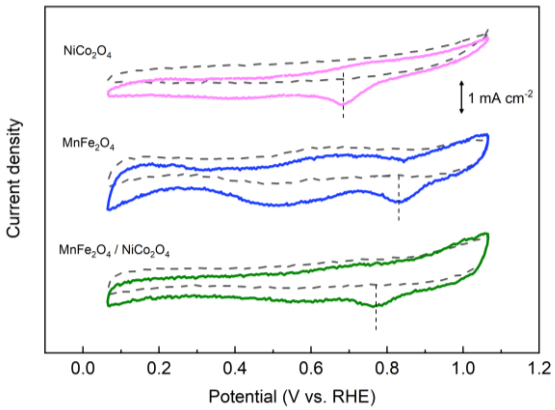

Figure 6.6 Cyclic voltammetry curves of $MnFe_2O_4$, $NiCo_2O_4$ and $MnFe_2O_4/NiCo_2O_4$ hybrid on glassy carbon electrodes in O_2-saturated (solid line) and Ar-saturated (dash line) 0.1 M KOH. Scan rate was 20 mV s^{-1}.

To reveal the ORR kinetics, the catalytic acticity of $MnFe_2O_4/NiCo_2O_4$ hybrid was further analyzed by the linear sweep voltammetry (LSV), using a rotating disk electrode (RDE) in O_2-saturated 0.1 M KOH. As benchmarks, the ORR catalytic activities of $MnFe_2O_4$ NPs, $NiCo_2O_4$ NSs and physically mixed composite as well as the commercial Pt/C electrocatalysts were evaluated. At 1600 rpm (Figure 6.7a), the $NiCo_2O_4$ NSs showed a diffusion-limited current density of 4.66 mA cm^{-2} at 0.3 V (vs. RHE). The ORR E_{onset} and $E_{1/2}$ of the $NiCo_2O_4$ were 0.785 and 0.702 V, respectively. When coupled with $MnFe_2O_4$, the $MnFe_2O_4/NiCo_2O_4$ hybrid achieved a comparably higher catalytic ORR activity, with a more positive onset potential (E_{onset} 0.881 V vs. RHE), half wave potential ($E_{1/2}$ 0.767 V), and higher diffusion-limited current density (5.01 mA cm^{-2} at 0.3 V). The physical mixed composite demonstrated a simiar ORR electrocatalytic activity, with an onset potential of 0.878 V and a half-wave potential of 0.783V. It is suggested that the redox couple of Mn^{3+}/Mn^{2+}within the hybrid contributes to an enhanced ORR activity. As Mn^{2+} has a higher tendency to adsorb O_2, the surface redox active centers of $MnFe_2O_4$ presumably facilitate the O_2 adsorption and activation in the ORR. [7, 14] With the onset potential of 0.912 V and

half-wave potential of 0.835 V, $MnFe_2O_4$ NPs demonstrate the best ORR activity among the resulting spinel oxide catalysts, approaching to the commercial Pt/C catalyst performance wise. To further investigate the reaction kinetics of the hybrid for ORR, polarization curves were obtained on all samples at the rotating speeds of 400 to 2500 rpm (Figures 6.7b, c ,d and e). The electron transfer numbers were estimated based on the slopes Koutecky-Levich equation at different potentials (ie., 0.3 V and 0.4 V). The electron transfer numbers (n) were calculated to be around 4.0 at 0.3–0.4 V for $MnFe_2O_4/NiCo_2O_4$ hybrid, slightly higher than that of $NiCo_2O_4$ NSs (Figure 6.7f). This indicates that the electron transfer pathway is dominated by a four-electron route in the $MnFe_2O_4/NiCo_2O_4$ hybrid.

The LSV curves of the $MnFe_2O_4/NiCo_2O_4$ electrocatalyst for OER were measured at 1600 rpm in O_2 saturated 0.1 M KOH (Figure 6.8a). Remarkably, the $MnFe_2O_4/NiCo_2O_4$ achieved the lowest overpotential of 344 mV at the current density of 10 mA cm^{-2}, significantly lower than that of $NiCo_2O_4$ NSs (456 mV). Of note, the $MnFe_2O_4$ NPs possess poor OER activity. Physically mixed composite, $MnFe_2O_4$+$NiCo_2O_4$, also showed an improved OER catalytic activity (418 mV) as compared to the $NiCo_2O_4$ NSs. The remarkable OER activity of the $MnFe_2O_4/NiCo_2O_4$ hybrid mainly originated from the $NiCo_2O_4$ NSs, where $MnFe_2O_4$ served as a synergist. It is also worth noting that the $MnFe_2O_4/NiCo_2O_4$ hybrid outperforms the $MnFe_2O_4$ + $NiCo_2O_4$ composite, with the overpotential (at 10 mA cm^{-2}) being 74 mV lower than the $MnFe_2O_4$ + $NiCo_2O_4$ electrocatalyst (Figure S6.6). It is deduced that the strong interfacial effects between $MnFe_2O_4$ NPs and $NiCo_2O_4$ NSs in the $MnFe_2O_4/NiCo_2O_4$ will contribute to a more efficient charge transfer between the NPs and the support NSs in comparison to the physically mixed composite.[15] The superb OER activity is also ascribed to the dual electroactive sites, i.e., the clean edge of the $NiCo_2O_4$ ultrathin NSs and the interfacial coupling sites between $MnFe_2O_4$ NPs and $NiCo_2O_4$ NSs.

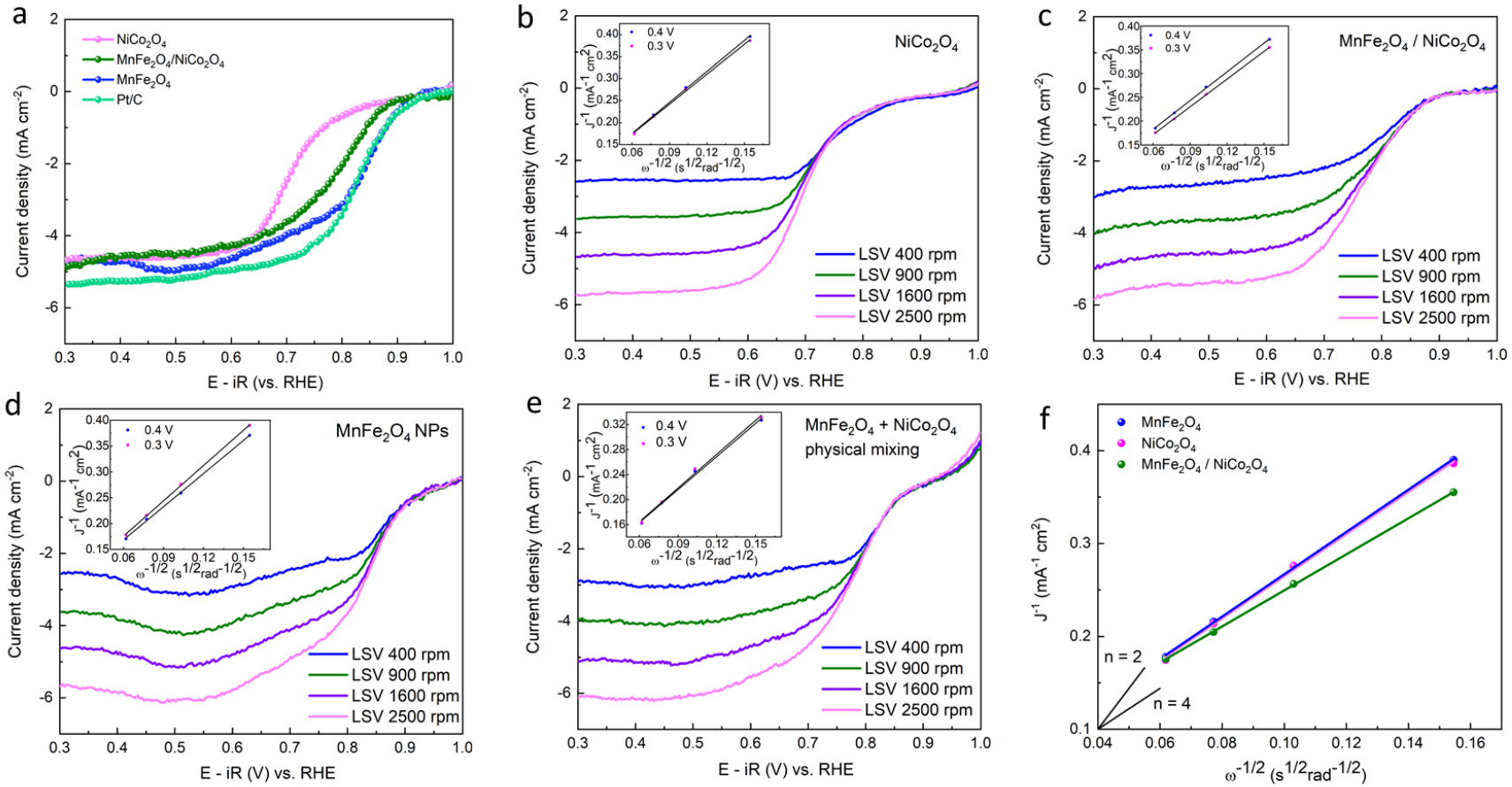

Figure 6.7 (a) ORR LSV curves at 1600 rpm for $NiCo_2O_4$ NSs, $MnFe_2O_4$ NPs, $MnFe_2O_4/NiCo_2O_4$, and Pt/C. ORR LSV curves of (b) $NiCo_2O_4$ NSs and (c) $MnFe_2O_4/NiCo_2O_4$ hybrid (d) $MnFe_2O_4$ NPs and (e) $MnFe_2O_4$ + $NiCo_2O_4$ physical mixing composite in 0.1 M KOH at different rotation speeds. (f) Electron transfer number of $NiCo_2O_4$ NSs, $MnFe_2O_4$ NPs, $MnFe_2O_4/NiCo_2O_4$ derived from K-L plots at 0.3 V vs RHE.

Importantly, the $MnFe_2O_4/NiCo_2O_4$ hybrid demonstrated a smaller Tafel slope (46.7 mV dec^{-1}) than $NiCo_2O_4$ NSs (77.9 mV dec^{-1}) and $MnFe_2O_4$ NPs (115.5 mV dec^{-1}), as shown in Figure 6.8b. A lower Tafel slope manifests a better OER activity as the electrode experiences smaller polarization upon increasing anodic current density. [16] Potentiostatic electrochemical impedance spectroscopy (EIS) conducted on $NiCo_2O_4$ ultrathin NSs and $MnFe_2O_4/NiCo_2O_4$ hybrid (Figure 6.8c) further verifies the enhanced interfacial properties of the $MnFe_2O_4/NiCo_2O_4$ hybrid under the OER potential. For example, at a bias potential of 0.65 vs. Ag/AgCl, the $MnFe_2O_4/NiCo_2O_4$ hybrid shows an interfacial charge-transfer resistance of 3.73 Ω cm^2 (Table S6.1), dramatically lower than that of $NiCo_2O_4$ (15.68 Ω cm^2, Table S6.1). The simulated results indicate that the $MnFe_2O_4/NiCo_2O_4$ hybrid possesses a faster interfacial charge transfer process. A further enhanced charge-transfer process was found on the $MnFe_2O_4/NiCo_2O_4$ hybrid when 1 M KOH was used as the electrolyte (Figure S6.8).

Table 6.1 Comparison of various parameters in the equivalent circuit of EIS curves for the $NiCo_2O_4$ NSs and the $MnFe_2O_4/NiCo_2O_4$ hybrid electrocatalysts at an applied bias potential of 0.65 V vs. Ag/AgCl.

Samples	Rs (Ω cm^2)	CPE_1 (Ω^{-1} cm^{-2} s^n)	n	Rp (Ω cm^2)	CPE_2 (Ω^{-1} cm^{-2} s^n)	n	Rct (Ω cm^2)
$NiCo_2O_4$	9.757	0.080	0.678	3.210	0.0484	0.907	15.680
$MnFe_2O_4$ / $NiCo_2O_4$	9.852	0.034	0.807	1.636	0.0363	0.976	3.729

(The R_s, R_f and R_{ct} represent the electrolyte, electrode film and charge transfer resistance, respectively. CPE1, CPE2 refer to the constant phase elements of the electrode film, and charge-transfer double-layer components, and n is the phase change values obtained from the fitting.)

Apart from the substantially enhanced electrocatalytic activity, the stability of the $MnFe_2O_4/NiCo_2O_4$ hybrid is also of great significance for the practical application. [17] To assess the stability, the galvanostatic long-term performances of $MnFe_2O_4/NiCo_2O_4$ were conducted at a constant current density load of 10 mA cm^{-2} in O_2-saturated 1 M KOH at 1600 rpm, as shown in Figure 6.8d. The OER potential of the $MnFe_2O_4/NiCo_2O_4$ hybrid was first plateaued at 1.56 V at a current density of 10 mA cm^{-2}, and the overpotential only experienced a 9 mV increase after polarized for 50 000 s.

The overall bifunctional activity of the $MnFe_2O_4/NiCo_2O_4$ hybrid was further confirmed by the potential difference between the OER potential of E_{10} and the ORR half-wave potential ($\Delta E = E_{10} - E_{1/2}$) in 0.1 M KOH. The bifunctional activities of the $MnFe_2O_4$ NPs, $NiCo_2O_4$ ultrathin NSs and Pt/Ru/C were also evaluated as shown in Figure 6.8e. The $MnFe_2O_4/NiCo_2O_4$ hybrid shows the smallest potential difference (0.807 V) among the catalysts studied, and is comparable with many good bifunctional catalysts in alkaline conditions (Figure 6.8f, listed in Table 6.2), which is indicative of the favorable bifunctionality of $MnFe_2O_4/NiCo_2O_4$. By integrating the $MnFe_2O_4$ NPs on the ultrathin $NiCo_2O_4$ NSs, the overall overpotential was successfully decreased by 177 mV.

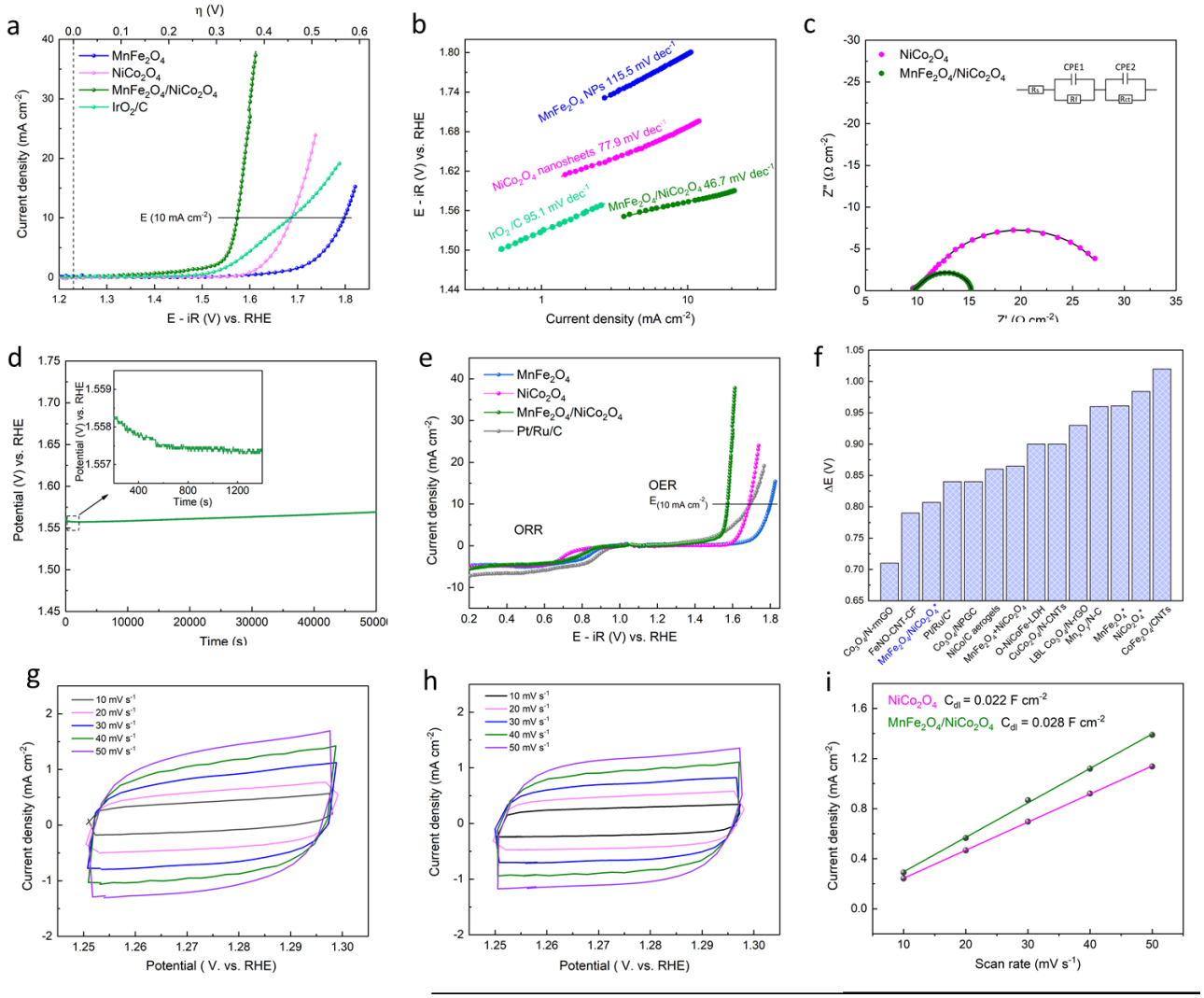

Figure 6.8 LSV curves (a) and corresponding Tafel curves of OER reaction on $NiCo_2O_4$ NSs, $MnFe_2O_4$ NPs, $MnFe_2O_4/NiCo_2O_4$, and IrO_2/C in 0.1 M KOH at 1600 rpm. (c) EIS curves of $MnFe_2O_4/NiCo_2O_4$ hybrid and $NiCo_2O_4$ NSs in 0.1 M KOH at a bias potential of 0.65 V vs. Ag/AgCl. Inset: equivalent circuit model for the Nyquist plots. (d) Long term stability test of $MnFe_2O_4$ / $NiCo_2O_4$ hybrid at a constant current density of 10 mA cm^{-2}. (e) LSV curves of an overall oxygen reaction on $MnFe_2O_4$ NPs, $NiCo_2O_4$ NSs, $MnFe_2O_4/NiCo_2O_4$ hybrid and Pt/Ru/C. (f) The comparison of overall overpotential for bifunctional electrocatalysts. CV curves of (g) $MnFe_2O_4/NiCo_2O_4$ hybrid and (h) $NiCo_2O_4$ nanosheets in the double layer region at different scan rates in 1.0 M KOH; (i) Measurements of the electrochemical double-layer capacitance (current density at the potential of 1.275 V vs. scan rate).

Table 6.2 The electrocatalytic performance of $NiCo_2O_4$ samples and the commercial bifunctional noble metal catalysts.

Samples	ORR			OER	
	Onset potential (V vs. RHE)	Half-wave potential (V vs. RHE)	Limited current density (mA cm^{-2})	Overpotential at 10 mA cm^{-2} (V vs. RHE)	Exchange current density (A cm^{-2}) [a]
$NiCo_2O_4$	0.785	0.702	4.66	0.456	4.6×10^{-6}
$MnFe_2O_4$	0.912	0.835	4.62	0.566	2.6×10^{-6}
$MnFe_2O_4$ + $NiCo_2O_4$	0.878	0.783	5.13	0.418	1.74×10^{-5}
$MnFe_2O_4$ / $NiCo_2O_4$	0.881	0.767	5.01	0.344	1.34×10^{-4}
Pt/Ru/C	0.952	0.852	6.70	0.457	2.4×10^{-4}

([a] Exchange current density was extrapolated from the intercept value from the Tafel curves (log(i) vs. overpotential) based on the OER LSV curve. The true values of exchange current densities can only be measured experimentally under equilibrium conditions and may be different from the extrapolated values reported here.)

On account of the architecture, chemical compositions and valence states of the $MnFe_2O_4$/$NiCo_2O_4$ hybrid, it is believed that the advanced bifunctionality is mainly attributed to the following two foundations. The uniform distribution of the ultrafine $MnFe_2O_4$ NPs on the porous ultrathin $NiCo_2O_4$ NSs results in a high electrolyte – material contact area and short ion diffusion paths, which facilitates the H_2O molecule adsorption and favors the charge-transfer; [18] the strong coupling of the $MnFe_2O_4$ NPs on the $NiCo_2O_4$ NSs suppresses the agglomeration of the nanoparticles during the long-term operation. [15, 19] In addition, a lager electrochemical double layer capacitance was found on $MnFe_2O_4$/$NiCo_2O_4$, suggesting an extended electrochemical active surface area. [20] The capacitance of the double layer (C_{dl}) was evaluated by measuring the CV curves at a non-faradic potential range at different scan rates (Figure 6.8g and h); [21] as shown in Figure 6.8i, the C_{dl} of $MnFe_2O_4$/$NiCo_2O_4$ is 0.028 F cm^{-2}, larger than that of $NiCo_2O_4$ (0.022 F

cm^{-2}). This is likely to be one of the reasons for the enhanced electrocatalytic activity from the $MnFe_2O_4/NiCo_2O_4$ hybrid. This heterostructured hybrid realizes efficient bifunctional catalytic activities from the full utilization of the catalyst surface and strong interaction between the $MnFe_2O_4$ NPs and $NiCo_2O_4$ matrix. The decreased overall potential difference between ORR and OER on $MnFe_2O_4/NiCo_2O_4$ indicates a small energy loss in the charging/discharging process.

Building on bifunctional electrochemical activities studied above on the RDE electrode, the oxygen catalytic activity of the $MnFe_2O_4/NiCo_2O_4$ hybrid was further evaluated in the rechargeable Zn-air battery. As shown in Figure 6.9a, a proof-of-concept rechargeable Zn-air battery was assembled with zinc plate as the anode, oxygen electrocatalyst coated gas diffusion layer (GDL) as the cathode. Figure 6.9b shows typical discharge−charge polarization curves of the rechargeable Zn-air battery. The $MnFe_2O_4/NiCo_2O_4$ hybrid exhibits a discharge−charge voltage gap of 0.80 V at 10 mA cm^{-2} and 1.10 V at 50 mA cm^{-2}, which are significant lower than those of $NiCo_2O_4$ (0.94 V at 10 mA cm^{-2} and 1.28 V at 50 mA cm^{-2}) and commercial Pt/Ru/C catalyst (0.87 at 10 mA cm^{-2} and 1.25 V at 50 mA cm^{-2}). The small voltage gaps between charging and discharging processes on $MnFe_2O_4/NiCo_2O_4$ hybrid suggest an enhanced voltaic efficiency of the $MnFe_2O_4/NiCo_2O_4$ hybrid. More importantly, the hybrid catalyst exhibits excellent durability with stable efficiency in Figure 6.9c. When being repeatedly charged-discharged at a constant current density of 10 mA cm^{-2} (10 min charging, 10 min discharging), no observable degradation was found on the $MnFe_2O_4/NiCo_2O_4$ hybrid after 100 cycles. The voltaic efficiency was found to be 59.7 % at the beginning and experienced a slight increase after 32 h of the operation (60.8%). In contrast, the Pt/Ru/C shows a much inferior stability during the charging-discharging process with the voltaic efficiency decreasing from 56.4 % to 49.7 %, caused by the passivation of Pt at positive potentials pertinent to OER and electrocatalyst detachment. [3a, 22]

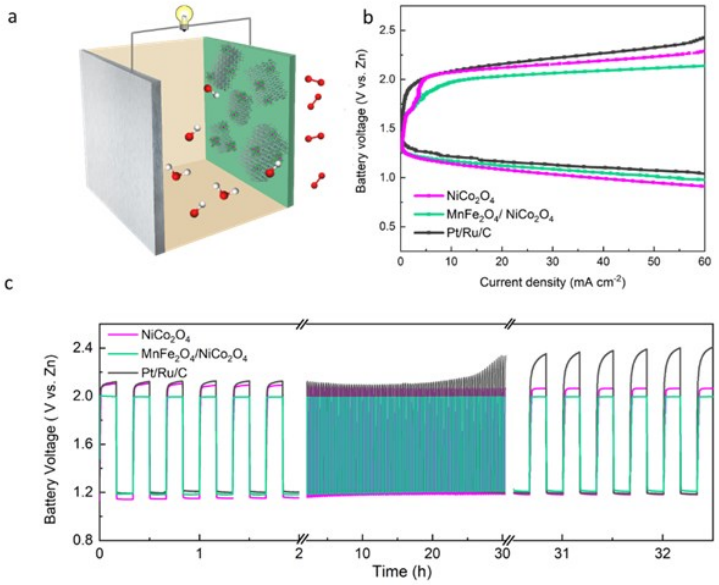

Figure 6.9 (a)The schematic figure of the custom built rechargeable Zn−air batteries. (b) Charge and discharge polarization curves of $NiCo_2O_4$ NSs, $MnFe_2O_4/NiCo_2O_4$, and Pt/Ru/C air electrode. (c) Galvanostatic charge−discharge curves at 10 mA cm^{-2} using $NiCo_2O_4$ NSs, $MnFe_2O_4/NiCo_2O_4$, and Pt/Ru/C air electrode.

6.4. Conclusions

In summary, we reported a desirable approach to preparing an efficient bifunctional oxygen electrocatalyst through synergistically integrating non-precious metal oxide nanoparticles on ultrathin NSs. This inexpensive, earth-abundant hybrid catalyst exhibits superior bifunctional catalytic activity in terms of its lower overall overpotential (ΔE = 0.807 V) than the $MnFe_2O_4$ and $NiCo_2O_4$ electrocatalyst. The fact that the $MnFe_2O_4/NiCo_2O_4$ hybrid outperforms the state-of-the-art precious metals Pt/Ru/C with respect to bifunctional activity and durability makes the discovery in this study more promising. We believe that the large surface area, high chemical stability of $NiCo_2O_4$ NSs and strong chemical coupling effects between $MnFe_2O_4$ NPs and $NiCo_2O_4$ afford the

enhanced bifunctional catalytic activity and durability. This work holds the promise to open a new possibility in designing novel transition metal based bifunctional catalysts as the alternatives to the noble metals for the application in energy related devices.

6.5. References

1. (a) Xue, Y.; Yu, D.; Dai, L.; Wang, R.; Li, D.; Roy, A.; Lu, F.; Chen, H.; Liu, Y.; Qu, J., Three-dimensional B, N-doped graphene foam as a metal-free catalyst for oxygen reduction reaction. *Physical Chemistry Chemical Physics* **2013,** *15* (29), 12220-12226; (b) Wang, X.; Li, Y.; Jin, T.; Meng, J.; Jiao, L.; Zhu, M.; Chen, J., Electrospun Thin-Walled CuCo2O4@ C Nanotubes as Bifunctional Oxygen Electrocatalysts for Rechargeable Zn–Air Batteries. *Nano letters* **2017,** *17* (12), 7989-7994.

2. Liu, X.; Park, M.; Kim, M. G.; Gupta, S.; Wu, G.; Cho, J., Integrating NiCo alloys with their oxides as efficient bifunctional cathode catalysts for rechargeable zinc–air batteries. *Angewandte Chemie International Edition* **2015,** *54* (33), 9654-9658.

3. (a) Zhang, J.; Zhao, Z.; Xia, Z.; Dai, L., A metal-free bifunctional electrocatalyst for oxygen reduction and oxygen evolution reactions. *Nature nanotechnology* **2015,** *10* (5), 444; (b) Amiinu, I. S.; Liu, X.; Pu, Z.; Li, W.; Li, Q.; Zhang, J.; Tang, H.; Zhang, H.; Mu, S., From 3D ZIF Nanocrystals to Co–Nx/C Nanorod Array Electrocatalysts for ORR, OER, and Zn–Air Batteries. *Advanced Functional Materials* **2017**; (c) Xiong, M.; Ivey, D. G., Electrodeposited Co-Fe as an oxygen evolution catalyst for rechargeable zinc-air batteries. *Electrochemistry Communications* **2017,** *75*, 73-77.

4. (a) Wang, H.-W.; Hu, Z.-A.; Chang, Y.-Q.; Chen, Y.-L.; Wu, H.-Y.; Zhang, Z.-Y.; Yang, Y.-Y., Design and synthesis of NiCo 2 O 4–reduced graphene oxide composites for high performance supercapacitors. *Journal of Materials Chemistry* **2011,** *21* (28), 10504-10511; (b) Bao, J.; Zhang, X.; Fan, B.; Zhang, J.; Zhou, M.; Yang, W.; Hu, X.; Wang, H.; Pan, B.; Xie, Y., Ultrathin Spinel-Structured Nanosheets Rich in Oxygen Deficiencies for Enhanced Electrocatalytic Water Oxidation. *Angewandte Chemie* **2015,** *127* (25), 7507-7512; (c) Yang, J.;

Yu, C.; Liang, S.; Li, S.; Huang, H.; Han, X.; Zhao, C.; Song, X.; Hao, C.; Ajayan, P. M., Bridging of ultrathin NiCo2O4 nanosheets and graphene with polyaniline: A theoretical and experimental study. *Chemistry of Materials* **2016,** *28* (16), 5855-5863.

5. (a) Zhang, G.; Xia, B. Y.; Wang, X., Strongly Coupled NiCo2O4-rGO Hybrid Nanosheets as a Methanol-Tolerant Electrocatalyst for the Oxygen Reduction Reaction. *Advanced Materials* **2014,** *26* (15), 2408-2412; (b) Moni, P.; Hyun, S.; Vignesh, A.; Shanmugam, S., Chrysanthemum flower like NiCo 2 O 4-nitrogen doped graphene oxide composite: An efficient electrocatalyst for Lithium-oxygen and Zinc-air batteries. *Chemical Communications* **2017**.

6. (a) Gao, G.; Wu, H. B.; Lou, X. W. D., Citrate-Assisted Growth of NiCo2O4 Nanosheets on Reduced Graphene Oxide for Highly Reversible Lithium Storage. *Advanced Energy Materials* **2014,** *4* (14); (b) Chen, S.; Qiao, S.-Z., Hierarchically porous nitrogen-doped graphene–NiCo2O4 hybrid paper as an advanced electrocatalytic water-splitting material. *Acs Nano* **2013,** *7* (11), 10190-10196.

7. Zhu, H.; Zhang, S.; Huang, Y.-X.; Wu, L.; Sun, S., Monodisperse M x Fe3–x O4 (M= Fe, Cu, Co, Mn) Nanoparticles and Their Electrocatalysis for Oxygen Reduction Reaction. *Nano letters* **2013,** *13* (6), 2947-2951.

8. Pérez-Mirabet, L.; Solano, E.; Martínez-Julián, F.; Guzmán, R.; Arbiol, J.; Puig, T.; Obradors, X.; Pomar, A.; Yáñez, R.; Ros, J., One-pot synthesis of stable colloidal solutions of MFe 2 O 4 nanoparticles using oleylamine as solvent and stabilizer. *Materials Research Bulletin* **2013,** *48* (3), 966-972.

9. Cozzoli, P. D.; Curri, M. L.; Agostiano, A.; Leo, G.; Lomascolo, M., ZnO nanocrystals by a non-hydrolytic route: synthesis and characterization. *The Journal of Physical Chemistry B* **2003,** *107* (20), 4756-4762.

10. Kim, J.-G.; Pugmire, D.; Battaglia, D.; Langell, M., Analysis of the NiCo 2 O 4 spinel surface with Auger and X-ray photoelectron spectroscopy. *Applied surface science* **2000,** *165* (1), 70-84.

11. Song, W.; Ren, Z.; Chen, S.-Y.; Meng, Y.; Biswas, S.; Nandi, P.; Elsen, H. A.; Gao, P.-X.; Suib, S. L., Ni-and Mn-promoted mesoporous Co3O4: a stable bifunctional catalyst with surface-structure-dependent activity for oxygen reduction reaction and oxygen evolution reaction. *ACS applied materials & interfaces* **2016,** *8* (32), 20802-20813.

12. Wang, H. Y.; Hsu, Y. Y.; Chen, R.; Chan, T. S.; Chen, H. M.; Liu, B., Ni3+-Induced Formation of Active NiOOH on the Spinel Ni–Co Oxide Surface for Efficient Oxygen Evolution Reaction. *Advanced Energy Materials* **2015,** *5* (10).

13. Yu, A.; Chen, Z.; Maric, R.; Zhang, L.; Zhang, J.; Yan, J., Electrochemical supercapacitors for energy storage and delivery: Advanced materials, technologies and applications. *Applied Energy* **2015,** *153*, 1-2.

14. Choi, C. H.; Park, S. H.; Woo, S. I., Oxygen reduction activity of Pd–Mn 3 O 4 nanoparticles and performance enhancement by voltammetrically accelerated degradation. *Physical Chemistry Chemical Physics* **2012,** *14* (19), 6842-6848.

15. Xi, Z.; Erdosy, D. P.; Mendoza-Garcia, A.; Duchesne, P. N.; Li, J.; Muzzio, M.; Li, Q.; Zhang, P.; Sun, S., Pd Nanoparticles Coupled to WO2. 72 Nanorods for Enhanced Electrochemical Oxidation of Formic Acid. *Nano Letters* **2017,** *17* (4), 2727-2731.

16. Doyle, R. L.; Lyons, M. E., The Oxygen Evolution Reaction: Mechanistic Concepts and Catalyst Design. In *Photoelectrochemical Solar Fuel Production*, Springer: 2016; pp 41-104.

17. Ma, T. Y.; Dai, S.; Jaroniec, M.; Qiao, S. Z., Metal–organic framework derived hybrid Co3O4-carbon porous nanowire arrays as reversible oxygen evolution electrodes. *Journal of the American Chemical Society* **2014,** *136* (39), 13925-13931.

18. (a) Aricò, A. S.; Bruce, P.; Scrosati, B.; Tarascon, J.-M.; Van Schalkwijk, W., Nanostructured materials for advanced energy conversion and storage devices. *Nature materials* **2005,** *4* (5), 366-377; (b) Liu, J.; Jiang, J.; Cheng, C.; Li, H.; Zhang, J.; Gong, H.; Fan, H. J., Co3O4 Nanowire@ MnO2 Ultrathin Nanosheet Core/Shell Arrays: A New Class of High-Performance Pseudocapacitive Materials. *Advanced Materials* **2011,** *23* (18), 2076-2081.

19. Hou, Y.; Cui, S.; Wen, Z.; Guo, X.; Feng, X.; Chen, J., Strongly Coupled 3D Hybrids of N-doped Porous Carbon Nanosheet/CoNi Alloy-Encapsulated Carbon Nanotubes for Enhanced Electrocatalysis. *Small* **2015,** *11* (44), 5940-5948.

20. Jung, S.; McCrory, C. C.; Ferrer, I. M.; Peters, J. C.; Jaramillo, T. F., Benchmarking nanoparticulate metal oxide electrocatalysts for the alkaline water oxidation reaction. *Journal of Materials Chemistry A* **2016,** *4* (8), 3068-3076.

21. (a) Merki, D.; Vrubel, H.; Rovelli, L.; Fierro, S.; Hu, X., Fe, Co, and Ni ions promote the catalytic activity of amorphous molybdenum sulfide films for hydrogen evolution. *Chemical Science* **2012,** *3* (8), 2515-2525; (b) Hu, H.; Guan, B.; Xia, B.; Lou, X. W., Designed formation of Co3O4/NiCo2O4 double-shelled nanocages with enhanced pseudocapacitive and electrocatalytic properties. *Journal of the American Chemical Society* **2015,** *137* (16), 5590-5595.

22. Jung, K.-N.; Jung, J.-H.; Im, W. B.; Yoon, S.; Shin, K.-H.; Lee, J.-W., Doped lanthanum nickelates with a layered perovskite structure as bifunctional cathode catalysts for rechargeable metal–air batteries. *ACS applied materials & interfaces* **2013,** *5* (20), 9902-9907.

6.6. Supporting information

6.6.1. Experimental procedure

Synthesis of the catalyst

The synthesis was carried out using commercial available reagent. The $Ni(NO_3)_2{\cdot}6H_2O$ (assay 99%), $Co(NO_3)_2{\cdot}6H_2O$ (assay ≥ 99%), Fe(III) acetylacetonate ($Fe(acac)_3$, assay ≥ 99%) were purchansed from Acros Organics. The Mn(II) acetylacetonate ($Mn(acac)_2$, assay ≥ 97%), p-aminobenzoic acid (PABA, assay ≥ 99%), Oleylamine (assay ≥ 98%), ammonium hydroxide solution (28 wt%), hexane (reagent grade, ≥99%) were ordered from Sigma Aldrich.

Synthesis of $NiCo_2O_4$ ultrathin nanosheets: $NiCo_2O_4$ ultrathin nanosheets were synthesized based on PABA intercalated Co–Ni hydroxides, according to a previous report. The synthesis procedure is briefly described as below: $Co(NO_3)_2{\cdot}6H_2O$ (5 mmol) and $Ni(NO_3)_2{\cdot}6H_2O$ (2.5 mmol) were first dissolved in 100 mL deionized water. p-aminobenzoic acid (6.75 mmol) was dissolved in 75 mL deionized solution with the addition of 5 mL NH_3 solution (28 wt%). The p-aminobenzoic acid solution was added dropwise to the metal nitrate solution under vigorous stirring. The solid product formed at this stage was immediately centrifuged and then dried at 60 °C for 12 h under vacuum. Afterwards, the product was washed with deionized water for several times to achieve a PH of 7. The suspension was sonicated for half an hour in ice bath, washed with ethanol for three times and then dried at 60 °C for 12 h under vacuum. Finally, the as-obtained Co–Ni hydroxides product was treated at 250 °C for 2 h to form $NiCo_2O_4$ ultrathin nanosheets.

Synthesis of $NiCo_2O_4/MnFe_2O_4$ hybrid: $MnFe_2O_4$ NPs were *in situ* grown on the ultrathin $NiCo_2O_4$ nanosheets through an non-hydrolytic thermal decomposition synthetic method. 0.25

mmol $Mn(acac)_2$, 0.50 mmol $Fe(acac)_3$ were added into in a three-necked flask with the addition of 25 ml oelylamine. The solution was heated to 100 °C with magnetic stirring followed by the addition of 60 mg $NiCo_2O_4$. The temperature of the solution was increased to 140 °C and kept at this temperature for 1 h to remove the residual water. Afterwards, the solution was quickly heated up to 250 ºC and refluxed at this temperature for 1.5 h. The $MnFe_2O_4$ NPs were precipitated by addition of ethanol and centrifuging (10000 rpm for 15 min). The as-synthesized product was collected and redispersed into hexane and precipitated out by addition of ethanol and centrifugation to remove all residual impurities. The final product was collected by centrifugation, then washed several times with hexane and ethanol to remove all residual impurities, and finally dried under vacuum at 60 °C.

Synthesis of $MnFe_2O_4$ nanoparticles: The synthetic procedure for free $MnFe_2O_4$ NPs is similar to the procedure for $NiCo_2O_4$ / $MnFe_2O_4$ hybrid, using 0.50 mmol $Mn(acac)_2$, 1.00 mmol $Fe(acac)_3$, while no $NiCo_2O_4$ nanosheets were added during the synthesis.

6.6.2. Preparation of electrodes

The as-synthesized electrocatalysts ($NiCo_2O_4$ nanosheets, $MnFe_2O_4$ NPs, and $NiCo_2O_4$ / $MnFe_2O_4$ hybrid) were mixed with carbon black (Cabot) with a mass ratio of 6:4, 5 mL hexane and 5 mL acetone were added into the mixture. The composite catalysts were centrifuged after sonication. The composite catalysts except $NiCo_2O_4$/C, were further annealed in air at 165 °C for 12 h to remove the surfactant. The IrO_2 and Pt/Ru/C catalyst inks were prepared with IrO_2 powder (Alfa Aesar, 99%), and commercial Pt/Ru/C catalyst (30 wt% Pt, and 15 wt% Ru on carbon black, Alfa Aesar), respectively. The catalyst ink for the RDE test was initially prepared by adding 20 mg of electrocatalysts powders in a solution containing 200 μL of 5wt. % Nafion (Aldrich) and 600 μL

of isopropyl alcohol and 200 μL deionized water. The as-prepared catalyst ink was sonicated for 1 h to obtain full homogenization. 5 μL of the catalysts ink was dispersed on the polished glassy carbon (GC) working electrode (glassy carbon rotating disc electrode, 5 mm in diameter from Pine Research Instrumentation). The Pt/C catalyst ink was prepared with commercial 40 wt% Pt/C (Alfa Aesar) as described in Chapter 4. Catalyst coated GC electrodes were then dried under ambient condition for 1 h.

6.6.3. Rechargeable zinc-air battery assembly and tests

A homemade rechargeable zinc-air battery was constructed, with a zinc plate anode and an electrocatalyst coated GDL cathode. The cell was filled by 6 M KOH and 0.2 M zinc acetate to ensure reversible Zn electrochemical reaction. The catalyst inks for the rechargeable zinc air battery (2 mg mL^{-1}) were prepared by sonicating 10 mg electrocatalysts, 3 mL isopropyl alcohol, 1 mL deionized water and 1 mL of 5wt. % Nafion (Aldrich). The cathode was prepared by drop casting the catalyst inks onto the center area of GDL (7/16" in diameter) followed by drying under ambient condition until a mass loading of 0.5 mg cm^{-2} was achieved. The battery tests were conducted by LSV at 10 mV s^{-1} with Solartron 1287. The galvanostatic discharge-charge cycling curves were measured at a current density of 10mA cm^{-2}, and each cycle was set to be 10 min charge and 10 min discharge.

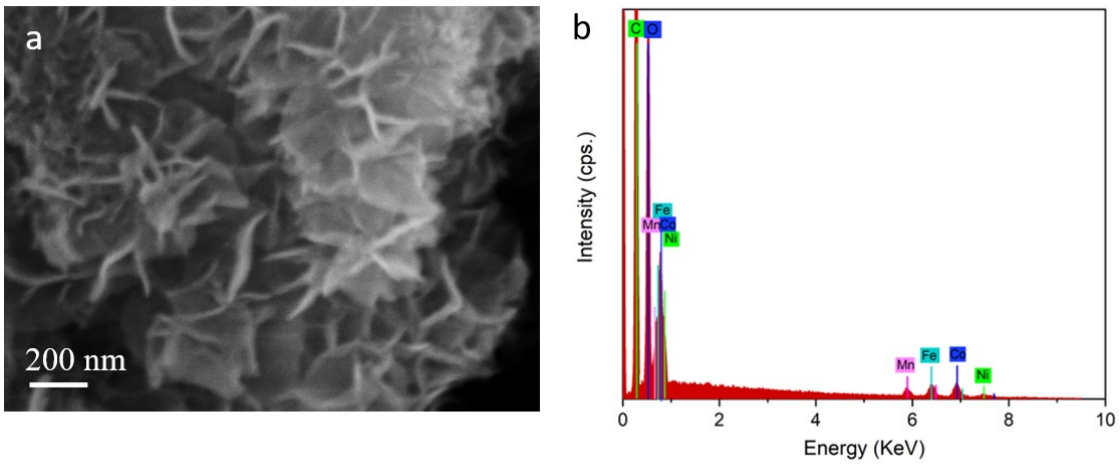

Figure S6. 1 (a) FESEM image of $MnFe_2O_4/NiCo_2O_4$ hybrid. (b) EDX spectrum of $MnFe_2O_4$ / NiCo2O4 hybrid (ICP: Mn : Fe : Ni : Co = 1.00 : 1.91 : 0.93 : 2.19).

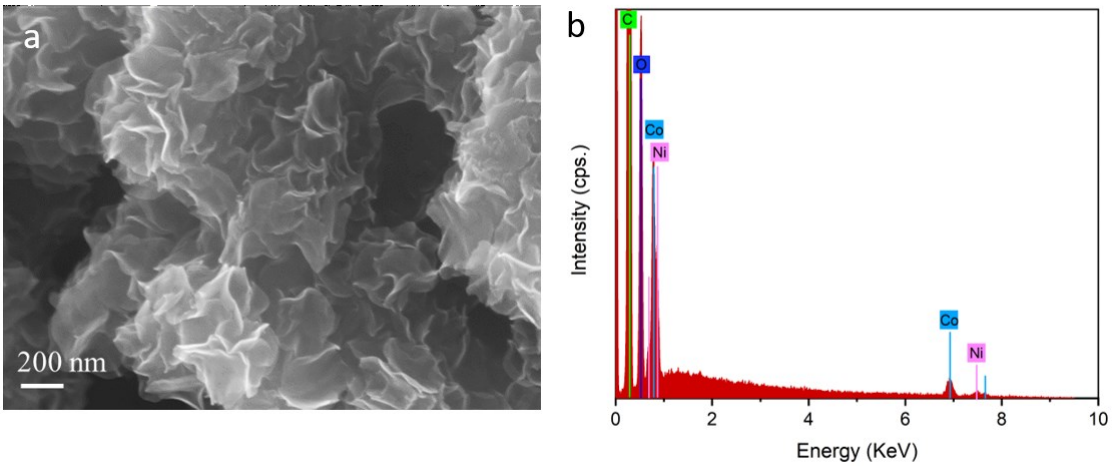

Figure S6. 2 (a) FESEM image of $NiCo_2O_4$ nanosheets. (b) EDX spectrum of $NiCo_2O_4$ NSs.

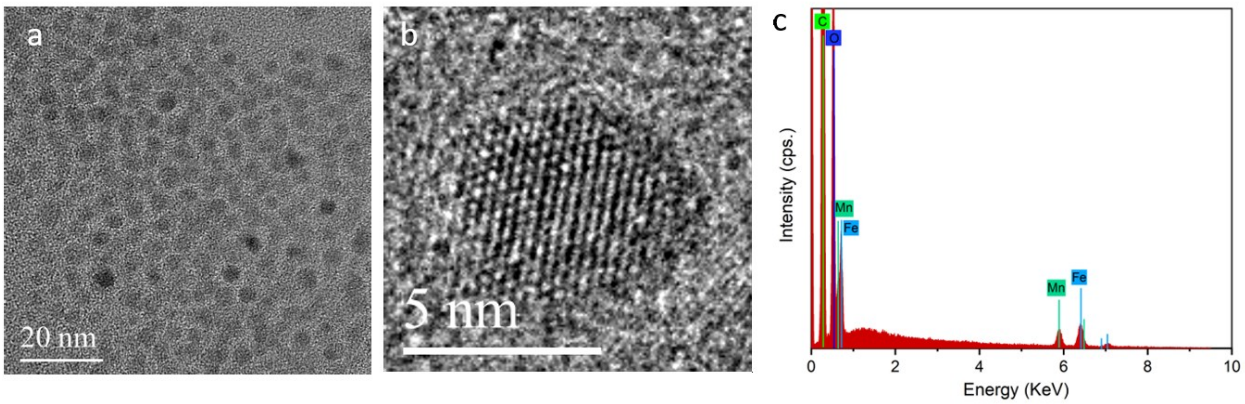

Figure S6. 3 TEM (a) and HR-TEM (b) images of monodispersed $MnFe_2O_4$ NPs. (c) EDX spectrum of $MnFe_2O_4$ NPs.

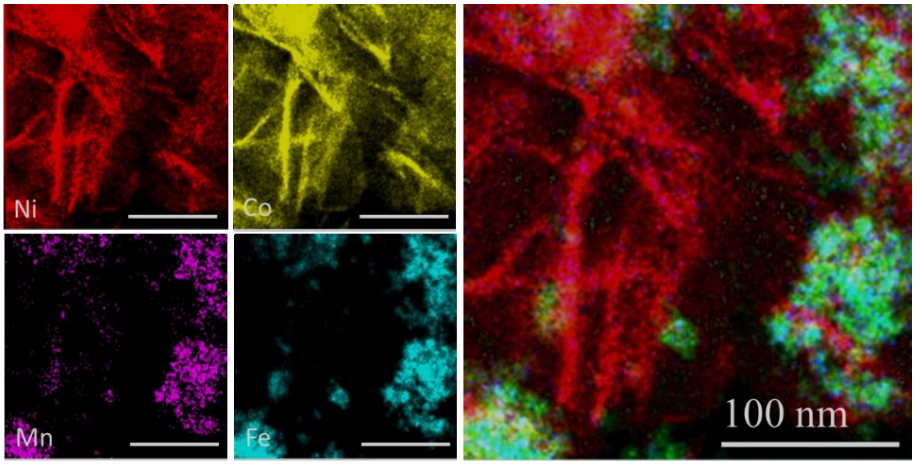

Figure S6. 4 EDX mapping of $MnFe_2O_4$ + $NiCo_2O_4$ physical mixing composite (showing the $MnFe_2O_4$ NPs is more likely to aggregate with each others).

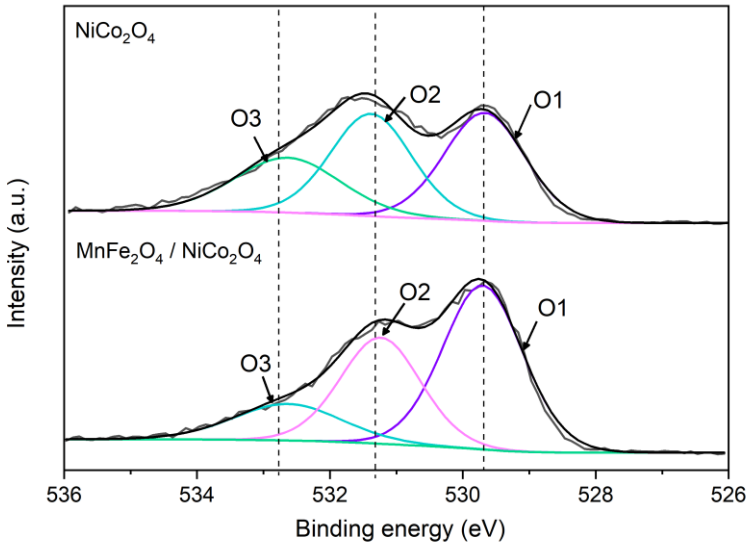

Figure S6. 5 The O 1s spectra of $NiCo_2O_4$ NSs and $MnFe_2O_4/NiCo_2O_4$ hybrid and its simulations. The peak at a binding energy of 530.8, 531.3 and 532.8 eV correspond to the typical metal oxygen bond (M–O–M), surface hydroxyl groups and C–O groups, respectively.

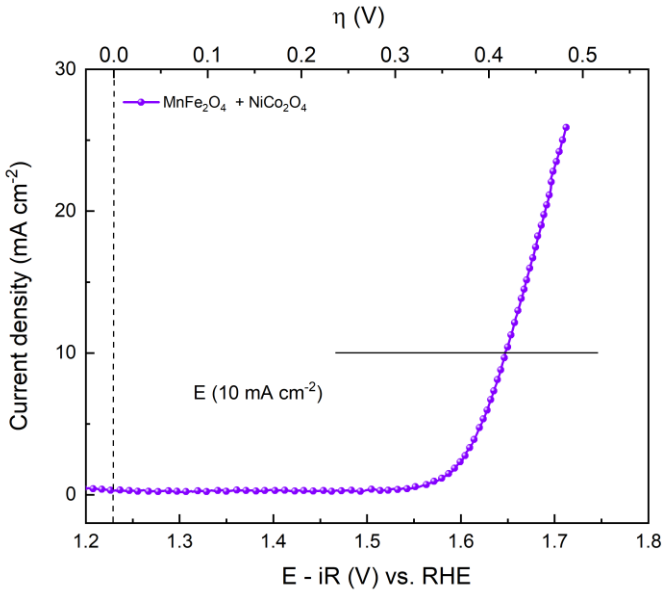

Figure S6. 6 OER LSV curves of $MnFe_2O_4$+$NiCo_2O_4$ physical mixture in 0.1 M KOH at 1600 rpm.

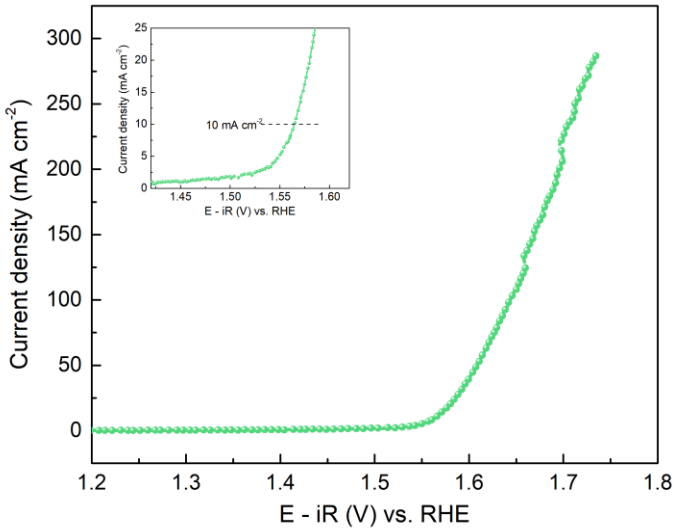

Figure S6. 7 OER LSV curves of $MnFe_2O_4/NiCo_2O_4$ hybrid in 1 M KOH at 1600 rpm.

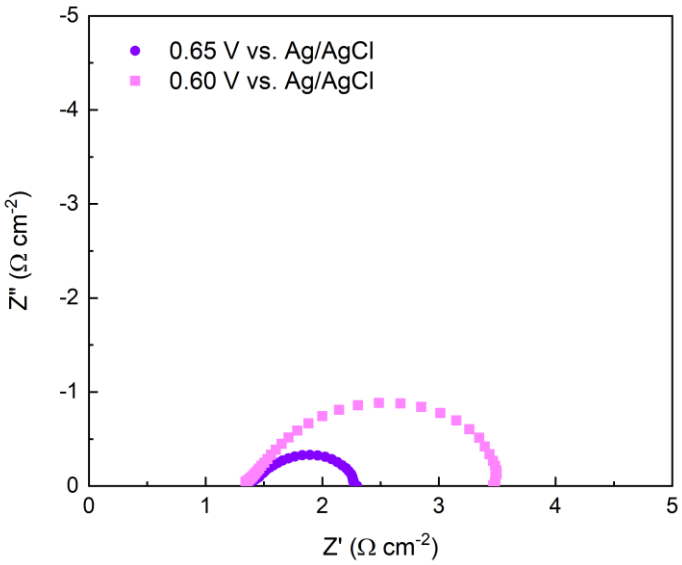

Figure S6. 8 EIS curves of $MnFe_2O_4/NiCo_2O_4$ hybrid in 1 M KOH at different bias potentials.

Table S6.1 The electrocatalytic activities of the recently reported bifunctional catalysts for ORR/OER.

Samples	ORR		OER		Overall overpotential	Reference
	Onset potential (V vs. RHE)	Half-wave potential (V vs. RHE)	Overpotential at 10 mA cm^{-2} (V)	Tafel slope (mV dec^{-1})		
Co_3O_4/N-rmGO	0.88	0.83	0.31	54	0.71	Nat. Mater., 2011, 10, 780-786.
FeNO-CNT-carbon nanofiber films	1.01	0.87	0.43	63	0.79	Chem. Mater., 2017, 4, 1665-1675.
$MnFe_2O_4$ / $NiCo_2O_4$	0.88	0.77	0.34	46.7	0.807	This work
Pomegranate-like Co_3O_4/NPGC	0.97	0.84	0.45		0.84	Angew. Chem. Int. Ed., 2016, 55, 4977-4982.
Flower-like $NiCo_2O_4$/N-rGO	0.87	0.78	0.4		0.85	Chem. Commun., 2017, 53, 7836–7839.
NiO/CoN Porous Nanowires	0.89	0.68	0.30	35	0.85	*ACS Nano,* 2017, 11, 2275–2283
NiCo/porous fibrous carbon aerogels	0.92	0.79	0.4		0.86	Nano Lett., 2016, 16 6516–6522.
O-NiCoFe-LDH	0.80	0.63	0.30	93	0.90	Adv. Energy Mater., 2015, 5, 1500245
$CuCo_2O_4$/N-CNTs	0.97	0.80	0.47	118.8	0.90	Adv. Funct. Mater.2017, 27, 1701833
Layer by layer Co_3O_4/N-rGO	0.90	0.79	0.49	101	0.90	Adv. Mater. 2017, 30, 1703657
$MnCoFeO_4$ / N-rGO	0.91	~0.78	0.48		0.93	J. Mater. Chem. A, 2014, 2, 16217-16223.
Mn_xO_y/N-C	0.85	0.76	0.46	82.6	0.93	Angew. Chem. Int. Ed., 2014, 53, 8508–8512.
3 D hollow-structured $NiCo_2O_4$/C		0.71	0.44	78.7	0.96	ChemCatChem., 2016, 4, 736-742.
Nanoporous carbon fiber films-1000	0.97	0.82	0.61	274	1.02	Adv. Mater., 2016, 28, 3000-3006.
$CoFe_2O_4$/CNTs	0.84	0.66	1.69		1.02	Electrochim. Acta, 2015, 177, 65-72.
Co_3O_4/Co_2MnO_4 nanocomposite	0.90	0.68	0.54		1.09	Nanoscale, 2013, 5, 5312-5315.
$Ba_{0.5}Sr_{0.5}Co_{0.8}Fe_{0.2}O_{3-\delta}$	0.67	~0.61	~ 0.50	129	1.12	Adv. Mater., 2015, 27, 266-271.

Chapter 7. Summary and Future Prospects

7.1 Summary

In this dissertation, I focused on exploring transition metal oxides based electrocatalyst for the application in electrochemical devices. Considerable efforts have been made in optimizing the perovskite and spinel oxides based electrocatalysts in an endeavour to boost their ORR/OER electrocatalytic activities. The proposed strategies, like stoichiometry and phase engineering, architecture design as well as hybrid formation have been proven as the effective ways for advancing the catalytic activity and durability of the electrocatalysts. The as-developed electrocatalysts show a promising potential to serve as an alternative oxygen electrocatalyst to noble metals (Pt, Ru and Ir). Besides enhancing the oxygen electrocatalytic activity, the systematic investigation relating the intrinsic material properties to electrocatalytic performance of transition metal oxides also helps to broaden their application in diverse electrochemical devices, such as HER (Chapter 5), high temperature CO_2 reduction (Appendix I) and SOFCs (Appendix II).

In Chapter 4, Ag decorated perovskite (Ag-$PBMO_5$) was successfully prepared and investigated as an ORR electrocatalyst in alkaline media. The electrocatalytic activity and stability were optimized by constructing a porous nanofibrous structure, ensuring strong intercalation of Ag nanoparticles (NPs) *via in situ* exsolution, and tuning the internal structures to form layered double perovskite. The as-obtained Ag-$PBMO_5$ catalyst exhibits more positive E_{onset} and $E_{1/2}$ in comparison to its counterparts ($Pr_{0.5}Ba_{0.5}MnO_{3-\delta}$, $PBAMO_3$ and $PBMO_5$). The DFT calculation suggests that the O p-band center shifts closely to the Fermi level in Ag-$PBMO_5$, while a charge transfer was found from Ag to Mn sites within the interface. This is expected to enhance the oxygen

exchange kinetics and facilitate O_2 adsorption on Ag site. In addition, it is discovered that the Ag-$PBMO_5$ electrocatalyst demonstrates a much positive onset potential and half-wave potential than the physically mixed Ag + $PBMO_5$ at the same mass loading. This further confirms the advantages of the *in-situ* exsolution. More importantly, the Ag-$PBMO_5$ exhibits competitive ORR activity and superior durability to the state-of-the-art Pt/C in alkaline solution and outperforms most of the transition metal based alternatives up to date. This work was reviewed and published in the Nano Energy.

Inspired by the as-mentioned approach, further investigation was conducted to develop CoP-PBSCF electrocatalysts, and to explore extended functionalities of the perovskite beyond ORR. Chapter 5 describes a facile approach that I developed to prepare CoP-PBSCF as a trifunctional electrocatalyst. An A-site deficient perovskite oxide with controlled nonstoichiometry (A-PBSCF) was initially synthesized through an electrospinning technique. The CoP NPs were formed upon the *in-situ* exsolution and the post phosphatization process, and they were simultaneously pinned on the perovskite surface. The as-synthesized CoP-PBSCF acts as a multifunctional electrocatalyst towards catalyzing three basic electrochemical reactions (ORR/OER/HER) in alkaline environment. Incorporating CoP NPs to the perovskites allows a more favorable H* adsorption, thus affording an extended HER functionality. The CoP-PBSCF demonstrates a half wave potential of 0.752 V in the ORR (0.1 M KOH), and it demonstrates a low overpotential of 340 mV and 240 mV at the operating current density of 10 mA cm^{-2} in OER and HER (1.0 M KOH). The excellent trifunctional electrocatalytic activities enable its wide application in rechargeable Zn-air batteries and water splitting systems. This part of work is to be submitted to Advanced Energy Materials for publication.

In Chapter 6, cooperative spinel nanohybrid was developed as a bifunctional oxygen electrocatalyst (ORR/OER) for Zn-air batteries. The ORR catalytic active $MnFe_2O_4$ nanocrystals have been integrated on $NiCo_2O_4$ ultrathin NSs through a non-hydrolytic thermal decomposition method. The mesoporous ultrathin NS structure of $NiCo_2O_4$ possesses a high specific surface area (131.8 $m^2\ g^{-1}$) and sufficient anchoring sites that allow subsequent growth of sub-10 nm $MnFe_2O_4$ NPs. An increased C_{dl} and a decreased interfacial charge-transfer resistance were found on $MnFe_2O_4/NiCo_2O_4$ in comparison to the $NiCo_2O_4$ NSs, suggesting that heterostructured hybrid realizes efficient bifunctional catalytic activities from the full utilization of the catalyst surface and strong interaction between the $MnFe_2O_4$ NPs and $NiCo_2O_4$ matrix. The $MnFe_2O_4/NiCo_2O_4$ hybrid electrocatalyst exhibits a positive ORR half-wave potential of 0.767 V and an overpotential of 0.344 V at 10 mA cm^{-2} for the OER (0.1 M KOH). The $MnFe_2O_4/NiCo_2O_4$ hybrid exhibits a discharge−charge voltage gap of 0.80 V at 10 mA cm^{-2} and a strong stability in the rechargeable Zn-air batteries, maintaining a voltaic efficiency of 60.8% after 100 cyclic tests. This part of work was reviewed and published in the Applied Catalysis B: Environmental.

Overall, the studies on material properties of the electrocatalyst in this dissertation respond to the challenges of developing efficient and stable oxygen electrocatalysts in alkaline environment and provide practical solutions in this field. The various nanostructures, high specific surface area and sufficient porosity are the main factors to promote the extrinsic catalytic activity of the oxygen electrocatalysis. The electronic configuration, abundant surface defects (anion vacancies, cation vacancies) and cooperative catalytic system are proved to be important factors to manipulate the intrinsic catalytic activities. The design and synthesis strategies proposed in this study hold the promise of advancing transition metal based bifunctional catalysts as the alternatives to the noble metals in energy related electrochemical devices.

7.2 Future prospects

7.2.1. *In situ* exsolution of metal/bimetal at room temperature

The exsolution of B-site metallic nanoparticles (NPs) or alloys from well-defined perovskite parents (ABO_3) has been proved as an effective way to broad material functionality and to enhanced catalytic activity for versatile electrocatalytic reactions in this study. The A- or B-site cations exsolution is a heterogeneous process which is generally associated with the low oxygen partial pressure and high/intermediate temperature environment. However, the simultaneous coarsening of exsolved NPs due to Ostwald ripening cannot be avoided even if their "socketed" structure grants enhanced metal-support interaction. Thereby, developing a facial synthesis method that allows exsolution under mild condition with low expense is of great significance in terms of energy saving, preparation feasibility and better exsolution quality. Further research effort is being made in this direction, i.e., aiming to achieve an *in situ* exsolution of metal/bimetal at room temperature with large population and uniform distributions.

7.2.2. Alternative catalyst supports

Although transition metal oxide based electrocatalyst shows promising oxygen electrocatalytic activity when forming the metal oxide/carbon composite, the pristine transition metal oxide shows limited ORR activity when employed without carbon support. Compared to the metal-based and carbon-based electrocatalysts, the transition metal oxides possess extremely low conductivities at room temperature, which impedes their practical applications in electrochemical devices. The support has been an essential component for transition metal oxide electrodes. However, as mentioned in the Chapter 2.3, carbon matrix generally suffers from electrochemical corrosion at

high polarization potential during OER, which hinders the stability during the long-term operation. To address this issue, alternative supports such as stainless steel, Ni mesh, titanium metal foil etc. with high electrical conductivity, high specific surface area and strong corrosion resistance need to be further explored for the transition metal oxides system.

7.2.3. Advanced characterizations

Advanced characterization is another important aspect that helps to better understand material properties under the electrochemical catalytic conditions. Switching the *ex situ* characterization to an operando visual observation of the ORR/OER helps to directly identify/quantify the electrocatalytic active spices, surface/adsorbates interaction, and/or possible phase transformation under operation conduction. An operando tracking of electrochemical reactions at solid/liquid interfaces can be conducted through high energy *in-situ* XPS. Electrochemical *in situ* liquid TEM provides great opportunities to accurately understand the potential- and time-dependent electrochemistry on bulk/interface of electrocatalysts under the reaction conditions. This technique also helps to identify the degradation mechanism of some transition metal oxides under operational conduction.

Bibliography

1. Edenhofer, O.; Pichs-Madruga, R.; Sokona, Y.; Seyboth, K.; Matschoss, P.; Kadner, S.; Zwickel, T.; Eickemeier, P.; Hansen, G.; Schlömer, S., IPCC special report on renewable energy sources and climate change mitigation. *Prepared By Working Group III of the Intergovernmental Panel on Climate Change, Cambridge University Press, Cambridge, UK* **2011.**

2. Stocker, T. F.; Qin, D.; Plattner, G.; Tignor, M.; Allen, S.; Boschung, J.; Nauels, A.; Xia, Y.; Bex, V.; Midgley, P., Contribution of working group I to the fifth assessment report of the intergovernmental panel on climate change. *Climate change 2013: the physical science basis* **2013**.

3. Choi, N. S.; Chen, Z.; Freunberger, S. A.; Ji, X.; Sun, Y. K.; Amine, K.; Yushin, G.; Nazar, L. F.; Cho, J.; Bruce, P. G., Challenges facing lithium batteries and electrical double-layer capacitors. *Angewandte Chemie International Edition* **2012,** *51* (40), 9994-10024.

4. Tsutsumi., A., Fuel cell/battery system Researchers' keyword commentaries. **2013**.

5. Zhao, Q.; Yan, Z.; Chen, C.; Chen, J., Spinels: controlled preparation, oxygen reduction/evolution reaction application, and beyond. *Chemical reviews* **2017,** *117* (15), 10121-10211.

6. Sawyer, D. T.; Roberts, J. L., *Experimental electrochemistry for chemists*. Wiley: 1974.

7. Hong, W. T.; Risch, M.; Stoerzinger, K. A.; Grimaud, A.; Suntivich, J.; Shao-Horn, Y., Toward the rational design of non-precious transition metal oxides for oxygen electrocatalysis. *Energy & Environmental Science* **2015,** *8* (5), 1404-1427.

8. Wang, Z.-L.; Xu, D.; Xu, J.-J.; Zhang, X.-B., Oxygen electrocatalysts in metal–air batteries: from aqueous to nonaqueous electrolytes. *Chemical Society Reviews* **2014,** *43* (22), 7746-7786.

9. Liang, Y.; Li, Y.; Wang, H.; Zhou, J.; Wang, J.; Regier, T.; Dai, H., Co 3 O 4 nanocrystals on graphene as a synergistic catalyst for oxygen reduction reaction. *Nature materials* **2011,** *10* (10), 780.

10. Holewinski, A.; Idrobo, J.-C.; Linic, S., High-performance Ag–Co alloy catalysts for electrochemical oxygen reduction. *Nature chemistry* **2014,** *6* (9), 828.

11. Goswami, C.; Hazarika, K. K.; Bharali, P., Transition metal oxide nanocatalysts for oxygen reduction reaction. *Materials Science for Energy Technologies* **2018**.

12. Nørskov, J. K.; Rossmeisl, J.; Logadottir, A.; Lindqvist, L.; Kitchin, J. R.; Bligaard, T.; Jonsson, H., Origin of the overpotential for oxygen reduction at a fuel-cell cathode. *The Journal of Physical Chemistry B* **2004,** *108* (46), 17886-17892.

13. Stamenkovic, V.; Mun, B. S.; Mayrhofer, K. J.; Ross, P. N.; Markovic, N. M.; Rossmeisl, J.; Greeley, J.; Nørskov, J. K., Changing the activity of electrocatalysts for oxygen reduction by tuning the surface electronic structure. *Angewandte Chemie* **2006,** *118* (18), 2963-2967.

14. Greeley, J.; Stephens, I.; Bondarenko, A.; Johansson, T. P.; Hansen, H. A.; Jaramillo, T.; Rossmeisl, J.; Chorkendorff, I.; Nørskov, J. K., Alloys of platinum and early transition metals as oxygen reduction electrocatalysts. *Nature chemistry* **2009,** *1* (7), 552.

15. Mazumder, V.; Chi, M.; More, K. L.; Sun, S., Core/shell Pd/FePt nanoparticles as an active and durable catalyst for the oxygen reduction reaction. *Journal of the American Chemical Society* **2010,** *132* (23), 7848-7849.

16. Yu, Y.; Yang, W.; Sun, X.; Zhu, W.; Li, X.-Z.; Sellmyer, D. J.; Sun, S., Monodisperse MPt (M= Fe, Co, Ni, Cu, Zn) nanoparticles prepared from a facile oleylamine reduction of metal salts. *Nano letters* **2014,** *14* (5), 2778-2782.

17. Chung, D. Y.; Jun, S. W.; Yoon, G.; Kwon, S. G.; Shin, D. Y.; Seo, P.; Yoo, J. M.; Shin, H.; Chung, Y.-H.; Kim, H., Highly durable and active PtFe nanocatalyst for electrochemical oxygen reduction reaction. *Journal of the American Chemical Society* **2015,** *137* (49), 15478-15485.

18. Zhang, G.; Shao, Z.-G.; Lu, W.; Li, G.; Liu, F.; Yi, B., One-pot synthesis of Ir@ Pt nanodendrites as highly active bifunctional electrocatalysts for oxygen reduction and oxygen evolution in acidic medium. *Electrochemistry Communications* **2012,** *22*, 145-148.

19. Chen, G.; Delafuente, D. A.; Sarangapani, S.; Mallouk, T. E., Combinatorial discovery of bifunctional oxygen reduction—water oxidation electrocatalysts for regenerative fuel cells. *Catalysis Today* **2001,** *67* (4), 341-355.

20. Zhang, Y.; Wang, C.; Wan, N.; Mao, Z., Deposited RuO2–IrO2/Pt electrocatalyst for the regenerative fuel cell. *International Journal of Hydrogen Energy* **2007,** *32* (3), 400-404.

21. Jung, K.-N.; Jung, J.-H.; Im, W. B.; Yoon, S.; Shin, K.-H.; Lee, J.-W., Doped lanthanum nickelates with a layered perovskite structure as bifunctional cathode catalysts for rechargeable metal–air batteries. *ACS applied materials & interfaces* **2013,** *5* (20), 9902-9907.

22. Dai, L.; Xue, Y.; Qu, L.; Choi, H.-J.; Baek, J.-B., Metal-free catalysts for oxygen reduction reaction. *Chemical reviews* **2015,** *115* (11), 4823-4892.

23. Dai, L., Functionalization of graphene for efficient energy conversion and storage. *Accounts of chemical research* **2012,** *46* (1), 31-42.

24. Xue, Y.; Yu, D.; Dai, L.; Wang, R.; Li, D.; Roy, A.; Lu, F.; Chen, H.; Liu, Y.; Qu, J., Three-dimensional B, N-doped graphene foam as a metal-free catalyst for oxygen reduction reaction. *Physical Chemistry Chemical Physics* **2013,** *15* (29), 12220-12226.

25. Zhang, J.; Zhao, Z.; Xia, Z.; Dai, L., A metal-free bifunctional electrocatalyst for oxygen reduction and oxygen evolution reactions. *Nature nanotechnology* **2015,** *10* (5), 444.

26. Li, Y.; Gong, M.; Liang, Y.; Feng, J.; Kim, J.-E.; Wang, H.; Hong, G.; Zhang, B.; Dai, H., Advanced zinc-air batteries based on high-performance hybrid electrocatalysts. *Nature communications* **2013,** *4*, 1805.

27. Toussaint, G.; Stevens, P.; Akrour, L.; Rouget, R.; Fourgeot, F., Development of a rechargeable zinc-air battery. *ECS Transactions* **2010,** *28* (32), 25-34.

28. Sørensen, O. T., *Nonstoichiometric oxides*. Elsevier: 2012.

29. Chen, D.; Chen, C.; Baiyee, Z. M.; Shao, Z.; Ciucci, F., Nonstoichiometric oxides as low-cost and highly-efficient oxygen reduction/evolution catalysts for low-temperature electrochemical devices. *Chemical reviews* **2015,** *115* (18), 9869-9921.

30. Bockris, J. O. M.; Otagawa, T., The electrocatalysis of oxygen evolution on perovskites. *Journal of the Electrochemical Society* **1984,** *131* (2), 290-302.

31. Kofstad, P., Defects and transport properties of metal oxides. *Oxidation of metals* **1995,** *44* (1-2), 3-27.

32. Du, Z.; Yang, P.; Wang, L.; Lu, Y.; Goodenough, J.; Zhang, J.; Zhang, D., Electrocatalytic performances of LaNi1− xMgxO3 perovskite oxides as bi-functional catalysts for lithium air batteries. *Journal of Power Sources* **2014,** *265*, 91-96.

33. Mefford, J. T.; Hardin, W. G.; Dai, S.; Johnston, K. P.; Stevenson, K. J., Anion charge storage through oxygen intercalation in LaMnO 3 perovskite pseudocapacitor electrodes. *Nature materials* **2014,** *13* (7), 726.

34. Zhang, Y.-Q.; Tao, H.-B.; Liu, J.; Sun, Y.-F.; Chen, J.; Hua, B.; Thundat, T.; Luo, J.-L., A rational design for enhanced oxygen reduction: Strongly coupled silver nanoparticles and engineered perovskite nanofibers. *Nano energy* **2017,** *38*, 392-400.

35. Suntivich, J.; May, K. J.; Gasteiger, H. A.; Goodenough, J. B.; Shao-Horn, Y., A perovskite oxide optimized for oxygen evolution catalysis from molecular orbital principles. *Science* **2011,** *334* (6061), 1383-1385.

36. Suntivich, J.; Gasteiger, H. A.; Yabuuchi, N.; Nakanishi, H.; Goodenough, J. B.; Shao-Horn, Y., Design principles for oxygen-reduction activity on perovskite oxide catalysts for fuel cells and metal–air batteries. *Nature chemistry* **2011,** *3* (7), 546.

37. Rossmeisl, J.; Qu, Z.-W.; Zhu, H.; Kroes, G.-J.; Nørskov, J. K., Electrolysis of water on oxide surfaces. *Journal of Electroanalytical Chemistry* **2007,** *607* (1-2), 83-89.

38. Sengodan, S.; Choi, S.; Jun, A.; Shin, T. H.; Ju, Y.-W.; Jeong, H. Y.; Shin, J.; Irvine, J. T.; Kim, G., Layered oxygen-deficient double perovskite as an efficient and stable anode for direct hydrocarbon solid oxide fuel cells. *Nature materials* **2015,** *14* (2), 205.

39. Huang, Y.-H.; Dass, R. I.; Xing, Z.-L.; Goodenough, J. B., Double perovskites as anode materials for solid-oxide fuel cells. *Science* **2006,** *312* (5771), 254-257.

40. Zhou, Q.; He, T.; Ji, Y., SmBaCo2O5+ x double-perovskite structure cathode material for intermediate-temperature solid-oxide fuel cells. *Journal of Power Sources* **2008,** *185* (2), 754-758.

41. Yoo, S.; Jun, A.; Ju, Y. W.; Odkhuu, D.; Hyodo, J.; Jeong, H. Y.; Park, N.; Shin, J.; Ishihara, T.; Kim, G., Development of double-perovskite compounds as cathode materials for low-temperature solid oxide fuel cells. *Angewandte Chemie* **2014,** *126* (48), 13280-13283.

42. Kim, S.; Jun, A.; Kwon, O.; Kim, J.; Yoo, S.; Jeong, H. Y.; Shin, J.; Kim, G., Nanostructured double perovskite cathode with low sintering temperature for intermediate temperature solid oxide fuel cells. *ChemSusChem* **2015,** *8* (18), 3153-3158.

43. Kim, G.; Wang, S.; Jacobson, A.; Reimus, L.; Brodersen, P.; Mims, C., Rapid oxygen ion diffusion and surface exchange kinetics in PrBaCo 2 O 5+ x with a perovskite related structure and ordered A cations. *Journal of Materials Chemistry* **2007,** *17* (24), 2500-2505.

44. Frontera, C.; Garcia-Munoz, J.; Llobet, A.; Aranda, M. A. G., Selective spin-state switch and metal-insulator transition in GdBaCo 2 O 5.5. *Physical Review B* **2002,** *65* (18), 180405. 45.

45. Grimaud, A.; May, K. J.; Carlton, C. E.; Lee, Y.-L.; Risch, M.; Hong, W. T.; Zhou, J.; Shao-Horn, Y., Double perovskites as a family of highly active catalysts for oxygen evolution in alkaline solution. *Nature communications* **2013,** *4*, 2439.

46. Fabbri, E.; Mohamed, R.; Levecque, P.; Conrad, O.; Kötz, R.; Schmidt, T. J., Ba0. 5Sr0. 5Co0. 8Fe0. 2O3-δ Perovskite Activity towards the Oxygen Reduction Reaction in Alkaline Media. *ChemElectroChem* **2014,** *1* (2), 338-342.

47. Davari, E.; Ivey, D. G., Synthesis and electrochemical performance of manganese nitride as an oxygen reduction and oxygen evolution catalyst for zinc–air secondary batteries. *Journal of Applied Electrochemistry* **2017,** *47* (7), 815-827.

48. Davari, E.; Johnson, A. D.; Mittal, A.; Xiong, M.; Ivey, D. G., Manganese-cobalt mixed oxide film as a bifunctional catalyst for rechargeable zinc-air batteries. *Electrochimica Acta* **2016,** *211*, 735-743.

49. Hua, B.; Li, M.; Sun, Y.-F.; Zhang, Y.-Q.; Yan, N.; Chen, J.; Thundat, T.; Li, J.; Luo, J.-L., A coupling for success: Controlled growth of Co/CoOx nanoshoots on perovskite mesoporous

nanofibres as high-performance trifunctional electrocatalysts in alkaline condition. *Nano Energy* **2017,** *32*, 247-254.

50. Wu, Z.; Sun, L.-P.; Xia, T.; Huo, L.-H.; Zhao, H.; Rougier, A.; Grenier, J.-C., Effect of Sr doping on the electrochemical properties of bi-functional oxygen electrode PrBa1− xSrxCo2O5+ δ. *Journal of Power Sources* **2016,** *334*, 86-93.

51. Lu, F.; Sui, J.; Su, J.; Jin, C.; Shen, M.; Yang, R., Hollow spherical La0. 8Sr0. 2MnO3 perovskite oxide with enhanced catalytic activities for the oxygen reduction reaction. *Journal of Power Sources* **2014,** *271*, 55-59.

52. Lee, D. U.; Park, H. W.; Park, M. G.; Ismayilov, V.; Chen, Z., Synergistic bifunctional catalyst design based on perovskite oxide nanoparticles and intertwined carbon nanotubes for rechargeable zinc–air battery applications. *ACS applied materials & interfaces* **2014,** *7* (1), 902-910.

53. Lee, D. U.; Park, M. G.; Park, H. W.; Seo, M. H.; Ismayilov, V.; Ahmed, R.; Chen, Z., Highly active Co-doped LaMnO3 perovskite oxide and N-doped carbon nanotube hybrid bi-functional catalyst for rechargeable zinc–air batteries. *Electrochemistry Communications* **2015,** *60*, 38-41.

54. Hua, B.; Li, M.; Zhang, Y. Q.; Sun, Y. F.; Luo, J. L., All-In-One Perovskite Catalyst: Smart Controls of Architecture and Composition toward Enhanced Oxygen/Hydrogen Evolution Reactions. *Advanced Energy Materials* **2017,** *7* (20), 1700666.

55. Park, H. W.; Lee, D. U.; Zamani, P.; Seo, M. H.; Nazar, L. F.; Chen, Z., Electrospun porous nanorod perovskite oxide/nitrogen-doped graphene composite as a bi-functional catalyst for metal air batteries. *Nano Energy* **2014,** *10*, 192-200.

56. Molina-García, M. A.; Rees, N. V., Dual-doped graphene/perovskite bifunctional catalysts and the oxygen reduction reaction. *Electrochemistry Communications* **2017,** *84*, 65-70.

57. Lee, D. G.; Gwon, O.; Park, H. S.; Kim, S. H.; Yang, J.; Kwak, S. K.; Kim, G.; Song, H. K., Conductivity-Dependent Completion of Oxygen Reduction on Oxide Catalysts. *Angewandte Chemie* **2015,** *127* (52), 15956-15959.

58. Wu, H.; Zhu, X., Perovskite Oxide Nanocrystals—Synthesis, Characterization, Functionalization, and Novel Applications. In *Perovskite Materials-Synthesis, Characterisation, Properties, and Applications*, InTech: 2016.

59. Xu, J.-J.; Wang, Z.-L.; Xu, D.; Meng, F.-Z.; Zhang, X.-B., 3D ordered macroporous LaFeO 3 as efficient electrocatalyst for Li–O 2 batteries with enhanced rate capability and cyclic performance. *Energy & environmental science* **2014,** *7* (7), 2213-2219.

60. Yang, F.; Deng, D.; Pan, X.; Fu, Q.; Bao, X., Understanding nano effects in catalysis. *National Science Review* **2015,** *2* (2), 183-201.

61. Wei, S.-H., Electronic Structure and Stability of Spinel Oxides. *Japanese Journal of Applied Physics* **2000,** *39* (S1), 251.

62. Elaheh, D., Bifunctional Electrocatalysts For Rechargeable Zinc-air Batteries. **2017**.

63. Zhao, Q.; Yan, Z.; Chen, C.; Chen, J., Spinels: controlled preparation, oxygen reduction/evolution reaction application, and beyond. *Chemical reviews* **2017,** *117* (15), 10121-10211.

64. Ryu, W.-H.; Yoon, T.-H.; Song, S. H.; Jeon, S.; Park, Y.-J.; Kim, I.-D., Bifunctional composite catalysts using Co3O4 nanofibers immobilized on nonoxidized graphene nanoflakes for high-capacity and long-cycle Li–O2 batteries. *Nano letters* **2013,** *13* (9), 4190-4197.

65. Hamdani, M.; Singh, R.; Chartier, P., Co3O4 and Co-based spinel oxides bifunctional oxygen electrodes. *Int. J. Electrochem. Sci* **2010,** *5* (4), 556-577.

66. Zhang, L.; Zhang, S.; Zhang, K.; Xu, G.; He, X.; Dong, S.; Liu, Z.; Huang, C.; Gu, L.; Cui, G., Mesoporous NiCo 2 O 4 nanoflakes as electrocatalysts for rechargeable Li–O 2 batteries. *Chemical communications* **2013,** *49* (34), 3540-3542.

67. Ge, X.; Liu, Y.; Goh, F. T.; Hor, T. A.; Zong, Y.; Xiao, P.; Zhang, Z.; Lim, S. H.; Li, B.; Wang, X., Dual-phase spinel MnCo2O4 and spinel MnCo2O4/nanocarbon hybrids for electrocatalytic oxygen reduction and evolution. *ACS applied materials & interfaces* **2014,** *6* (15), 12684-12691. 66.

68. Wei, C.; Feng, Z.; Scherer, G. G.; Barber, J.; Shao-Horn, Y.; Xu, Z. J., Cations in Octahedral Sites: A Descriptor for Oxygen Electrocatalysis on Transition-Metal Spinels. *Advanced Materials* **2017,** *29* (23), 1606800.

69. Dai, L.; Liu, M.; Song, Y.; Liu, J.; Wang, F., Mn3O4-decorated Co3O4 nanoparticles supported on graphene oxide: Dual electrocatalyst system for oxygen reduction reaction in alkaline medium. *Nano Energy* **2016,** *27*, 185-195.

70. Feng, J.; Liang, Y.; Wang, H.; Li, Y.; Zhang, B.; Zhou, J.; Wang, J.; Regier, T.; Dai, H., Engineering manganese oxide/nanocarbon hybrid materials for oxygen reduction electrocatalysis. *nano research* **2012,** *5* (10), 718-725;

71. Liu, Y.; Li, J.; Li, W.; Li, Y.; Chen, Q.; Zhan, F., Nitrogen-doped graphene aerogel-supported spinel CoMn2O4 nanoparticles as an efficient catalyst for oxygen reduction reaction. *Journal of Power Sources* **2015,** *299*, 492-500.

72. Wu, Z.-S.; Yang, S.; Sun, Y.; Parvez, K.; Feng, X.; Müllen, K., 3D nitrogen-doped graphene aerogel-supported Fe3O4 nanoparticles as efficient electrocatalysts for the oxygen reduction reaction. *Journal of the American Chemical Society* **2012,** *134* (22), 9082-9085.

73. Indra, A.; Menezes, P. W.; Sahraie, N. R.; Bergmann, A.; Das, C.; Tallarida, M.; Schmeißer, D.; Strasser, P.; Driess, M., Unification of catalytic water oxidation and oxygen reduction reactions: amorphous beat crystalline cobalt iron oxides. *Journal of the American chemical society* **2014,** *136* (50), 17530-17536.

74. Lee, J. S.; Nam, G.; Sun, J.; Higashi, S.; Lee, H. W.; Lee, S.; Chen, W.; Cui, Y.; Cho, J., Composites of a Prussian Blue Analogue and Gelatin-Derived Nitrogen-Doped Carbon-Supported Porous Spinel Oxides as Electrocatalysts for a Zn–Air Battery. *Advanced Energy Materials* **2016,** *6* (22), 1601052.

75. Lee, D. U.; Choi, J. Y.; Feng, K.; Park, H. W.; Chen, Z., Advanced Extremely Durable 3D Bifunctional Air Electrodes for Rechargeable Zinc-Air Batteries. *Advanced Energy Materials* **2014,** *4* (6), 1301389.

76. Bard, A. J.; Faulkner, L. R.; Leddy, J.; Zoski, C. G., *Electrochemical methods: fundamentals and applications*. wiley New York: 1980; Vol. 2.

77. Hong, W. T.; Risch, M.; Stoerzinger, K. A.; Grimaud, A.; Suntivich, J.; Shao-Horn, Y., Toward the rational design of non-precious transition metal oxides for oxygen electrocatalysis. *Energy & Environmental Science* **2015,** *8* (5), 1404-1427.

78. Liang, Y.; Li, Y.; Wang, H.; Zhou, J.; Wang, J.; Regier, T.; Dai, H., Co3O4 nanocrystals on graphene as a synergistic catalyst for oxygen reduction reaction. *Nature materials* **2011,** *10* (10), 780-786.

79. Whitesides, G. M.; Crabtree, G. W., Don't forget long-term fundamental research in energy. *science* **2007,** *315* (5813), 796-798.

80. Cao, L.; Lv, F.; Liu, Y.; Wang, W.; Huo, Y.; Fu, X.; Sun, R.; Lu, Z., A high performance O 2 selective membrane based on CAU-1-NH 2@ polydopamine and the PMMA polymer for Li–air batteries. *Chemical Communications* **2015,** *51* (21), 4364-4367.

81. Holewinski, A.; Idrobo, J.-C.; Linic, S., High-performance Ag–Co alloy catalysts for electrochemical oxygen reduction. *Nature chemistry* **2014,** *6* (9), 828.

82. Sofer, Z. k.; Jankovský, O. e.; Šimek, P.; Klímová, K. i.; Macková, A.; Pumera, M., Uranium-and thorium-doped graphene for efficient oxygen and hydrogen peroxide reduction. *ACS nano* **2014,** *8* (7), 7106-7114.

83. Lai, L.; Potts, J. R.; Zhan, D.; Wang, L.; Poh, C. K.; Tang, C.; Gong, H.; Shen, Z.; Lin, J.; Ruoff, R. S., Exploration of the active center structure of nitrogen-doped graphene-based catalysts for oxygen reduction reaction. *Energy & Environmental Science* **2012,** *5* (7), 7936-7942.

84. Yang, Z.; Yao, Z.; Li, G.; Fang, G.; Nie, H.; Liu, Z.; Zhou, X.; Chen, X. a.; Huang, S., Sulfur-doped graphene as an efficient metal-free cathode catalyst for oxygen reduction. *ACS nano* **2011,** *6* (1), 205-211.

85. Jung, J. I.; Jeong, H. Y.; Lee, J. S.; Kim, M. G.; Cho, J., A bifunctional perovskite catalyst for oxygen reduction and evolution. *Angewandte Chemie International Edition* **2014,** *53* (18), 4582-4586.

86. Liu, Y.; Cao, L.-J.; Cao, C.-W.; Wang, M.; Leung, K.-L.; Zeng, S.-S.; Hung, T.; Chung, C.; Lu, Z.-G., Facile synthesis of spinel CuCo 2 O 4 nanocrystals as high-performance cathode catalysts for rechargeable Li–air batteries. *Chemical Communications* **2014,** *50* (93), 14635-14638.

87. Tan, S. M.; Chua, C. K.; Sedmidubský, D.; Sofer, Z.; Pumera, M., Electrochemistry of layered GaSe and GeS: applications to ORR, OER and HER. *Physical Chemistry Chemical Physics* **2016,** *18* (3), 1699-1711.

88. Wu, G.; Cui, G.; Li, D.; Shen, P.-K.; Li, N., Carbon-supported Co1. 67Te2 nanoparticles as electrocatalysts for oxygen reduction reaction in alkaline electrolyte. *Journal of Materials Chemistry* **2009,** *19* (36), 6581-6589.

89. Lin, L.; Zhu, Q.; Xu, A.-W., Noble-metal-free Fe–N/C catalyst for highly efficient oxygen reduction reaction under both alkaline and acidic conditions. *Journal of the American Chemical Society* **2014,** *136* (31), 11027-11033.

90. Jiang, W.-J.; Gu, L.; Li, L.; Zhang, Y.; Zhang, X.; Zhang, L.-J.; Wang, J.-Q.; Hu, J.-S.; Wei, Z.; Wan, L.-J., Understanding the High Activity of Fe–N–C Electrocatalysts in Oxygen Reduction: Fe/Fe3C Nanoparticles Boost the Activity of Fe–N x. *Journal of the American Chemical Society* **2016,** *138* (10), 3570-3578.

91. Suntivich, J.; Gasteiger, H. A.; Yabuuchi, N.; Nakanishi, H.; Goodenough, J. B.; Shao-Horn, Y., Design principles for oxygen-reduction activity on perovskite oxide catalysts for fuel cells and metal–air batteries. *Nature chemistry* **2011,** *3* (7), 546.

92. Hong, W. T.; Risch, M.; Stoerzinger, K. A.; Grimaud, A.; Suntivich, J.; Shao-Horn, Y., Toward the rational design of non-precious transition metal oxides for oxygen electrocatalysis. *Energy & Environmental Science* **2015,** *8* (5), 1404-1427.

93. Jung, J. I.; Jeong, H. Y.; Kim, M. G.; Nam, G.; Park, J.; Cho, J., Fabrication of Ba0. 5Sr0. 5Co0. 8Fe0. 2O3–δ Catalysts with Enhanced Electrochemical Performance by Removing an Inherent Heterogeneous Surface Film Layer. *Advanced Materials* **2015,** *27* (2), 266-271.

94. Xu, X.; Su, C.; Zhou, W.; Zhu, Y.; Chen, Y.; Shao, Z., Co-doping Strategy for Developing Perovskite Oxides as Highly Efficient Electrocatalysts for Oxygen Evolution Reaction. *Advanced Science* **2016,** *3* (2).

95. Mefford, J. T.; Rong, X.; Abakumov, A. M.; Hardin, W. G.; Dai, S.; Kolpak, A. M.; Johnston, K. P.; Stevenson, K. J., Water electrolysis on La1-xSrxCoO3-[delta] perovskite electrocatalysts. *Nature communications* **2016,** *7*.

96. Chen, D.; Chen, C.; Baiyee, Z. M.; Shao, Z.; Ciucci, F., Nonstoichiometric oxides as low-cost and highly-efficient oxygen reduction/evolution catalysts for low-temperature electrochemical devices. *Chem. Rev* **2015,** *115* (18), 9869-9921.

97. Zhu, Y.; Zhou, W.; Shao, Z., Perovskite/Carbon Composites: Applications in Oxygen Electrocatalysis. *small* **2017**.

98. Zhu, Y.; Zhou, W.; Chen, Y.; Yu, J.; Xu, X.; Su, C.; Tadé, M. O.; Shao, Z., Boosting oxygen reduction reaction activity of palladium by stabilizing its unusual oxidation states in perovskite. *Chemistry of Materials* **2015,** *27* (8), 3048-3054.

99. Park, S.-A.; Lee, E.-K.; Song, H.; Kim, Y.-T., Bifunctional enhancement of oxygen reduction reaction activity on Ag catalysts due to water activation on LaMnO3 supports in alkaline media. *Scientific reports* **2015,** *5*.

100. Serra, J. M.; Buchkremer, H.-P., On the nanostructuring and catalytic promotion of intermediate temperature solid oxide fuel cell (IT-SOFC) cathodes. *Journal of Power Sources* **2007,** *172* (2), 768-774.

101. Zhu, Y.; Zhou, W.; Ran, R.; Chen, Y.; Shao, Z.; Liu, M., Promotion of oxygen reduction by exsolved silver nanoparticles on a perovskite scaffold for low-temperature solid oxide fuel cells. *Nano letters* **2015,** *16* (1), 512-518.

102. Zhao, Y.; Xu, L.; Mai, L.; Han, C.; An, Q.; Xu, X.; Liu, X.; Zhang, Q., Hierarchical mesoporous perovskite La0. 5Sr0. 5CoO2. 91 nanowires with ultrahigh capacity for Li-air batteries. *Proceedings of the National Academy of Sciences* **2012,** *109* (48), 19569-19574.

103. Park, H. W.; Lee, D. U.; Zamani, P.; Seo, M. H.; Nazar, L. F.; Chen, Z., Electrospun porous nanorod perovskite oxide/nitrogen-doped graphene composite as a bi-functional catalyst for metal air batteries. *Nano Energy* **2014,** *10*, 192-200.

104. Xu, J. J.; Xu, D.; Wang, Z. L.; Wang, H. G.; Zhang, L. L.; Zhang, X. B., Synthesis of Perovskite-Based Porous La0. 75Sr0. 25MnO3 Nanotubes as a Highly Efficient Electrocatalyst for Rechargeable Lithium–Oxygen Batteries. *Angewandte Chemie International Edition* **2013,** *52* (14), 3887-3890.

105. Shin, T. H.; Myung, J.-H.; Verbraeken, M.; Kim, G.; Irvine, J. T., Oxygen deficient layered double perovskite as an active cathode for CO2 electrolysis using a solid oxide conductor. *Faraday Discuss.* **2015,** *182*, 227-239.

106. Sengodan, S.; Choi, S.; Jun, A.; Shin, T. H.; Ju, Y.-W.; Jeong, H. Y.; Shin, J.; Irvine, J. T.; Kim, G., Layered oxygen-deficient double perovskite as an efficient and stable anode for direct hydrocarbon solid oxide fuel cells. *Nature materials* **2015,** *14* (2), 205.

107. De la Rosa, J. R.; Hernandez, A.; Rojas, F.; Ledezma, J. J., Sol–gel synthesis and characterization of novel La, Mn and Fe doped zirconia: Catalytic combustion activity of trichloroethylene. *Colloids and Surfaces A: Physicochemical and Engineering Aspects* **2008,** *315* (1), 147-155.

108. Hirano, T.; Purwanto, H.; Watanabe, T.; Akiyama, T., Self-propagating high-temperature synthesis of Sr-doped LaMnO 3 perovskite as oxidation catalyst. *Journal of alloys and compounds* **2007,** *441* (1), 263-266.

109. Zhou, X.; Zhao, Y.; Cao, X.; Xue, Y.; Xu, D.; Jiang, L.; Su, W., Fabrication of polycrystalline lanthanum manganite (LaMnO 3) nanofibers by electrospinning. *Materials Letters* **2008,** *62* (3), 470-472.

110. Romand, M.; Roubin, M.; Deloume, J.-P., X-ray photoelectron emission studies of mixed selenides AgGaSe 2 and Ag 9 GaSe 6. *Journal of solid state chemistry* **1978,** *25* (1), 59-64.

111. Kaushik, V. K., XPS core level spectra and Auger parameters for some silver compounds. *Journal of Electron Spectroscopy and Related Phenomena* **1991,** *56* (3), 273-277.

112. Zhu, Y.; Zhou, W.; Yu, J.; Chen, Y.; Liu, M.; Shao, Z., Enhancing Electrocatalytic Activity of Perovskite Oxides by Tuning Cation Deficiency for Oxygen Reduction and Evolution Reactions. *Chemistry of Materials* **2016,** *28* (6), 1691-1697.

113. Du, Z.; Yang, P.; Wang, L.; Lu, Y.; Goodenough, J.; Zhang, J.; Zhang, D., Electrocatalytic performances of LaNi 1− x Mg x O 3 perovskite oxides as bi-functional catalysts for lithium air batteries. *Journal of Power Sources* **2014,** *265*, 91-96.

114. Stoerzinger, K. A.; Risch, M.; Suntivich, J.; Lü, W.; Zhou, J.; Biegalski, M. D.; Christen, H. M.; Venkatesan, T.; Shao-Horn, Y., Oxygen electrocatalysis on (001)-oriented manganese perovskite films: Mn valency and charge transfer at the nanoscale. *Energy & Environmental Science* **2013,** *6* (5), 1582-1588.

115. Blizanac, B.; Ross, P.; Markovic, N., Oxygen electroreduction on Ag (111): the pH effect. *Electrochimica Acta* **2007,** *52* (6), 2264-2271.

116. Zhang, P.; Sun, F.; Xiang, Z.; Shen, Z.; Yun, J.; Cao, D., ZIF-derived in situ nitrogen-doped porous carbons as efficient metal-free electrocatalysts for oxygen reduction reaction. *Energy & Environmental Science* **2014,** *7* (1), 442-450.

117. Hua, B.; Zhang, Y. Q.; Yan, N.; Li, M.; Sun, Y. F.; Chen, J.; Li, J.; Luo, J. L., The excellence of both worlds: developing effective double perovskite oxide catalyst of oxygen reduction reaction for room and elevated temperature applications. *Advanced Functional Materials* **2016,** *26* (23), 4106-4112.

118. Ye, Y.; Kuai, L.; Geng, B., A template-free route to a Fe 3 O 4–Co 3 O 4 yolk–shell nanostructure as a noble-metal free electrocatalyst for ORR in alkaline media. *Journal of Materials Chemistry* **2012,** *22* (36), 19132-19138.

119. Prabu, M.; Ramakrishnan, P.; Ganesan, P.; Manthiram, A.; Shanmugam, S., LaTi 0.65 Fe 0.35 O 3− δ nanoparticle-decorated nitrogen-doped carbon nanorods as an advanced hierarchical air electrode for rechargeable metal-air batteries. *Nano Energy* **2015,** *15*, 92-103.

120. Lu, F.; Sui, J.; Su, J.; Jin, C.; Shen, M.; Yang, R., Hollow spherical La 0.8 Sr 0.2 MnO 3 perovskite oxide with enhanced catalytic activities for the oxygen reduction reaction. *Journal of Power Sources* **2014,** *271*, 55-59.

121. Mueller, D. N.; Machala, M. L.; Bluhm, H.; Chueh, W. C., Redox activity of surface oxygen anions in oxygen-deficient perovskite oxides during electrochemical reactions. *Nature communications* **2015,** *6*.

122. Gupta, S.; Kellogg, W.; Xu, H.; Liu, X.; Cho, J.; Wu, G., Bifunctional perovskite oxide catalysts for oxygen reduction and evolution in alkaline media. *Chemistry–An Asian Journal* **2016,** *11* (1), 10-21.

123. Hibino, M.; Kimura, T.; Suga, Y.; Kudo, T.; Mizuno, N., Oxygen rocking aqueous batteries utilizing reversible topotactic oxygen insertion/extraction in iron-based perovskite oxides Ca1–xLaxFeO3− δ. *Scientific reports* **2012,** *2*, 601.

124. Lee, Y.-L.; Kleis, J.; Rossmeisl, J.; Shao-Horn, Y.; Morgan, D., Prediction of solid oxide fuel cell cathode activity with first-principles descriptors. *Energy & Environmental Science* **2011,** *4* (10), 3966-3970.

125. Liu, J.; Liu, J.; Song, W.; Wang, F.; Song, Y., The role of electronic interaction in the use of Ag and Mn 3 O 4 hybrid nanocrystals covalently coupled with carbon as advanced oxygen reduction electrocatalysts. *Journal of Materials Chemistry A* **2014,** *2* (41), 17477-17488.

126. Slanac, D. A.; Lie, A.; Paulson, J. A.; Stevenson, K. J.; Johnston, K. P., Bifunctional catalysts for alkaline oxygen reduction reaction via promotion of ligand and ensemble effects at Ag/MnO x nanodomains. *The Journal of Physical Chemistry C* **2012,** *116* (20), 11032-11039.

127. Lima, F.; Zhang, J.; Shao, M.; Sasaki, K.; Vukmirovic, M.; Ticianelli, E.; Adzic, R., Catalytic Activity− d-Band Center Correlation for the O2 Reduction Reaction on Platinum in Alkaline Solutions. *The Journal of Physical Chemistry C* **2007,** *111* (1), 404-410.

128. Nørskov, J. K.; Rossmeisl, J.; Logadottir, A.; Lindqvist, L.; Kitchin, J. R.; Bligaard, T.; Jonsson, H., Origin of the overpotential for oxygen reduction at a fuel-cell cathode. *The Journal of Physical Chemistry B* **2004,** *108* (46), 17886-17892.

129. Slanac, D. A.; Hardin, W. G.; Johnston, K. P.; Stevenson, K. J., Atomic ensemble and electronic effects in Ag-rich AgPd nanoalloy catalysts for oxygen reduction in alkaline media. *Journal of the American Chemical Society* **2012,** *134* (23), 9812-9819.

130. Wei, C.; Feng, Z.; Scherer, G. G.; Barber, J.; Shao-Horn, Y.; Xu, Z. J., Cations in Octahedral Sites: A Descriptor for Oxygen Electrocatalysis on Transition-Metal Spinels. *Advanced Materials* **2017**.

131. F. Cheng; J. Chen. Metal–air batteries: from oxygen reduction electrochemistry to cathode catalysts. *Chemical Society Reviews* **2012,** *41* (6), 2172-2192.

132. B. C. Steele; A. Heinzel. Materials for fuel-cell technologies. In *Materials For Sustainable Energy: A Collection of Peer-Reviewed Research and Review Articles from Nature Publishing Group*; World Scientific: 2011; pp 224-231.

133. J. Wang; W. Cui; Q. Liu; Z. Xing; A. M. Asiri; X. Sun. Recent progress in cobalt-based heterogeneous catalysts for electrochemical water splitting. *Advanced materials* **2016,** *28* (2), 215-230.

134. X. Wang; W. Li; D. Xiong; D. Y. Petrovykh; L. Liu. Bifunctional nickel phosphide nanocatalysts supported on carbon fiber paper for highly efficient and stable overall water splitting. *Advanced Functional Materials* **2016,** *26* (23), 4067-4077.

135. C. Hu; L. Dai. Multifunctional Carbon-Based Metal-Free Electrocatalysts for Simultaneous Oxygen Reduction, Oxygen Evolution, and Hydrogen Evolution. *Advanced Materials* **2017,** *29* (9), 1604942.

136. Y. Jia; L. Zhang; A. Du; G. Gao; J. Chen; X. Yan; C. L. Brown; X. Yao. Defect graphene as a trifunctional catalyst for electrochemical reactions. *Advanced materials* **2016,** *28* (43), 9532-9538.

137. M. Pena; J. Fierro. Chemical structures and performance of perovskite oxides. *Chemical reviews* **2001,** *101* (7), 1981-2018.

138. D. Chen; C. Chen; Z. M. Baiyee; Z. Shao; F. Ciucci. Nonstoichiometric oxides as low-cost and highly-efficient oxygen reduction/evolution catalysts for low-temperature electrochemical devices. *Chemical reviews* **2015,** *115* (18), 9869-9921.

139. J. Suntivich; K. J. May; H. A. Gasteiger; J. B. Goodenough; Y. Shao-Horn. A perovskite oxide optimized for oxygen evolution catalysis from molecular orbital principles. *Science* **2011,** *334* (6061), 1383-1385.

140. J. Suntivich; H. A. Gasteiger; N. Yabuuchi; H. Nakanishi; J. B. Goodenough; Y. Shao-Horn. Design principles for oxygen-reduction activity on perovskite oxide catalysts for fuel cells and metal–air batteries. *Nature chemistry* **2011,** *3* (7), 546.

141. X. Xu; Y. Chen; W. Zhou; Z. Zhu; C. Su; M. Liu; Z. Shao. A perovskite electrocatalyst for efficient hydrogen evolution reaction. *Advanced Materials* **2016,** *28* (30), 6442-6448.

142. Y. Zhu; J. Dai; W. Zhou; Y. Zhong; H. Wang; Z. Shao. Synergistically enhanced hydrogen evolution electrocatalysis by in situ exsolution of metallic nanoparticles on perovskites. *Journal of Materials Chemistry A* **2018**.

143. Y. Zhu; G. Chen; X. Xu; G. Yang; M. Liu; Z. Shao. Enhancing electrocatalytic activity for hydrogen evolution by strongly coupled molybdenum nitride@ nitrogen-doped carbon porous nano-octahedrons. *ACS Catalysis* **2017,** *7* (5), 3540-3547.

144. J. Wang; Y. Gao; D. Chen; J. Liu; Z. Zhang; Z. Shao; F. Ciucci. Water Splitting with an Enhanced Bifunctional Double Perovskite. *ACS catalysis* **2017,** *8* (1), 364-371.

145. B. Hua; M. Li; Y.-F. Sun; Y.-Q. Zhang; N. Yan; J. Chen; T. Thundat; J. Li; J.-L. Luo. A coupling for success: Controlled growth of Co/CoOx nanoshoots on perovskite mesoporous nanofibres as high-performance trifunctional electrocatalysts in alkaline condition. *Nano Energy* **2017,** *32*, 247-254.

146. B. Hua; M. Li; J.-L. Luo. A facile surface chemistry approach to bifunctional excellence for perovskite electrocatalysis. *Nano energy* **2018,** *49*, 117-125.

147. Y.-F. Sun; Y.-L. Yang; J. Chen; M. Li; Y.-Q. Zhang; J.-H. Li; B. Hua; J.-L. Luo. Toward a rational photocatalyst design: a new formation strategy of co-catalyst/semiconductor heterostructures via in situ exsolution. *Chemical Communications* **2018,** *54* (12), 1505-1508.

148. D. Neagu; T.-S. Oh; D. N. Miller; H. Ménard; S. M. Bukhari; S. R. Gamble; R. J. Gorte; J. M. Vohs; J. T. Irvine. Nano-socketed nickel particles with enhanced coking resistance grown in situ by redox exsolution. *Nature communications* **2015,** *6*, 8120.

149. D. Neagu; G. Tsekouras; D. N. Miller; H. Ménard; J. T. Irvine. In situ growth of nanoparticles through control of non-stoichiometry. *Nature chemistry* **2013,** *5* (11), 916.

150. B. Zhao; L. Zhang; D. Zhen; S. Yoo; Y. Ding; D. Chen; Y. Chen; Q. Zhang; B. Doyle; X. Xiong. A tailored double perovskite nanofiber catalyst enables ultrafast oxygen evolution. *Nature communications* **2017,** *8*, 14586.

151. Y. Zhu; W. Zhou; J. Yu; Y. Chen; M. Liu; Z. Shao. Enhancing electrocatalytic activity of perovskite oxides by tuning cation deficiency for oxygen reduction and evolution reactions. *Chemistry of Materials* **2016,** *28* (6), 1691-1697.

152. J. I. Jung; H. Y. Jeong; M. G. Kim; G. Nam; J. Park; J. Cho. Fabrication of Ba0. 5Sr0. 5Co0. 8Fe0. 2O3–δ Catalysts with Enhanced Electrochemical Performance by Removing an Inherent Heterogeneous Surface Film Layer. *Advanced Materials* **2015,** *27* (2), 266-271.

153. J. Yu; Y. Zhong; X. Wu; J. Sunarso; M. Ni; W. Zhou; Z. Shao. Bifunctionality from Synergy: CoP Nanoparticles Embedded in Amorphous CoOx Nanoplates with Heterostructures for Highly Efficient Water Electrolysis. *Advanced Science* **2018**, 1800514.

154. F. Yang; Y. Chen; G. Cheng; S. Chen; W. Luo. Ultrathin nitrogen-doped carbon coated with CoP for efficient hydrogen evolution. *ACS Catalysis* **2017,** *7* (6), 3824-3831.

155. L. Zheng; W. Hu; X. Shu; H. Zheng; X. Fang. Ultrafine CoPx Nanoparticles Anchored on Nitrogen Doped Reduced Graphene Oxides for Superior Hydrogenation in Alkaline Media. *Advanced Materials Interfaces* **2018**, 1800515.

156. N. Danilovic; R. Subbaraman; D. Strmcnik; K. C. Chang; A. Paulikas; V. Stamenkovic; N. M. Markovic. Enhancing the alkaline hydrogen evolution reaction activity through the bifunctionality of Ni (OH) 2/metal catalysts. *Angewandte Chemie* **2012,** *124* (50), 12663-12666.

157. W. Sheng; H. A. Gasteiger; Y. Shao-Horn. Hydrogen oxidation and evolution reaction kinetics on platinum: acid vs alkaline electrolytes. *Journal of The Electrochemical Society* **2010,** *157* (11), B1529-B1536.

158. T. Devic; C. Serre. High valence 3p and transition metal based MOFs. *Chemical Society Reviews* **2014,** *43* (16), 6097-6115.

159. D. N. Mueller; M. L. Machala; H. Bluhm; W. C. Chueh. Redox activity of surface oxygen anions in oxygen-deficient perovskite oxides during electrochemical reactions. *Nature communications* **2015,** *6*, 6097.

160. D. N. Mueller; R. A. De Souza; J. Brendt; D. Samuelis; M. Martin. Oxidation states of the transition metal cations in the highly nonstoichiometric perovskite-type oxide Ba 0.1 Sr 0.9 Co 0.8 Fe 0.2 O 3− δ. *Journal of Materials Chemistry* **2009,** *19* (14), 1960-1963.

161. J. Suntivich; W. T. Hong; Y.-L. Lee; J. M. Rondinelli; W. Yang; J. B. Goodenough; B. Dabrowski; J. W. Freeland; Y. Shao-Horn. Estimating hybridization of transition metal and oxygen states in perovskites from Ok-edge x-ray absorption spectroscopy. *The Journal of Physical Chemistry C* **2014,** *118* (4), 1856-1863.

162. C.-C. Hou; S. Cao; W.-F. Fu; Y. Chen. Ultrafine CoP nanoparticles supported on carbon nanotubes as highly active electrocatalyst for both oxygen and hydrogen evolution in basic media. *ACS applied materials & interfaces* **2015,** *7* (51), 28412-28419.

163. Kresse, G.; Hafner, J. Ab Initio Molecular Dynamics for Liquid Metals. *Phys. Rev. B* **1993**, *47*, 558–561.

164. Kresse, G.; Hafner, J. Ab Initio Molecular-Dynamics Simulation of the Liquid-Metal–amorphous-Semiconductor Transition in Germanium. *Phys. Rev. B* **1994**, *49*, 14251–14269.

165. Kresse, G.; Furthmüller, J. Efficiency of Ab-Initio Total Energy Calculations for Metals

and Semiconductors Using a Plane-Wave Basis Set. *Comput. Mater. Sci.* **1996**, *6*, 15–50.

166. Kresse, G.; Furthmüller, J. Efficient Iterative Schemes for Ab Initio Total-Energy Calculations Using a Plane-Wave Basis Set. *Phys. Rev. B* **1996**, *54*, 11169–11186.

167. Blöchl, P. E. Projector Augmented-Wave Method. *Phys. Rev. B* **1994**, *50*, 17953–17979.

168. Kresse, G. From Ultrasoft Pseudopotentials to the Projector Augmented-Wave Method. *Phys. Rev. B* **1999**, *59*, 1758–1775.

169. Hammer, B.; Hansen, L. B.; Nørskov, J. K. Improved Adsorption Energetics within Density-Functional Theory Using Revised Perdew-Burke-Ernzerhof Functionals. *Phys. Rev. B* **1999**, *59*, 7413–7421.

170. Monkhorst, H. J.; Pack, J. D. Special Points for Brillouin-Zone Integrations. *Phys. Rev. B* **1976**, *13*, 5188–5192.

171. Choi, S.; Yoo, S.; Kim, J.; Park, S.; Jun, A.; Sengodan, S.; Kim, J.; Shin, J.; Jeong, H. Y.; Choi, Y.; et al. Highly Efficient and Robust Cathode Materials for Low-Temperature Solid Oxide Fuel Cells: PrBa0.5Sr0.5Co2−xFe x O5+δ. *Sci. Rep.* **2013**, *3*, 2426.

172. Zhao, B.; Zhang, L.; Zhen, D.; Yoo, S.; Ding, Y.; Chen, D.; Chen, Y.; Zhang, Q.; Doyle, B.; Xiong, X.; et al. A Tailored Double Perovskite Nanofiber Catalyst Enables Ultrafast Oxygen Evolution. *Nat. Commun.* **2017**, *8*, 1–9.

173. Grimaud, A.; May, K. J.; Carlton, C. E.; Lee, Y.-L.; Risch, M.; Hong, W. T.; Zhou, J.; Shao-Horn, Y. Double Perovskites as a Family of Highly Active Catalysts for Oxygen Evolution in Alkaline Solution. *Nat. Commun.* **2013**, *4*, 1–7.

174. Hong, W.; Stoerzinger, K. A.; Lee, Y.-L.; Giordano, L.; Grimaud, A. J. L.; Johnson, A. M.; Hwang, J.; Crumlin, E.; Yang, W.; Shao-Horn, Y. Charge-Transfer-Energy-Dependent Oxygen Evolution Reaction Mechanisms for Perovskite Oxides. *Energy Environ. Sci.* **2017**, *10*, 2190–2200.

175. Jacobs, R.; Booske, J.; Morgan, D. Understanding and Controlling the Work Function of Perovskite Oxides Using Density Functional Theory. *Adv. Funct. Mater.* **2016**, *26*, 5471–5482.

176. Gong, Q.; Wang, Y.; Hu, Q.; Zhou, J.; Feng, R.; Duchesne, P. N.; Zhang, P.; Chen, F.; Han, N.; Li, Y.; et al. Ultrasmall and Phase-Pure W2C Nanoparticles for Efficient Electrocatalytic and Photoelectrochemical Hydrogen Evolution. *Nat. Commun.* **2016**, *7*.

177. Wu, H.; Xiao, W.; Guan, C.; Liu, X.; Zang, W.; Zhang, H.; Ding, J.; Feng, Y. P.; Pennycook, S. J.; Wang, J. Hollow Mo-Doped CoP Nanoarrays for Efficient Overall Water Splitting. *Nano Energy* **2018**, *48*, 73–80.

178. Nørskov, J. K.; Rossmeisl, J.; Logadottir, A.; Lindqvist, L.; Kitchin, J. R.; Bligaard, T.; Jónsson, H. Origin of the Overpotential for Oxygen Reduction at a Fuel-Cell Cathode. *J. Phys. Chem. B* **2004**, *108*, 17886–17892.

179. Liu, S.; Tao, H.; Zeng, L.; Liu, Q.; Xu, Z.; Liu, Q.; Luo, J.-L. Shape-Dependent Electrocatalytic Reduction of CO2 to CO on Triangular Silver Nanoplates. *J. Am. Chem. Soc.* **2017**, *139*, 2160–2163.

180. Zhang, R.; Tang, C.; Kong, R.; Du, G.; Asiri, A. M.; Chen, L.; Sun, X. Al-Doped CoP Nanoarray: A Durable Water-Splitting Electrocatalyst with Superhigh Activity. *Nanoscale* **2017**, *9*, 4793–4800.

181. Cramer, C. J. *Essentials of Computational Chemistry Theories and Models*, Second Edi.; John Willey & Sons Ltd: Chichester, 2004.

182. Rosen, J.; Hutchings, G. S.; Lu, Q.; Rivera, S.; Zhou, Y.; Vlachos, D. G.; Jiao, F. Mechanistic Insights into the Electrochemical Reduction of CO2 to CO on Nanostructured Ag Surfaces. *ACS Catal.* **2015**, *5*, 4293–4299.

183. Xue, Y.; Yu, D.; Dai, L.; Wang, R.; Li, D.; Roy, A.; Lu, F.; Chen, H.; Liu, Y.; Qu, J., Three-dimensional B, N-doped graphene foam as a metal-free catalyst for oxygen reduction reaction. *Physical Chemistry Chemical Physics* **2013,** *15* (29), 12220-12226.

184. Wang, X.; Li, Y.; Jin, T.; Meng, J.; Jiao, L.; Zhu, M.; Chen, J., Electrospun Thin-Walled CuCo2O4@ C Nanotubes as Bifunctional Oxygen Electrocatalysts for Rechargeable Zn–Air Batteries. *Nano letters* **2017,** *17* (12), 7989-7994.

185. Liu, X.; Park, M.; Kim, M. G.; Gupta, S.; Wu, G.; Cho, J., Integrating NiCo alloys with their oxides as efficient bifunctional cathode catalysts for rechargeable zinc–air batteries. *Angewandte Chemie International Edition* **2015,** *54* (33), 9654-9658.

186. Zhang, J.; Zhao, Z.; Xia, Z.; Dai, L., A metal-free bifunctional electrocatalyst for oxygen reduction and oxygen evolution reactions. *Nature nanotechnology* **2015,** *10* (5), 444.

187. Amiinu, I. S.; Liu, X.; Pu, Z.; Li, W.; Li, Q.; Zhang, J.; Tang, H.; Zhang, H.; Mu, S., From 3D ZIF Nanocrystals to Co–Nx/C Nanorod Array Electrocatalysts for ORR, OER, and Zn–Air Batteries. *Advanced Functional Materials* **2017**.

188. Xiong, M.; Ivey, D. G., Electrodeposited Co-Fe as an oxygen evolution catalyst for rechargeable zinc-air batteries. *Electrochemistry Communications* **2017,** *75*, 73-77.

189. Wang, H.-W.; Hu, Z.-A.; Chang, Y.-Q.; Chen, Y.-L.; Wu, H.-Y.; Zhang, Z.-Y.; Yang, Y.-Y., Design and synthesis of NiCo 2 O 4–reduced graphene oxide composites for high performance supercapacitors. *Journal of Materials Chemistry* **2011,** *21* (28), 10504-10511.

190. Bao, J.; Zhang, X.; Fan, B.; Zhang, J.; Zhou, M.; Yang, W.; Hu, X.; Wang, H.; Pan, B.; Xie, Y., Ultrathin Spinel-Structured Nanosheets Rich in Oxygen Deficiencies for Enhanced Electrocatalytic Water Oxidation. *Angewandte Chemie* **2015,** *127* (25), 7507-7512.

191. Yang, J.; Yu, C.; Liang, S.; Li, S.; Huang, H.; Han, X.; Zhao, C.; Song, X.; Hao, C.; Ajayan, P. M., Bridging of ultrathin NiCo2O4 nanosheets and graphene with polyaniline: A theoretical and experimental study. *Chemistry of Materials* **2016,** *28* (16), 5855-5863.

192. Zhang, G.; Xia, B. Y.; Wang, X., Strongly Coupled NiCo2O4-rGO Hybrid Nanosheets as a Methanol-Tolerant Electrocatalyst for the Oxygen Reduction Reaction. *Advanced Materials* **2014,** *26* (15), 2408-2412.

193. Moni, P.; Hyun, S.; Vignesh, A.; Shanmugam, S., Chrysanthemum flower like NiCo 2 O 4-nitrogen doped graphene oxide composite: An efficient electrocatalyst for Lithium-oxygen and Zinc-air batteries. *Chemical Communications* **2017**.

194. Gao, G.; Wu, H. B.; Lou, X. W. D., Citrate-Assisted Growth of NiCo2O4 Nanosheets on Reduced Graphene Oxide for Highly Reversible Lithium Storage. *Advanced Energy Materials* **2014,** *4* (14).

195. Chen, S.; Qiao, S.-Z., Hierarchically porous nitrogen-doped graphene–NiCo2O4 hybrid paper as an advanced electrocatalytic water-splitting material. *Acs Nano* **2013,** *7* (11), 10190-10196.

196. Zhu, H.; Zhang, S.; Huang, Y.-X.; Wu, L.; Sun, S., Monodisperse M x Fe3–x O4 (M= Fe, Cu, Co, Mn) Nanoparticles and Their Electrocatalysis for Oxygen Reduction Reaction. *Nano letters* **2013,** *13* (6), 2947-2951.

197. Pérez-Mirabet, L.; Solano, E.; Martínez-Julián, F.; Guzmán, R.; Arbiol, J.; Puig, T.; Obradors, X.; Pomar, A.; Yáñez, R.; Ros, J., One-pot synthesis of stable colloidal solutions of MFe 2 O 4 nanoparticles using oleylamine as solvent and stabilizer. *Materials Research Bulletin* **2013,** *48* (3), 966-972.

198. Cozzoli, P. D.; Curri, M. L.; Agostiano, A.; Leo, G.; Lomascolo, M., ZnO nanocrystals by a non-hydrolytic route: synthesis and characterization. *The Journal of Physical Chemistry B* **2003,** *107* (20), 4756-4762.

199. Kim, J.-G.; Pugmire, D.; Battaglia, D.; Langell, M., Analysis of the NiCo 2 O 4 spinel surface with Auger and X-ray photoelectron spectroscopy. *Applied surface science* **2000,** *165* (1), 70-84.

200. Song, W.; Ren, Z.; Chen, S.-Y.; Meng, Y.; Biswas, S.; Nandi, P.; Elsen, H. A.; Gao, P.-X.; Suib, S. L., Ni-and Mn-promoted mesoporous Co3O4: a stable bifunctional catalyst with surface-structure-dependent activity for oxygen reduction reaction and oxygen evolution reaction. *ACS applied materials & interfaces* **2016,** *8* (32), 20802-20813.

201. Wang, H. Y.; Hsu, Y. Y.; Chen, R.; Chan, T. S.; Chen, H. M.; Liu, B., Ni3+-Induced Formation of Active NiOOH on the Spinel Ni–Co Oxide Surface for Efficient Oxygen Evolution Reaction. *Advanced Energy Materials* **2015,** *5* (10).

202. Yu, A.; Chen, Z.; Maric, R.; Zhang, L.; Zhang, J.; Yan, J., Electrochemical supercapacitors for energy storage and delivery: Advanced materials, technologies and applications. *Applied Energy* **2015,** *153*, 1-2.

203. Choi, C. H.; Park, S. H.; Woo, S. I., Oxygen reduction activity of Pd–Mn 3 O 4 nanoparticles and performance enhancement by voltammetrically accelerated degradation. *Physical Chemistry Chemical Physics* **2012,** *14* (19), 6842-6848.

204. Xi, Z.; Erdosy, D. P.; Mendoza-Garcia, A.; Duchesne, P. N.; Li, J.; Muzzio, M.; Li, Q.; Zhang, P.; Sun, S., Pd Nanoparticles Coupled to WO2. 72 Nanorods for Enhanced Electrochemical Oxidation of Formic Acid. *Nano Letters* **2017,** *17* (4), 2727-2731.

205. Doyle, R. L.; Lyons, M. E., The Oxygen Evolution Reaction: Mechanistic Concepts and Catalyst Design. In *Photoelectrochemical Solar Fuel Production*, Springer: 2016; pp 41-104.

206. Ma, T. Y.; Dai, S.; Jaroniec, M.; Qiao, S. Z., Metal–organic framework derived hybrid Co3O4-carbon porous nanowire arrays as reversible oxygen evolution electrodes. *Journal of the American Chemical Society* **2014,** *136* (39), 13925-13931.

207. Aricò, A. S.; Bruce, P.; Scrosati, B.; Tarascon, J.-M.; Van Schalkwijk, W., Nanostructured materials for advanced energy conversion and storage devices. *Nature materials* **2005,** *4* (5), 366-377.

208. Liu, J.; Jiang, J.; Cheng, C.; Li, H.; Zhang, J.; Gong, H.; Fan, H. J., Co3O4 Nanowire@ MnO2 Ultrathin Nanosheet Core/Shell Arrays: A New Class of High-Performance Pseudocapacitive Materials. *Advanced Materials* **2011,** *23* (18), 2076-2081.

209. Hou, Y.; Cui, S.; Wen, Z.; Guo, X.; Feng, X.; Chen, J., Strongly Coupled 3D Hybrids of N-doped Porous Carbon Nanosheet/CoNi Alloy-Encapsulated Carbon Nanotubes for Enhanced Electrocatalysis. *Small* **2015,** *11* (44), 5940-5948.

210. Jung, S.; McCrory, C. C.; Ferrer, I. M.; Peters, J. C.; Jaramillo, T. F., Benchmarking nanoparticulate metal oxide electrocatalysts for the alkaline water oxidation reaction. *Journal of Materials Chemistry A* **2016,** *4* (8), 3068-3076.

211. Merki, D.; Vrubel, H.; Rovelli, L.; Fierro, S.; Hu, X., Fe, Co, and Ni ions promote the catalytic activity of amorphous molybdenum sulfide films for hydrogen evolution. *Chemical Science* **2012,** *3* (8), 2515-2525.

212. Hu, H.; Guan, B.; Xia, B.; Lou, X. W., Designed formation of Co3O4/NiCo2O4 double-shelled nanocages with enhanced pseudocapacitive and electrocatalytic properties. *Journal of the American Chemical Society* **2015,** *137* (16), 5590-5595.

213. Jung, K.-N.; Jung, J.-H.; Im, W. B.; Yoon, S.; Shin, K.-H.; Lee, J.-W., Doped lanthanum nickelates with a layered perovskite structure as bifunctional cathode catalysts for rechargeable metal–air batteries. *ACS applied materials & interfaces* **2013,** *5* (20), 9902-9907.

214. Zhang, Y.Q.; Li, M.; Hua, B.; Wang, Y.; Sun, Y.F.; Luo, J.L., A strongly cooperative spinel nanohybrid as an efficient bifunctional oxygen electrocatalyst for oxygen reduction reaction and oxygen evolution reaction. *Applied Catalysis B: Environmental* **2018**, *236* (15) 413-419.

215. Zhang, Y.Q.; Li, J.H.; Sun, Y.F.; Hua, B.; Luo, J.L., Highly active and redox-stable Ce-doped LaSrCrFeO-based cathode catalyst for CO_2 SOECs. *ACS applied materials & interfaces*, **2016**, *8*(10) 6457-6463.

Appendix I: A Highly Active and Redox-Stable Ce doped LaSrCrFeO Based Cathode Catalyst for CO_2 SOECs

A I.1. Abstract

Lanthanum chromate-based perovskite oxides have attracted great attention as the cathode materials in the high temperature CO_2 electrolysis due to its good redox stability. However, the unsatisfied electrochemical catalytic activity and insufficient adsorption of CO_2 at operating temperature still hindered the further improvement of electrochemical performance and the Faraday efficiency of the electrolysis cell. In this work, the catalytic and redox active Ce was doped into A site of $La_{0.7}Sr_{0.3}Cr_{0.5}Fe_{0.5}O_{3-\delta}$ (LSCrF) to promote the catalytic performance, and to introduce oxygen vacancies in the lattice *in-situ* after reduction under the operational condition. The increased amount of oxygen vacancies not only facilitates the mobility of oxygen ions, but also provides favorable accommodation for chemical adsorption of CO_2. The CO_2 electrolysis tests demonstrated the superior electrochemical performances, higher Faraday efficiencies of the Ce-doped LSCrF cathode catalyst in comparison with that without Ce doping, indicating the perspective application of this functional material.

A I.2. Introduction

The present dependence of human society on fossil fuels has led to inevitable increase of greenhouse gases emission, most notably, carbon dioxide (CO_2), resulting in severe climate changes in the recent decades.[1-3] Under external applied potentials, solid oxide electrolysis cells (SOECs) can electrochemically convert CO_2 into CO fuel and oxygen ions at cathode side, and the released oxygen ions can transport through the ion conducing solid oxide electrolyte to anode side and form O_2 at the triple-phase boundaries (TPB). [3, 4]

Usually, the potential candidates for electrode applied in SOECs are the materials derived from solid oxide fuel cells (SOFCs). [3-10] However, there are still many problems left because of the different operational conditions between these two processes.[3,4,10] For example, Ni/YSZ cermet, a preferentially used anode material for hydrogen oxidation in SOFCs, suffered from the loss of electrical conductivity and deactivation in SOEC, as Ni may get oxidized to NiO in CO_2 atmosphere.[11] In addition, the redox cycle and carbon deposition in Ni-YSZ cermet also shorten the lifetime of the cells[4]. Therefore, redox stable perovskite oxides materials have been used as the alternative cathode materials for Ni/YSZ in SOECs. Doped lanthanum chromate based perovskite oxides, $(La_{1-x}Sr_x)(Cr_yM_{1-y})O_{3-\delta}$ (M = Mn, Fe, Ti, Co),[12-14] have been proved to be the efficient anode materials in SOFCs. The mixed ionic and electronic conductivity as well as the good redox stability also makes this type of materials the promising cathode materials candidates in SOECs. Among this group of materials, the perovskite oxide $La_{0.75}Sr_{0.25}Cr_{0.5}Mn_{0.5}O_{3-\delta}$ (LSCM) has been demonstrated as a potential catalyst for CO_2 reduction because it showed great stability and acceptable polarization resistance in CO_2 electrolysis.[11, 15] Nonetheless, the electrochemical

performance of LSCM is still insufficient, mainly due to its relatively low catalytic activity and electrical conductivity.[16]

Another challenge for improving efficiency of the high temperature electrolysis of CO_2 is the poor adsorbability of CO_2 on the solid oxide surface. Although some basic sites could be introduced by chemical modification to enhance the adsorption ability, the CO_2 desorption will start at a temperature far below the operating temperature for CO_2 electrolysis.[17, 18] Thus, the starvation of adsorbed CO_2 on the surface of the catalyst at the operating temperature will lead to a low current efficiency.[10, 19] Research has shown that the formation of sufficient oxygen vacancies could effectively enhance the chemical adsorption at elevated temperature as the CO_2 could be incorporated into the oxygen vacancy sites and form strong chemical bonding even in a high temperature region[9].

Previous studies on $(La_{1-x}Sr_x)(Cr_yM_{1-y})O_{3-\delta}$ perovskite oxides have shown that the electrochemical catalytic properties and the stability mainly rely on the nature of substitution of B-site cations[20]. When Cr was partially replaced by Fe, the perovskite oxides exhibited much improved electrochemical performance for H_2 and hydrocarbon oxidations compared with the one having Mn substitution. The doped perovskite oxides maintained its desirable redox stability when Fe concentration was lower than 50% ($y \geq 0.5$) in $(La_{1-x}Sr_x)(Cr_yFe_{1-y})O_{3-\delta}$. Ceria, which possesses active catalytic activity in CO_2 reduction, is also regarded as a promising cathode material towards CO_2 electrolysis.[11, 22] Recent studies in our group demonstrated that when the A-site of $La_{0.7}Sr_{0.3}Cr_{0.5}Fe_{0.5}O_{3-\delta}$ (LSCrF) was doped with Cerium, the electrochemical catalytic performance and carbon deposition resistance in oxidation of syngas were significantly improved.[23] The concentration of oxygen vacancies could be increased in the reduced

$La_{0.65}Sr_{0.3}Ce_{0.05}Cr_{0.5}Fe_{0.5}O_{3-\delta}$ (Ce-LSCrF) catalyst because of the mixed oxidation states of the introduced cerium ions.[23] The increase in the oxygen vacancies facilitates the transportation of oxygen ions and provides favorable sites for the adsorption of CO_2. These properties make Ce doped $La_{0.7}Sr_{0.3}Cr_{0.5}Fe_{0.5}O_{3-\delta}$ a promising candidate cathode material for CO_2 reduction.

In this work, the catalytically and redox active Ce is doped into LSCrF matrix, and the chemical adsorption and desorption of CO_2 on the surface of reduced Ce-LSCrF are investigated in comparison with the undoped catalyst. The potential of Ce-LSCrF/YSZ as a cathode material for CO_2 electrolysis is investigated, and its electrochemical performance is evaluated at different applied voltages and various CO_2/CO ratios. The stability of the cell with the Ce-LSCrF/YSZ composite cathode is also evaluated.

A I.3. Experimental

The cathode materials, Ce-LSCrF and LSCrF, were synthesized via a glycine nitrate combustion method, similar to that described in our previous report. Stoichiometric amounts of $La(NO_3)_3 \cdot 6H_2O$, $Sr(NO_3)_2$, $Fe(NO_3)_3 \cdot 9H_2O$, $Cr(NO_3)_3 \cdot 9H_2O$, $Ce(NO_3)_3 \cdot 6H_2O$ were first dissolved in deionized water. Glycine was added into the solution with a molar ratio of 2:1 to the total amount of the metal cations. The solution was heated under vigorous stirring on a hot plate until self-combustion occurred. The Ce-LSCrF and LSCrF catalysts were obtained by calcination at 1200 ºC for 4 hours.

The phase formation was analyzed by X-ray diffraction (XRD) using a Rigaka D/max-2500 X-ray diffractometer with a Cu Kα radiation. The micromorphology of the materials was examined using a JEOL 6301F Scanning Electron Microscope (SEM). The oxygen nonstoichiometry was analyzed

by thermogravimetry analysis (TGA) on SDT Q600 (TA instrument) at a heating rate of 20 ºC min^{-1} under 5% H_2/N_2. The temperature programmed desorption of CO_2 (CO_2-TPD) was recorded with a Micromeritics AutoChem II 2920 instrument. The reduced powder samples were pretreated at 400 ºC in Ar for 1h to eliminate adsorbed species, followed by purged adsorption of CO_2 with 5% CO_2-He flow at 100 ºC for 1 h. The CO_2-TPD was conducted from 100 ºC to 900 ºC at 10 ºC min^{-1} with He flow of 30 ml min^{-1}. The X-ray photoelectron spectroscopy (XPS) analysis was performed using Kratos Analytical AXIS 165 with monochromatic Al Kα source (hv = 1486.6 eV) to investigate the fresh and reduced LSCrF and Ce-LSCrF powders. The spectra were referenced to C 1s bonding energy (284.6 eV) and fitted with Gaussian-Lorenz function and Shirley-type background subtraction method.

The electrode composites of the anode (50 wt% Ce-LSCrF / 50 wt% YSZ, Fuel Cell Materials), cathode (50 wt% $(La_{0.60}Sr_{0.40})_{0.95}Co_{0.2}Fe_{0.8}O_{3-\delta}$ (LSCoF)/ 50 wt% $Gd_{0.10}Ce_{0.90}O_{2-x}$ (GDC), Fuel Cell Materials) were dispersed in alpha terpineol mixed with 10% poltethylene glycol respectively to form the electrode inks. The cell with the configurations of LSCoF+GDC / YSZ / GDC / Ce-LSCrF+YSZ was fabricated based on the commercial YSZ support (Fuel Cell Materials) with the thickness of 300 μm and diameter of 25 mm. GDC was first printed on the YSZ substrate and sintered at 1300 ºC for 4 hours to form a buffer layer. The cathode composite electrode was prepared by mixing Ce-LSCrF powder or LSCrF with YSZ power (TOSHO Company) by ball milling with a weight ratio of 50:50. Then it was printed on YSZ pellets with a surface area of 1 cm^{-2} and sintered at 1200 ºC for 4 hours. The LSCoF/GDC was subsequently printed on the GDC buffer layer, and treated at 950 ºC for 4 hours. Au paste (Heraeus C5729) was painted on both sides of the cell as the electrode current collectors. The silver wire with the diameter of 0.5 mm was connected to the current collectors using silver paste plus (SPI Supplies). The fabricated cell

was sealed on a coaxial two-tube set up with Ceramabond 503 and tested at 850 ºC on Thermolyne tubular furnace.

The AC impedance measurements of the cells were conducted in the atmosphere of CO_2/CO at the open circuit voltage and various applied voltages (0, 0.5, 0.7, 1.0, 1.2 V vs. OCV) from 10^5 Hz to 0.1 Hz with a 10 mV amplitude using Solartron 1255B frequency response analyzer and Solartron 1287 instrument. The obtained results were further analyzed by equivalent circuit modelling using ZSimpwin V3.10 to evaluate the value of polarization resistance. The inlet gases were controlled at a flow rate of 50 ml min^{-1} using mass flow meters. The outlet gases from the cathode side are evaluated by online gas chromatograph.

A I.4. Results and Discussion

A I.4.1. Textural and structural properties

Figure A I.1 shows the XRD patterns of Ce-LSCrF and LSCrF perovskite oxides. No signal of CeO_2 (2θ = 28.5°, 47.7°and 56.6°) is present in the pattern of Ce-LSCrF, which confirms the single phase of perovskite and verifies the appropriate accommodation of the Ce substituted in the LSCrF perovskite at 5 at%. The slight shift of the peak position of (002) peak from LSCrF (2θ =32.55°) to Ce-LSCrF (2θ =32.6°) could be explained by decrease of the cell volume caused by reducing radius of the cerium substitution, as the average ionic radii calculated from Shannon ionic radii for 12-fold coordination of the A site of Ce^{3+} and Ce^{4+} are 1.34 Å and 1.14 Å, which is smaller than the La^{3+} (1.36 Å). [1]

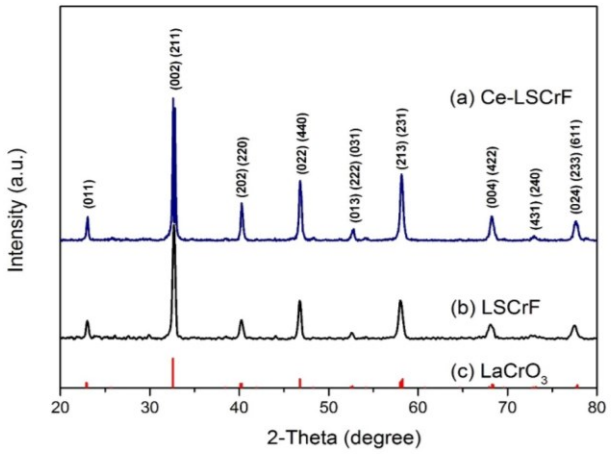

Figure AI. 1 XRD patterns of (a) Ce-LSCrF and (b) LSCrF sintered at 1200 ºC for 4 h and (c) standard XRD pattern of $LaCrO_3$ ((JCPDS no. 24-1016).

Figure A I.2 shows the micromorphology of the Ce-LSCrF/YSZ and LSCrF/YSZ composites. It could be observed that the glycine-nitrate combustion method permits obtaining fine and homogenous nanoparticles, with the particle size of both Ce-LSCrF and LSCrF less than 100 nm. The SEM images of the cathode materials demonstrated that the YSZ is well distributed in the composite, with the particle size similar to Ce-LSCrF and LSCrF. The well distribution of the two phases in the composites significantly extended the TPB and increased the reaction area.

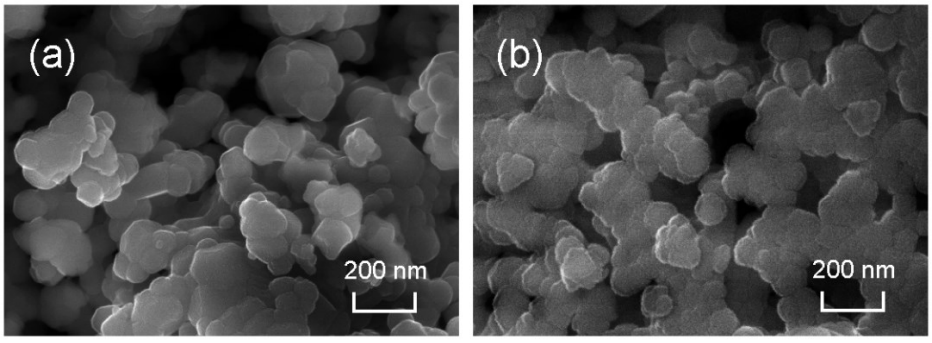

Figure AI. 2 SEM images of (a) Ce-LSCrF/YSZ and (b) LSCrF/YSZ composite cathode materials.

TGA analysis was conducted from room temperature to 950 ºC in 5% H_2/N_2 to investigate the oxygen vacancy generation in LSCrF and Ce-LSCrF materials in the reducing atmosphere. As shown in Figure A I.3, the gradual weight loss below 380 ºC was due to the loss of absorbed water. When the temperature was further increased to 570 ºC, the weight experienced a sharp drop followed by a continuous decrease at the higher temperatures. This region is referred to as the oxygen vacancy formation regions. In Figure A I.3, the weight loss of LSCrF in stepIIwas 1.98%, while the weight loss in Ce-LSCrF was 2.65%, which indicates the increased oxygen vacancy generations in Ce-LSCrF. This is consistent with the TPO results in our previous studies.[23]

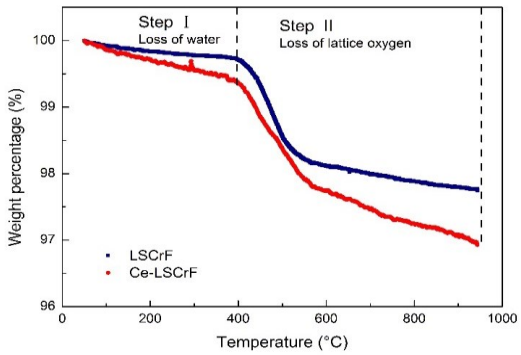

Figure AI. 3 TGA analysis of LSCrF and Ce-LSCrF in 5% H_2/N_2.

To investigate the influence of Ce dopant on CO_2 adsorption behavior of LSCrF, CO_2-TPD was conducted to study the adsorption of CO_2 on the candidate materials. Generally speaking, the adsorption of CO_2 on the surface of catalysts can be classified into the physical adsorption and chemical adsorption. As Figure A I.4 shows, both fresh LSCrF and Ce-LSCrF exhibited the similar low temperature desorption behavior below 500 ºC. Specifically, the desorption peak located at 150 ºC can be ascribed to the physical desorption of CO_2, while the wide peaks between 350 and 550 ºC were mainly attributed to the basic sites on the surface of perovskite oxides. However,

unlike LSCrF, which had no obvious higher temperature peak, the Ce-LSCrF demonstrated a strong chemical desorption peak at around 680 ºC, coupling with a slightly weaker desorption peak at higher than 750 ºC. This is mainly due to the existence of large amount of oxygen vacancies in Ce doped LSCrF perovskite. Since CO_2 molecules could be incorporated into oxygen vacancies in the lattice, sufficient oxygen vacancies in the Ce doped LSCrF could provide accommodation sites for CO_2 molecules at elevated temperatures. The notable improvement of CO_2 adsorption on the surface of catalysts accounted for the improvement of cell performance.

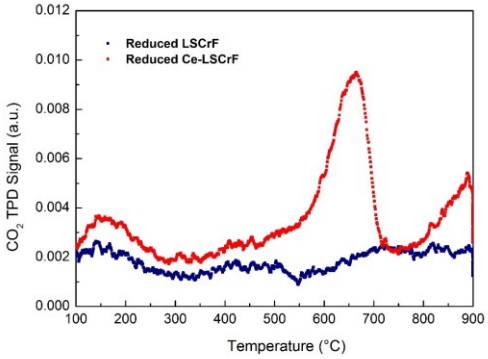

Figure AI. 4 CO_2-TPD analysis of LSCrF and Ce-LSCrF.

XPS analysis was conducted to investigate the different valence states of elements in fresh and reduced LSCrF and Ce-LSCrF samples. It is well known that the oxidation state of +4 is predominant in the oxidized cerium based oxide, whereas the ratio of Ce^{3+}/Ce^{4+} would dramatically increase in the reduced sample surface. The redox couple of Ce^{4+}/Ce^{3+} in Ce-LSCrF significantly contributes to the catalytic activity and oxygen vacancy formation. However, because of the complex shape of the spectrum in Ce 3d core-level and low dopant concentration of Ce in the LSCrF, it is not an easy task to quantitatively analyze the valence state changes of Ce before and after reduction.

Figure A I.5 shows the XPS spectra of Cr 2p 3/2 excitation in LSCrF and Ce-LSCrF. The fresh LSCrF catalyst shows the peaks of Cr^{3+} (2p 3/2) and Cr^{6+} (2p 3/2) at 576.2 eV and 579.7 eV, respectively. Peaks of Cr^{3+} (2p 3/2) and Cr^{6+}(2p 3/2) are also observed in the fresh Ce-LSCrF XPS spectra, with the binding energy positioned at 576.1 eV and 579.6 eV. Due to the similar binding energies of Cr^{3+} and Cr^{4+}, it is difficult to separate the peaks of Cr^{3+} and Cr^{4+} from the spectra as Cr^{4+} also shows weak peak at around 576.1 eV[26]. The peaks area of $Cr^{3+,\,4+}$ and Cr^{6+} reveals the atomic ratio of 65.4%/34.6% ($Cr^{3+,\,4+}/Cr^{6+}$), while in fresh Ce-LSCrF sample, the atomic ratio of $Cr^{3+,\,4+}/Cr^{6+}$ increased to 70.4%/29.6%. The difference in the ratio of the valence states between the two samples illustrates that Cr tends to exist at lower valence state in the fresh Ce-LSCF. This is mainly due to the existence of Ce^{4+} in the A sites as the perovskite oxide tends to maintain the stability of the structure by decreasing the valence state in B site (electronic compensation) [25]. As shown in Figures A I.5b and 5d, after sufficient reduction, the Cr^{3+} became the only valence state existed in both reduced LSCrF and Ce-LSCrF. The relatively higher proportion of the Cr^{3+}in B site gave the favorable stability of the structure in both oxidizing and reducing environments.

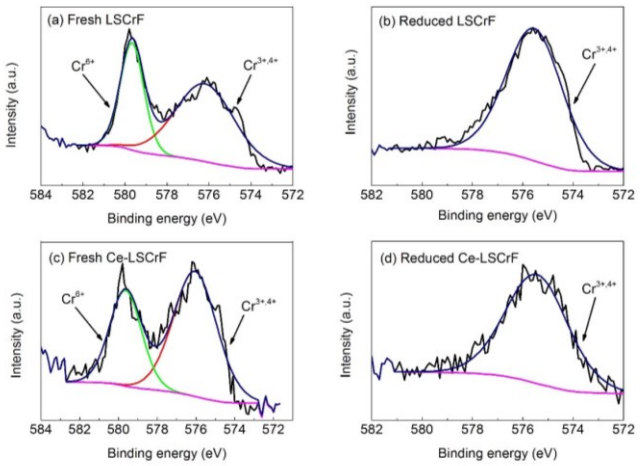

Figure AI. 5 XPS results of Cr 2p 3/2 spectra in (a) fresh LSCrF, (b) reduced LSCrF, (c) fresh Ce-LSCrF, and (d) reduced Ce-LSCrF.

In Figure A I.6a, the Fe^{3+} (2p 3/2) and Fe^{2+} (2p 3/2) peaks are presented at 711.1 and 709.6 eV, respectively. The fresh Ce-LSCrF also showed similar peaks of Fe^{3+} 2p 3/2 and Fe^{2+} 2p 3/2. The Fe element existed in the form of Fe^{3+}/Fe^{2+}on the surface of fresh LSCrF with the composition of 63.2%/36.8%, while in fresh Ce-LSCrF, Fe existed as Fe^{3+} and Fe^{2+} with the composition of 58.25%/41.75%. The valence state of Fe^{3+} on LSCrF surface was slightly higher than that on Ce-LSCrF, which also confirmed the existence of higher valence state of cerium in the A site of LSCrF due to the electronic compensation[25]. After reduction, the atomic percentages of Fe^{3+} and Fe^{2+} were changed to 51.2%/48.8% and 41.9%/58.1% in reduced LSCrF and Ce-LSCrF, respectively. During the reducing treatment, the Ce redox couple facilitated the state changes of Fe^{3+} in Ce-LSCrF, leading to a higher generation of Fe^{2+} in Ce-LSCrF compared with that in LSCrF. The process of Fe^{2+} generation facilitated the introduction of oxygen vacancy in the perovskite oxide, which contributed to the electronic conductivity. Moreover, the Fe^{2+} ions were found to be more catalytically active and therefore, were expected to further improve the kinetics of electrochemical reaction[27].

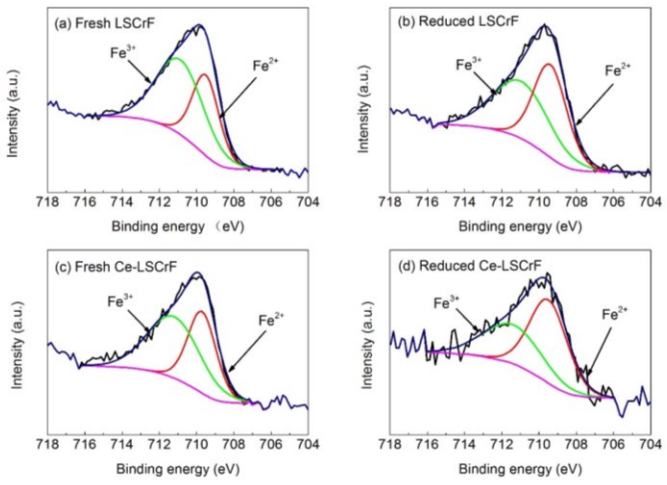

Figure AI. 6 XPS results of Fe 2p 3/2 spectra in (a) fresh LSCrF, (b) reduced LSCrF, (c) fresh Ce-LSCrF and (d) reduced Ce-LSCrF.

A I.4.2. Impedance Studies on Ce-LSCrF/YSZ Cathode

The electrochemical impedance spectroscopy (EIS) studies for the cell with the Ce-LSCrF/YSZ cathode were further conducted to investigate the polarization resistances of the cells in the atmosphere of CO_2/CO at 850 °C under different working conditions. The obtained Nyquist spectra were analyzed with ZSimpwin and the equivalent circuit is shown in Figure A I.7. The simulated results are in accordance with the experimentally measured values, suggesting the validity of the proposed circuit model. The cell impedance consisted four major parts including one inductive impedance, an ohmic resistance and two resistance constant phases, R_1CPE_1 and R_2CPE_2, which is consistent with the model proposed for CO_2 electrolysis with LSCM cathode.[11] The high frequency resistance of the intercept is mainly contributed by the ohmic resistances which is around 0.4 Ω cm^2, associated with the resistance value for 300 μm YSZ pellet at 850 ºC. The low frequency arc, R_1 and R_2, is corresponding to the polarization resistance of the cell. It has been proposed that the two arcs of the impedances R_1 and R_2 are corresponding to the charge transfer process and mass transfer process, respectively.[15] The low frequency arc (R_2), which makes up the major proportion of the Rp, stands for the rate controlling step of the reaction. As shown in Figure A I.8a, the values of R1 and R2 changed remarkably with the ratio of CO_2/CO. The lowest Rp of the cell was achieved in the CO_2/CO (50:50) and the value of Rp increased with the concentration of CO_2, indicating that the reducing condition is more favorable for CO_2 electrolysis. This is mainly due to the decrease of the valence state in the reducing condition, which leads to an increase in the electronic conductivity and oxygen vacancies. Particularly, the significant decrease of R2 suggests that the increased oxygen vacancies of the perovskite not only facilitates the oxygen ions mobility but also results in more conducive chemical adsorption/desorption and surface diffusion of CO_2.[11] However, even in the pure CO_2 atmosphere, the electrolysis cell showed a Rp value of 1.74 Ω cm^2,

demonstrating its excellent redox stability and promising potential for applications in CO_2 electrolysis.

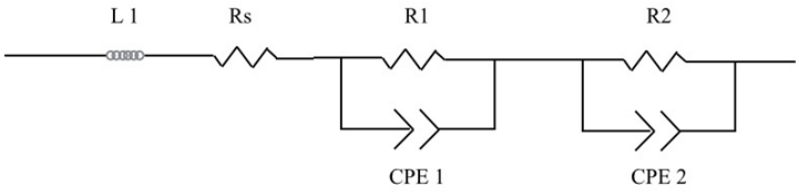

Figure AI. 7 Equivalent circuit for Ce-LSCrF electrolysis cells.

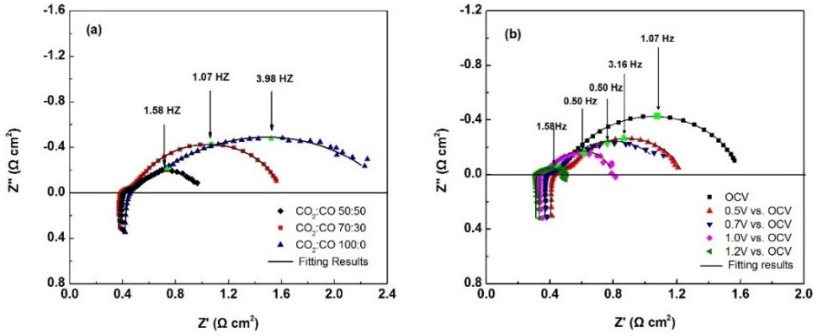

Figure AI. 8 Experimental and simulated EISs of the electrolysis cell with the Ce-LSCrF cathode (a) at OCV in different ratios of CO_2/CO and (b) at different applied voltages in the atmosphere of CO_2/CO (70:30).

Table A I.1 summarizes the impedance values for the electrolysis cell with Ce-LSCrF cathode working at a series of applied voltages. The values of R2 arcs decreased significantly with increasing applied voltage from 1.071 Ω cm^2 (OCV) to 0.663 Ω cm^2 (0.5 V vs. OCV), indicating the activation of the electrode materials at low voltages. As the voltage is increasing, the increased electrode polarization during CO_2 reduction created a more reducing condition, which greatly improved surface kinetics of the adsorption/desorption of active species and their diffusion into

the triple phase boundary sites. This resulted to a further gradual decrease of polarization resistance, in accordance with the results in Figure A I.8b. The remarkable enhancement of the reaction kinetics indicates the application potential of electrolysis at high applied voltage.

Table A I. 1 Simulated EIS results of the electrolysis cell with Ce-LSCrF cathode at different applied voltages in CO2/CO (70:30)

Applied Voltages	Rs (Ω cm^2)	R1(Ω cm^2)	R2 (Ω cm^2)	Rp (Ω cm^2)
OCV in CO_2/CO	0.358	0.182	1.071	1.253
0.5 V in CO_2/CO	0.392	0.183	0.663	0.845
0.7V in CO_2/CO	0.364	0.132	0.627	0.759
1.0 V in CO_2/CO	0.333	0.123	0.336	0.459
1.2 V in CO_2/CO	0.316	0.021	0.190	0.211

A I.4.3. Electrochemical performance of Ce-LSCrF in SOECs

The electrochemical performances of SOECs using Ce-LSCrF/YSZ and LSCrF/YSZ composite cathodes were evaluated at 850 °C. The polarization curves (I-V) of the cell were recorded in the CO_2/CO atmosphere with the ratio of 70/30 under both electrolysis mode (negative current densities) and fuel cell mode (positive current densities) with the applied voltage varying from 0 to 1.2V (vs. OCV) and 0 to –0.7 V (vs. OCV), respectively. The open circuit potentials of the cells in the CO_2/CO (70/30) were around 0.86 V, which was quite close to the theoretical value predicted by the Nernst equation. Figure A I.9 shows that the I-V curve went smoothly from the SOFC mode to SOEC mode, suggesting the good reversibility of the cells. The current density of LSCrF/YSZ composite cathode cell reached 0.564 A cm^{-2} at the applied voltage of 0.7 V (vs. OCV), and 1.041 A cm^{-2} at the applied voltage of 1.2 V, while with the cerium doped LSCrF composite, the current density increased to 0.814 A cm^{-2} at the applied voltage of 0.7 V, and 1.283 A cm^{-2} at the applied voltage of 1.2 V. The remarkable high current density of the cell with the Ce-LSCrF/YSZ cathode demonstrated its excellent electrochemical catalytic properties in CO_2 reduction.

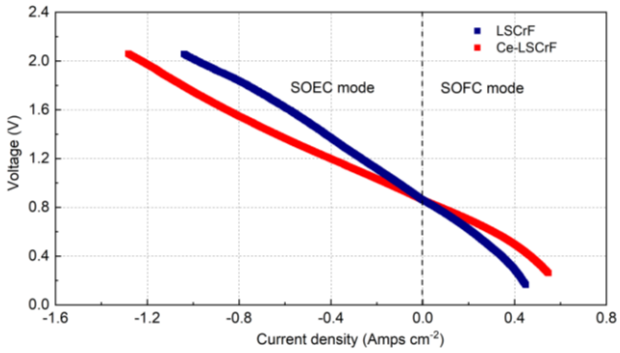

Figure AI. 9 I-V curves of the cell with the LSCrF/YSZ and Ce-LSCrF/YSZ composite cathodes in SOEC mode and SOFC mode at 850 ºC.

The cells with the Ce-LSCF/YSZ cathode were further investigated in the electrolysis process at a series of applied voltages in comparison with LSCrF/YSZ. The current density and outlet gas compositions were measured to evaluate the Faraday efficiencies of the cells. As is shown in Figure A I.10, the current densities of Ce-LSCF/YSZ and LSCrF/YSZ cathode based electrolysis cells increased in step with increasing applied voltages, with current density increasing from 0.53 A cm^{-2} (0.5 V) to 1.13 A cm^{-2} (1.2V) for Ce-LSCrF/YSZ and from 0.44 A cm^{-2} (0.5 V) to 0.90 A cm^{-2} (1.2V) for LSCrF/YSZ. The CO generation rate also significantly increased with increasing the applied voltage, reaching 6.66 ml min^{-1} and 4.07 ml min^{-1} for Ce-LSCrF/YSZ and LSCrF/YSZ, respectively, at the applied voltage of 1.2 V. The current efficiencies were calculated from the CO production rate and current density of the cells. It is shown in Figure A I.11 that the Faraday efficiencies of both Ce-LSCrF/YSZ and LSCrF/YSZ composite cathode-based cells increased dramatically with increasing applied voltage from 0.5V to 0.7 V, reaching the peak values of around 86.9% and 64.7% at 0.7 V. The current density and Faraday efficiency of the Ce-LSCrF/YSZ cathode at the applied voltages are significantly higher than those reported for LSCM cathode and LSCrF cathode.[7, 16, 26] In addition, the current efficiency experienced a downtrend at

higher applied voltages, since the SOECs with the Ce-LSCrF/YSZ operating at the applied voltages higher than 1 V have the current densities higher than 1 A cm^{-2}, which has been referred to as the ‘“harsh conditions”. The oxygen evolution and CO_2 consumption are processed so fast that lead to the degradation of the cell and starvation of the CO_2 on the reaction sites[3].

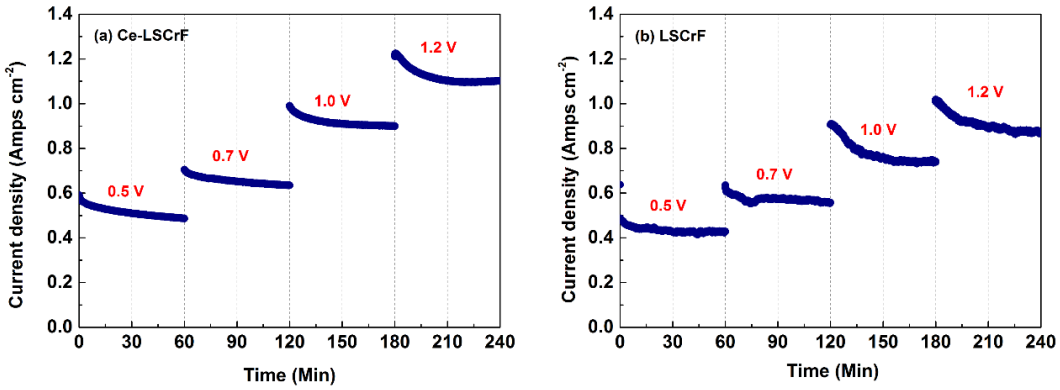

Figure AI. 10 Electrochemical performance of the electrolysis cells with (a) Ce-LSCrF and (b) LSCrF cathodes at 850 ºC at various applied voltages.

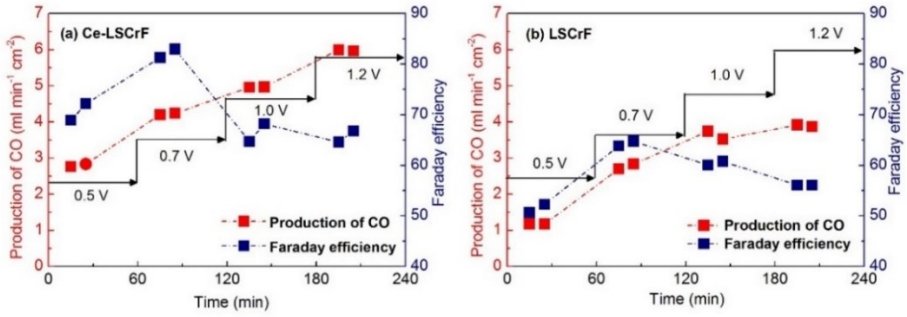

Figure AI. 11 The production of CO and Faraday efficiency of the electrolysis cell with (a) Ce-LSCrF and (b) LSCrF cathode at 850 ºC at various applied voltages.

Short term durability tests were performed at the CO_2/CO (70:30) at 850 ºC for 24 hours at the optimal applied voltage of 0.7 V to study the stability of the cell with the Ce-LSCrF/YSZ cathode. As shown in Figure A I.12, the current density experienced a slight decrease in the first hour and

then remained stable at approximately 0.65 A cm^{-2} for the duration of the tests. The 24 h short term durability test suggests that there is no evident degradation of the Ce-LSCrF/YSZ based cell during the electrolysis of CO_2.

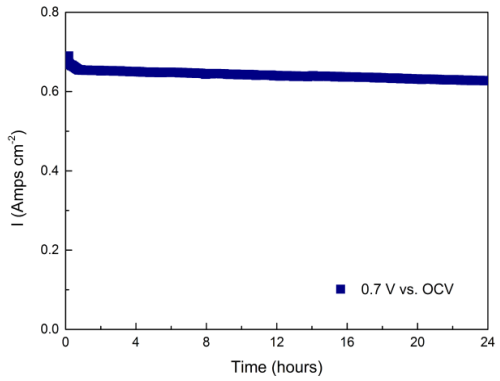

Figure A I. 12 Short term stability based on Ce-LSCrF cathode at 850 ºC and applied voltage of 0.7 V. vs OCV.

A I.5. Conclusions

In this work, Ce-LSCrF based composite cathode has been investigated as a potential cathode material for high temperature CO_2 electrolysis. The cell with the Ce-LSCrF/YSZ composite cathode has shown a significant improvement on electrochemical catalytic performance as well as Faraday efficiency in comparison with the cell using LSCrF/YSZ cathode. The current efficiency for Ce-LSCrF based SOECs reached around 86.9% at applied voltage of 0.7 V (vs. OCV), notably higher than that of un-doped LSCrF samples (64.7%), and also higher than those reported for LSCM and LSCrF cathode.[7, 16, 26] The Ce-LSCrF/YSZ composite cathode, therefore, has demonstrated a strong potential for its application in the CO_2 electrolysis.

Reprinted with permission from (28) Copyright (2016) American Chemical Society.

A I.6. References

1. Xu, S.; Li, S.; Yao, W.; Dong, D.; Xie, K. Direct Electrolysis of CO_2 Using an Oxygen-Ion Conducting Solid Oxide Electrolyzer based on $La_{0.75}Sr_{0.25}Cr_{0.5}Mn_{0.5}O_{3-\delta}$ Electrode. *J. Power Sources.* **2013**, 230, 115-121.

2. Xie, K.; Zhang, Y.; Meng, G.; and Irvine, J. T. Direct Synthesis of Methane from CO_2/H_2O in an Oxygen-Ion Conducting Solid Oxide Electrolyser. *Energy Environ. Sci*. **2011**, 4, 2218-2222.

3. Ebbesen, S. D.; Jensen, S. H.; Hauch, A.; Mogensen. M. B. High Temperature Electrolysis in Alkaline Cells, Solid Proton Conducting Cells, and Solid Oxide Cells. *Chem. Rev*. **2014**, 114, 10697-10734.

4. Bidrawn, F.; Kim, G.; Corre, G.; Irvine, J. T.; Vohs, J. M; Gorte, R. J. Efficient Reduction of CO_2 in a Solid Oxide Electrolyzer. *Electrochem. Solid-State Lett.* **2008**, 11, B167-B170.

5. Li, Y.; Wang, Y.; Doherty, W.; Xie, K.; Wu, Y. Perovskite Chromates Cathode with Exsolved Iron Nanoparticles for Direct High-Temperature Steam Electrolysis. *ACS Appl. Mater. Interfaces*. **2013**, 5, 8553-8562.

6. Bi, L.; Boulfrad, S.; Traversa, E. Steam Electrolysis by Solid Oxide Electrolysis Cells (SOECs) with Proton-Conducting Oxides. *Chem. Soc. Rev*. **2014**, 43, 8255-8270.

7. Xu, S.; Chen, S.; Li, M.; Xie, K.; Wang, Y.; Wu, Y. Composite Cathode based on Fe-Loaded LSCM for Steam Electrolysis in an Oxide-Ion-Conducting Solid Oxide Electrolyser. *J. Power Sources*. **2013**, 239, 332-340.

8. Zhang, J.; Xie, K.; Wei, H.; Qin, Q.; Qi, W.; Yang, L.; Ruan, C.; Wu, Y. *In Situ* Formation of Oxygen Vacancy in Perovskite $Sr_{0.95}Ti_{0.8}Nb_{0.1}M_{0.1}O_3$ (M=Mn, Cr) toward Efficient Carbon Dioxide Electrolysis. *Sci. Rep.* **2014**, 4, 7082-7095

9. Qi, W.; Gan, Y.; Yin, D.; Li, Z.; Wu, G.; Xie K.; Wu, Y. Remarkable Chemical Adsorption of Manganese-Doped Titanate for Direct Carbon Dioxide Electrolysis. *J. Mater. Chem. A.* **2014**, 2, 6904-6915.

10. Ebbesen, S.D.; Mogensen, M. Electrolysis of Carbon Dioxide in Solid Oxide Electrolysis Cells. *J. Power Sources*. **2009**, 193, 349-358.

11. Yue, X.; Irvine, J. T. Alternative Cathode Material for CO_2 Reduction by High Temperature Solid Oxide Electrolysis Cells. *J. Electrochem. Soc.* **2012**, 159, F442-F448.

12. Danilovic, N.; Vincent, A.; Luo, J; Chuang, K. T.; Hui, R.; Sanger, A. R. Correlation of Fuel Cell Anode Electrocatalytic and *ex situ* Catalytic Activity of Perovskites $La_{0.75}Sr_{0.25}Cr_{0.5}X_{0.5}O_{3-\delta}$ (X= Ti, Mn, Fe, Co). *Chem. Mater.* **2009**, 22, 957-965.

13. Tao, S.; Irvine, J. T. A Redox-Stable Efficient Anode for Solid-Oxide Fuel Cells. *Nat. Mater*. **2003**, 2, 320-323.

14. Tao, S.; Irvine, J. T. Synthesis and Characterization of $(La_{0.75}Sr_{0.25})Cr_{0.5}Mn_{0.5}O_{3-\delta}$, a Redox-Stable, Efficient Perovskite Anode for SOFCs. *J. Electrochem. Soc.* **2004**, 151, A252-A259.

15. Yue, X.; Irvine, J. T. Impedance Studies on LSCM/GDC Cathode for High Temperature CO_2 Electrolysis. *Electrochem. Solid-State Lett.* **2012**, 15, B31-B34.

16. Li, H.; Sun, G.; Xie, K.; Qi, W.; Qin, Q.; Wei, H.; Chen, S.; Wang, Y.; Zhang Y.; Wu, Y. Chromate Cathode Decorated with *in-situ* Growth of Copper Nanocatalyst for High Temperature Carbon Dioxide Electrolysis. *Int. J. Hydrogen Energy.* **2014**, 39, 20888-20897.

17. Yong, Z.; Mata, V.; Rodrigues, A. R. Adsorption of Carbon Dioxide at High Temperature—a Review. *Sep. Purif. Technol*. **2002**, 26, 195-205.

18. Liao, L.; Lien, C.; Shieh, D.; Chen M.; Lin. J. FTIR Study of Adsorption and Photoassisted Oxygen Isotopic Exchange of Carbon Monoxide, Carbon Dioxide, Carbonate, and Formate on TiO_2. *J. Phys. Chem. B.* **2002**, 106, 11240-11245.

19. Li, S.; Li, Y.; Gan, Y.; Xie, K.; Meng, G. Electrolysis of H_2O and CO_2 in an Oxygen-Ion Conducting Solid Oxide Electrolyzer with a $La_{0.2}Sr_{0.8}TiO_{3+\delta}$ Composite Cathode. *J. Power Sources.* **2012**, 218, 244-249.

20. Oishi, M.; Yashiro, K.; Sato, K.; Mizusaki, J.; Kawada, T. Oxygen Nonstoichiometry and Defect Structure Analysis of B-site Mixed Perovskite-Type Oxide (La, Sr)(Cr, M) $O_{3-\delta}$ (M= Ti, Mn and Fe). *J. Solid State Chem.* **2008**, 181, 3177-3184.

21. Tao, S.; Irvine, J. T. Catalytic Properties of the Perovskite Oxide $La_{0.75}Sr_{0.25}Cr_{0.5}Fe_{0.5}O_{3-\delta}$ in Relation to its Potential as a Solid Oxide Fuel Cell Anode Material. *Chem. Mater.* **2004**, 16, 4116-4121.

22. Green, R. D.; Liu, C. C.; Adler, S. B. Carbon Dioxide Reduction on Gadolinia-Doped Ceria Cathodes. *Solid State Ionics.* **2008**, 179, 647-660.

23. Sun, Y.; Li, J.; Chuang K.; Luo, J. Electrochemical Performance and Carbon Deposition Resistance of Ce-Doped $La_{0.7}Sr_{0.3}Fe_{0.5}Cr_{0.5}O_{3-\delta}$ Anode Materials for Solid Oxide Fuel Cells Fed with Syngas. *J. Power Sources.* **2015**, 274, 483-487.

24. Jia, Y. Crystal Radii and Effective Ionic Radii of the Rare Earth Ions. *J. Solid State Electrochem.* **1991**, 95, 184-187

25. Trofimenko, N. E.; Ullmann, H. Oxygen Stoichiometry and Mixed Ionic-Electronic Conductivity of $Sr_{1-a}Ce_aFe_{1-b}Co_bO_{3-x}$ Perovskite-Type Oxides. *J. Eur. Ceram. Soc.* **2000**, 20, 1241-1250.

26. Yao, W.; Duan, T.; Li, Y.; Yang, L.; Xie, K. Perovskite Chromate Doped with Titanium for Direct carbon Dioxide Electrolysis. *New J. Chem.* **2015**, 39, 2956 -2965.

27. Nitadori, T. H.; Misono, M. Catalytic Properties of $La_{1-x}A_xFeO_3$ (A= Sr, Ce) and $La_{1-x}Ce_xCoO_3$. *J. Catal.* **1985**, 93, 459-466

28. Zhang, Y. Q.; Li, J. H.; Sun, Y. F.; Hua, B.; Luo, J. L. Highly active and redox-stable Ce-doped LaSrCrFeO-based cathode catalyst for CO_2 SOECs. ACS Appl. Mater. Interfaces. **2016**, 8, 6457−6463.

Appendix II: The Excellence of Both Worlds: Developing Effective Double Perovskite Oxide Catalyst of Oxygen Reduction Reaction for Room and Elevated Temperature Applications

A II.1. Abstract

The efficiencies of a number of electrochemical devices (*e.g.*, fuel cells and MABs) are mainly governed by the kinetics of the oxygen reduction reaction (ORR). Among all the good ORR catalysts, the partially substituted double perovskite oxide ($AA'B_2O_{5+\delta}$) has the unique layered structure, providing a great flexibility regarding the optimization of its electronic structures and physicochemical properties. Herein, we demonstrate that the double perovskite oxide, *i.e.*, $NdBa_{0.75}Ca_{0.25}Co_{1.5}Fe_{0.5}O_{5+\delta}$, is a good ORR catalyst at both room and elevated temperatures. Under ambient condition, its half-wave potential of ORR in alkaline media was as low as 0.74 V vs RHE; at 650 °C, the cathodic polarization resistance was merely 0.0276 Ω cm^2 according to a symmetric cell measurement, whereas the solid oxide fuel cells using this cathode exhibited a maximum power density of 1982 mW cm^{-2}. From various materials characterizations, we hypothesize that its excellent ORR activity is strongly correlated with the crystallographic, electronic and defect structures of the materials.

A II.2. Introduction

Energy conversion is an important process that provides diversified forms of energy, e.g., electricity, for industrial productions as well as the daily life uses in human society. Since tremendous amount of fossil fuels is used to generate electrical power each year, energy conversion efficiency is, therefore, a key factor in reducing the environmental impacts and utilizing the valuable natural resources responsibly. In comparison with the conventional electricity generation methods, fuel cells are perhaps among the most promising alternatives, showing excellent environmental-friendliness, high efficiency and reasonable energy density. [1, 2, 3, 4] Practically, in each type of fuel cells, the rate-determining step is always believed to be the oxygen reduction reaction (ORR), due to the lack of the affordable yet high-performance electrocatalyst. [5, 6, 7, 8] For instance, the high cathodic overpotential loss is a major factor in undermining the performances of the state-of-the-art solid oxide fuel cells (SOFCs) at temperatures between 500~700 °C. [7] Similarly, in the researches on proton exchange membrane fuel cells (PEMFCs), desperate efforts are devoted to the development of highly active ORR catalysts to replace the state-of-the-art carbon supported platinum. [8]

Indeed, the noble metal contained materials, including Pt and its alloys, [8] were proven to be superior ORR catalysts. However, the problem is the very limited precious metals resources on this planet for large scale commercialization of the electrochemical devices referred above, not to mention their high prices and the ease of suffering degradations due to poisoning and/or leaching of metals. Alternatively, non-precious metals and compounds [9, 10] as well as metal-free materials, [11, 12, 13] *e.g.*, organometallic compounds and heteroatom-doped carbon materials, were developed that showed good ORR performances. In spite of that, the gradual deactivations of these catalysts

during the stability test were commonly observed, and the complicated synthesis protocols posted another challenge regarding the practical application. Recently, studies on perovskite oxides [4, 5, 6, 7, 14, 15, 16, 17, 18, 19, 20, 21, 22, 23, 24], such as $La_{0.5}Sr_{0.5}CoO_{2.91}$ (LSC), [16] $Ba_{0.5}Sr_{0.5}Co_{0.8}Fe_{0.2}O_{3-\delta}$ (BSCF), [17, 18] $PrBa_{0.5}Sr_{0.5}Co_{2-x}Fe_xO_{5+\delta}$ (PBSCF) [19] and $Sr_{0.95}Ag_{0.05}Nb_{0.1}Co_{0.9}O_{3-\delta}$ [20], offered a new dimension in tackling these challenges. Specifically, the double perovskite catalyst with a general formula of $AA'B_2O_{5+\delta}$ demonstrated much higher oxygen ion diffusion rate and surface-exchange coefficient relative to the ABO_3-type, contributing to a faster oxygen reduction reaction. [4, 7, 19, 20, 21, 22, 23, 24, 25, 26, 27, 28, 29]

Considering their fascinating features, one would envision intuitively that an excellent double perovskite ORR catalyst might perform well at both room and elevated temperatures, expanding their practical applications. [19, 26] The $LnBaCo_2O_{5+\delta}$ (Ln is the lanthanide element, *e.g.*, Sm, Nd or Pr) family is such a good example enabling the "best of both worlds", which has already exhibited great potentials as the cathode of SOFC. [19, 27, 28, 29, 30, 31] In this work, we report a novel ORR catalyst, $NdBa_{0.75}Ca_{0.25}Co_xFe_{2-x}O_{5+\delta}$ (NBCaCF, x=2, 1.5, 1, 0.5). The substitution of Ba with Ca contributed to a higher electronic conductivity without compromising the structural stability, [29] and the Fe dopant greatly promoted the ORR activity at both room and high temperatures. The origin of its excellent performance was also hypothesized.

A II.3. Results and discussions

A II.3.1. Crystal structure of the layered double perovskite

NBCaCF catalysts were prepared through the classic sol-gel method. A final calcination at 950 °C was applied to obtain the double perovskite phase (see the Supporting Information for details). Figure A II.1a shows the X-ray diffraction (XRD) patterns of NBCaCF, all suggesting the

formation of the double perovskite structure ($NdBaCo_2O_{5.92}$). The diffraction peaks shifted when increasing the Fe doping ratio. The Rietveld refinement, performed based on the orthorhombic structure, shows that the size of the unit cell increased in step with the Fe content (see Table A II.S1 and Figure A II.S1 in the Supporting Information). Typically in this double perovskite ($AA'B_2O_{5+\delta}$), the substitution of A (Nd) site cation by lower-valence A' (Ba, Ca) cation gave a layered structure with the A and A' cations alternating along the *c*-direction (…-[A'O]-[BO_2]-[AO_δ]-[BO_2]-…). Meanwhile, oxygen vacancies ($\delta<1$) concurrently formed to maintain the electroneutrality (see the crystal structure in Figure A II.1b and c). These oxygen vacancies were not randomly distributed, but located at the AO_δ layers, forming long-range ordered defect structures and rendering higher mobility of oxygen ions. [30, 31] In the transition metal layer, octahedral (BO_6) and pyramidal (BO_5) structures coexisted. Since Co^{3+}/Co^{4+} cation was slightly smaller than Fe^{3+}/Fe^{4+} cation, the substitution of Co by Fe resulted in the expansion of the unit cell (*c.f.* Table A II. 1 and Figure A II.S1).

Table A II. 1 The refined lattice parameters of the as-prepared samples.

Co	Space group	a(Å)	b(Å)	c(Å)	α(°)	β(°)	γ(°)
2.0	P/mmm(123)	3.8746	3.8892	7.6478	90	90	90
1.5	P/mmm(123)	3.8831	3.8953	7.6590	90	90	90
1.0	P/mmm(123)	3.8972	3.9056	7.6758	90	90	90
0.5	P/mmm(123)	3.9146	3.9213	7.6913	90	90	90

Transmission electron microscope (TEM) was also performed to study the crystal structure of $NdBa_{0.75}Ca_{0.25}Co_{1.5}Fe_{0.5}O_{5+\delta}$ (NBCaCF-1.5). The high-resolution TEM (HRTEM) micrographs and the electron diffraction patterns in Figures A II.1c reveal the [010] zone axis of the NBCaCF-1.5 double perovskite crystal. The yellow arrows indicate the domain boundaries, a typical type of defect in magnetic materials. The investigation of the diffractograms confirmed that NBCaCF-1.5

possessed an orthorhombic crystal lattice (P/mmm space group) which was in good agreement with the Rietveld refinement studies above. The crystal structure inset shows that oxygen vacancies preferred to locate at the [NdO_δ] layer, forming good channels for oxygen diffusion. More detailed studies are shown in Figure A II.S2. From the enlarged image in Figure A II.1d, we obtained the lattice parameters of the crystal (a=3.885 Å and c=7.661 Å) via measuring d-spacings, the results were very close to the refinement data in Table A II.S1. Besides, from the HRTEM image of the crystal surface (Figure A II.1e), we did not observe any dopant segregation, proving the advantage of using Ca as the dopant. In contrast, the ones incorporated with Sr often suffered from the performance degradation due to the enrichment of Sr near the surface [18, 32].

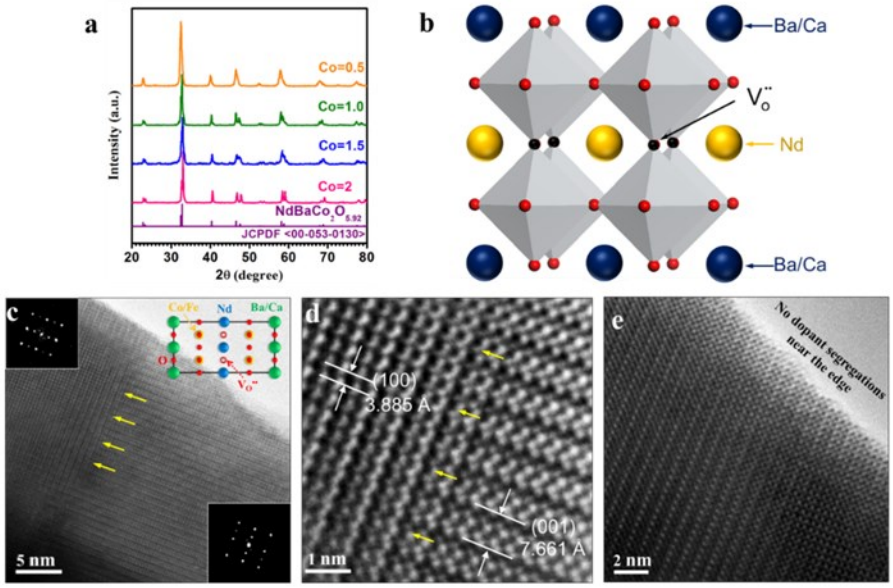

Figure A II. 1 (a) XRD patterns of the as-prepared NBCaCF powders; (b) a schematic of the crystal structure of NBCaCF; (c) HRTEM micrograph of NBCaCF-1.5, the arrows indicate the boundaries of two mutually perpendicular domains, the insets show the diffractograms of the two domains; (d) enlarged HRTEM image of the domain boundary shown in (c); (e) HRTEM image of NBCaCF-1.5 surface.

A II.3.2. ORR performance at elevated temperatures

The ORR activities of the NBCaCF catalysts were initially evaluated at high temperatures (≥500 °C) using $Gd_{0.1}Ce_{0.9}O_{1.9}$ (GDC) supported symmetrical cells, *i.e.*, NBCaCF-GDC/GDC/NBCaCF-GDC. Figure A II.S3a-d shows the Nyquist plots of the cells at temperatures between 500 and 700 °C. The value of the charge-transfer resistance (R_p) reflects the electro-catalytic properties of the catalyst employed. [33, 34] Among all the investigated doping ratios, the NBCaCF-1.5-GDC cathode exhibited the lowest R_p values of 0.315, 0.120, 0.055, 0.0276 and 0.015 Ω cm^2 at 500, 550, 600, 650 and 700 °C, respectively, implying that it is the best ORR catalyst among these compounds. Using the same cell configuration, we also measured the R_p of the state-of-the-art $Ba_{0.5}Sr_{0.5}Co_{0.8}Fe_{0.2}O_{3-\delta}$ (BSCF) catalyst for comparison. At 500, 550, 600, 650 and 700 °C, The R_p values were 0.985, 0.398, 0.163, 0.057 and 0.0285 Ω cm^2, respectively (see Figure A II.S3e). Albeit these values were essentially identical with those reported in the literature, [35] they were approximately 100 to 200% higher than those of NBCaCF-1.5 cathode. Figure A II.2a shows the Arrhenius plots of reciprocal R_p, from which the activation energies were calculated. The NBCaCF-1.5 catalyst also demonstrated the lowest activation energy (E_a = 95.18 kJ mol^{-1}) which was more than 10% lower than that of BSCF (E_a=112.24 kJ mol^{-1}). We also measured the total conductivity of NBCaCF shown in Figure A II.S4. For instance, the conductivity of NBCaCF-1.5 reached 641 S cm^{-1} at 550 °C, much higher than that of BSCF. [36, 37] Therefore, we speculated that the superior ORR performance of NBCaCF catalysts pertained to 1) the disorder-free channels of oxygen vacancies that enhance the mobility of oxygen ions as well as the surface oxygen exchange rate; 2) the increased electronic conductivity which is a critical requirement of a good electro-catalyst.

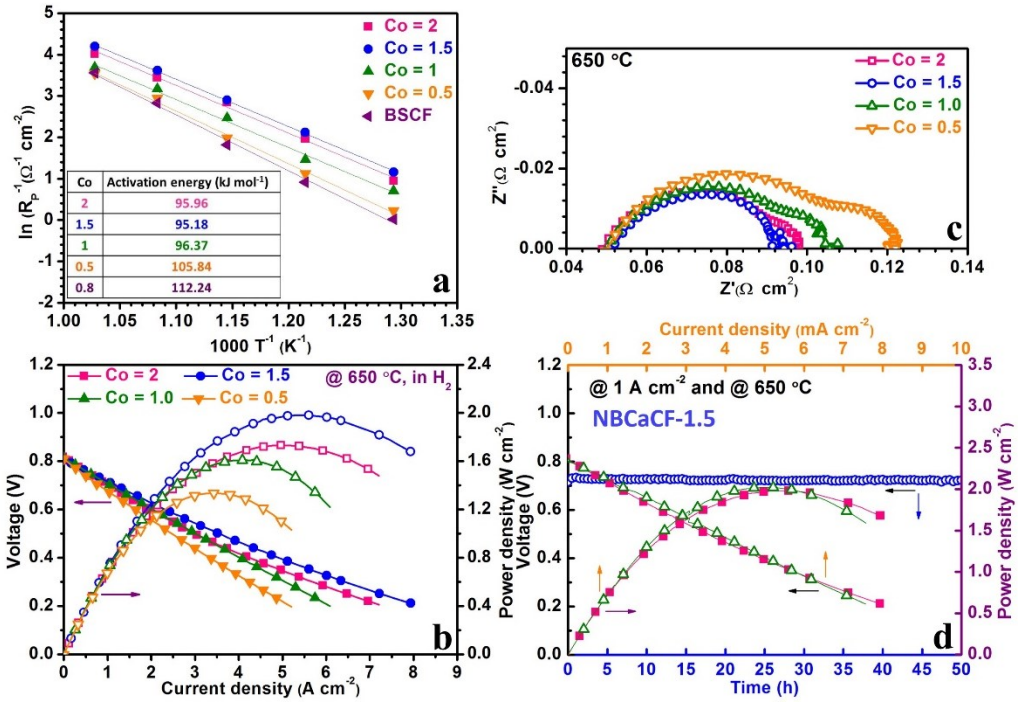

Figure A II. 2 (a) The Arrhenius plots of reciprocal R_p for different catalysts; (b) J-V and power density curves of Ni-GDC anode supported cells employed with different NBCaCF cathode and (c) the corresponding impedance spectra measured at 650 °C in H_2; (d) stability test of NBCaCF-1.5 cell operated at 650 °C under a constant current load of 1 A cm^{-2} in H_2, and the J-V/power density curves of the same cell before (triangle) and after (square) the test.

The exceptional ORR activity of NBCaCF enabled its practical application in low-temperature SOFCs (500~650 °C). [38] We then examined the performance of NBCaCF-GDC cathode using the state-of-the-art anode supported button cells. The current density-voltage (J-V) curves and the corresponding power density plots of the cells at 650 °C in the stream of hydrogen are shown in Figure A II.2b. The open-circuit voltage (OCV) was ~0.81 V for all cells, which was reasonable since the GDC electrolyte shows electronic conductivity. Nonetheless, the NBCaCF-1.5-GDC cell outperformed the rest and showed a high peak power density (PPD) of 1982 mW cm^{-2}, which is

among the best in the literature. [17, 38, 39, 40] More J-V and power density plots at the temperature range between 550 and 650 °C can be found in Figure A II.S6.

In the corresponding impedance spectra given in Figure A II.2c, the ohmic resistances (R_Ω) for all cells were roughly the same, ranging from 0.048 to 0.052 Ω cm^2. However, the cells with NBCaCF-1.5 cathode had the lowest R_p. The stability test of the NBCaCF-1.5 cell was shown in Figure A II.2d. The voltage was recorded as a function of time under a constant current load of 1 A cm^{-2} at 650 °C. The J-V/power density curves of the cell before (square) and after (triangle) the stability test were also recorded. Apparently, negligible degradation was observed after 50 h test, suggesting the excellent chemical-electrochemical stability and electrolyte compatibility of this cathode material under real SOFC operating conditions.

A II.3.3. ORR performance at room temperature

NBCaCF catalysts also demonstrated good ORR activity at room temperature. The detailed preparation protocol of the glassy carbon rotating disc electrode (RDE) was discussed in the Supporting Information. In the cyclic voltammetry (CV) measurement in 0.1 M KOH aqueous solution, no reduction peak was recorded in the Ar-saturated electrolyte whereas a strong reduction signal was seen in the O_2-saturated one (Figure A II.S7). Hence, we confirmed that this redox process was linked to the reduction of O_2. Meanwhile, NBCaCF-1.5 possessed the highest cathodic reduction peak current (-0.81 mA cm^{-2}), and the half-wave potential ($E_{1/2}$) for ORR reached 0.74 V vs RHE.

Linear sweep voltammetry (LSV) was then performed to compare the activities of various NBCaCF catalysts. It was logic to find that the limiting current density had a positive correlation

with the rotation rate (400 rpm to 2500 rpm) while the ORR onset potential (E_{onset}) was independent of it (see Figure A II.S8). Figure 3a compares the LSV curves of various catalysts obtained at 1600 rpm. The E_{onset} of BSCF was 0.86 V (vs RHE), which was 90 mV negative to that of the state-of-the-art Pt/C catalyst (0.95 V) that we had measured before. [41] For NBCaCF series, the E_{onset} increased in step with the rising of iron doping ratio (*x*). Again, similar to the test in SOFC, the best ORR activity was also achieved using the NBCaCF-1.5 catalyst. It exhibited the most positive E_{onset} (0.91 V), the highest limiting current density (5.87 mA cm^{-2}) and the most positive $E_{1/2}$ (0.74 V). Indeed, this performance was lower than that of the Pt/C catalyst but was among the best alternative ORR catalysts documented in the literature. A detailed comparison of $E_{1/2}$ was summarized in Table A II.S2 in the Supporting Information.

To understand the oxygen reduction pathway, we drew the Koutecky-Levich (K-L) plots for both NBCaCF and BSCF catalysts, in which the inverse current density (J^{-1}) was plotted as a function of the inverse of the square root of the rotation speed ($\omega^{-1/2}$) at 0.4, 0.3, 0.2 and 0.1 V (see Figures A II.3b and S9). The number of electrons transferred were then determined by the empirical K-L equations (Equations A II.S1~S4). Notably, the electron-transfer number *n* for the NBCaCF-1.5 catalyst was approximately 3.7~3.8 in the potential range from 0.4 to 0.1 V (Figure A II.3c), implying that almost all reacted O_2 was fully reduced to H_2O. This four-electron pathway is preferable in terms of achieving high efficiency during the electrochemical energy conversion. We also studied the stability of NBCaCF-1.5 catalyst via a chronoamperometric measurement (see Figure A II.3d). After biasing the cell for 20000 s at a constant voltage of 0.624 V, the oxygen reduction current density of the NBCaCF-1.5 cell decreased by ~10.0%. Conversely, the BSCF cell exhibited a 23.6% decrease under the same condition.

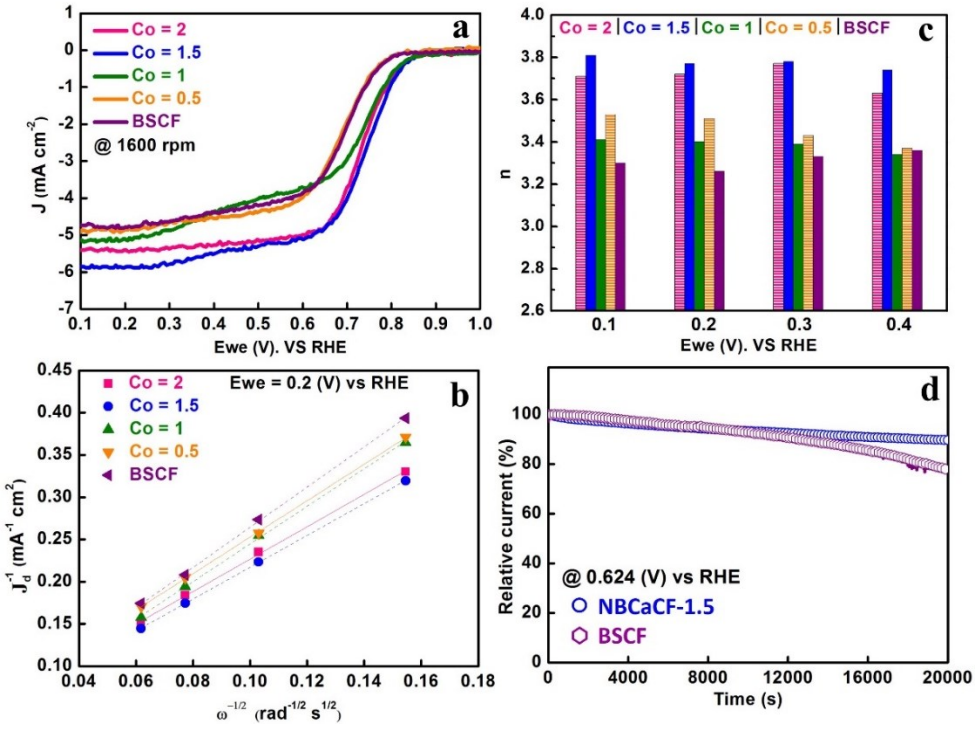

Figure A II. 3 (a) LSV plots of NBCaCF and BSCF catalysts; (b) Koutecky-Levich plots of NBCaCF and BSCF catalysts at Ewe=0.2 V vs RHE; (c) the plot of electron transfer number during ORR versus voltage; (d) chronoamperometric test for NBCaCF-1.5 and BSCF catalysts in O_2-saturated 0.1 M KOH solution at 0.624 V vs RHE.

A II.3.4. Mechanistic discussions

In the scenarios of both PEMFC and SOFC, the developed layered-perovskite NBCaCF cathode catalysts exhibited substantially increased ORR activity relative to the conventional perovskite counterparts (e.g., BSCF). Note that the examined catalysts in this work showed similar specific surface areas (Table A II.S3) and the electrodes exhibited essentially identical pore-size distributions (see the plots in Figure A II.S10). We then asserted that the electrochemical activity differences among these materials did not stem from the contribution of the varied surface areas. Indeed, the unique crystal structure might be a key factor influencing ORR activity as discussed

above. The layered structure provides well-defined oxygen vacancy channels, facilitating the oxygen transport in the planes of $[NdO_{\delta}]//[Co/FeO_2]$. This is particularly important in SOFC applications since the entire NBCaCF surface becomes the triple-phase boundary (TPB) due to the mixed ionic-electronic conductivity. Compared with the conventional TPB that only locates in the adjacent areas of electrolyte-electrode interfaces, the expanded TPB provides many more active sites for the electrochemical reaction.

Besides the crystallographic structure, the surface chemistry (defects, electronic structure, etc.) of the catalyst can also greatly affect the kinetics of ORR. [41] X-ray photoelectron spectroscopy (XPS) measurement was then performed on all NBCaCF catalysts. The deconvoluted spectra were shown in Figure A II.4. For all the samples, the O1s spectra presented two partially superimposed peaks at 528.2~528.5 eV and 530.9~531.2 eV, respectively. Generally, the peak with lower binding energy (BE) is associated with the lattice oxygen (O_L), whereas the one with higher BE corresponds to the adsorbed or loosely bonded oxygen (O_A) that, in this case, is correlated with the surface oxygen vacancies. [42] Apparently, NBCaC and NBCaCF-1.5 had higher proportions of surface oxygen vacancies with respect to lattice oxygen as summarized in Table A II.1. These surface defects usually have higher energy states and might be important active sites for the O_2 adsorption/dissociation. [4] Although the total amount of oxygen vacancies of NBCaCF-1.5 was lower than that of NBCaC according to the nonstoichiometric oxygen measurement (Figure A II.S12), NBCaCF-1.5 had the highest concentration of surface oxygen vacancies, making it the most electrochemically active catalyst among the series (see Figures A II.2 and 3).

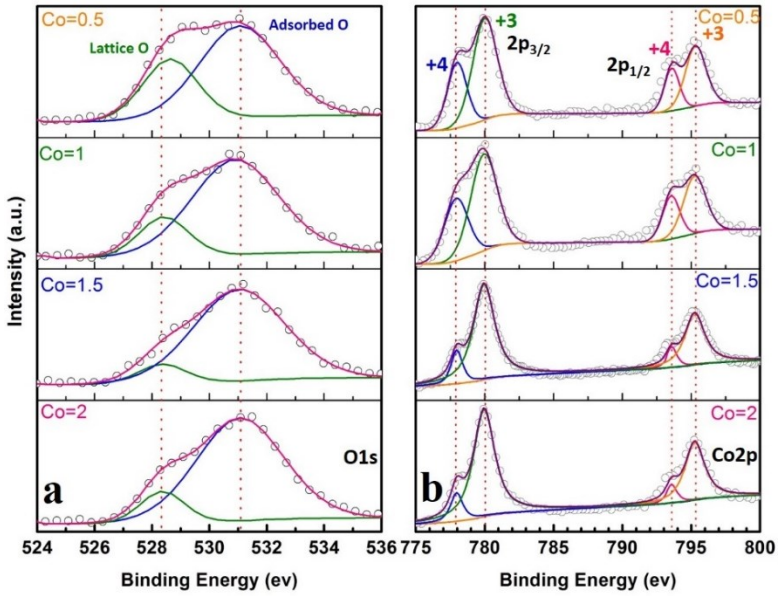

Figure A II. 4 XPS spectra of NBCaCF catalysts obtained for (a) O1s and (b) Co2p.

This conclusion was also supported by the temperature programmed desorption measurement (O_2-TPD, Figure A II.S13). Remarkably, all the investigated materials exhibited two distinct regimes of O_2 desorption. The first regime appeared below 500 °C, pertaining to the desorption of chemisorbed oxygen species. The higher desorption temperatures for NBCaC and NBCaCF (~400 °C *vs* 250 °C for BSCF) showed that the bonds between the catalyst and the adsorbate were stronger, implying that O_2 was more easily adsorbed and dissociated on the layered perovskite oxide. Moreover, NBCaCF also exhibited the highest amount of adsorbed oxygen, revealing the highest surface coverage of oxygen atoms. This might also stem from its high concentration of surface oxygen vacancies (*c.f.* the XPS data in Figure A II.4a). The second regime appeared between 700 to 850 °C and was attributable to the release of lattice oxygen. The intensity of the peak strongly correlated to the amount of oxygen vacancies generated at elevated temperatures. Notably, the layered perovskite oxides had more defects than BSCF, leading to easier oxygen activation, incorporation, and diffusion when employed as the cathode of SOFC.

Additionally, the redox properties of the B-site metal ions are believed to strongly affect the ORR activity of perovskite catalyst. [43, 44] Hence, we also analyzed the XPS spectra of these elements. The results in Figures A II.4b and S10 reveal the coexistence of two redox couples, *i.e.*, Co^{3+}/Co^{4+} and Fe^{3+}/Fe^{4+}, in NBCaCF samples. Both of them can contribute to the oxygen reduction reaction. Presumably due to the presence of stronger Fe-O bonds in the lattice, NBCaCF showed improved structure stability compared with NBCaC, as reflected by the lower thermal expansion coefficient (Figure A II.S14) and the better redox stability (Figure A II.S15). We can also explain the advantages of Fe doping from the perspective of the electronegativity of the material, which was considered to influence the ORR activity. [45] The Pauling electronegativity of Co^{3+}/Co^{4+} (1.88) is larger than that of Fe^{3+}/Fe^{4+} (1.83). Thus, the global electronegativity of NBCaC was lowered by doping suitable amount of Fe that enhanced the charge transfer rate during electrochemical ORR. However, the addition of Fe decreased the electrical conductivity (Figure A II.S5) and the total amount of oxygen vacancies (Figure A II.S12), which undermined the electrocatalytic performances. Thus, finding the right compromise (doping ratio) is critical to maximize the electro-activity.

Table A II. 1 Quantitative analysis of the O_L and O_A on the surface of NBCaCF catalysts.

Co	**Area of O_L**	**Area of O_A**	**$O_A/(O_A+O_L)$ (%)**
2.0	1370.31	8684.76	86.37
1.5	935.94	8144.12	89.69
1.0	1943.37	8036.94	80.53
0.5	4167.24	9189.31	68.8

A II.4. Conclusions

We found that the layered perovskite-type cobaltite, *i.e.*, $NdBa_{0.75}Ca_{0.25}Co_{1.5}Fe_{0.5}O_{5+\delta}$ demonstrates good activity towards ORR at both room and elevated temperatures, which makes it suitable for wide range applications. The unique crystal structure provided distortion-free channels for oxygen transfers; the addition of appropriate amount of Fe dopant (x=1.5) drastically optimized the physicochemical properties of the catalyst, rendering a high ORR onset potential (0.91 V) at room temperature and excellent SOFC performances at 650 °C (PPD = 1982 mW cm^{-2}). This cost-effective material promises to replace the Pt/C ORR catalyst in PEMFCs, and to further lower the operating temperature of SOFCs.

A II.5. References

(1) a. P. S. Y. Gogotsi. True Performance Metrics in Electrochemical Energy Storage. *Science* **2011,** *334*, 917-918.

(2) J. R. Miller; P. Simon. Materials science. Electrochemical capacitors for energy management. *Science* **2008,** *321* (5889), 651-2.

(3) L. Mai; X. Tian; X. Xu; L. Chang; L. Xu. Nanowire electrodes for electrochemical energy storage devices. *Chem. Rev.* **2014,** *114* (23), 11828-62.

(4) D. Chen; C. Chen; Z. M. Baiyee; Z. Shao; F. Ciucci. Nonstoichiometric Oxides as Low-Cost and Highly-Efficient Oxygen Reduction/Evolution Catalysts for Low-Temperature Electrochemical Devices. *Chem. Rev.* **2015,** *115* (18), 9869-921.

(5) W. T. Hong; M. Risch; K. A. Stoerzinger; A. Grimaud; J. Suntivich; Y. Shao-Horn. Toward the rational design of non-precious transition metal oxides for oxygen electrocatalysis. *Energy Environ. Sci.* **2015,** *8* (5), 1404-1427.

(6) Z. Ma; X. Yuan; L. Li; Z.-F. Ma; D. P. Wilkinson; L. Zhang; J. Zhang. A review of cathode materials and structures for rechargeable lithium–air batteries. *Energy Environmen. Sci.* **2015,** *8* (8), 2144-2198.

(7) D. Ding; X. Li; S. Y. Lai; K. Gerdes; M. Liu. Enhancing SOFC cathode performance by surface modification through infiltration. *Energy Environmen. Sci.* **2014,** *7* (2), 552.

(8) Y. J. Wang; N. Zhao; B. Fang; H. Li; X. T. Bi; H. Wang. Carbon-supported Pt-based alloy electrocatalysts for the oxygen reduction reaction in polymer electrolyte membrane fuel cells: particle size, shape, and composition manipulation and their impact to activity. *Chem. Rev.* **2015,** *115* (9), 3433-67.

(9) M.-Q. Wang; W.-H. Yang; H.-H. Wang; C. Chen; Z.-Y. Zhou; S.-G. Sun. Pyrolyzed Fe–N–C Composite as an Efficient Non-precious Metal Catalyst for Oxygen Reduction Reaction in Acidic Medium. *ACS Catal.* **2014,** *4* (11), 3928-3936.

(10) N. Ranjbar Sahraie; J. P. Paraknowitsch; C. Gobel; A. Thomas; P. Strasser. Noble-metal-free electrocatalysts with enhanced ORR performance by task-specific functionalization of carbon using ionic liquid precursor systems. *J. Am. Chem. Soc.* **2014,** *136* (41), 14486-97.

(11) L. Dai; Y. Xue; L. Qu; H. J. Choi; J. B. Baek. Metal-free catalysts for oxygen reduction reaction. *Chem. Rev.* **2015,** *115* (11), 4823-92.

(12) C. Li; X. Han; F. Cheng; Y. Hu; C. Chen; J. Chen. Phase and composition controllable synthesis of cobalt manganese spinel nanoparticles towards efficient oxygen electrocatalysis. *Nat. Commun.* **2015,** *6*, 7345.

(13) J. Zhang; Z. Zhao; Z. Xia; L. Dai. A metal-free bifunctional electrocatalyst for oxygen reduction and oxygen evolution reactions. *Nat. Nanotechnol.* **2015,** *10* (5), 444-52.

(14) C. C. Matthew S. Dyer, Darren Hodgeman, Philip A. Chater, Antoine Demont, Simon Romani, Ruth Sayers, Michael F. Thomas, John B. Claridge, George R. Darling, Matthew J. Rosseinsky. Computationally Assisted Identification of Functional Inorganic Materials. *Science* **2013,** *340*, 847-852.

(15) K. J. M. Jin Suntivich, Hubert A.Gasteiger, John B. Goodenough, Yang Shao-Horn. A Perovskite Oxide Optimized for Oxygen Evolution Catalysis from Molecular Orbital Principles. *Science* **2011,** *334*, 1383-1385.

(16) Y. Zhao; L. Xu; L. Mai; C. Han; Q. An; X. Xu; X. Liu; Q. Zhang. Hierarchical mesoporous perovskite La0.5Sr0.5CoO2.91 nanowires with ultrahigh capacity for Li-air batteries. *Proc. Natl. Acad. Sci. USA* **2012,** *109* (48), 19569-74.

(17) S. M. H. Zongping Shao. A high-performance cathode for the next generation of solid-oxide fuel cells. *Nature* **2004,** *431*, 170-173.

(18) J. I. Jung; H. Y. Jeong; M. G. Kim; G. Nam; J. Park; J. Cho. Fabrication of $Ba_{0.5}Sr_{0.5}Co_{0.8}Fe_{0.2}O_{(3-\delta)}$ catalysts with enhanced electrochemical performance by removing an inherent heterogeneous surface film layer. *Adv. Mater.* **2015,** *27* (2), 266-71.

(19) S. Choi; S. Yoo; J. Kim; S. Park; A. Jun; S. Sengodan; J. Kim; J. Shin; H. Y. Jeong; Y. Choi; G. Kim; M. Liu. Highly efficient and robust cathode materials for low-temperature solid oxide fuel cells: PrBa0.5Sr0.5Co(2-x)Fe(x)O(5+delta). *Sci. Rep.* **2013,** *3*, 2426.

(20) Y. Zhu; W. Zhou; R. Ran; Y. Chen; Z. Shao; M. Liu. Promotion of Oxygen Reduction by Exsolved Silver Nanoparticles on a Perovskite Scaffold for Low-Temperature Solid Oxide Fuel Cells. *Nano Lett.* **2016,** *16* (1), 512-8.

(21) Y. Zhu; W. Zhou; Y. Chen; J. Yu; X. Xu; C. Su; M. O. Tadé; Z. Shao. Boosting Oxygen Reduction Reaction Activity of Palladium by Stabilizing Its Unusual Oxidation States in Perovskite. *Chem. Mater.* **2015,** *27* (8), 3048-3054.

(22) W. Zhou; J. Sunarso; Z.-G. Chen; L. Ge; J. Motuzas; J. Zou; G. Wang; A. Julbe; Z. Zhu. Novel B-site ordered double perovskite Ba2Bi0.1Sc0.2Co1.7O6−xfor highly efficient oxygen reduction reaction. *Energy Environ. Sci.* **2011,** *4* (3), 872-875.

(23) W. Zhou; J. Sunarso; M. Zhao; F. Liang; T. Klande; A. Feldhoff. A highly active perovskite electrode for the oxygen reduction reaction below 600 degrees ºC. *Angew. Chem. Int. Ed.* **2013,** *52* (52), 14036-40.

(24) J. Yu; J. Sunarso; Y. Zhu; X. Xu; R. Ran; W. Zhou; Z. Shao. Activity and Stability of Ruddlesden-Popper-Type $La_{n+}1Ni_n\ O_{3n+1}$ (n=1, 2, 3, and ∞) Electrocatalysts for Oxygen Reduction and Evolution Reactions in Alkaline Media. *Chemistry* **2016,** *22* (8), 2719-27.

(25) M. Burriel; J. Peña-Martínez; R. J. Chater; S. Fearn; A. V. Berenov; S. J. Skinner; J. A. Kilner. Anisotropic Oxygen Ion Diffusion in Layered PrBaCo2O5+δ. *Chem. Mater.* **2012,** *24* (3), 613-621.

(26) A. Chroneos; B. Yildiz; A. Tarancón; D. Parfitt; J. A. Kilner. Oxygen diffusion in solid oxide fuel cell cathode and electrolyte materials: mechanistic insights from atomistic simulations. *Energy Environ. Sci.* **2011,** *4* (8), 2774.

(27) S. Yoo; S. Choi; J. Kim; J. Shin; G. Kim. Investigation of layered perovskite type $NdBa_{1-x}Sr_xCo_2O_{5+\delta}$ (x=0, 0.25, 0.5, 0.75, and 1.0) cathodes for intermediate-temperature solid oxide fuel cells. *Electrochim. Acta* **2013,** *100*, 44-50.

(28) S. Kim; A. Jun; O. Kwon; J. Kim; S. Yoo; H. Y. Jeong; J. Shin; G. Kim. Nanostructured Double Perovskite Cathode With Low Sintering Temperature For Intermediate Temperature Solid Oxide Fuel Cells. *ChemSusChem* **2015,** *8* (18), 3153-8.

(29) S. Yoo; A. Jun; Y. W. Ju; D. Odkhuu; J. Hyodo; H. Y. Jeong; N. Park; J. Shin; T. Ishihara; G. Kim. Development of double-perovskite compounds as cathode materials for low-temperature solid oxide fuel cells. *Angew. Chem. Int. Ed.* **2014,** *53* (48), 13064-7.

(30) J.-H. Kim; A. Manthiram. Layered $LnBaCo_2O_{5+\delta}$ perovskite cathodes for solid oxide fuel cells: an overview and perspective. *J. Mater. Chem. A* **2015,** *3* (48), 24195-24210.

(31) H. Tellez; J. Druce; J. A. Kilner; T. Ishihara. Relating surface chemistry and oxygen surface exchange in $LnBaCo_2O_{(5+\delta)}$ air electrodes. *Faraday discussions* **2015,** *182*, 145-57,.

(32) M. Finsterbusch; A. Lussier; J. A. Schaefer; Y. U. Idzerda. Electrochemically driven cation segregation in the mixed conductor La0.6Sr0.4Co0.2Fe0.8O3−δ. *Solid State Ionics* **2012,** *212*, 77-80.

(33) J. W. Curtis Conner, and John L. Falconer. Spillover in Heterogeneous Catalysis. *Chem. Rev.* **1995,** *95*, 759-788.

(34) S. B. Adler. Factors Governing Oxygen Reduction in Solid Oxide Fuel Cell Cathodes. *Chem. Rev.* **2004,** *104*, 4791-4843.

(35) J. G. Lee; J. H. Park; Y. G. Shul. Tailoring gadolinium-doped ceria-based solid oxide fuel cells to achieve 2 W cm^{-2} at 550 degrees ºC. *Nat. Commun.* **2014,** *5*, 4045.

(36) J.-I. Jung; S. T. Misture; D. D. Edwards. Oxygen stoichiometry, electrical conductivity, and thermopower measurements of BSCF (Ba0.5Sr0.5CoxFe1−xO3−δ, 0≤x≤0.8) in air. *Solid State Ionics* **2010,** *181* (27-28), 1287-1293.

(37) J.-I. Jung; S. T. Misture; D. D. Edwards. Seebeck coefficient and electrical conductivity of BSCF (Ba0.5Sr0.5CoxFe1−xO3−δ, 0≤x≤0.8) as a function of temperature and partial oxygen pressure. *Solid State Ionics* **2012,** *206*, 50-56.

(38) J. T. Chuancheng Duan, Meng Shang, Stefan Nikodemski, Michael Sanders, Sandrine Ricote, Ali Almansoori, Ryan O'Hayre. Readily processed protonic ceramic fuel cells with high performance at low temperatures. *Science* **2015,** *349*, 1321-1326.

(39) M. Li; W. Zhou; V. K. Peterson; M. Zhao; Z. Zhu. A comparative study of $SrCo_{0.8}Nb_{0.2}O_{3-\delta}$ and $SrCo_{0.8}Ta_{0.2}O_{3-\delta}$ as low-temperature solid oxide fuel cell cathodes: effect of non-geometry factors on the oxygen reduction reaction. *J. Mater. Chem. A* **2015,** *3* (47), 24064-24070.

(40) J. Kim; S. Sengodan; G. Kwon; D. Ding; J. Shin; M. Liu; G. Kim. Triple-conducting layered perovskites as cathode materials for proton-conducting solid oxide fuel cells. *ChemSusChem* **2014,** *7* (10), 2811-5.

(41) D. Eisenberg; W. Stroek; N. J. Geels; C. S. Sandu; A. Heller; N. Yan; G. Rothenberg. A Simple Synthesis of an N-Doped Carbon ORR Catalyst: Hierarchical Micro/Meso/Macro Porosity and Graphitic Shells. *Chemistry* **2016,** *22* (2), 501-5.

(42) J.-W. Yin; Y.-M. Yin; J. Lu; C. Zhang; N. Q. Minh; Z.-F. Ma. Structure and Properties of Novel Cobalt-Free Oxides $Nd_xSr_{1-x}Fe_{0.8}Cu_{0.2}O_{3-\delta}$ ($0.3 \leq x \leq 0.7$) as Cathodes of Intermediate Temperature Solid Oxide Fuel Cells. *J. Phy. Chem. C* **2014,** *118* (25), 13357-13368.

(43) T. Takeguchi; T. Yamanaka; H. Takahashi; H. Watanabe; T. Kuroki; H. Nakanishi; Y. Orikasa; Y. Uchimoto; H. Takano; N. Ohguri; M. Matsuda; T. Murota; K. Uosaki; W. Ueda. Layered perovskite oxide: a reversible air electrode for oxygen evolution/reduction in rechargeable metal-air batteries. *J. Am. Chem. Soc.* **2013,** *135* (30), 11125-30.

(44) J. Sunarso; A. A. J. Torriero; W. Zhou; P. C. Howlett; M. Forsyth. Oxygen Reduction Reaction Activity of La-Based Perovskite Oxides in Alkaline Medium: A Thin-Film Rotating Ring-Disk Electrode Study. *J. Phy. Chem. C* **2012,** *116* (9), 5827-5834.

(45) R. T. Sanderson. Electronegativity and Bond Energy. *J. Am. Chem. Soc.* **1983,** *105*, 2259-2261

A II.6. Supporting information

A II.6.1. Materials preparation

Preparation of catalyst powders. To prepare $NdBa_{0.75}Ca_{0.25}Co_xFe_{2-x}O_{5+\delta}$ powders, stoichiometric amounts of $Nd(NO_3)_3 \cdot 6H_2O$, $Ba(NO_3)_2$, $Ca(NO_3)_2$, $Co(NO_3)_3 \cdot 6H_2O$ and $Fe(NO_3)_3 \cdot 9H_2O$ were initially dissolved in distilled water using citric acid (CA) and ethylenediaminetetraacetic acid (EDTA) as the chelating agents. All the chemicals were purchased from Fisher scientific. The molar ratio of EDTA : CA : total metal ions was 2:2:1. Then the solution was heated up to 300 °C in an oven till water was fully vaporized. The sequentially obtained powder was finally calcined at 950 °C for 5 h to form the double perovskite phase. $Ba_{0.5}Sr_{0.5}Co_{0.8}Fe_{0.2}O_{3-\delta}$ (BSCF) catalyst was also prepared via the same method.

Fabrication of dense NBCaCF. NBCaCF powders were pressed into bars for the electrical conductivity measurements, and rods for the thermal expansion coefficient measurements, using suitable dies. Then, they were sintered in air at 1150 °C for 12 hours for densification.

Fabrication of symmetrical cells. 10 mol% Gd_2O_3 stabilized CeO_2 (GDC) electrolyte-supported symmetrical cells were employed to evaluate the electrochemical activity for the ORR at elevated temperatures. Dense GDC electrolyte substrates were fabricated by dry pressing GDC powder (TC-grade, FCM) in a cylindrical die, followed by sintering in air at 1450 °C for 5 h. NBCaCF-GDC or BSCF-GDC (weight ratio was 60:40) cathodes were prepared by brush painting the slurry on both sides of the GDC electrolyte, followed by sintering in air at 950 ºC for 5 h. The active area of the cathode was 0.5 cm^2.

Fabrication of anode-supported cells. To prepare the Ni-GDC anode support, NiO (Fisher scientific), GDC powder and corn starch were mixed and ball-milled in isopropyl, the weight ratio

of NiO : GDC : corn starch is 60:40:10. The anode substrate was fabricated by dry pressing 1 g of the mixed powder in a cylindrical die, followed by pre-sintering at 1050 °C in air for 2 h. Thin GDC electrolyte was prepared using a slurry coating technique. GDC slurry was prepared by dispersing 2 g GDC powder in 6 g ethanol with a small amount of cellulose and triethanolamine as binder and dispersant, respectively. This slurry was spin-coated on the strong Ni-GDC substrate. The thickness of GDC membrane was well controlled via varying the times of coating. The coated Ni-GDC substrate was then co-sintered at 1450 °C for 5 h. To prepare the cathode, NBCaCF-GDC (weight ratio is 60:40) paste was then brush-painted on the surface of the densified GDC electrolyte, followed by calcination at 950 °C for 4 h. The active area of the cathode was 0.316 cm^2.

Preparation of the working electrode. For the low temperature ORR test, the catalyst ink was initially prepared by adding 0.1 g of catalyst powders and 0.1 g carbon black (Cabot) in a solution containing 2 mL of 5wt. % Nafion (Aldrich) and 8 mL of isopropyl alcohol. 3 h of sonication was applied to obtain full homogenization. 5 μL of the catalysts ink was dispersed on the polished glassy carbon (GC) working electrode (glassy carbon rotating disc electrode, 5 mm in diameter, model AFE5T050GC from Pine Research Instrumentation). Catalyst-coated GC electrodes were then dried under ambient condition for 1 h.

A II.6.2. Electrochemical test procedure

In the SOFC test, Au paste was painted on both electrodes and then baked in air at 750 °C for 2 h. Then, Pt mesh was applied on the paste as the current collector that was connected with Pt wires. The open-circuit electrochemical impedance spectroscopy (EIS) measurement of the symmetrical cells was carried out at temperatures ranging from 500 to 700 °C in air. The anode support cell (anode side) was sealed to an alumina tube using the Ceramabond® glass sealant (Aremco Product,

Inc.) and reduced *in-situ* in H_2 at 650 °C for 2 h prior to the electrochemical measurements. The open-circuit EIS, the current-voltage (J-V) and power density curves of the full cell were obtained at temperatures ranging from 550 to 650 °C in H_2. All tests were conducted using an impedance/gain-phase analyzer (Solartron 1255) and an electrochemical interface (Solartron 1287). The flow rates of H_2 and air were 40 mL min^{-1} and 150 mL min^{-1}, respectively.

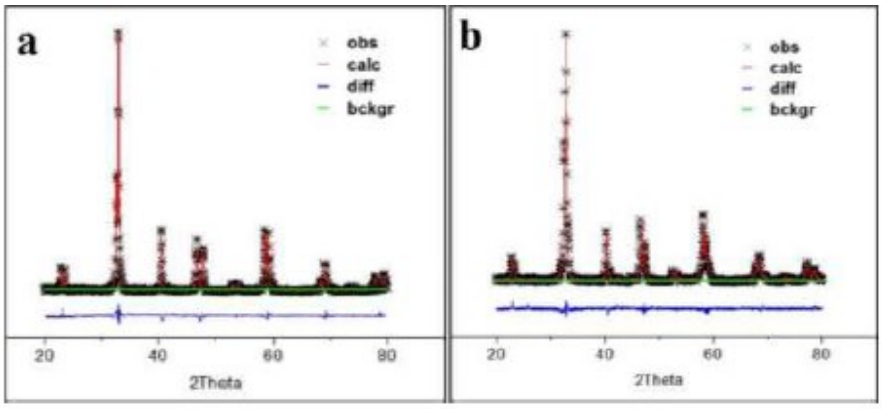

Figure AII.S 1 Rietveld refinement data for (a) $NdBa_{0.75}Ca_{0.25}Co_2O_{5+\delta}$ (NBCaC, x=2), and (b) $NdBa_{0.75}Ca_{0.25}CoFeO_{5+\delta}$ (NBCaCF-1, x=1). The refinement was performed based on the orthorhombic lattice geometry and P/mmm space group.

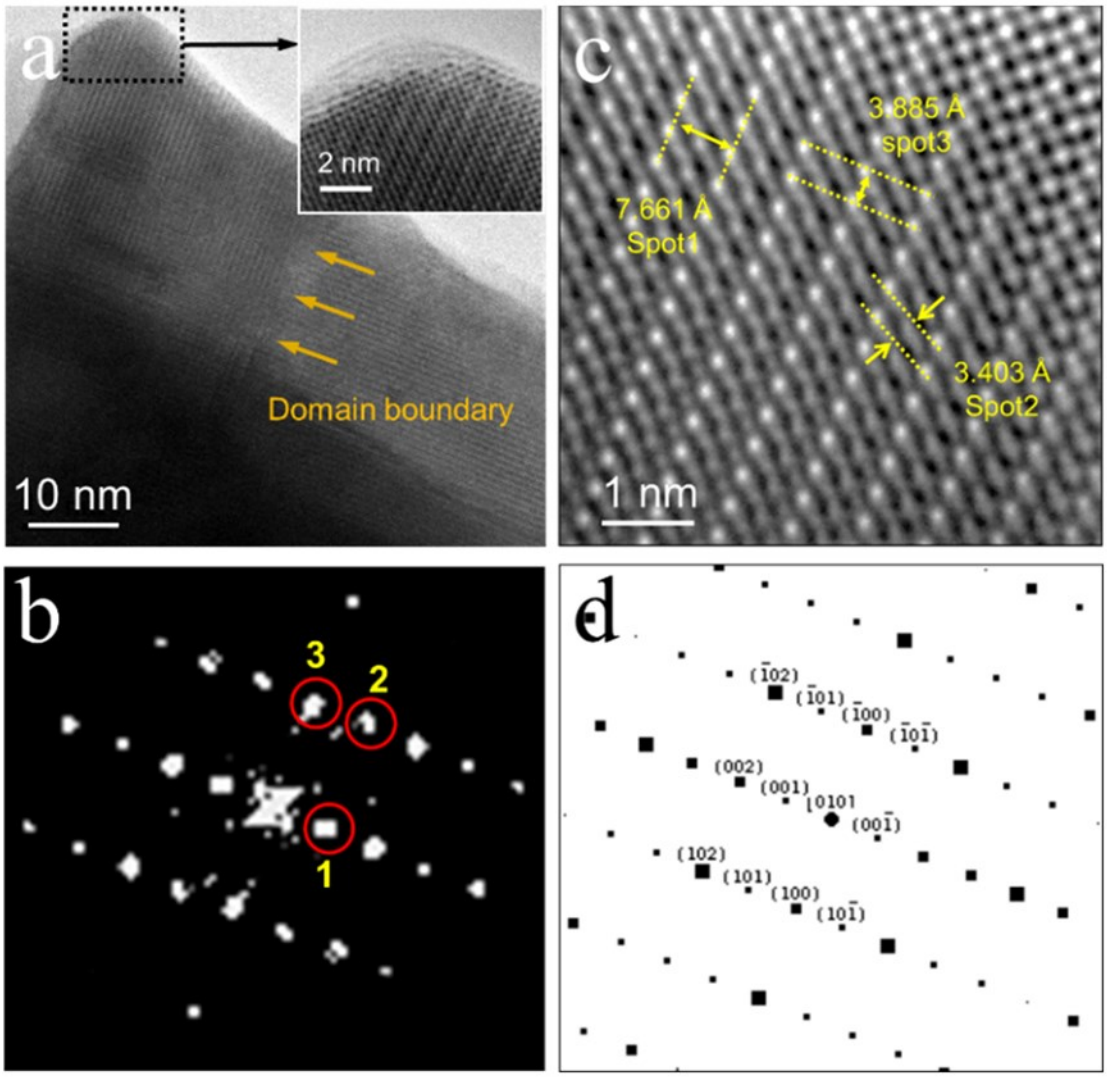

Figure AII.S 2 (a) A high-resolution TEM image of a $NdBa_{0.75}Ca_{0.25}Co_{1.5}Fe_{0.5}O_{5+\delta}$ (NBCaCF- 1.5); (b) the diffractogram from electron diffraction analysis and (c) the corresponding crystal planes shown in (c); (e) the simulated diffractogram of orthorhombic $NdBaCo_2O_{5.38}$ (space group: P/mmm). The zone axis is [010].

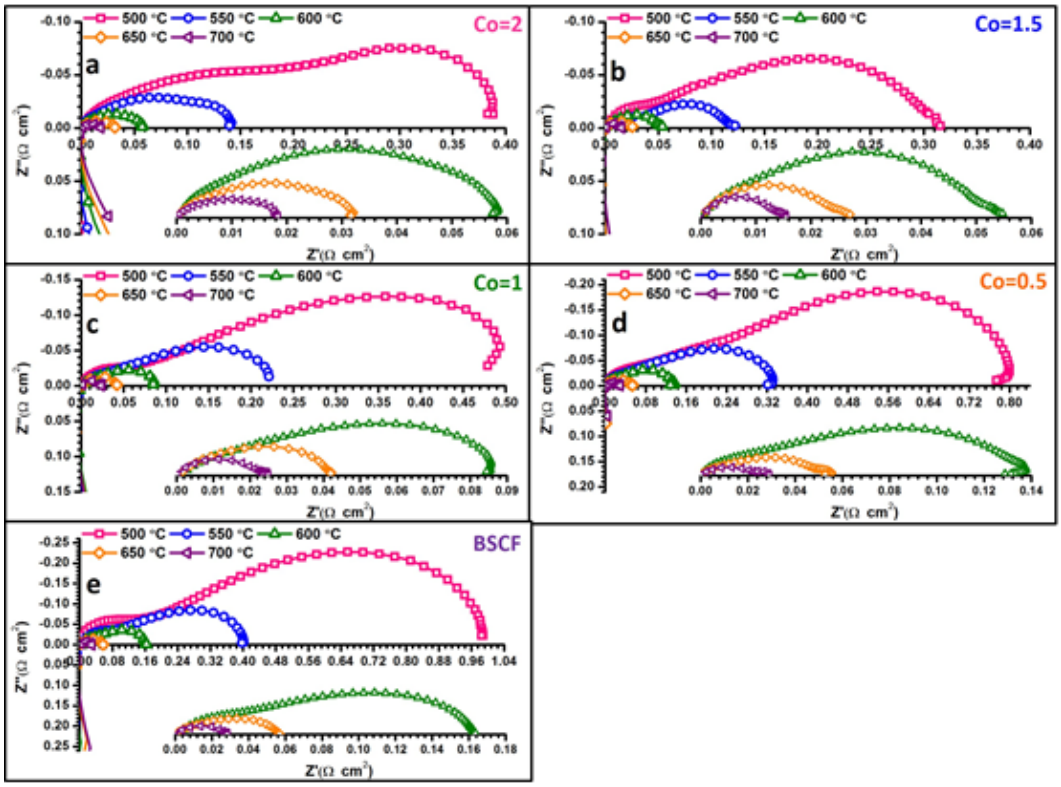

Figure AII.S 3 EIS of symmetrical cell with (a-d) NBCaCF-GDC and (e) BSCF-GDC electrode materials.

The $NdBa_{0.75}Ca_{0.25}Co_{1.5}Fe_{0.5}O_{5+\delta}$ (NBCaCF-1.5)-GDC cells exhibited the best performance among all the samples. The values of its Rp were 0.315, 0.12, 0.055, 0.027 and 0.015 Ω cm^2 at 500, 550, 600, 650 and 700 °C, respectively.

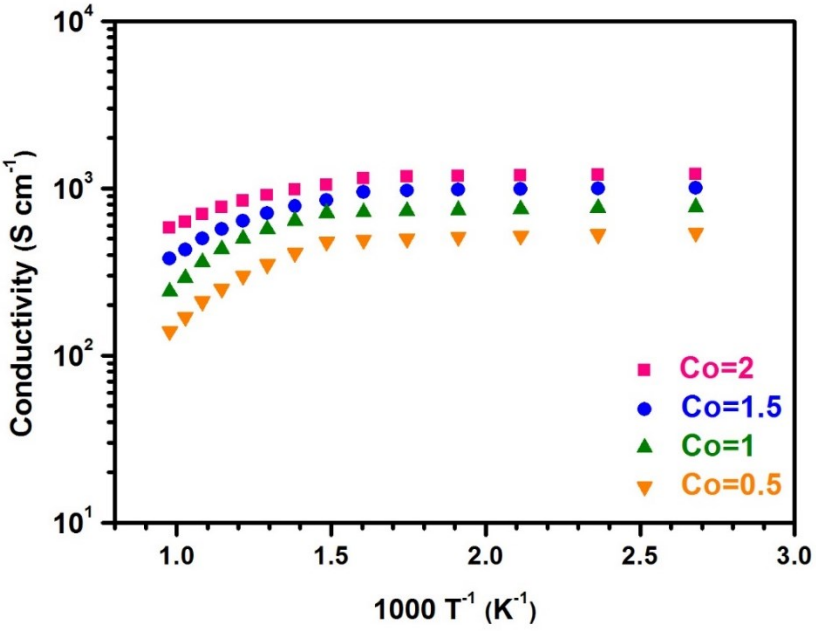

Figure AII.S 4 The electrical conductivity plots of NBCaCF as a function of temperature.

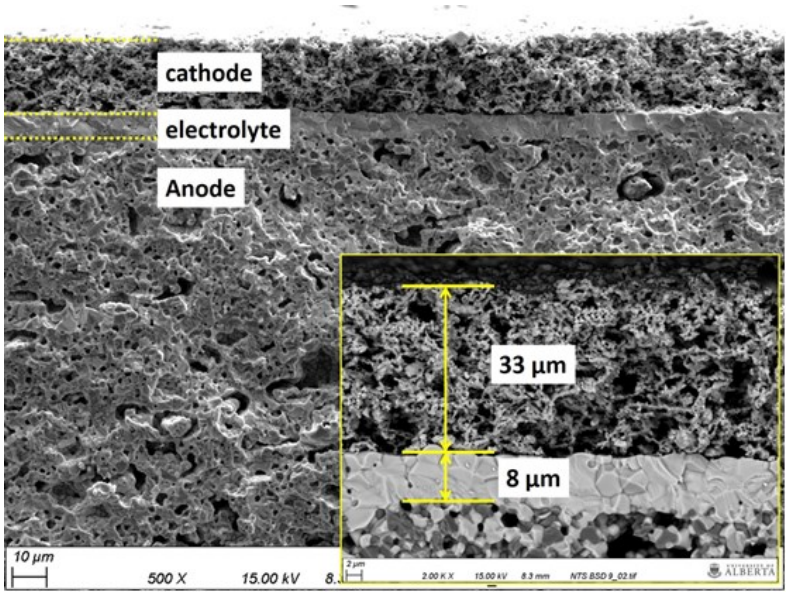

Figure AII.S 5 A typical SEM image of the cross-section microstructure of the anode-supported SOFC.

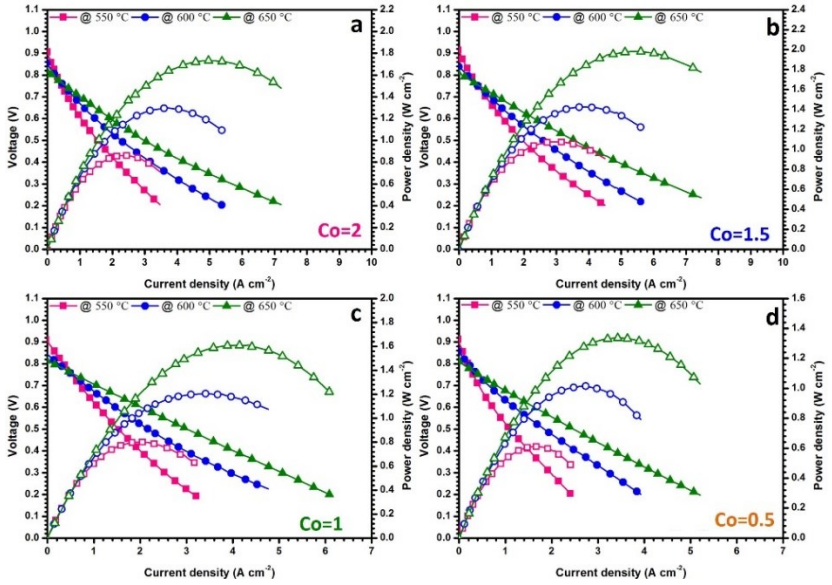

Figure AII.S 6 J-V and power density curves of NBCaCF cells in H_2 at temperatures between 550 °C and 650 °C.

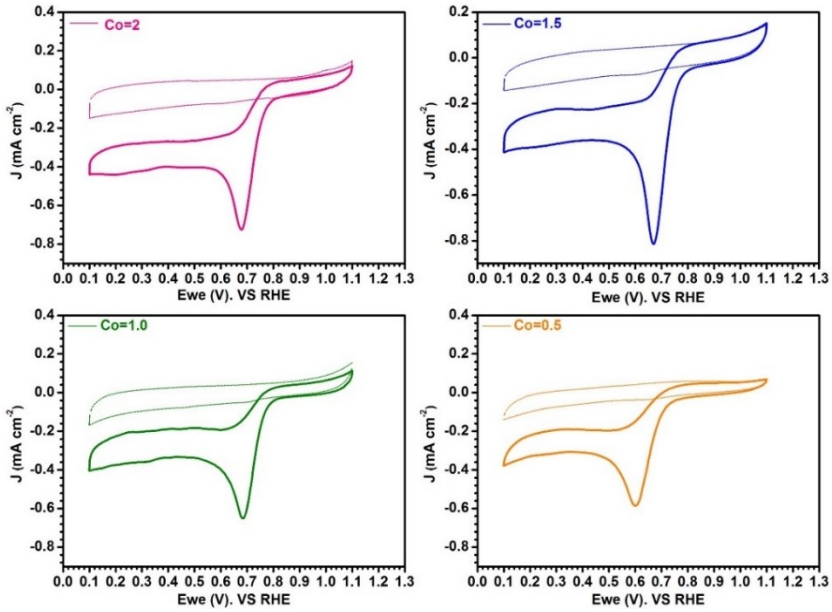

Figure AII.S 7 Cyclic voltammetry curves of NBCaCF catalysts in O_2-saturated (solid line) or Ar-saturated electrolyte solution (dotted line).

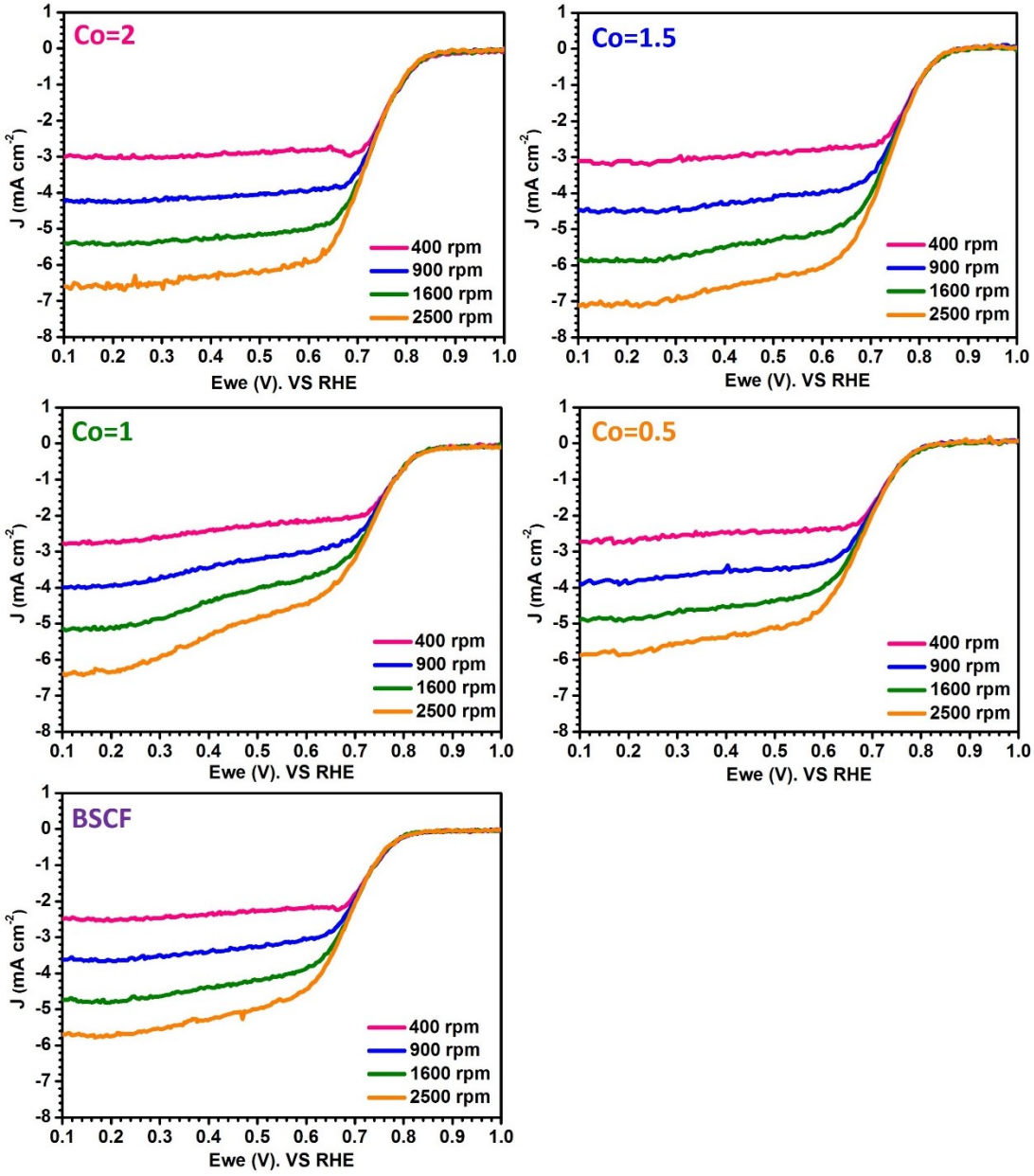

Figure AII.S 8 Linear sweep voltammetry of NBCaCF and BSCF catalysts.

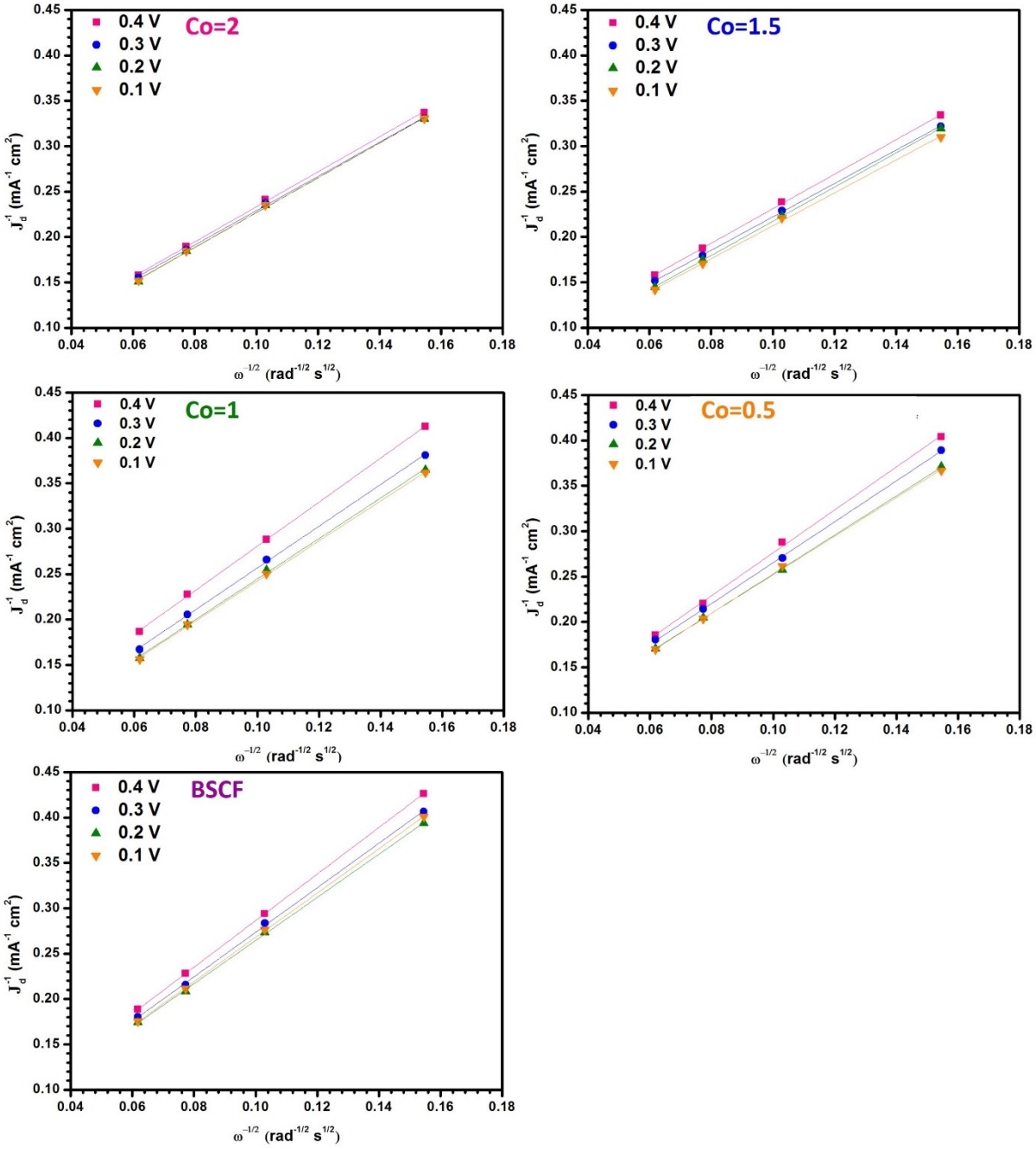

Figure AII.S 9 Koutecky-Levich plots of NBCaCF and BSCF catalysts at different potentials.

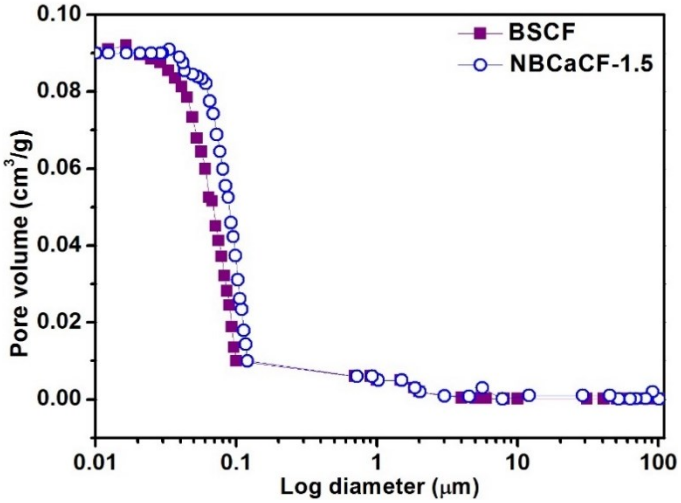

Figure AII.S 10 Pore size distribution measurement of NBCaCF-1.5 and BSCF. The two electrodes exhibited essentially identical pore-size distribution.

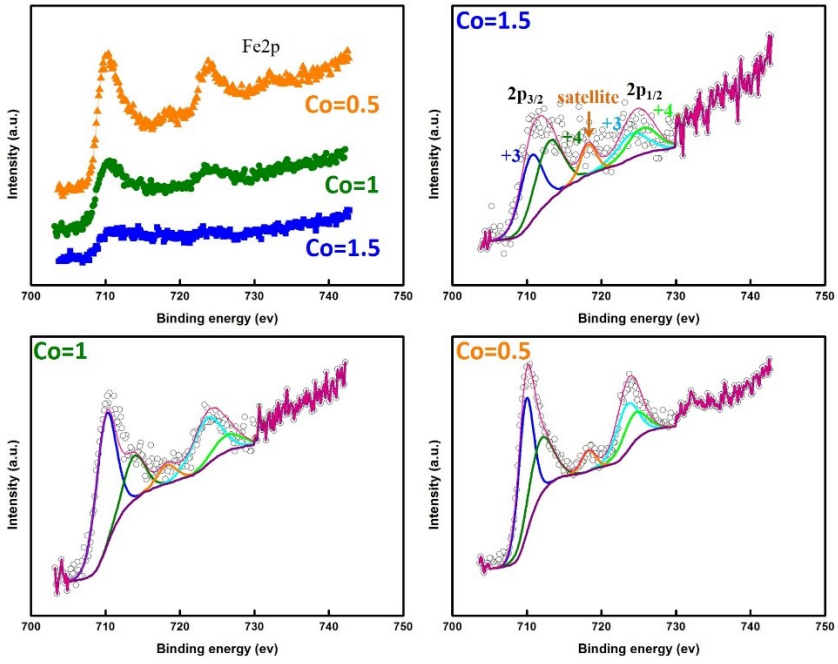

Figure AII.S 11 High resolution XPS spectra of Fe 2p for NBCaCF samples. The Fe^{4+} / (Fe^{4+} + Fe^{3+}) ratio increased with increasing the content of Fe in order to maintain the electrical neutrality.

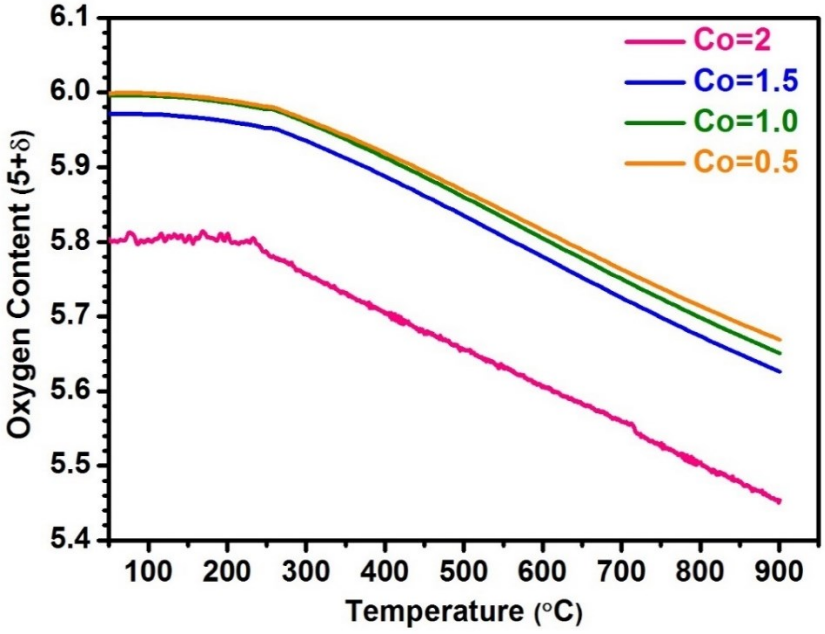

Figure AII.S 12 Oxygen nonstoichiometry of NBCaCF as function of temperature.

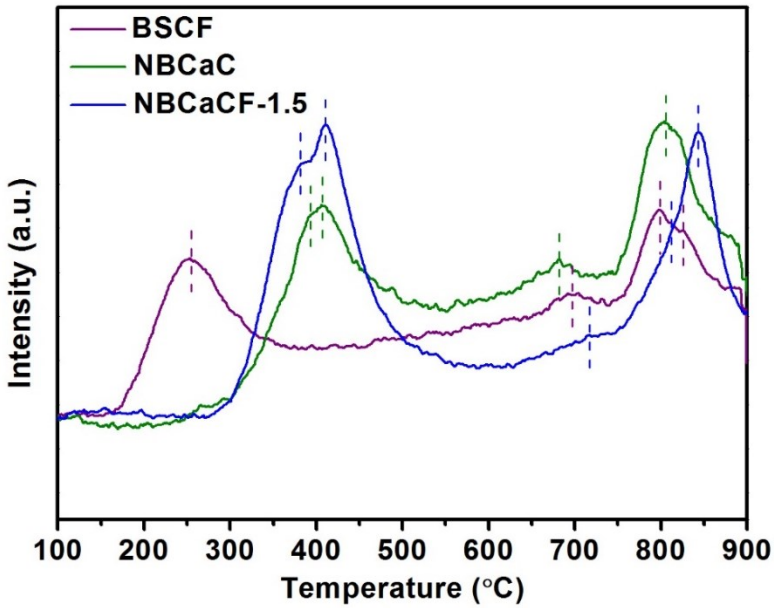

Figure AII.S 13 O_2-TPD spectra for different catalysts

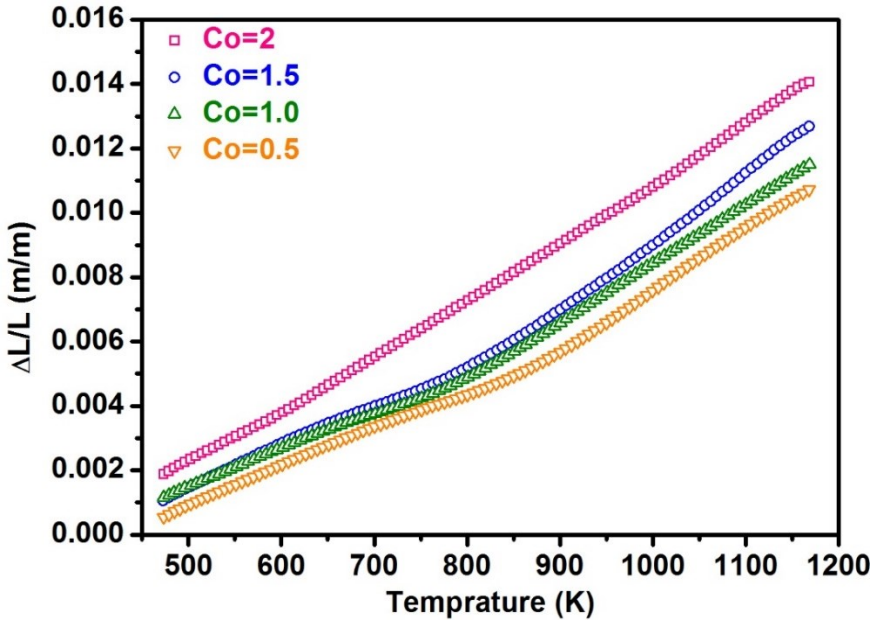

Figure AII.S 14 Temperature-dependent thermal expansion of the NBCaCF materials.

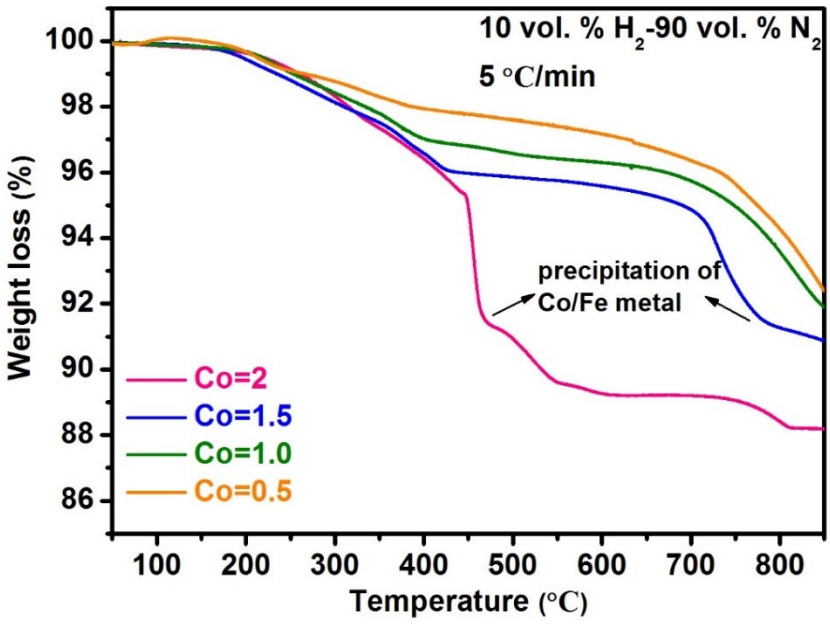

Figure AII.S 15 Temperature-dependent thermal expansion of the NBCaCF materials.

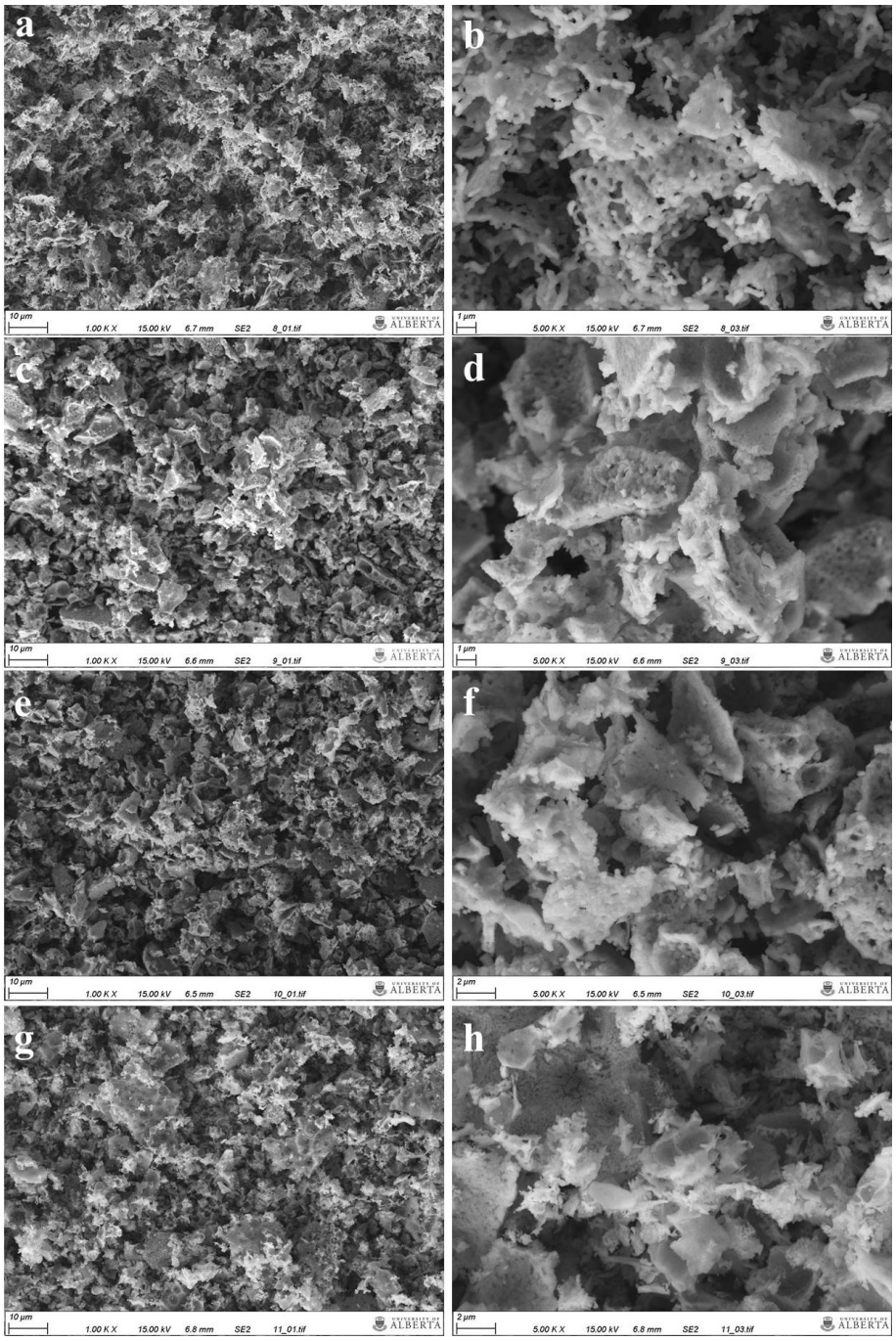

Figure AII.S 16 Microstructures of as-prepared NBCaCF powders for (a, b) Co=2, (c, d) Co=1.5, (e, f) Co=1.0 and (g, h) for Co=0.5.

Table AII S.1 A comparison of the half-wave reduction potentials ($E_{1/2}$) for ORR of the noblemetal-free electrocatalysts published recently.

Materials	**Journal, Year, volume, first page**	**$E_{1/2}$ vs RHE**	**Electrolyte**
$MnCo_2O_4$/N-rmGO	J. Am. Chem. Soc., 2012, 134, 3517	0.88	0.1 M KOH
N-doped	Chem. Eur. J., 2016, 22, 501	0.75	0.1 M KOH
N, S, O-doped mesoporous carbon	J. Am. Chem. Soc., 2014 136, 8875	0.75	0.1 M KOH
Nanostructured Mn oxide	J. Am. Chem. Soc., 2010, 132, 13612	0.75	0.1 M KOH
NBCaCF-1.5	This study	0.74	0.1 M KOH
LT-$Li_{0.5}CoO_2$	Nat. Commun., 2014, 5, 3949	0.68	0.1 M KOH
$LaCu_{0.5}Mn_{0.5}O_3$	Nat. Chem. 2011, 3, 546	0.64	0.1 M KOH
Fe_3O_4/N-GAs	J. Am. Chem. Soc., 2012, 134, 9082	0.56	0.1 M KOH

Table AII S.2 Specific surface areas of the catalysts.

Sample name	**Specific surface areas (m^2 g^{-1})**
NBCaCF-1.5	11.71
BSCF	11.75